EFFECT OF IMPACT DEFORMATION ON MATERIAL MICROSTRUCTURE

ZHANG BAO

NATIONAL UNIVERSITY OF SINGAPORE

2010

EFFECT OF IMPACT DEFORMATION ON MATERIAL MICROSTRUCTURE

ZHANG BAO

(B.Eng., Xi'an Jiao Tong Univ.)

A THESIS SUBMITTED FOR THE DEGREE OF DOCTOR OF PHILOSOPHY

DEPARTMENT OF MECHANICAL ENGINEERING

NATIONAL UNIVERSITY OF SINGAPORE

2010

Acknowledgements

In the course of carrying out this research, I received great help and careful guidance from my supervisor, Professor Victor P.W. Shim. I would like to express my sincere gratitude to him for his patience, and his efforts in creating a positive research environment. From our interactions, I gained not only knowledge related to research, but also an awareness of the importance of being an effective communicator. He has impressed me with his mentorship.

I would also like to thank the laboratory officers, Mr. Joe Low Chee Wah and Mr. Alvin Goh Tiong Lai, for their technical support in the undertaking of this research, and for their pleasant disposition that made interactions in the laboratory a positive experience. Heartfelt thanks are also especially due to friends and colleagues in the Impact Mechanics Laboratory; they shared their invaluable experience and contributed to building an enjoyable environment in the Laboratory.

My special thanks to the lecturers of courses I read, for imparting their knowledge and sparing precious time to answer questions I raised.

I would also like to express my heartfelt gratitude to my parents for their constant support and encouragement.

Lastly, I am grateful to Singapore and NUS for providing me a Research Scholarship, and to NUS staff for their indispensable help.

Table of Contents

Summary

Efforts to improve material strength are of practical significance for engineering applications. Improvement in material strength leads to an extension of the range at which a material can be used to sustain a load, as well as savings in material usage in fabricating structures to carry given loads. Grain refinement is an effective approach to improving the strength of polycrystalline materials. A method that has attracted growing interest in the past two decades is subjecting a material to large deformation. Several techniques for this have been developed, such as reciprocating extrusion, equal-channel angular pressing and high pressure torsion. These techniques are characterized by low-strain-rate deformation at room temperature, and exhibit several associated limitations. With regard to gross deformation, a concern is how the microstructure evolves as a result of different work hardening rates in different stages of deformation. As with efforts towards grain refinement, studies on work hardening are undertaken mostly at low strain rates and room temperature. This motivates the present investigation into the effect of varying strain rate and ambient temperature on the resulting microstructure of materials subjected to large deformation. Oxygen-free high conductivity (OFHC) copper is chosen as the material of study, and uniaxial single compression is the deformation mode.

The strain rates imposed in the present study encompasses those in the order of $10^3 s^{-1}$, resulting in significant temperature increases during plastic deformation. This potentially affects the microstructure evolution, and therefore evaluation of the temperature rise is made by determining the inelastic heat fraction (IHF) value. An approach that combines dynamic deformation, infrared (IR) photography and finite element simulation is established to determine the IHF value of metals subjected to uniaxial single compression. OFHC copper specimens are dynamically compressed

and infrared thermographs captured at a rate of 1,000 images/s. FEM simulation of the deformation using ABAQUS is undertaken and the initial IHF value input adjusted until the computed average surface temperature as well as the temperature distribution matches the experimental data. A value of 0.7 is identified as the IHF value of OFHC copper. It differs from the commonly-assumed figure of 0.9, but is similar to values obtained experimentally by others for deformation by tension and compression, thus supporting the validity of the current approach. This value is subsequently used to calculate the temperature rise and to analyze the associated microstructural change.

The effect of varying ambient temperature on the resulting microstructure is investigated. Material samples are deformed by uniaxial single compression at two ambient temperatures – room temperature (RT) and liquid nitrogen temperature (LNT). At RT, dynamically-deformed samples become softer, in contrast to quasi-statically deformed samples, which show a hardness close to the saturation value. This is the case for both initially hardened and annealed samples. The microstructure of impacted samples is characterized by deformation twins existing either individually, or intersecting one another, as well as equiaxed micron-sized grains. The temperature rise predicted using a modified Johnson-Cook model and an analysis of the kinetics of recrystallization suggest that grains nucleate during impact and grow thereafter, leading to softening of the material. At LNT, the hardness of quasi-statically-deformed samples is slightly higher than the saturation HV value. This is attributed to the suppression of dynamic recovery. Nano-scale twins are observed in the deformed material. The hardness of dynamically-deformed samples at LNT exceeds the saturation HV value by 16%, and the resulting microstructure includes nano and ultrafine grains, as well as shear bands with a composite structure comprising

amorphous and crystalline phases, while twins are scarce. The nano-grains observed are deduced to have been evolved through rotational dynamic recrystallization, and a true strain exceeding 2.3 is required for the formation of such fine grains. Initiation of the shear bands results from very high localized strains, and the variation in gain size between neighbouring bands is associated with the direction of shear that initiates them. The generation of nanograins points to a higher dislocation storage capacity at LNT than at RT.

The effect of strain rate on the resulting microstructure of materials subjected to uniaxial single compression at LNT is examined using TEM, XRD and DSC. A difference in strain rate leads to a change in the density, character and arrangement of dislocations, as well as the size and configuration of dislocations cells/(sub)grains in the deformed sample. At the lowest strain rate, in the order of 10^{-2} /s, dislocations are almost homogeneously distributed. When the strain rate is increased to 10^{0}-10^{5} /s, dislocations group together and collect at the walls of dislocation cells. In general, the increase in strain rate leads to two effects – enhancement of dislocation storage and a rise in temperature. The former contributes to a reduction in the size of (sub)grains and an increase in the misorientation angle of dislocation cells, while the latter favours the initiation of recovery, leading to a change in the character and arrangement of dislocations with strain rate. A threshold strain rate of $10^{3}s^{-1}$ is identified for the formation of localized deformation bands. These bands are composed of grains that are significantly smaller than those outside them, as well as those obtained at strain rates lower than $10^{3}s^{-1}$. Amorphization is identified as a deformation mechanism in structures consisting of grains smaller than ~13nm and this offers an explanation for the 'inverse Hall-Petch effect'. A model that illustrates the initiation and propagation of an amorphous phase during deformation is proposed.

Based on experimental results, two findings are highlighted regarding techniques for grain refinement by subjecting materials to gross deformation: (i) an increase in the value of the Zener-Hollomon parameter, which incorporates strain rate and temperature in a single expression, leads to higher strength, for deformation to a common strain; (ii) a strain rate in the order of $10^2 s^{-1}$ facilitates generation of nanometer-sized grains.

List of Tables

List of Figures

Chapter 1 – Introduction

The plastic deformation of metallic materials to moderate final plastic strains (<0.5) has been extensively studied by researchers; Taylor [1] and Hirsch [2] developed quantitative theories to predict the stress-strain behavior of a deformed material, while Zerilli and Armstrong [3], Follansbee and Kocks [4] established constitutive models to describe the responses of materials deformed to moderate strains. Others such as Bay et al. [5], Kuhlmann-Wilsdorf and Hansen [6] have summarized the resulting microstructural characteristics.

Over the past two decades, much research interest has been focused on metallic materials deformed to large strains. The investigations can be classified into two categories according to their objectives: (i) to elucidate the evolution of the microstructure to account for different work hardening behaviors corresponding respectively to Stages Ⅲ, Ⅳ and Ⅴ [7-11]; (ii) to refine an originally coarse-grained structure to the ultrafine/nanometer regime in order to improve the mechanical properties of the processed material [12-14]. Studies connected with work hardening have revealed different rates of generation and annihilation of dislocations in Stages Ⅲ, Ⅳ and Ⅴ, occurring either in dislocation cell walls or the cell interior [7, 15], or associated with specific types of dislocations (i.e. screw or edge dislocations) interacting in each stage [16, 17], that cause different rates of work hardening. However, these investigations have mostly been carried out at relatively low strain rates, usually below 10/s (cf. [19-29] for more recent examples). This leaves a relatively unexplored area of study in terms of microstructure evolution at higher rates deformation.

Investigations that focus on grain refinement have demonstrated gradual subdivision of coarse grains, leading to the formation of a structure with refined grains and high-angle grain boundaries [12, 18]. Several severe plastic deformation (SPD) techniques such as equal-channel angular pressing (ECAP) [30], high-pressure torsion (HPT) [31], accumulative roll-bonding (ARB) [32] and multiple forging (MF) [33] have been developed to produce ultrafine grained structure. However, the grains obtained from these techniques exhibit a saturation size; e.g. for copper, the grain sizes resulting from ECAP, HPT and MF all saturate at a minimum of 0.2-0.3 microns (μm) [34, 35, 19]. Tao and Lu [36] attributed this saturation to the low strain rates (<1 /s) applied in these conventional SPD techniques, which favors the initiation of recovery and hence lowers the dislocation storage in the deformed material. Therefore, high rate deformation, which is envisaged to be capable of suppressing recovery kinetics [37], is undertaken in the present study to examine whether the saturation grain size can be reduced.

At high strain rates, plastic deformation is essentially adiabatic. Consequently, the material being deformed would experience rapid heating due to conversion of plastic work into heat, leading to a significant rise in temperature if the plastic strain is large. This rise in temperature may cause a change in the microstructure; e.g. when the temperature is increased to ~0.4 T_m (melting temperature), the microstructure formed during deformation can be eliminated through the operation of thermally activated recrysallization. Thus, quantification of the temperature rise is useful in understanding the evolution of microstructural changes during deformation. The temperature rise increases with the value of the inelastic heat fraction (IHF), also termed the Taylor-Quinney constant. However, there seems to be no consensus on the value of the IHF.

Therefore, determination of the IHF is necessary in order to analyze the temperature rise and the associated microstructural change.

The present work aims to investigate the effect of varying the strain rate on the microstructure of a metallic material deformed to a large strain, and to explore the possibility of producing grains smaller than that corresponding to saturation associated with conventional SPD techniques; this is done via impact deformation. This study complements existing investigations on the microstructure of materials subjected to gross plastic deformation and has significant implications regarding values of high strain rate that can potentially lead to finer grains. In this work, polycrystalline OFHC copper is selected as the material studied because it is easily available, possesses good ductility and there is abundant existing data that can be used for comparing the results obtained with. This thesis is organized as follows: Chapter 2 is a literature review of investigations related to the mechanical properties and microstructure of metallic materials deformed to large strains; in Chapter 3, an approach that combines dynamic deformation, infrared (IR) photography and finite element simulation is established to determine the IHF value of metals. This is applied to OFHC copper, and yields an IHF value that is subsequently used to calculate temperature increases. Chapter 4 describes the microstructure and strength of samples deformed at two different ambient temperatures – room temperature (RT) and liquid nitrogen temperature (LNT). At RT, the saturation grain size and strength are re-examined by subjecting the samples to multiple forging. In addition, evolution of the microstructure and strength of samples subjected to quasi-static and dynamic deformation are examined. At LNT, samples are deformed at two strain rates in the order of 10^{-2} /s and 10^{4} /s, and the resulting microstructure and strength are compared with those for deformation at RT. Chapters 5 focuses on comparison of the

microstructure and strength of samples deformed at a common LNT but at different strain rates, ranging from 10^{-2}-10^{5}/s. Attention is paid to the defect energy stored as well as the mechanisms and models accounting for the microstructure formed at each strain rate. In addition, the effect of strain rate on the density, interaction and arrangement of dislocations is also discussed. Finally, Chapter 6 draws conclusions from the work done and provides recommendations for future work.

Chapter 2 – Literature Review

2.1 Work hardening at large strains

2.1.1 Rate of work hardening

It is well-known that for metallic materials subjected to cold deformation, the resistance to dislocation glide gradually increases with the degree of plastic deformation; this is reflected by the rise in stress with strain, as shown schematically in Figure 2.1(a). The rise of stress with strain is termed "work hardening" and the slope of the stress-strain curve is labeled the work hardening rate or work hardening coefficient. According to the characteristics of the work hardening rate, the plastic flow characteristics of a metallic material experiences five stages, as shown in Figure 2.1(b).

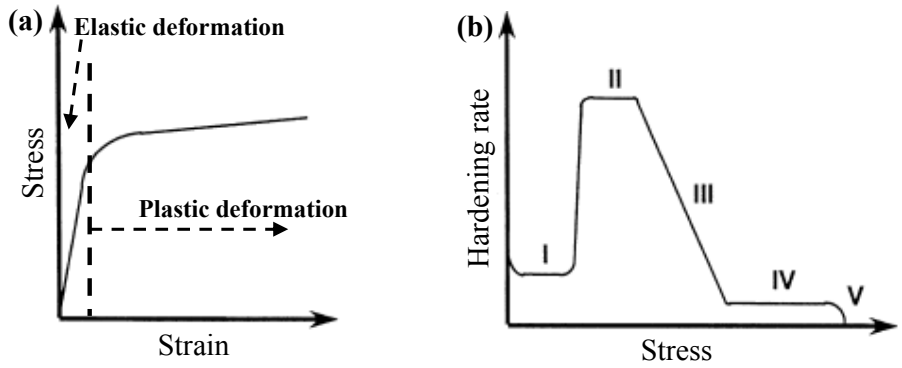

Figure 2.1 Schematic depictions of the variation of (a) stress with strain (b) work hardening rate with stress, during deformation [38]

Stages I and II are characterized by constant hardening rates and are considered athermal hardening processes. In stage III, the hardening rate decreases with stress due to the initiation of dynamic recovery, whereas in stage IV it assumes a constant low value. Stage V represents the transition to a steady state at which the stress achieves saturation. The work hardening behavior depends on the dislocation

structure [38], which is affected by the strain rate and temperature applied during deformation. Therefore, the differences in the hardening rates shown in Figure 2.1(b) reflect the changes in the dislocation structure when deformation progresses from one stage to the next.

2.1.2 Dislocation structure

In stage I, dislocation glide takes place on the primary slip system – i.e. the one with the largest resolved shear stress, and the dislocation structure is characterized by the formation of dislocation dipoles. This results from elastic interaction of dislocations of opposite signs generated from sources on different but parallel slip planes [39]. Moreover, the dislocation dipoles are principally of an edge type, because edge dislocations of opposite signs gliding on parallel planes tend to form stable dipoles, whereas screw dislocations of opposite signs attract each other and can annihilate by cross slip.

Upon approaching stage II, non-primary slip systems are activated due to their resolved shear stresses attaining the critical value for slip. These dislocations react with those on the primary slip system, resulting in the formation of barriers to dislocation glide, and thus the hardening rate in stage II is elevated compared to that in stage I. The dislocation structure in stage II is characterized by a Taylor lattice with one or more Burgers vector [8].

In stage III, dislocations densify locally to form walls and the dislocation structure is characterized by a roughly equiaxed mosaic block structure [8]. Dislocation-based models [40-45] have been proposed to describe the gradual decrease in the work hardening rate. These models, relating stress to total dislocation density, are able to account for the hardening behavior in stage III. However, they predict a continual

decrease of the work hardening rate to zero, which contradicts the fact that the decrease in the hardening rate is interrupted by the appearance of stages IV and V. Nevertheless, it is now generally accepted that the decrease in the work hardening rate in stage III is a result of dynamic recovery [38, 39].

Argon and Haasen [15] proposed a model that focused on explanation of athermal hardening in stage IV. They idealized the microstructure in stage III and IV as consisting of dislocation cells with a high dislocation density at cell walls and negligible dislocation density within cells. They also assumed that recovery occurs only in the cell walls, whereas hardening takes place in both cell walls and within cells by the accumulation of dislocations and the build-up of long range stresses resulting from increasing misorientation between cell walls and the cell interior. According to their model, at the end of stage III, hardening and recovery in the cell walls have reached a balance, so that the athermal hardening in stage IV arises only from hardening in the cell interior. The authors further stated that when the long range stress in cells interiors in stage Ⅳ increases to a critical value that triggers stress relaxation by dislocation glide on non-primary slip systems, stage IV terminates and stage V starts. Based on this model, the hardening rate in stage IV was correctly predicted.

Although models such those in [40-45, 15] have resulted in the prediction of hardening rates consistent with experimental results, they work only for a specific work hardening stage. Subsequently, Estrin et al. [7] presented a model capable of predicting all the stages of work hardening at large strains, encompassing stages III, IV and V. This model is based on the experimental finding that the volume faction of dislocation cell walls decreases with strain. The predicted work hardening rate at each stage agreed closely with experimental results. It was also found that contrary to the

idealization made in [15], which assumed that the dislocation density in the cell interiors was many orders of magnitude fewer than that in the cell walls, the dislocation density within cells is a few percent of that in the cell walls. More importantly, these cell interior dislocations contribute to work hardening significantly and thus can not be neglected. Furthermore, it is realized that the decrease in the volume fraction of cell walls is a crucial factor leading to the occurrence of hardening behavior in stages IV and V.

The preceding models, although different, have a common characteristic that attributes the different work hardening characteristics in stages III, IV and V to dissimilar outcomes of hardening and softening operating simultaneously during deformation. Alternatively, Zehetbauer and Seumer [16] related the difference in hardening characteristics to the different type of dislocations interacting in each stage. Numerous experiments have shown that stages II and IV correspond to dislocation storage, while stages III and V are characterized by simultaneous occurrence of dislocation storage and annihilation. Experimental results also revealed that in stage III, annihilation proceeds by cross slip of screw dislocations, whereas in stage Ⅴ, it does so by the climbing of edge dislocations. Therefore, a model related to the type of dislocation was formulated to describe the different hardening behaviors in each stage. At the beginning of deformation, e.g. stage Ⅱ, both screw and edge dislocations are stored. With the progression of deformation, the stress increases to a critical value that enables cross slip of screw dislocations, and dislocation annihilation is activated, marking the start of stage III. An increase in stress causes greater annihilation of dislocations, and finally the generation and annihilation of screw dislocations reach a balance. This means that screw dislocations become ineffective in generating hardening in subsequent stages, whereas edge dislocations which are continuously

stored in stage III will dominate the hardening processes. Therefore, the constant hardening rate in stage IV is a consequence of the storage of edge dislocations. As with stage III, edge dislocations annihilate each other in stage V, leading to a decrease in the work hardening rate, and eventually also reaching a balance in terms of the generation and annihilation of edge dislocations. Consequently, after stage V, the total dislocation density becomes constant, resulting in a saturation of stress and hardening disappears. This model was adopted by Zehetbauer [17] and was substantiated by successful prediction of hardening behavior at large strains.

The models in [7, 15-17] are concerned primarily with the variation in the density of dislocations as the cause of different hardening rates in stages III, IV and V. Ungar and Zehetbauer [10], and Muller et al. [9] have shown that the dislocation structure in cell walls experiences a fundamental change when deformation proceeds from stage III to stage IV. In stage III, the cell wall structure assume the form of polarized dipolar walls (PDWs), whereas during the transition to and in stage IV, polarized tilt walls (PTWs) gradually form. Zehetbauer et al. [46] and Zhong et al. [47] confirmed the transition of the dislocation structure from PDWs to PTWs accompanying the deformation from stage III to stage IV. Furthermore, they noticed that such a transition in the dislocation structure is related to the variation of a parameter termed "dislocation arrangement". In the transition between stages III and IV, the value of the dislocation arrangement displays a local minimum. A more recent description of dislocation structure transition and the variation in the value of the dislocation arrangement was provided by Schafler et al. [11] and reproduced in Figure 2.2. Figure 2.2 depicts schematic diagrams of cell structures in stages III and IV respectively. As shown in Figure 2.2(a), the cell walls in stage Ⅲ are thick and most of the dislocations along the interface between the cell walls and the cell interior align with

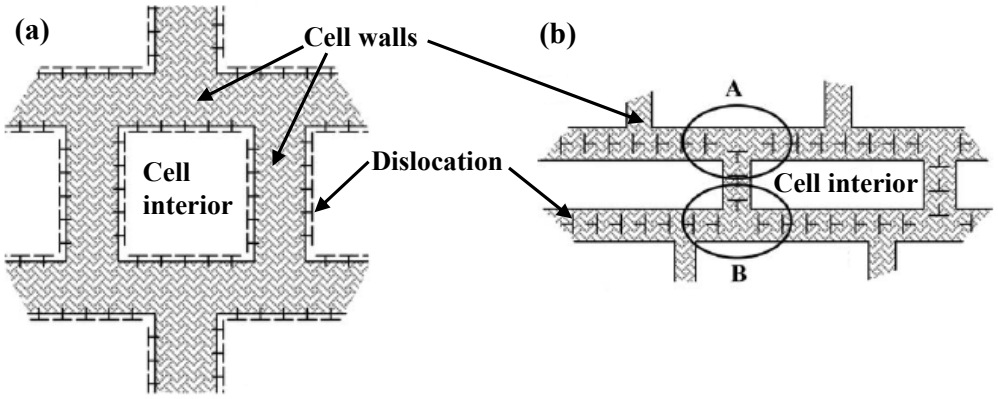

Figure 2.2 Schematic drawing of the cell structures in (a) stage III (b) stage IV [11]

the respective cell walls. (However, these boundary dislocations glide along different slip systems.) Note that dislocations on different sides of a cell wall are of opposite sign because of polarization between dislocations on opposite sides of a cell (interior). Such a dislocation structure in is termed "PDW" (polarized dipolar walls). In stage IV, the cells are elongated, the cell walls become thinner than those in stage III, and the dislocation arrangement becomes typical of low angle grain boundaries; such a dislocation structure, shown in Figure 2.2(b) is termed "PTW". Note that symmetry of the PTW structure is less than that of the PDW structure. For example, at the positions labeled A and B in Figure 2.2(b), symmetry of the tilt walls is frustrated along a complete path around a cell-interior region. The transition of the dislocation structure from stage III to stage IV is reflected by the decrease in the value of the dislocation arrangement parameter, as shown in Figure 2.3. At early stages of deformation, the value of the dislocation arrangement parameter is relatively high. However, towards stage IV, it gradually decreases and maintains an almost constant low level. This indicates that effective screening of the strain field of dislocations occurs during the transition from stage III to stage IV. The decrease in the dislocation arrangement parameter also indicates the transition range in which fragmentation of original grains takes place, leading to the generation of new grains with low angle boundaries.

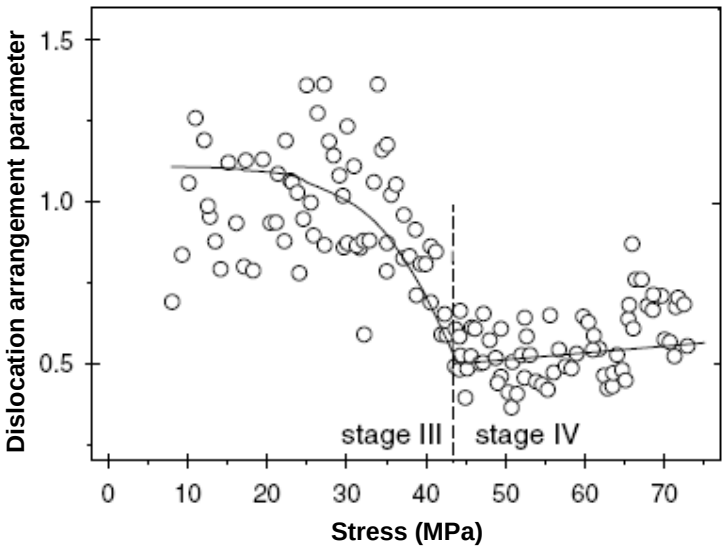

Figure 2.3 Value of dislocation arrangement parameter in stages III and IV [11]

2.2 Severe plastic deformation to refine grains

2.2.1 Background

The attainment of grain refinement has long been the objective of metallurgical research, and numerous papers have been published on this theme. However, the prevailing focus on nano-crystalline metals in recent years is attributed to the development of commonly available tools capable of identifying forces and spacings as small as picoNewtons (pN) and nanometers (nm). This enables probing of the mechanical response of materials and structure in the nano-regime.

From the perspective of grain size, metals are usually classified into three categories - micro-, ultrafine- and nano-crystalline regimes, with grain sizes larger than 1 micrometer (μ m), in the range of 100-1000nm, and smaller than 100 nm respectively. A notable characteristic of grain refinement is the increase in the volume fraction of grain boundaries, which may alter the physical, mechanical and chemical properties compared to conventional coarse-grained materials [48, 49]. Figure 2.4

shows the variation of the volume fraction of inter-crystal regions and triple-junctions with grain size. It is noted that more atoms are associated with grain boundaries as the grain size decreases.

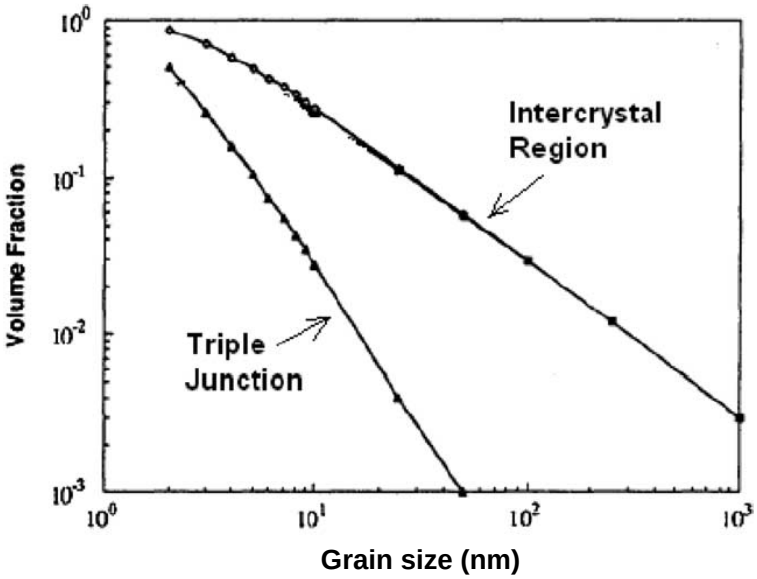

Figure 2.4 Effect of grain size on volume fraction of inter-crystal regions and triple junctions, assuming a grain-boundary thickness of 1 nm [50]

When a metal is refined into the ultrafine- and nano- regimes, it exhibits a range of positive characteristics associated with engineering applications, including higher yield and fracture strengths, higher ductility, superior wear resistance, and enhanced super-plasticity at lower temperatures and higher strain rates, compared with its microcrystalline counterparts. An example of the variation of flow stress with average grain size is shown in Figure 2.5. When grain sizes are in the micro- and ultrafine range, the yield strength is traditionally described by the Hall-Petch relationship [51, 52], where the values of σ_0 and k depend on the material. Here, the mechanism of strengthening from grain refinement is envisioned to be linked to the pile-up of dislocations at grain boundaries. However, in the nano-crystalline regime, the relationship between flow stress and grain size deviates from that at larger grain sizes, and the material is weakened when the grain size is less than 10 nm. Currently,

efforts involving experiments and computation [53] are being directed at gaining insights into this phenomenon.

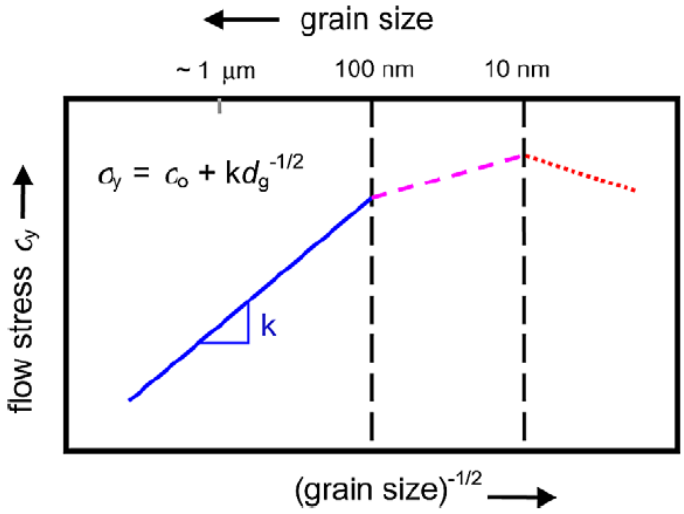

Figure 2.5 Schematic representation of the variation of yield stress as a function of grain size in micro-, ultrafine- and nano-crystalline metals and alloys [13]

Because of the unique properties of ultrafine and nano-crystalline materials, various techniques have been developed to produce ultrafine-/nano- grains. These techniques include inert gas condensation [54], mechanical alloying [55, 56], electro-deposition [57-59], crystallization from amorphous material [60, 61] and severe plastic deformation (SPD). Among these techniques, SPD possesses advantages in overcoming the difficulties associated with other techniques, such as residual porosity in samples produced by inert gas condensation and impurities in ball milling, and therefore has attracted increasing interest in recent years. In the following Sections 2.2.2, 2.2.3 and 2.2.4, SPD techniques, models describing microstructural evolution during SPD and limitations of SPD techniques will be presented.

2.2.2 SPD techniques

There are a number of processing techniques that have been used to refine grains. Humphreys et al. [18] classified these techniques into two types: redundant strain processes and directional strain processes. Redundant strain processes are performed by reversing the strain paths in each deformation cycle. Examples illustrating this to achieve high levels of redundant strains are shown in Figures 2.6 (a) and 2.6(b),

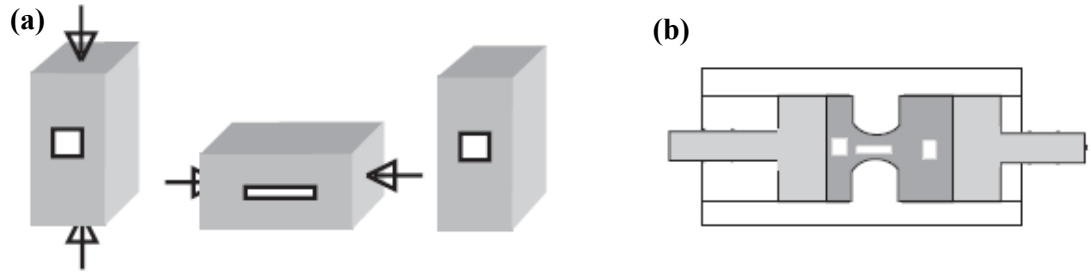

Figure 2.6 Redundant strain processes used to achieve high plastic strains (a) multiple forging (b) reciprocating extrusion [18]

which correspond respectively to multiple forging and reciprocating extrusion. Redundant strain processes have the advantage of easy execution in commercial practice. In addition, the technique of reciprocating extrusion possesses the additional advantage of being able to be applied to less ductile materials, because the material is fully constrained during processing. However, these processes are less efficient in terms of storing dislocations and breaking up the originally coarse grained structure, compared with directional strain processes. Directional strain processes have the characteristic that the strain path is not reversed. High pressure torsion (HPT) and equal channel angular pressing (ECAP), shown schematically in Figures 2.7(a) and 2.7(b) respectively, are two typical directional strain processes that have been widely used. HPT produces disk type samples, usually 10-20 millimeters (mm) in diameter and ~1 mm in thickness. Valiev et al. [62] have reported the significant change in the microstructure of a processed sample after applying half a rotation. However, several rotations are usually required for HPT to generate a homogeneous grain structure. ECAP involves fabrication of billets with a cross sectional diameter of ~20mm. The

billet is pressed through the channel as shown in Figure 2.7(b), and the strain induced during each pass is determined by the angle ϕ. As with HPT, ECAP is applied repeatedly.

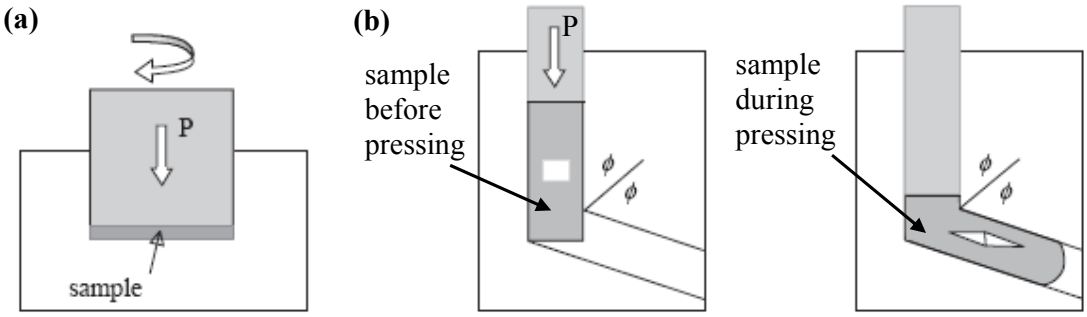

Figure 2.7 Directional strain processes used to achieve high plastic strains (a) HPT (b) ECAP [18]

2.2.3 Microsturctural evolution during SPD

From the perspective of the distribution of subgrains and grain boundaries, Humphreys et al. [18] proposed a model, describing the evolution of microstructure with increasing strain. One starts with an equiaxed grain structure, shown in Figure 2.8(a); at an intermediate strain, the initial grain is subdivided by high angle grain boundaries into regions consisting of dislocation cells or subgrains (Figure 2.8(b)).

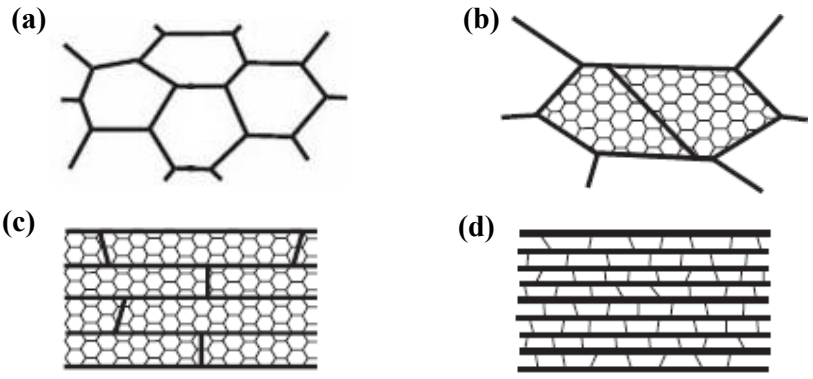

Figure 2.8 Evolution of microstructure with increasing strain (a) initial grain structure (b) subgrain and grain subdivision (c) increase in high angle grain boundaries (d) ribbon grain structure [18]

With further straining, the areas comprising high angle grain boundaries increase, although the newly formed grain boundaries exhibit no difference with that of the original grains (Figure 2.8(c)). At very large strains, some subgrains transform into high angle grains and a ribbon grain structure is formed (Figure 2.8(d)).

During plastic deformation, dislocations are generated and they move and interact with one another. By considering these, Valiev et al. [62] proposed a model, illustrating the formation of high angle grains. Figure 2.9 shows schematically the evolution of a dislocation structure; in Figure 2.9(a), the dislocations generated during deformation accumulate at the walls of dislocation cells. Due to the annihilation of dislocations of opposite signs, the cell wall becomes thinner (Figure 2.9(b)). This annihilation process also leads to the dislocation walls composed only of excess dislocations of a single sign. With the accumulation of excess dislocations at cell walls, misorientation between cells gradually increases, resulting in the transformation of a cellular structure into a granular one (Figure 2.9(c)).

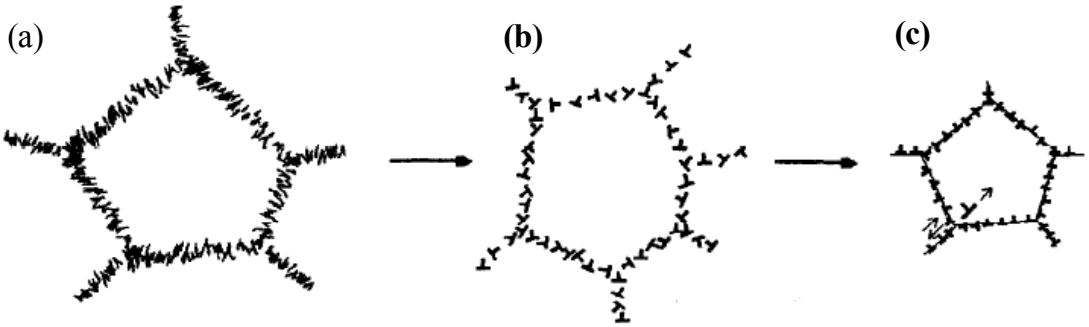

Figure 2.9 Schematic model of dislocation structure evolution during SPD [62]

The models shown in Figures 2.8 and 2.9 reveal two aspects of the roles played by dislocations – formation of a network of walls subdividing an originally coarse grain into smaller domains and dislocation accumulation at the walls, transforming dislocation cells into grains. Therefore, the size of new grains after SPD processes depends on the density of dislocations stored in the deformed material.

2.2.4 Evaluation of SPD techniques

Although SPD for grain refinement has attracted increasing interest in recent years, it is not a new technology; as early as the 1960s, grain sizes in the range of 200-500 nm in iron-0.003% carbon subjected to large strains by wire drawing have already been reported by Langford and Cohen [81]. Directional strain processes are more efficient and hence more extensively studied than redundant strain processes. In comparison with traditional metal forming techniques such as cold rolling and drawing which result in generally cellular substructures, the techniques described in Section 2.2.2 have the advantage that the resulting structures are generally granular and contain mainly high angle grain boundaries. In addition, these techniques can produce bulk materials that have a wider range of application than the thin samples from rolling. Moreover, HPT is able to refine grains of certain materials (e.g. high carbon steel [63] and Al alloys [64]) into the nano-regime and can even be applied to process brittle materials such as semiconductors and intermetallics. Despite these advantages, a noticeable limitation associated with these techniques is the saturation in grain size and strength of processed samples. Take copper for example, Zhang et al. [34] found that the size of grains from ECAP saturates at 0.26 μm, while Belyakov et al. [19] reported similar saturation values for samples prepared by MF. Figure 2.10

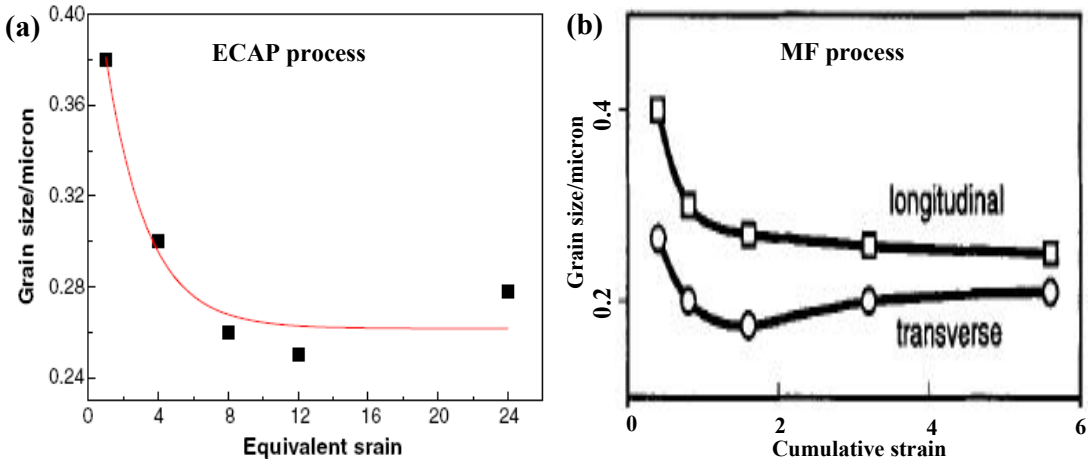

Figure 2.10 Variation of grain size with strain for copper processed by (a) ECAP [34] (b) MF [19]

shows the variation of grain size with strain. It is observed that, for both ECAP and MF processes, the grain size decreases rapidly at the early stage of deformation but changes negligibly when the strain becomes sufficiently large. Such saturation is also exhibited in terms of sample strength. Figure 2.11 show the Vickers microhardness of copper processed by HPT and ECAP. The hardness initially increases, then tends to saturation between 120 and 130 with further straining.

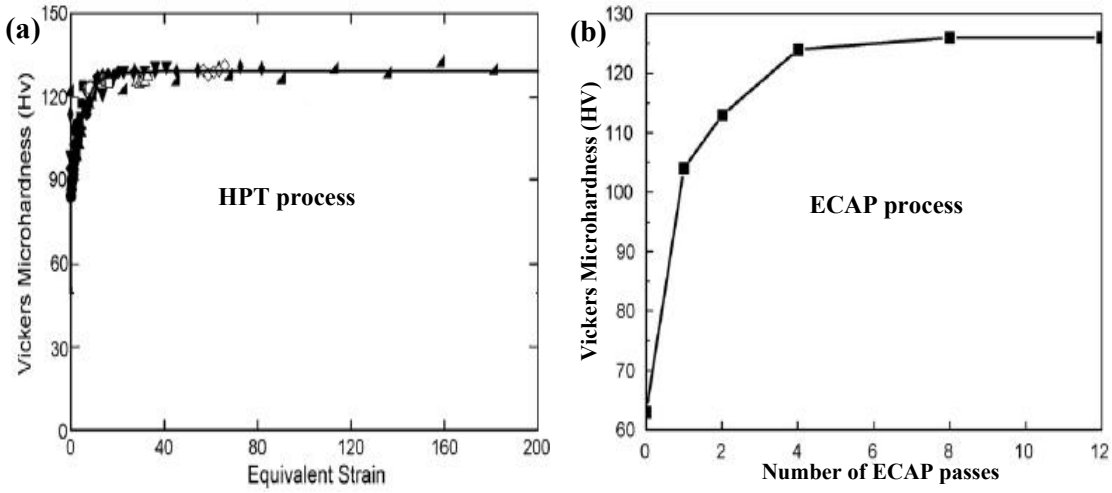

Figure 2.11 Variation of hardness with increasing straining for copper processed by (a) HPT [29] (b) ECAP [65]

2.3 Microstructure of dynamically deformed metallic materials

The severe plastic deformation techniques described in Section 2.2 are usually carried out at strain rates below 10^0 /s and at room temperature (processing brittle or hard-to-deform materials requires an elevated temperature). Investigations into the microstructure of materials subjected to deformation at higher strain rates are now reviewed. The deformations are induced at room temperature. Depending on the shape of the specimens, the following description assumes two components: (i)

dynamic deformation of hat-shaped specimens; (ii) dynamic deformation of disk shaped specimens.

2.3.1 Dynamic deformation of hat-shaped specimens

Polycrystalline fcc copper and hcp zirconium alloy have been studied [66, 67] and dynamic deformation was applied using a Hopkinson Bar. Figure 2.12 shows schematically loading of a hat-shaped specimen and the region of shear induced after deformation. For both copper and zirconium alloy, the strain rate in the shear region is

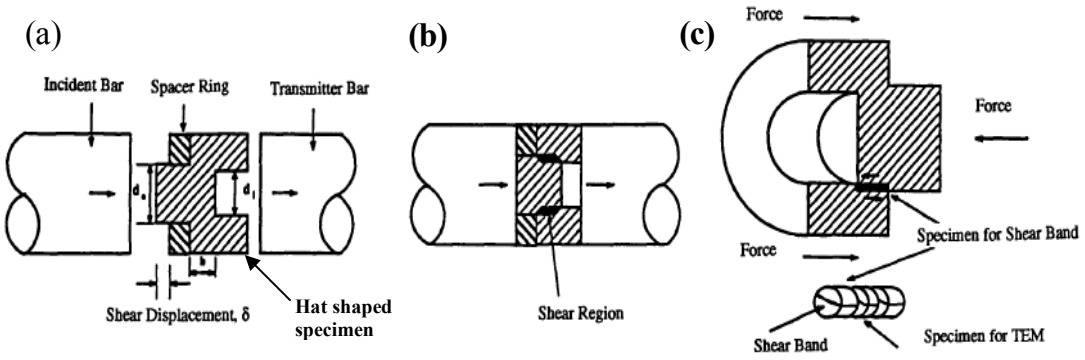

Figure 2.12 Schematic diagram of loading on a hat-shaped specimen by a Hopkinson Bar (a) specimen before compression (b) specimen after compression (c) extraction of specimen for TEM [66]

in the order of ~10^4 /s, and the resulting microstructure is characterized by equiaxed grains with sizes between 0.1-0.2 μm. Andrade et al. [66] attributed this generation of ultrafine grains to the occurrence of dynamic recrystallization, triggered by the significant temperature rise in the shear bands. Diagrammatic models have been proposed by Andrade et al. [66] and Meyers et al. [68] to depict the formation of ultrafine grains in the shear bands. Recently, more detailed descriptions of these models have been presented by Kad et al. [67] and shown in Figure 2.13. Figure 2.13(a) illustrates the generation of dislocations that accompany plastic deformation. To minimize the free energy associated with them, the dislocations rearrange to form elongated dislocation cells, as shown in Figure 2.13(b). As deformation progresses,

the cells transform into subgrains, and newly-created dislocations are blocked by the subgrain boundaries (Figure 2.13(c)). With increased deformation, the elongated subgains break up into the equiaxed structure shown in Figure 2.13(d). Subsequent deformation results in the reorientation of these equiaxed structures, arising from minimization of the interfacial energy, and leading to the formation of ultrafine grains (Figure 2.13(e)). Mishra et al. [69] noticed the similarity between the microstructure of samples prepared by ECAP and that within the shear bands; he concluded that the grain refinement model depicted in Figure 2.13 is applicable to ECAP processing.

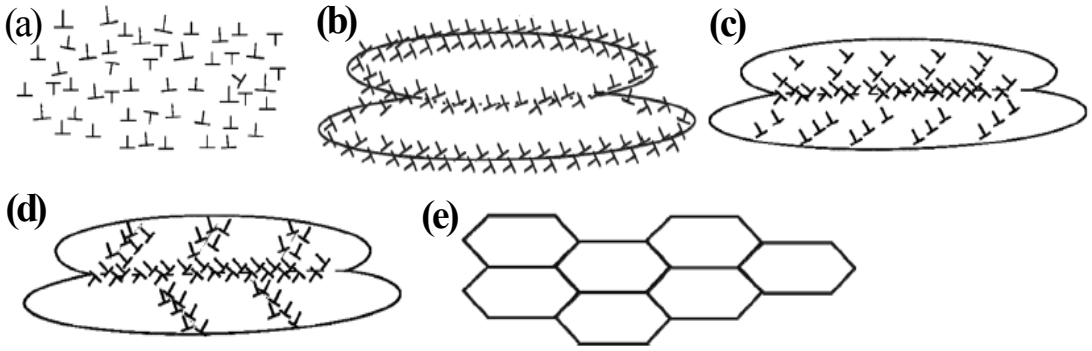

Figure 2.13 Schematic illustration of model for the formation of ultrafine grains (a) random distribution of dislocations; (b) formation of elongated cells; (c) dislocations blocked by subgrain boundaries; (d) break up of elongated sub grains; (e) reorientation of subgrain boundaries and formation of ultrafine grains [67]

Although the shear bands with ultrafine grains are only tens of microns in width, this points to the potential of using dynamic deformation to refine grains. Furthermore, dynamic deformation only requires one cycle of deformation and thereby provides a higher processing efficiency compared with the SPD techniques introduced in Section 2.2.

2.3.2 Dynamic deformation of disk shaped specimens

This line of investigation was initiated by the discovery that the density of clusters of point defects in samples deformed to fracture at high strain rates is much higher than that reported in literature. Figure 2.14 shows a disk shaped sample for

compression tests. Different impact masses, as well as different devices (e.g. gas gun, drop tester, Instron type mechanical test machine [70]) were employed to generate strain rates ranging from 10^{-2} /s to 10^{6}/s. Kiritani et al. [70, 71] deformed several fcc metals, including aluminium, gold, copper and nickel, at strain rates in the order of 10^{5} /s and observed anomalously

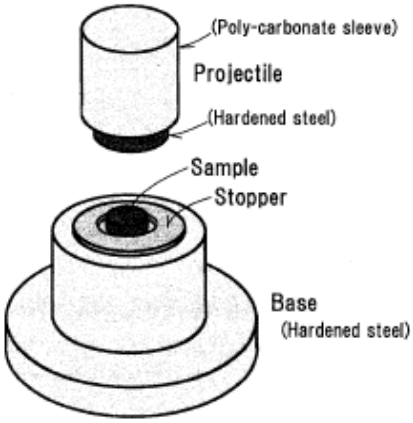

Figure 2.14 Setup of samples for compression experiments [70]

high densities of vacancy clusters at fracture tips in the deformed materials. These vacancy clusters exhibit a stacking-fault tetrahedron structure and are homogenously distributed. In addition, they noted that in regions with a high density of vacancy clusters, dislocations are totally absent. Based on experimental observations, they claimed that plastic deformation at high strain rates proceeds without the involvement of dislocations, but by the movement of small areas of atomic planes. These areas are termed glide elements, and their movement is driven by the high internal stresses generated at high strain rates. Glide elements on the same atomic plane join to form a larger glide element, while those on nearby atomic planes interact, leading to the generation of point defects. Kiritani et al. [72] described schematically, the formation of vacancy and vacancy complexes, shown in Figure 2.15, wherein the glide elements and vacancies generated are represented respectively by line segments and circles. Figures 2.15(a), 2.15(b), 2.15(c) and 2.15(d) show respectively the generation of

vacancies and vacancy complexes corresponding to different relative positions of two glide elements. Kiritani et al. [72] further analyzed that glide elements might not be very wide because of the non-uniform distribution of internal stress and non-uniform thermal vibration of atoms. Therefore,

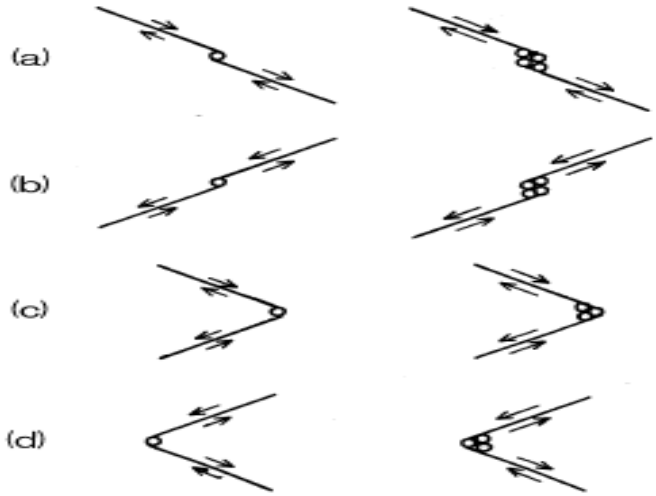

Figure 2.15 Schematic illustration of the formation of vacancies and vacancy complexes corresponding to different relative positions of two glide elements [72]

there must be an extremely high density of glide elements present to accommodate large plastic deformation. Consequently, the schematic model shown in Figure 2.16 was proposed to illustrate the evolution of microstructure during high rate deformation. In Figure 2.16, the glide elements, represented by the line segments, constitute the mechanism for plastic deformation at high strain rates (i.e. they are not dislocations that accommodate plastic deformation in conventional plasticity). Due to the high density of glide elements at large strains, considerable vacancies are generated and form vacancy clusters by diffusion. Kiritani et al. [70] and Tawara et al. [73] observed that for fcc metals, the mechanism proposed in Figure 2.16 came into operation when the strain rate exceeded 10^3 /s, below which vacancies were observed in deformed samples, but these were generated through the interaction between dislocations. In addition, they also found that 10^3 /s is the threshold strain rate for the dispersion of dislocations. Below 10^3 /s, dislocations entangle to form cell boundaries,

while above 10^3 /s, dislocations become randomly distributed. Yasunaga et al. [74] investigated the microstructure of bcc metals – vanadium, niobium and molybdenum – deformed at strain rates in the range of 10^0-10^6 /s and reported findings similar to those for fcc metals; i.e. 10^3/s is critical strain rate for the activation of the mechanism shown in Figure 2.16 leading to generation of a high density of vacancies and the transition strain rate for the dispersion of dislocations.

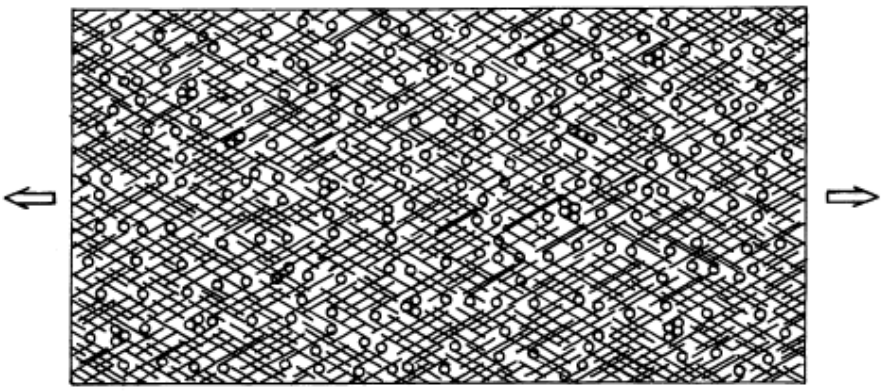

Figure 2.16 Schematic illustration of model showing the generation of vacancies through interaction of glide elements [72]

2.3.3 Evaluation of studies on microstructure of dynamically deformed metallic materials

The studies described in Sections 2.3.1 and 2.3.2 were carried out at room temperature. Both investigations show that materials with different crystal structures (i.e. fcc, bcc, hcp, etc.) subjected to the same mode of deformation, undergo similar microstructure evolution mechanisms and exhibit similar resulting microstructural characteristics after deformation. However, differences were also identified; at a strain rate of ~10^4/s, studies on hat-shaped specimens indicate that deformation occurs mainly by dislocation glide, while tests on disk shaped specimens reveal movement of atomic planes as an alternative primary mechanism that accommodates plastic deformation. Moreover, the two investigations indicate contradictions in terms of

dislocation distribution. The model shown in Figure 2.13 demonstrates that the formation of dislocation cells is an indispensable step in the production of ultrafine grains. However, the results described in Section 2.3.2 suggest that in shear bands that have experienced a strain rate is ~10^4 /s, dislocations should be randomly distributed rather than clustered at cell walls.

2.4 Microstructure of materials deformed at temperatures lower than room temperature (RT)

The microstructures and models described in Sections 2.2 and 2.3 correspond to deformation at room temperature. In this Section, the microstructures of materials deformed at temperatures lower than room temperature are presented. Three examples, referring to three different modes of deformation – multiple forging, drawing and surface mechanical grinding – are discussed to illustrate the microstructural characteristics associated with them.

2.4.1 Multiple forging

Kobayashi et al. [75] analyzed the microstructure of copper processed by multiple forging at 195K. The resulting microstructure is characterized by the intersection of deformation bands. Figures 2.17(a) and 2.17(b) are optical micrographs showing respectively the microstructures corresponding to cumulative strains of 6 and 18. The deformations bands are curved and kinked where they meet one another, and are considered microshear bands, similar to those reported in [141]. Figure 2.17 shows that an increase in strain causes an increase in the number of deformation bands, and for a strain value of 18, the deformation bands are uniformly distributed throughout the entire sample. Transmission electron microscopy observations reveal that ultrafine

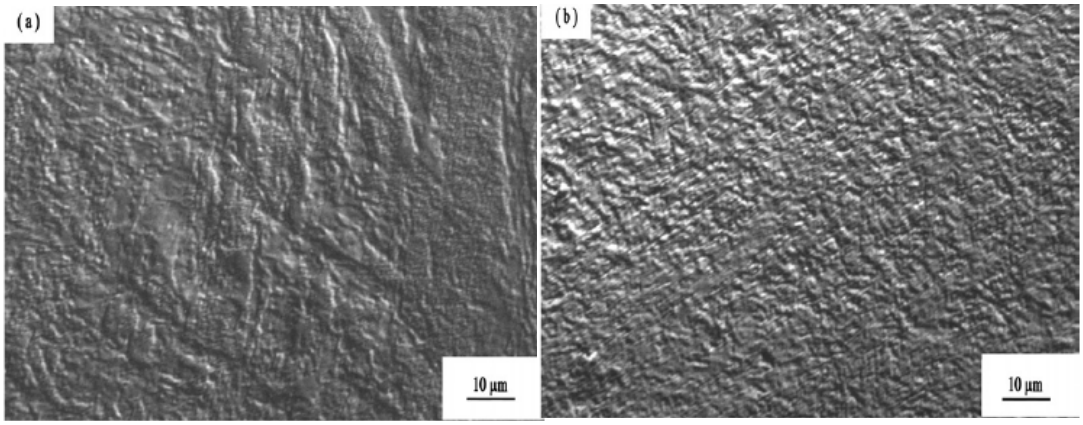

Figure 2.17 Optical micrographs showing the microstructure of copper processed by multiple forging at 195K (a) strain=6; (b) strain=18 [75]

grains of 160 nm are formed primarily at the intersections of microshear bands. However, the volume fraction of these newly formed ultrafine grains is quite small for smaller final overall strains; for example, for a final strain of 6, corresponding to Figure 2.17(a), the volume fraction is less than 0.1. Nevertheless, an increase in strain leads to an increase in the volume fraction of these new grains, resulting from the higher number of microshear bands. For an overall final strain of 18, corresponding to Figure 2.17(b), the volume fraction rises to 0.7. Apart from an increase in the volume fraction of ultrafine grains, a higher deformation also contributes to an increase in the misorientation of deformation-induced boundaries. Figure 2.18 shows the variation of angle of misorientation with strain. It is observed that the average values of misorientation (denoted by solid circles) between neighbouring microstructural features, which include subgrains, grains, microshear bands, etc, increases with deformation. However, the misorientation angles in regions remote from the kinks in microshear bands vary negligibly with deformation. This means that in the vicinity of the microshear band kinks, where ultrafine grains are generated, the angle of misorientation increases rapidly with strain; this correlates with the occurrence of continuous dynamic recrystallization in these areas.

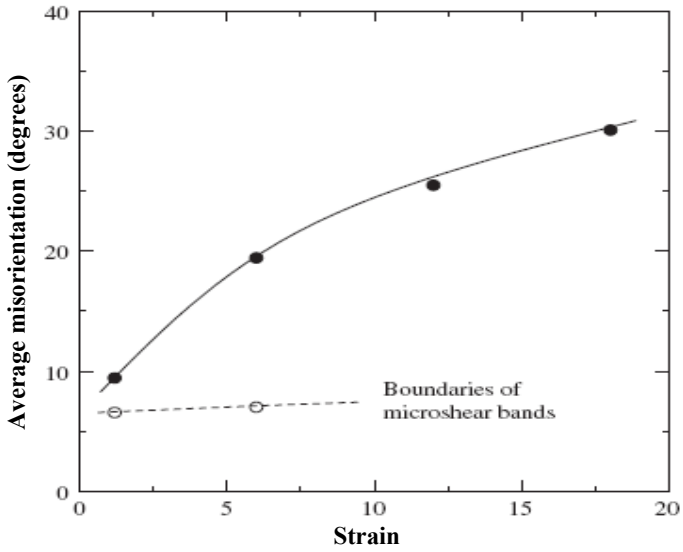

Figure 2.18 Variation of average misorientation of deformation-induced boundaries with strain [75]

2.4.2 Deformation corresponding to drawing processes

Han et al. [76] processed copper through drawing at liquid nitrogen temperatures (77K) and compared the resulting microstructure with that for drawing at room temperature (295K). In terms of the morphology of dislocation cells, three differences were identified, as illustrated in Figures 2.19(a) and 2.19(b): (i) at 77K, the cells are almost equiaxed, whereas they are elongated at 295K; (ii) for deformation at 77K, the cell sizes are smaller than that for 295K; (iii) for 77K, the cell boundaries are thicker than those corresponding to 295K. Han et al. attributed these differences to the lower

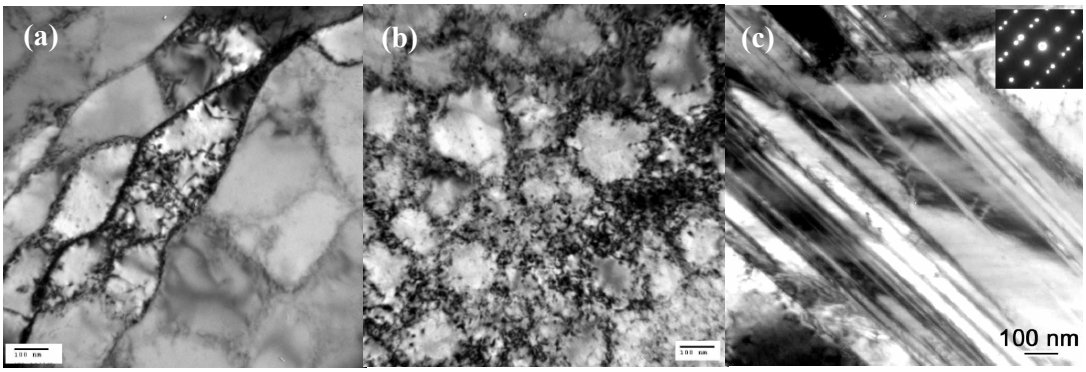

Figure 2.19 Microstructure obtained after drawing at; (a) 295K – dislocation cells; (b) 77K – dislocation cells; (c) 77K – nanotwins [76]

efficiency of dislocation annihilation at 77K, which results in more dislocations remaining in deformed samples. Apart from the dislocation cells, another difference in the microstructure lies in the appearance of nanotwins for deformation at 77K, as shown in Figure 2.19(c). Nanotwins start to form at a strain of 0.4, and at higher strains, the boundaries of nanotwins are deformed and characterized by the accumulation of dislocations. These nanotwins, together with the higher dislocation density, contribute to the higher strength and greater stored defect energy of samples prepared at 77K, compared to those drawn at 295K; this is reflected by the measured data shown in Figure 2.20.

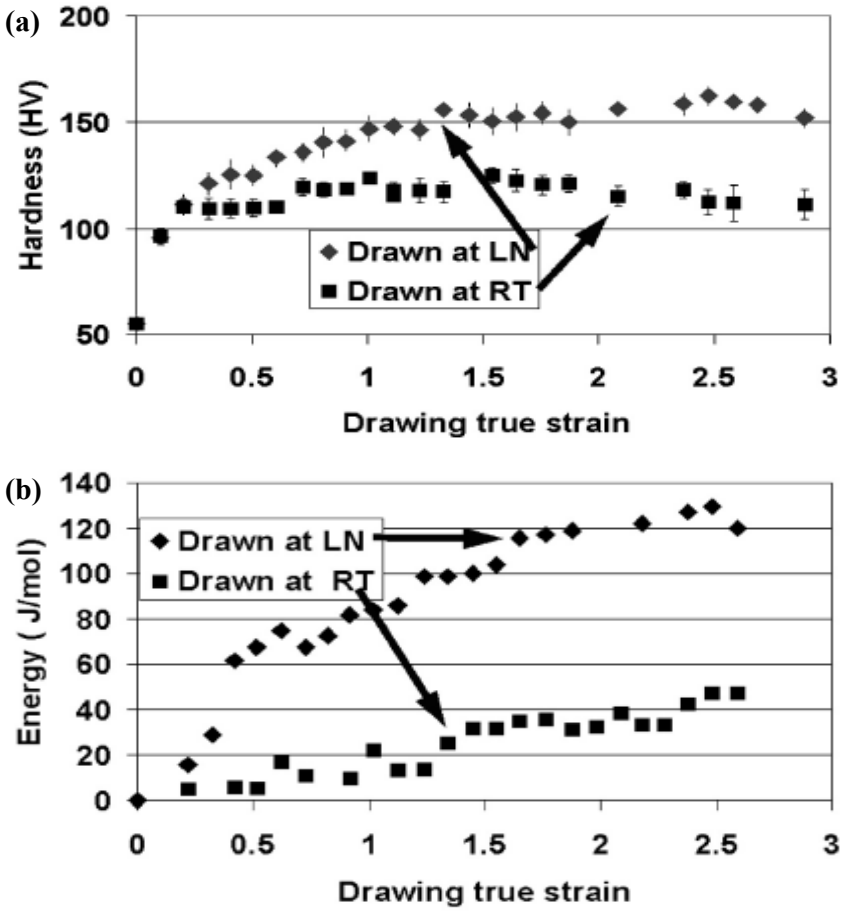

Figure 2.20 (a) Variation of hardness with strain at RT (295K) and LNT (77K) (b) Variation of stored defect energy with strain at RT and LNT [76]

2.4.3 Surface mechanical grinding treatment (SMGT)

Section 2.4.2 describes the observation of nanotwins, which contribute to strengthening of deformed material; this has actually been reported in earlier work [77, 78]. More recent findings on the evolution of nanotwins into nanograins are now discussed. This is observed in copper samples processed by SMGT at 173K [79]. SMGT is a newly developed technique to synthesize a graded nano-micro-structure in the surface layer; to achieve a significant reduction in grain sizes, the SMGT processes must be repeated. Figure 2.21 illustrates schematically the experimental arrangement and the resulting deformed layer produced by SMGT. In Figure 2.21(a), a cylindrical sample rotates around a horizontal axis while a hemispherical WC/Co tip

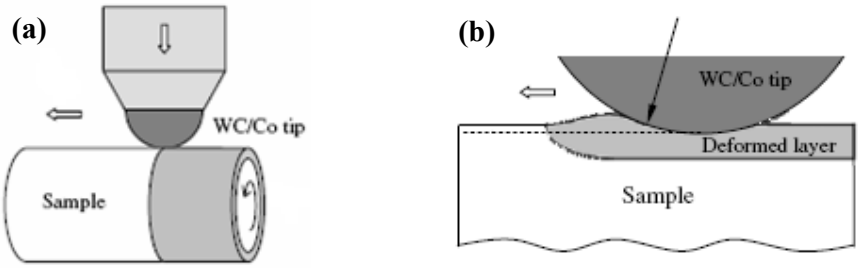

Figure 2.21 Schematic illustrations of (a) SMGT setup (b) deformed layer induced during SMGT [79]

is pressed along the sample surface. This creates a layer of plastic deformation shown in Figure 2.21(b). Microstructural observation of the deformed layer reveals the formation of secondary twins in the twin/matrix lamellae generated by the refinement of originally coarse grains. Tao and Lu [80] proposed a model illustrating the transformation of nanotwins into nanograins; this is shown in Figure 2.22. In Figure 2.22(a), the boundaries of primary nanotwins formed during deformation subdivide the original grain into a twin/matrix lamellar structure, and the boundaries of the secondary twins formed within the primary twins and matrix further subdivide the lamellae into prismatic nano-sized blocks. Due to the accumulation of dislocations

during subsequent deformation, coherence of the boundaries between twins is gradually lost and finally a nanosized grain structure is formed, as shown in Figure 2.22(b).

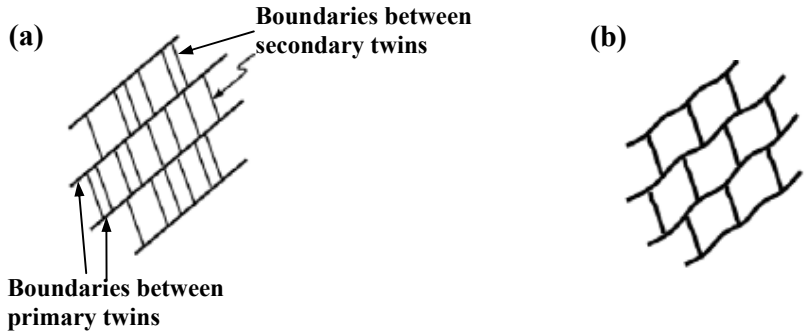

Figure 2.22 Schematic drawing showing the evolution of nanotwins into nanograins (a) primary and secondary twins (b) nanosized grain structure [80]

2.4.4 Evaluations of studies on microstructure of materials deformed at temperatures lower than room temperature

The results of various researchers, presented in Sections 2.4.1, 2.4.2 and 2.4.3, indicate three characteristics of deformation at temperatures lower than the room temperature: (i) dynamic recrystallization occurs at low temperatures and the grains obtained are finer than those at room temperature (see Section 2.2.4); (ii) recovery is suppressed at low temperatures so that defect storage capacity is elevated compared to deformation at room temperature; (iii) nanotwins are formed at low temperatures and exhibit two influences – enhancing sample strength and acting as potential sources for the formation of nanograins. However, it is noted that these all reflect the result of increasing deformation on microstructure evolution; the influence of strain rate on the microstructure is not examined.

2.5 Summary

Investigations related to the microstructure of metallic materials deformed to large strains have been reviewed. Generally speaking, these studies have been directed at two objectives: (i) eliciting the mechanism that accounts for different hardening behaviors at different stages of deformation; (ii) refinement of grain structure. Investigations related to the former attribute the constant (stages II and IV) and decreasing hardening rate (in stages III and V) respectively to the athermal storage of dislocations and the occurrence of dynamic recovery. There are differences in perspective with regard to the sources (i.e. dislocation cell walls and cell interiors) contributing to hardening during a particular stage of deformation, as well as the mechanisms governing hardening and softening. However, it is commonly accepted that macroscopic hardening is linked to the density of dislocations stored in a deformed sample, which result from dislocation generation, annihilation, interaction, etc. It is also found that the different hardening behaviors are associated with the type of dislocation interaction in each stage of deformation. Apart from dislocation density and type, dislocation arrangement also changes with deformation, and this is reflected by the value of the dislocation arrangement parameter. A reduction in value with strain indicates more effective screening of dislocation strain fields. In addition, it signifies the initiation and evolution of dislocation cells into low angle grain boundaries, which is the initial phase of microstructural changes during grain refinement, one of the objectives of the studies reviewed. Commonly adopted SPD techniques used to refine grains are evaluated; these techniques, which are usually applied at room temperature and low strain rates (< 1/s), facilitate the generation of ultrafine and even nanometer-sized grains, but require repeated processes and exhibit saturation values in both the grain sizes and material strengths obtained. Deformation

at higher strain rates (~ 10^4 /s; see Section 2.3) and at temperatures below room temperature (Section 2.4) can result in grains smaller than the saturation values associated with current SPD techniques. However, for deformation at high strain rates, there are differing views on the evolution of microstructure, while for deformation at low temperatures, a systematic study on how strain rate influences the resulting microstructure is lacking. Therefore, unlike previous investigations that have focused on microstructure evolution in terms of the degree of strain induced, this work examines the effect of strain rate and temperature on the microstructure of materials deformed to large strains.

Chapter 3 – Establishment of an approach to determine IHF values for metals

As discussed in the preceding chapter 2, the microstructure of a material is affected by the temperature during deformation. In high strain deformation, there is a sudden rise in temperature, which may induce microstructure evolution that is different from that in quasi-static deformation. To examine the temperature change in a material during high strain rate deformation, the value of the inelastic heat fraction (IHF) needs to be determined. Currently, there seems to be no common consensus on what the IHF value is. This chapter describes the establishment of an approach to determine the IHF value, by combining dynamic deformation, infrared (IR) photography and finite element simulation. The approach is applied to OFHC copper and the IHF value obtained is used in subsequent analysis.

3.1 Introduction

During plastic deformation of metals, external work is transformed into both elastic strain energy and plastic work. Upon unloading, the elastic energy is released; however, the plastic work that has gone into activating Frank-Read dislocation sources [39], overcoming resistance to dislocation movement and initiating twinning, grain boundary sliding, grain rotation and other deformation mechanisms, is irreversible. A temperature rise generally accompanies this and the temperature increase is more significant in high speed deformation. As negligible heat is lost by conduction during the short deformation duration, the process can be assumed to be

adiabatic. The heat generated by plastic dissipation generally follows the Clausius-Duhem's inequality [82, 83], which relates the heat produced to plastic work, energy of defects and dissipation by thermal conduction. In the development of a constitutive relationship for the inelastic deformation of materials and structures, Chaboche [84] ignored conductive losses; consequently, the heat generated, together with the energy of defects (e.g. point defects, dislocations, stacking faults), constitutes the total plastic work. The inelastic heat fraction (IHF) parameter, also known as the Taylor-Quinney constant, is generally used to define the fraction of plastic work converted into heat, and this determines the temperature rise. However, there appears to be no general consensus on its value and it is usually estimated to be in the range of 0.8-1 for metals [85-87]. According to the work of Ravichandran et al. [88], the IHF value is less than 0.8, indicating a diversity of opinion.

From the atomic level perspective, the temperature of a material corresponds to the average kinetic energy of all the atoms. Consequently, at elevated temperatures, the atomic arrangement would adjust to lower the total energy, as highlighted by Virial's Theorem [89, 90]. For larger length scales, experiments have demonstrated the completion of recrystallization due to sufficient elevation in temperature via plastic deformation, and this causes softening of the impacted material [91, 66]. Simulation results [92] have illustrated the competition between strain-hardening and dynamic recovery, and also attribute material softening to significant temperature increases for deformation at high strain rates. As temperature has a strong influence on material microstructure and thereby its mechanical properties, determination of the IHF value becomes a pertinent objective, from which the temperature rise, and even the recrystallization temperature under impact deformation, can be estimated. There have been other experimental investigations directed at measuring the IHF of various

materials, ranging from copper to polycarbonate, and these have resulted in reports of values lower than 0.9, which is often assumed for metals, as summarised by Macdougall [93]. Essentially, an infrared radiometer was employed to measure the average surface temperature of a deformed specimen and an assumption made that it represented the temperature of the entire specimen when calculating the IHF value. However, in reality, the temperature at the centre of the sample is usually higher than that at the surface and use of the surface temperature will result in underestimation of the IHF. The present study employs high-speed infrared imaging to examine the surface temperature distribution of OFHC copper samples deformed by impact to an engineering strain of 44-60% at strain rates of ~1,000/s, in order to elicit the IHF by correlating the experimental data with finite element simulation.

3.2 Theoretical considerations

With reference to the Clausius-Duhem inequality and Bouferra et al. [94], the heat generated during plastic deformation is described by:

$$q_H = \boldsymbol{\sigma} : \dot{\boldsymbol{\varepsilon}}^p - A_k \cdot \dot{V}_k \tag{3.1}$$

where q_H is the heat generated per unit volume, $\boldsymbol{\sigma}$ and $\dot{\boldsymbol{\varepsilon}}^p$ are respectively the stress and plastic strain rate tensors; A_k is the scalar micro-force related to $\dot{V}_k$, where $\dot{V}_k$ is the rate of change of defects (point defects, dislocation, twinning boundaries, etc, for metals); $A_k \cdot \dot{V}_k$ represents the power related to the defects induced in the deformed metal (alternatively termed the rate of stored work or stored power). Incorporation of Fourier's linear heat conduction law into Equation (3.1) yields:

$$\rho_C c \dot{T} - div(\kappa \cdot gradT) = \boldsymbol{\sigma} : \dot{\boldsymbol{\varepsilon}}^p - A_k \cdot \dot{V}_k \tag{3.2}$$

where κ is the thermal conductivity and grad$T$ is the temperature gradient.

The right hand side of Equation (3.2) represents the rate of plastic work transformed into heat, and is obtained by subtracting the defect energy induced from the total plastic dissipation. Direct measurement of the defect energy is difficult; however, by introducing a parameter defined as the inelastic heat fraction or IHF (β), which quantifies the fraction of plastic work converted into heat, the defect energy can be determined by $(1-\beta)\boldsymbol{\sigma} : \dot{\boldsymbol{\varepsilon}}^{\mathrm{p}}$. If the deformation is adiabatic, i.e., $\mathrm{div}(\kappa \cdot \mathrm{grad}T)=0$, equation (3.2) can be further simplified:

$$\rho_C c\dot{\mathrm{T}} = \beta\,\sigma : \dot{\varepsilon}^{p} \tag{3.3}$$

where ρ_C is the material density, c the specific heat, and β the IHF; T, $\dot{T}$ and ΔT are respectively the temperature, rate of temperature change and temperature rise.

By integrating equation (3.3) with respect to time, the IHF value can be correlated to the temperature rise:

$$\beta = \frac{\rho_C c \Delta T}{\int_t \boldsymbol{\sigma} : \dot{\boldsymbol{\varepsilon}}^{p}\,\mathrm{dt}} \tag{3.4}$$

In equation (3.4), $\int_t \boldsymbol{\sigma} : \dot{\boldsymbol{\varepsilon}}^{p} dt$ represents the plastic work and is denoted by W henceforth. Consequently, β can be determined once the temperature rise and plastic work are known.

3.3 Experimental procedure

3.3.1 Sample preparation

Polycrystalline OFHC copper of high purity (>99.99%) is the material examined. Commercially-available cylindrical OFHC copper bars with a diameter of 35 mm are annealed at 450^{o}C over a dwell time of three hours to dissipate stored energy in the

form of defects such as vacancies, dislocations, etc, induced by cold-working during manufacture. Recrystallisation occurs during the heat-treatment, leading to the formation of a new grain structure compared to the as-received material, as illustrated in Figure 3.1. Cuboid impact test specimens measuring 4x4x6mm are wire-cut from the annealed copper bars. All six surfaces of each sample are polished using SiC paper (1500 grit size), to remove any oxidation film and to yield smooth and uniform surface conditions. The surfaces are then cleaned, using absorbent tissue and cotton balls dipped in acetone, to remove any residual powder that remains after polishing. The polishing process leads to a small reduction in sample size, whereby the sample length ranges from 5.88-6mm, while the sides of the cross-section measure 3.84-4mm.

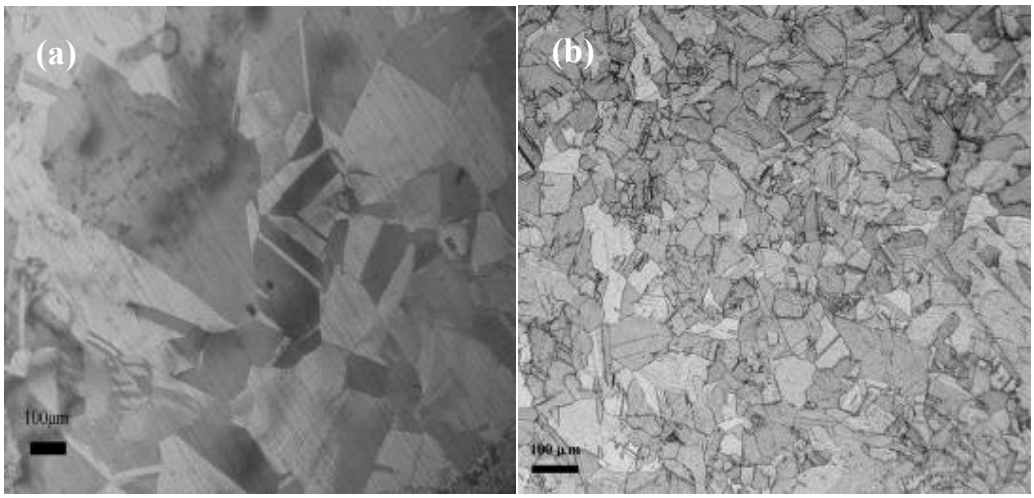

Figure 3.1 Optical micrographs (a) as-received copper (b) annealed copper

3.3.2 Experiments

Dynamic compression tests are conducted at an ambient temperature of around 21.3^{o}C. Figure 3.2 shows the experimental arrangement. Pressurized nitrogen is released from a gas cylinder to propel a striker through a barrel to impact a specimen

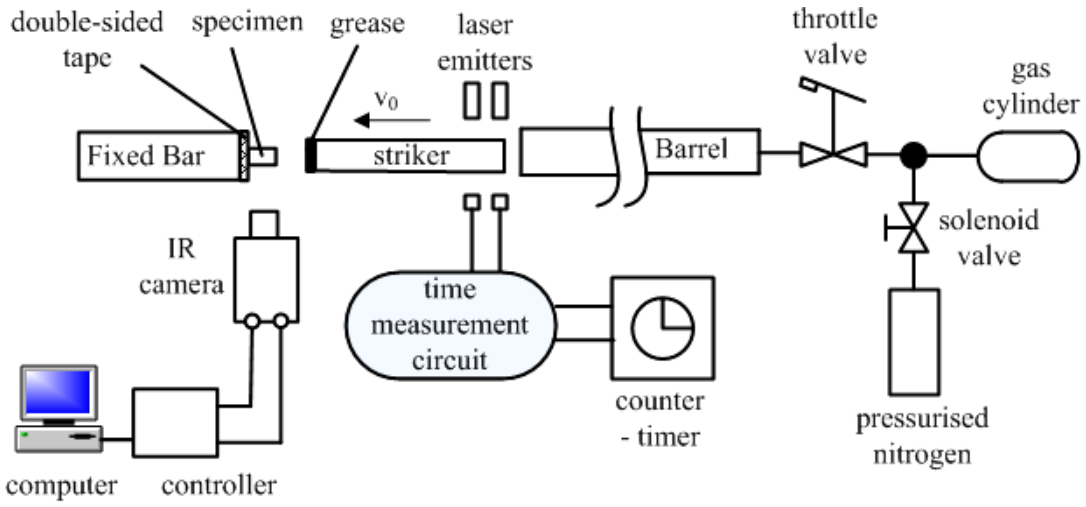

Figure 3.2 Experimental arrangement

mounted on a fixed bar by means of thin double-sided tape (to ensure continued connection with the bar after deformation). Molybdenum disulphide grease is applied to the striker surface that makes contact with the specimen, to reduce friction during compression. AISI O1 steel strikers of different lengths are employed to generate different final strains. A Cedip Emerald infrared (IR) camera with a temperature measurement resolution accuracy of ±2K is employed to capture thermal images of the specimen during deformation and thereby measure the surface temperature of the deformed sample. The camera lens, from the same manufacturer, is designated the reference code L0106, and the detector material of the camera is mercury cadmium telluride (MCT), which responds to infra-red radiation with wavelengths in the range of 3.7~4.8 μm. The noise equivalent temperature difference (NETD) of the camera is less than 18 milliKelvin (mK) at ambient temperature, without the use of a filter. The camera is activated just prior to launching of the striker and continuously captures thermographic images until it is stopped once a test is completed. Earlier images are overwritten by latter ones and the camera's memory is sufficiently large so that the images of interest have not yet been overwritten by the time a test ends. The framing rate is programmable and depends on both the integration time and frame size –

generally, a higher the framing rate results in a smaller the frame size. Even so, there is an upper limit for the framing rate, which is determined by the integration time. For example, with an integration time of 800 μs, the maximum attainable framing rate is 1,250 Hz, no matter how small the frame size is. The integration time is correlated with the standardised temperature range of the IR camera, and this is selected by the user. Once the temperature range is chosen, the associated integration time is also determined. The IR camera is connected to and controlled by a computer, installed with the relevant software ('CIRRUS' and 'ALTAIR'). Test calibration files are prescribed for each temperature range and calibration of the camera is accomplished before triggering it by linking the calibration file to the corresponding temperature range using the 'CIRRUS' software. In this study, the temperature range corresponding to an integration time of 800 μs is 35-100 ^{o}C. Taking into consideration the balance between frame size and framing rate, the camera was set to a framing rate of 1,000 Hz, whereby the resolution of the thermal images corresponds to 132 pixels in width and 136 pixels in height, with each pixel measuring 38 μm in terms of the image captured by the camera; this is illustrated in Figures 3.3(a) and 3.3(b). Figure 3.3(a) shows a photo of a sample adhered to the fixed bar and the sample surface is 3.98 mm in height. Its image captured by the IR camera is depicted in Figure 3.3(b), where the two horizontal lines represent respectively the upper and lower edges of the sample surface. The distance between the two lines corresponds to 105 pixels, indicating a pixel size of around 38 μm. Only part of the sample surface is shown in Figure 3.3(b), because the image is 5 mm (= 132 pixels x 38 μm/pixel) in length, which is smaller than the full sample length of 6 mm. The fixed bar is not visible in Figure 3.3(b), as its out-of-plane curved side is outside the focal plane of the camera. The emissivity corresponding to the side of the deformed sample is obtained by

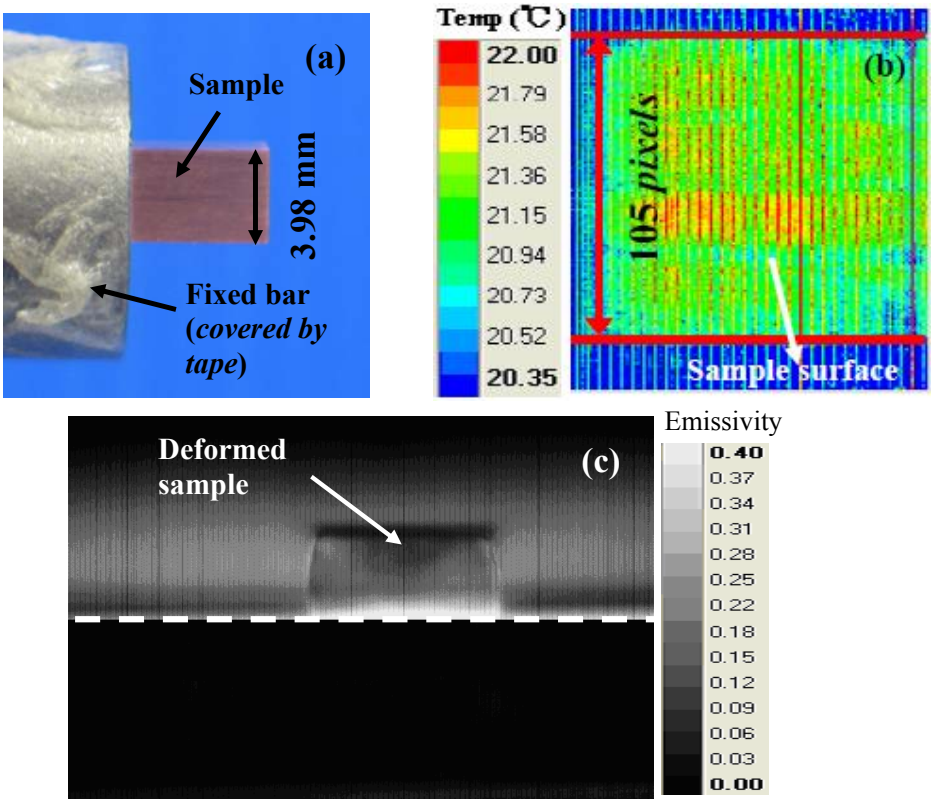

Figure 3.3 (a) Sample (b) IR camera image of sample surface (c) Emissivity map displaying the emissivity of side surface of deformed sample

creating an emissivity map using the 'ALTAIR' software. Figure 3.3(c) shows the emissivity map of the deformed sample, whereby the region below the dashed line corresponds to the plate supporting the sample, but is again invisible because of its deviation from the camera focal plane. The emissivity of the deformed sample is used in calculating the surface temperature, and the final strain of the deformed sample is defined as $\varepsilon_p = (L_0 - L)/L_0 \times 100\%$, where L_0 and L are respectively the initial and final lengths of the sample.

3.4 FEM simulation

3.4.1 Validation of ABAQUS code for heat generation and conduction

Before using ABAQUS to investigate the temperature rise, the software is validated by comparing computed results with analytical solutions. Equation (3.4) indicates that the temperature rise is related to the instantaneous stress, strain and IHF, and can be calculated analytically. Equation (3.4) can be written as:

$$\Delta T = \frac{\beta}{\rho_C c} \int_t \sigma : \dot{\varepsilon}^p dt \tag{3.5}$$

The case of a copper specimen deformed at a constant velocity of 6 m/s, as shown in Figure 3.4(a), is examined. Symmetric boundary conditions are applied and the temperature rise can be calculated using Equation (3.5) and by simulation. Figure 3.4(b) shows the final temperature of a specimen deformed to various strains at an ambient temperature of 21.3 ℃ and a strain rate of 1000 /s. The simulation results match the analytical solutions very well for different values of final strain, indicating the suitability of using ABAQUS for this analysis.

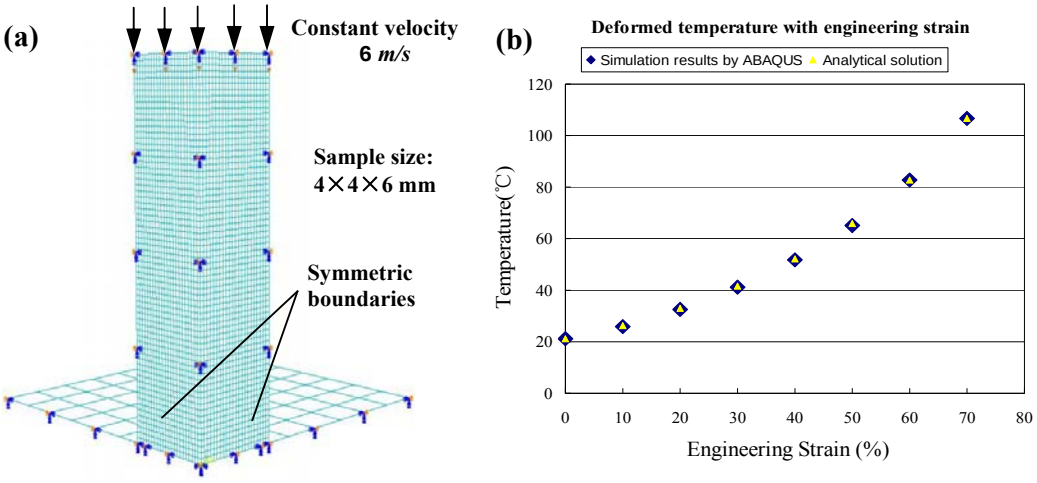

Figure 3.4(a) FEM model and boundary conditions (b) Temperature of deformed copper at different final strains by analytical solution and simulation

Apart from the temperature rise, the ability of ABAQUS to simulate heat conduction is also evaluated. Consider a plate with its two opposite surfaces maintained at different temperatures T_1, T_2, as shown in Figure 3.5 ($T_1 > T_2$). The

heat transmitting through the surface per unit area per unit time (q_t) is governed by Fourier's linear heat conduction law:

$$q_t = \kappa \frac{dT}{dx} = \frac{\kappa(T_1 - T_2)}{d} \quad (3.6)$$

Within an infinitesimal time increment dt, the heat flow per unit area through the plate is $q_t \cdot dt$. This will cause a temperature change δT, described by:

$$q_t \cdot dt = c \cdot (\rho d) \cdot \delta T \quad (3.7)$$

By combining equations (3.6) and (3.7), the temperature change is expressed as:

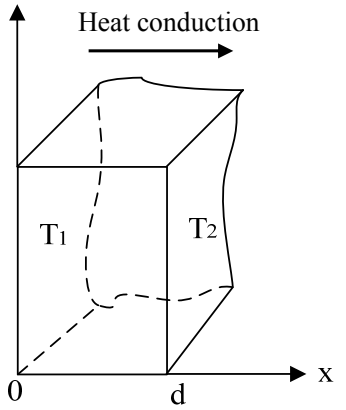

Figure 3.5 Schematic diagram of heat conduction

$$\delta T = \frac{\kappa(T_1 - T_2)}{\rho c d^2} \cdot dt \quad (3.8)$$

Alternatively, equation (3.8) can be written in terms of the rate of temperature change:

$$\frac{\delta T}{dt} = \frac{\kappa(T_1 - T_2)}{\rho c d^2} \quad (3.9)$$

FEM simulation is used to predict the temperature distribution in a deformed sample, and Figure 3.6(b) shows the temperature contours in two neighbouring layers (L1, L2) of elements. Figure 3.6(c) shows the variation of the average temperature in L1 and L2 with time.

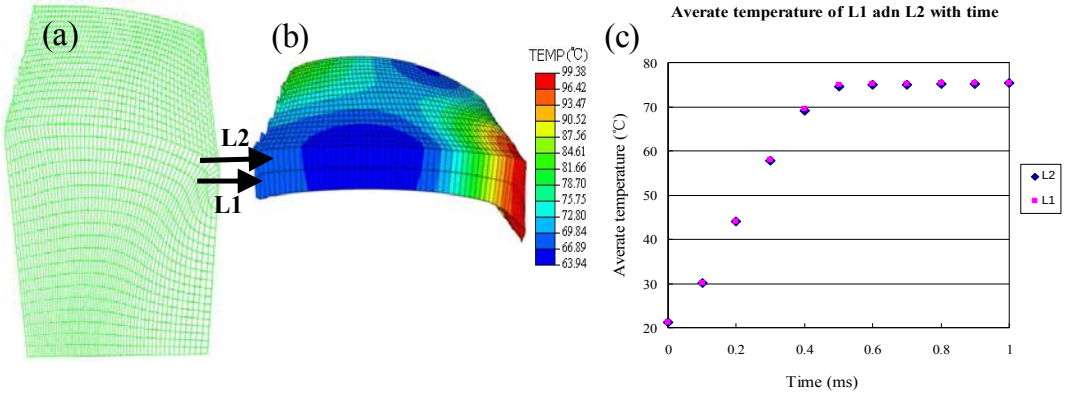

Figure 3.6 (a) Deformed mesh of specimen (b) Temperature distribution in L1 and L2 (c) Variation of average temperature in L1 and L2 with time

Before 0.6 ms, the temperature rises rapidly, as a result of plastic work being converted into heat. After completion of deformation, the temperatures in L1 and L2 change relatively slowly with time via heat conduction. The rate of temperature change in L2 from FEM simulation can be calculated from Figure 3.6(c), and its theoretical solution estimated using equation (3.9). Figure 3.7 shows a comparison of the rates of temperature change from simulation with the analytical solution. It is observed that there is some difference between the FEM prediction and the analytical solution for results calculated at 0.1 ms intervals. The reason is that analytically, the rate of temperature change calculated using equation (3.9) assumes that the temperatures in L1 and L2 are constant within the 0.1 ms time interval; however, in the simulation, the temperatures in L1 and L2 vary continually, and this would result in a changing temperature gradient between L1 and L2. Nevertheless, the rates of temperature change obtained from simulations and theoretical analysis are of the same order and differ by 10% at most. This substantiates the validity of employing ABAQUS to simulate heat conduction situations.

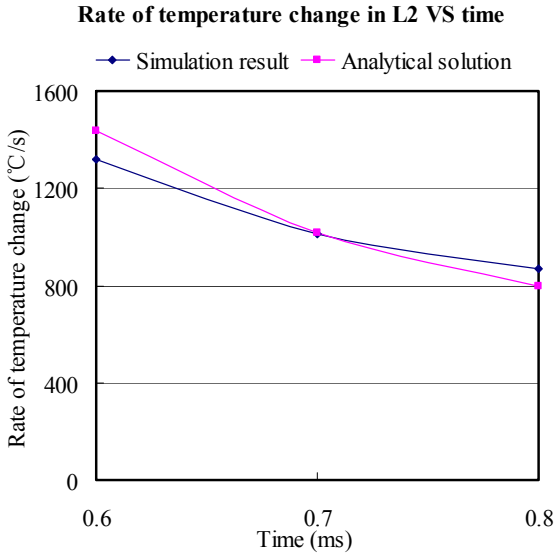

Figure 3.7 Variation of the rate of temperature change with time from simulation and theoretical analysis

3.4.2 Finite element simulations

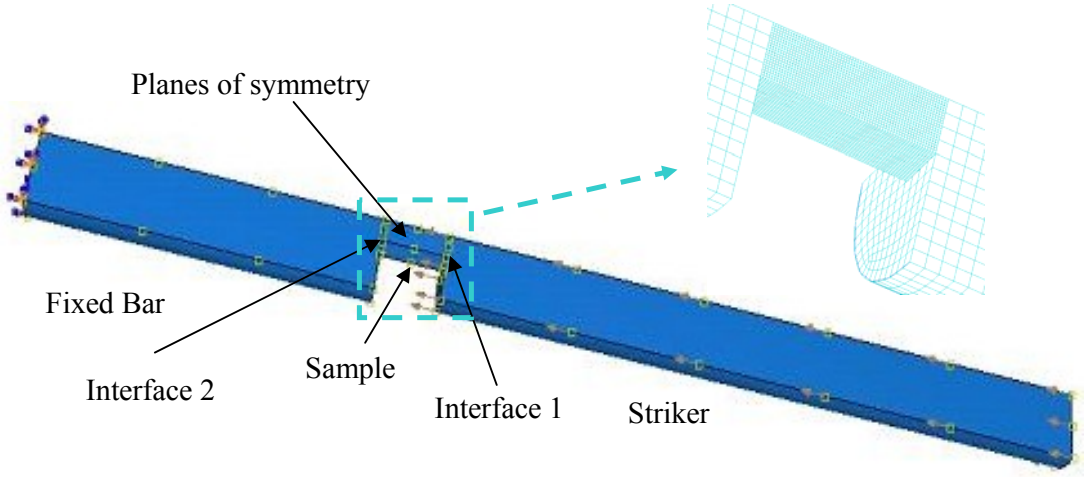

Figure 3.8 Quarter FE model

Figure 3.8 shows the FEM model of the experimental arrangement depicted in Figure 3.2. Symmetric boundary conditions are imposed on the surfaces indicated by the arrows, resulting in only one quarter of the fixed bar, specimen and striker being modelled. Interaction between the sample and the fixed bar and striker is described by surface-to-surface contact, whereby the surface of the sample is defined as the "slave", and the fixed bar and striker are assigned "master" surfaces. It is expected that the surface temperature of a deformed specimen is lower than that of its interior; consequently, direct substitution of the surface temperature rise into equation (3.4) will lead to an underestimation of the IHF value. Another parameter to be considered is the continuous change in strain rate during impact deformation, which makes explicit determination of the total plastic work corresponding to the denominator of equation (3.4) difficult. Consequently, finite element (FE) simulation using ABAQUS-Explicit is undertaken to model the deformation process. This enables identification of the temperature difference between the specimen surface and its interior, and also facilitates calculation of the instantaneous strain rate, from which the total plastic work can be obtained. By adjusting the IHF value for each simulation, the

surface temperatures change and the predictions are compared with data captured by the infrared camera. This process is continued until there is a match between simulation and the experimental results in terms of the average surface temperature. The corresponding IHF value is then taken to be the appropriate one.

3.4.3 Johnson-Cook constitutive model and its validation

Computation of the sample temperature rise resulting from plastic deformation involves a fully coupled dynamic thermal-stress explicit integration procedure. Equation (3.4) shows that the IHF β is related to the amount of plastic work. Ideally, the stress-strain relationship during impact would be obtained from experiments and implemented in the simulations to calculate the value of β. For instance, a sample can be deformed using a Split Hopkinson Pressure Bar (SHPB) in conjunction with an IR camera that measures the surface temperature. The stress-strain data from such tests can then be used to describe the mechanical response of OFHC copper, and simulations run to match the surface temperature recorded by the IR camera by adjusting the value of β. Owing to experimental limitations, the IR camera working at a framing rate of 1,000 Hz is unable to capture thermal images of a sample deformed dynamically by the SHPB setup, because the sample is also moved physically in the direction of compression, out of the field of view of the camera, before an image is captured. Consequently, the sample is restrained from being moved in the loading direction (see Figure 3.2), and the Johnson-Cook (J-C) constitutive model [95] is assumed to be an appropriate description of the stress-strain behaviour of OFHC copper. The J-C model relates the flow stress to the plastic strain, strain rate and temperature:

$$\sigma^{j} = (\mathrm{A} + \mathrm{B}\varepsilon^{\mathrm{n}})[1 + \mathrm{C}\ln(\dot{\varepsilon}^{*})][1 - (\mathrm{T}^{*})^{\mathrm{m}}] \tag{3.10}$$

where σ^j is the equivalent stress, ε the equivalent plastic strain, and *A, B, C, n, m* are material constants.

The normalized equivalent strain-rate ($\dot{\varepsilon}^*$) and temperature (T^*) in equation (3.10) are defined by:

$$\dot{\varepsilon}^* = \frac{\dot{\varepsilon}}{\dot{\varepsilon}_0}$$
$$T^* = \frac{T - T_r}{T_m - T_r} \tag{3.11}$$

Here, $\dot{\varepsilon}$ is the instantaneous equivalent strain-rate, $\dot{\varepsilon}_0$ a reference strain rate; T_r, T and T_m are respectively the reference temperature, current temperature and melting point. For annealed OFHC copper, the material constants for the J-C model are listed in Table 3.1 [95].

Table 3.1 Parameters in J-C model for OFHC copper

A (MPa)	B(MPa)	C	n	m	$\dot{\varepsilon}_0$ (/s)	T_r	T_m
90	292	0.025	0.31	1.09	1.0	294	1356

Applicability of the J-C model is examined in the present study. Figure 3.9 shows typical stress-strain curves from experiments in the current investigation and their match with the J-C model. The low strain-rate test (0.1 /s) was performed using an INSTRON servo-hydraulic testing machine, whereby an extensometer was attached to the compression platens to measure the specimen deformation. An SHPB was employed to determine the dynamic response at two strain rates – 2770/s and 4160/s – using cylindrical samples measuring 3.3 mm in length and 5 mm in diameter. The results demonstrate that the J-C model for copper exhibits good correlation with experimental data in terms of strain hardening and strain-rate sensitivity, indicating its applicability in describing the mechanical response of the OFHC copper in this study.

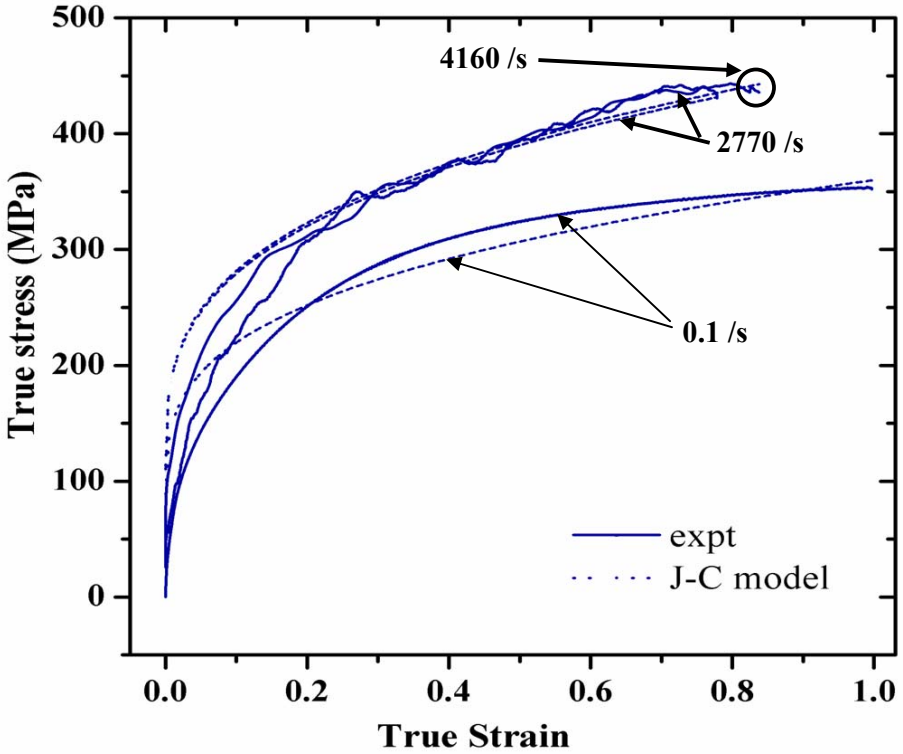

Figure 3.9 Experimental stress-strain curves for OFHC copper and fit with J-C model

Since the J-C model is assumed, it is instructive to assess how much β varies with different amounts of plastic work, from simulations based on the J-C equation and comparisons with experimental stress-strain data. For uniaxial deformation at a constant strain rate, the plastic work per unit volume W is:

$$W = \int \sigma_t \, d\varepsilon_t \tag{3.12}$$

where σ_t and ε_t represent respectively the true stress and true strain.

Denoting the stress-strain conjugates associated with the J-C model and experiments respectively by σ_t^j-ε_t^j and σ_t^e-ε_t^e, the corresponding plastic work is defined by:

$$\begin{aligned} W_j &= \int \sigma_t^j \, d\varepsilon_t^j \\ W_e &= \int \sigma_t^e \, d\varepsilon_t^e \end{aligned} \tag{3.13}$$

Substitution of (13) into (4) yields values of β corresponding to the J-C model and experimental data:

$$\beta_j = \frac{\rho_C \, \mathrm{c} \Delta T}{\mathrm{W_j}}$$
$$\beta_e = \frac{\rho_C \, \mathrm{c} \Delta T}{\mathrm{W_e}} \qquad (3.14)$$

Equation (3.14) implies that for the same temperature rise (ΔT), the β value obtained is inversely proportional to the plastic work calculated from the constitutive relationship used. This leads to the following:

$$\beta_e = \frac{\mathrm{W_j}}{\mathrm{W_e}} \beta_j \qquad (3.15)$$

Therefore, if the J-C model is used in simulations, the β_j value obtained should be multiplied by the factor of W_j/W_e to obtain the actual value β_e; i.e. the one determined in the case whereby the stress-strain relationship during impact is known exactly. A value of W_j/W_e is thus estimated from the test data in Figure 3.9. W_j and W_e are calculated respectively by integrating the stress with respect to strain according to the stress-strain curves in Figure 3.9. Figure 3.10 shows the variation of W_j/W_e with true

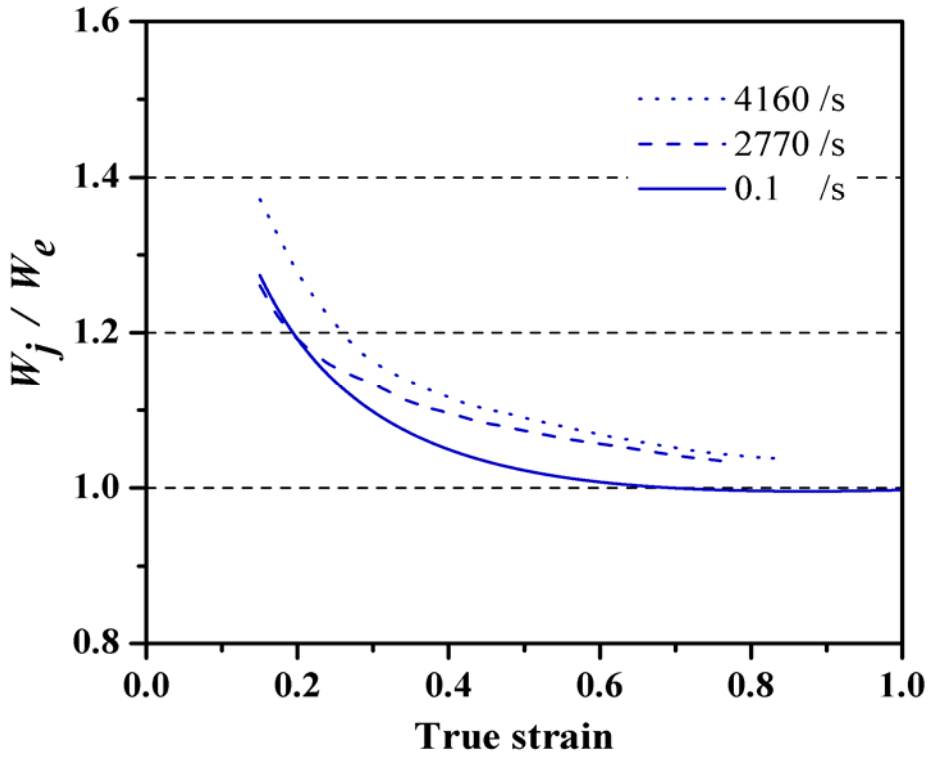

Figure 3.10 Variation of W_j / W_e with true strain

strain; it is observed that W_j/W_e can exceed 1.2 for strains less than 0.2 because of smaller experimental stress values compared to the J-C model. However, at larger strains, W_j/W_e decreases rapidly and tends toward a constant value of around unity for true strains in excess of 0.6. A comparison of the three curves in Figure 3.10 shows that W_j/W_e increases with strain rate; nevertheless, the two curves corresponding to strain rates in the order of 1,000/s show convergence in the W_j/W_e value as the strain increases; both decline asymptotically to a value between 1.03 and 1.04. This provides a value of W_j/W_e (to facilitate evaluation of β) that can be considered a close approximation of the actual value indicated by Equation (3.15).

Apart from the material constants for the J-C model in Table 3.1, the thermal properties and elastic behaviour of OFHC copper are needed in the FEM simulations, and these are listed in Table 3.2. ρ, c, κ, E and ν represent respectively the density, heat capacity, thermal conductivity, Young' modulus and Poisson's ratio; their values are specified in consistent units according to the ABAQUS software documentation.

Table 3.2 Thermal and elastic properties of OFHC copper [95, 96]

ρ_C (tonne/mm^3)	c (mJ/tonne * K)	κ(mJ/mm * K * s)	E (MPa)	ν
8.94e-9	4.14e8	3.91e2	1.2e5	0.33

Figures 3.11(a) and 3.11(b) show respectively the initial mesh of the fixed bar and the sample (not drawn to the same scale). For the fixed bar, solid hexahedral elements

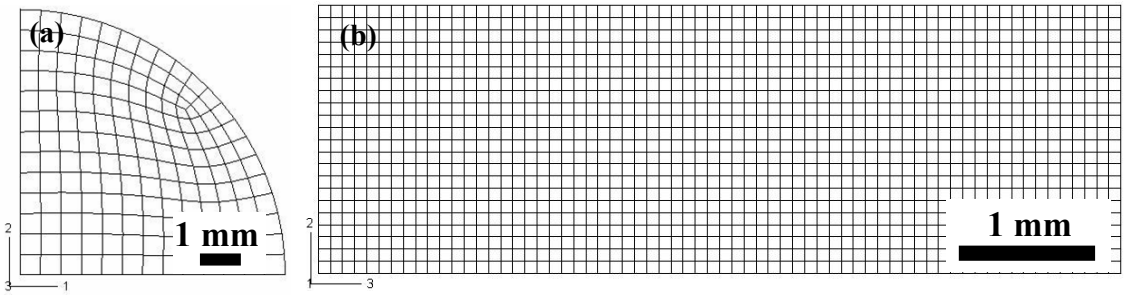

Figure 3.11 Initial mesh (a) fixed bar (b) sample

(ABAQUS C3D8R) with edges measuring approximately 0.5 mm are employed; the samples are also modelled by solid hexahedral elements (ABAQUS C3D8RT in this instance), but with edges measuring 0.09 mm. The striker has the same element type and size as the fixed bar. To ascertain convergence of the calculated temperatures using the mesh sizes described (denoted as size A), the element sizes of the fixed bar, sample and striker were all reduced by half (denoted as size B), and a comparison made with respect to the average temperature as well as the surface temperature distribution. For generality, a 125 mm long striker is assumed and the sample is impacted at an initial velocity of 15 m/s. The deformation process is simulated according to the model in Figure 3.8, with a common IHF (β=1) and boundary conditions (frictionless at interfaces '1' and '2'), but with different mesh sizes corresponding to A and B. Figure 3.12(a) shows the variation of the kinetic energy

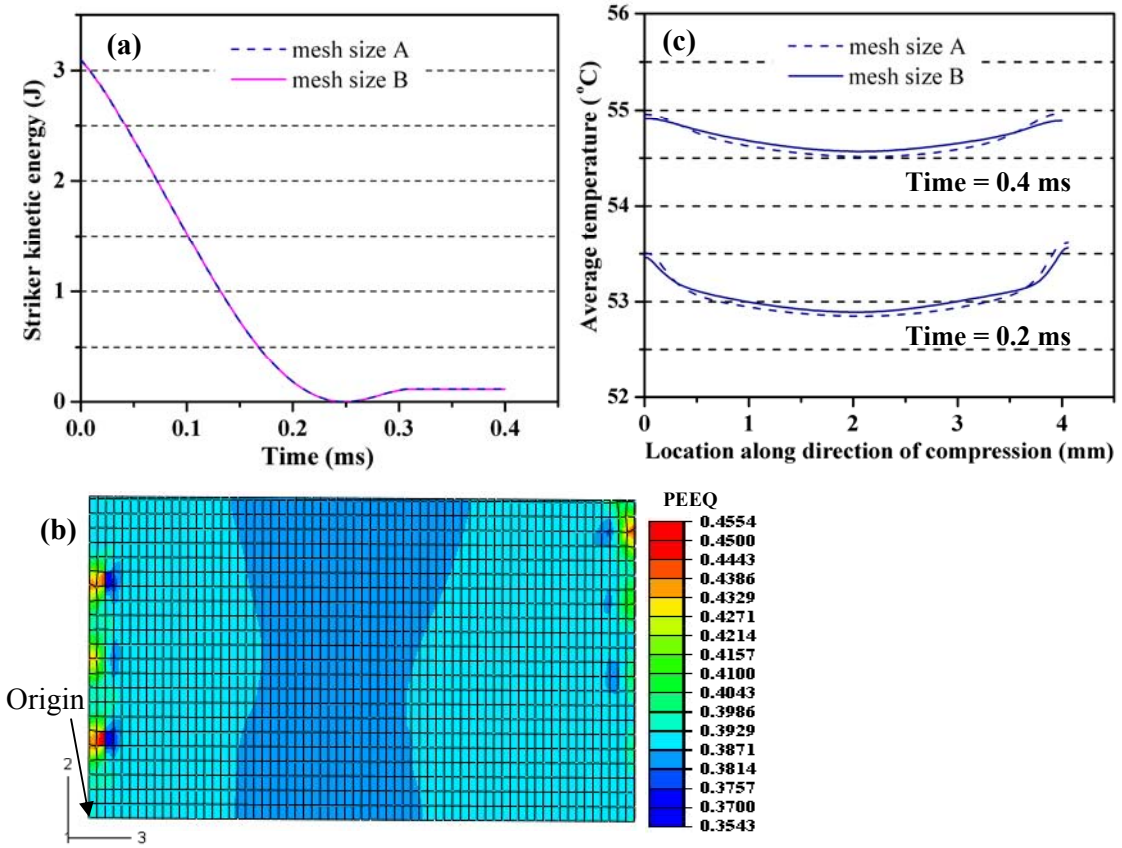

Figure 3.12 (a) Variation of striker KE with time (b) Distribution of equivalent plastic strain in deformed sample (mesh size A), at 0.2 ms (c) Variation of average temperature with location along loading direction (3-axis)

(KE) of the striker with time. The KE begins to decrease upon commencement of impact until 0.25 ms later, when it drops to zero, at the instant the sample experiences maximum compression. After this, the KE increases slightly, signifying rebound of the striker as the specimen releases its elastic energy. Ultimately, a constant value is reached, when the striker separates from the sample. From energy conservation, the plastic work in deforming the sample is defined by the loss in kinetic energy of the striker after contact with the specimen ceases. The two KE histories in Figure 3.12(a) essentially overlap each other, demonstrating that the coarse mesh is sufficiently fine in terms of evaluating the plastic work done. Therefore, it is expected that the average sample temperature predicted using mesh sizes A and B should also be similar, and the distributions of average surface temperature for the two mesh sizes are depicted in Figures 3.12(b) and 3.12(c). Figure 3.12(b) shows the deformed mesh of the sample surface with initial mesh size A. The left edge corresponds to the interface between the sample and the fixed bar, while the right edge defines the interface between the sample and the striker. The sample is compressed along the 3-axis, so the elements expand in the direction of the 2-axis. The position of the node at bottom left corner is taken to be the origin. The average temperature at each position along the 3-axis is calculated from the temperatures of all the 23 nodes in the direction of the 2-axis with the same 3-axis coordinate. Figure 3.12(c) shows the distribution of average temperature along the 3-axis direction at two instants of time – 0.2 ms and 0.4 ms – which correspond respectively to the state just before full compression of the specimen and after completion of deformation, as described by Figure 3.12(a). Distributions of average temperature for mesh size B are also determined and depicted by solid lines in Figure 3.12(c). All the curves indicate higher temperatures near the two specimen interfaces; this signifies a larger degree of plastic work in these regions,

as shown by the equivalent plastic strain in Figure 3.12(b). The temperature at 0.4ms after impact is higher than that at 0.2ms by around 1.5^{o}C, because the sample undergoes further compression from 0.2-0.25ms, as indicated in Figure 3.12(a). A comparison of the curves corresponding to 0.2 ms with those corresponding to 0.4 ms shows that the temperature difference in the specimen decreases because of heat flux from higher to lower temperature regions. Although the number of elements in the model with mesh size B is eight times that of the model with the coarser mesh, the maximum temperature difference between the two models is only around 0.05^{o}C for results corresponding to 0.2 ms and 0.4 ms after impact; this is negligible, considering that the surface temperature exceeds 50^{o}C. Consequently, the FEM model with mesh size A is sufficiently fine.

3.4.4 Boundary conditions

The boundary conditions at interfaces '1' and '2' of the FEM model (Figure 3.8) are derived from the shape of a deformed sample. Figure 3.13 is a photograph of the side of an impacted sample. E1 and E2 denote respectively the edges that were in contact with the striker and fixed bar. The side profile of the deformed specimen has become trapezoidal, providing some insight into the boundary constraints imposed by

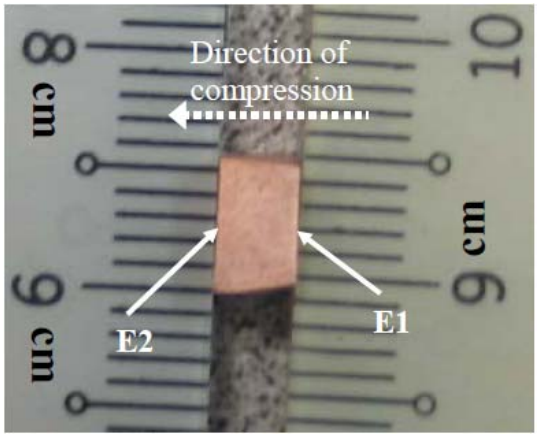

Figure 3.13 Side profile of deformed sample

the fixed bar and striker. At the sample-striker interface (interface '1' in Figure 3.8), friction is still present, even though lubrication was applied. The dynamic friction coefficient, denoted by 'μ', which defines the contact properties at interface '1' in the simulation, is estimated experimentally, as illustrated in Figure 3.14(a). A weight is placed on top of a copper specimen, and the force to maintain relative motion between the specimen and the (AISI O1) steel plate measured. (The specimen mass is small compared with the weight and is neglected.) Figure 3.14(b) shows the variation of the tangential force with weight. A linear fit is applied and the slope of ~0.13 is taken as the value of the dynamic friction coefficient ($\mu = F/mg$).

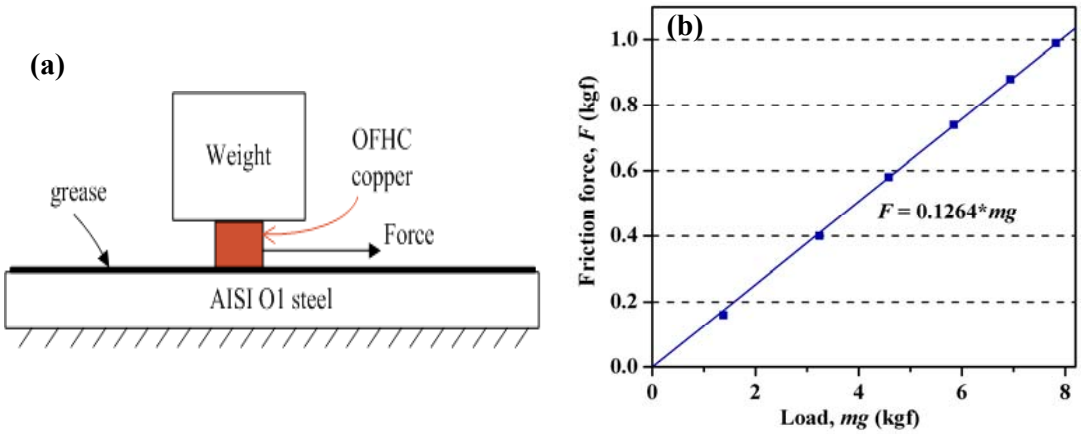

Figure 3.14 (a) Measurement of dynamic friction coefficient (b) Variation of friction force with load on sample

The double-sided tape that secures the specimen to the fixed bar exerts a different degree of resistance to transverse expansion of the sample compared to grease. This is examined via FEM simulation. A friction coefficient of $\mu = 0.13$ is defined for the interfaces '1' and '2' of the model corresponding to Figure 3.12(b) and the simulation is repeated. Figure 3.15 depicts the upper half of the deformed specimen and demonstrates that the presence of equal interfacial friction causes bulging in the middle. However, Figure 3.13 shows that the actual shape of deformed samples is frustum-like, indicating that the boundary conditions at interface '2' (Figure 3.8) actually differs from that of interface '1'. Examination of the double-sided tape after

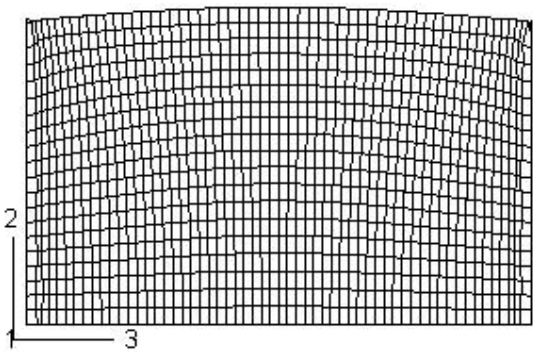

Figure 3.15 Mesh of deformed sample

impact tests reveals that it is stretched in the transverse direction by the sample during deformation. Therefore, its effect is considered equivalent to a constant tangential resistance along the sample surface. The stress associated with this is determined by matching the specimen-bar contact area from experiments and simulation. Figure 3.16(a) shows the initial cross-section of the specimen (painted blue) in contact with the fixed bar. This surface is then adhered to the fixed bar using double-sided tape. A piece of double-sided tape is also placed on the surface of the specimen which will make contact with the striker. Figure 3.16(b) shows the sample cross-section after impact. Unpainted copper appears at the edges, indicating the resistance to transverse

(a)  (b) 

Figure 3.16 Sample surface in contact with fixed bar (a) before deformation (b) after deformation

expansion arising from the presence of the tape (otherwise the entire surface would appear blue). The deformation process is simulated using the FEM model with shear stresses applied at interfaces ‘1’ and ‘2’. The stress is adjusted until the computed contact area matches experimental data. It was found that the lateral stress exerted by the tape is in the order of 10 MPa, and can vary with striker mass and impact velocity.

3.5 Determination of IHF of OFHC copper

Determination of the IHF value is now described, through an example of a sample deformed to a final strain of 57.5%. Figures 3.17(a), 3.17(b) and 3.17(c) show the first three thermographs after commencement of impact. In each image, colours other than the background blue indicate the side of the deformed sample, because they represent higher temperatures (and plastic deformation). The striker and fixed bar are not visible as their cylindrical surfaces are out of the camera focal plane. A comparison of the three images shows that there is no discernible change in both sample dimensions along the loading (negative x) direction and in the surface temperature distribution. This implies that compression has been completed before the camera captures the first image. However, the position of the sample varies from one image to the next, because of vibration of the fixed bar to which the sample is attached. The edges of the higher temperature regions define the boundaries between the deformed sample and the striker / fixed bar. Figures 3.17(a) and 3.17(d)-(f) illustrate how the specimen boundary is determined in Figure 3.17(a). An arbitrary area (outlined in red) is labelled 'γ' and consists respectively of 119 and 78 pixels in the horizontal (x) and vertical (y) directions. The position of each pixel is defined by its coordinates with respect to the origin at the top left corner. The average temperature of pixels with the same x-coordinate in area 'γ' is calculated and shown in Figure 3.17(d). The rightmost arrow in Figure 3.17(d) indicates the 89^{th} pixel along the x-axis and defines the location in the sample beyond which the temperature decreases. This is taken to be the right edge of the specimen, while the arrow at the 24^{th} x-pixel position defines the location 2.5 mm (thickness of deformed sample) from the rightmost arrow, and hence represents the left edge of the deformed sample. From the 36^{th} to the 24^{th} x-pixel, there is a temperature decrease; this is caused by the presence of the double-sided tape

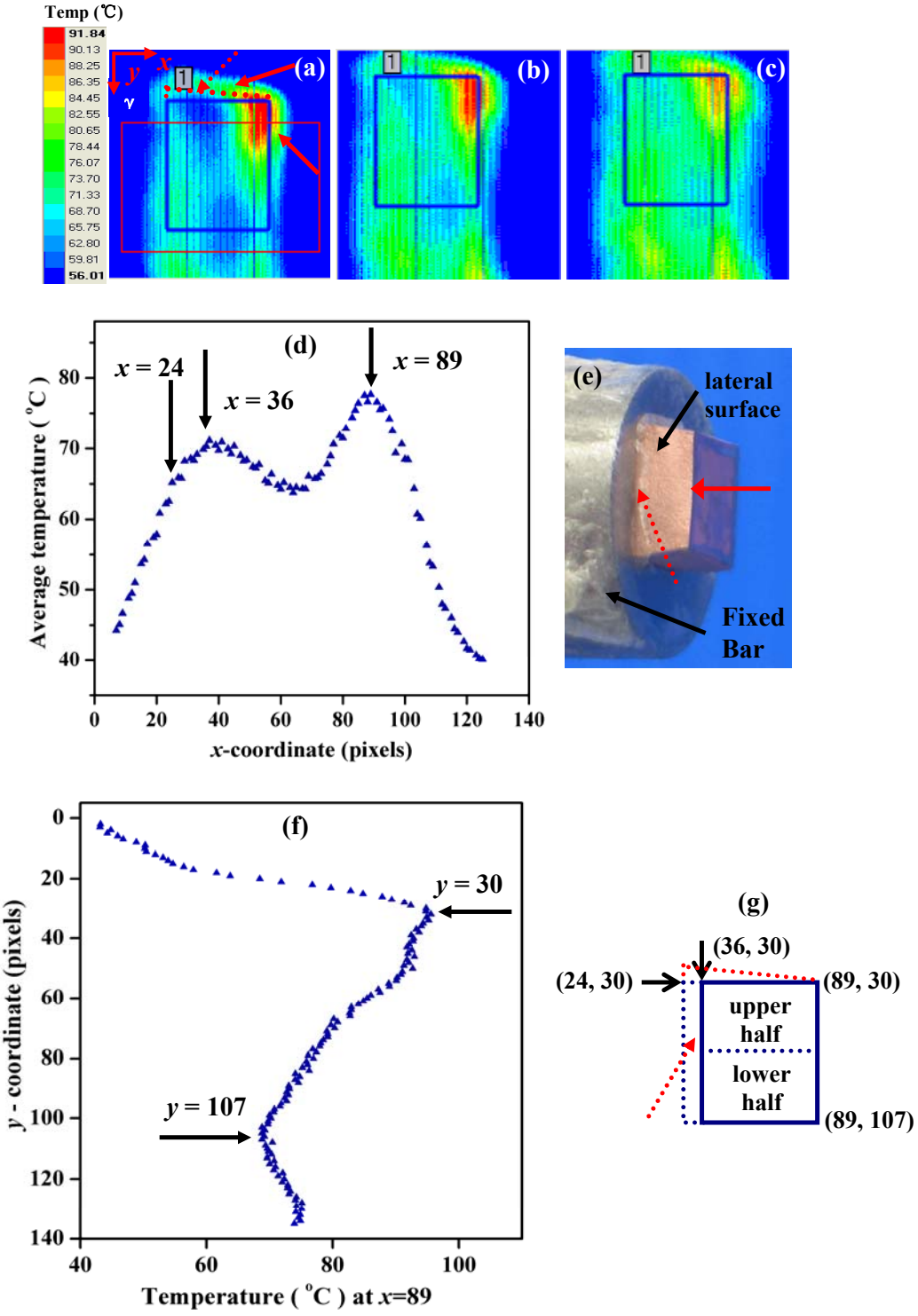

Figure 3.17 (a) 1st image (b) 2nd image (c) 3rd image (d) Variation of average temperature along x-axis in area 'γ' (e) Deformed sample (f) Variation of temperature with y-coordinate at x=89 (g) Relationship between (a), (d) and (f)

(indicated by the dashed arrow in Figure 3.17(e)) that covers this region and attenuates the infra-red radiation emitted. Consequently, the pixels from the 36th to the 89th x-coordinates in Figure 3.17(d) represent the surface temperature distribution along the deformed sample. The left and right sides of the blue frame in Figure 3.17(a) correspond respectively to the 36th and 89th x-pixels positions in Figure 3.17(d). The frame height, encompassing 78 y-pixels, is half the height of the sample vertical right edge (indicated by the solid red arrow in Figure 3.17(e)). Thus, the area within the blue frame, labelled '1' in Figures 3.17(a)-(c), is half of the sample side profile and excludes the portion covered by the double-sided tape (the small triangle above the blue frame, indicated by the dotted red arrow in Figure 3.17(a) is neglected). The temperatures in area '1' can be considered representative of that in the lower half because of symmetry in geometry and loading.

The upper boundary between the sample and the surrounding air is defined by the inclined red dashed line in Figure 3.17(a) and the pixels beyond this edge should also indicate a drop in temperature beyond the specimen ends in the loading direction, as shown by the curve in Figure 3.17(d). The top right corner of area '1' corresponds to the 89th x-pixel and the column of pixels at this location is examined; the individual pixel temperatures are shown in Figure 3.17(f). Again, the upper arrow identifies the 30th pixel above which the temperature drops sharply, indicating the specimen upper edge. Consequently, the coordinates of the top right corner of area '1' are (89, 30). The lower horizontal edge of the blue frame in Figure 3.17(a) corresponds to the y=107 pixel and the lower arrow in Figure 3.17(f). The temperature distribution in Figure 3.17(f) exhibits symmetry with respect to the lower arrow, supporting the assumption that the deformed sample comprises symmetrical upper and lower halves divided by the lower edge of the blue frame – i.e. area '1' is the upper half of the

sample. Although the regions indicated by the two solid arrows in Figure 3.17(a) have colours different from the blue background, they are not part of the sample, but correspond to a boundary layer surrounding the sample. Figure 3.17(g) is a schematic diagram showing the relationship between the thermograph in Figure 3.17(a) and the side profile of the sample in Figure 3.17(e). The trapezoidal outermost boundary in Figure 3.17(g) defines the side profile of the upper half of the sample, and the dashed arrow indicates the area shielded by the double-sided tape. It is noted that the temperature distribution in the upper portion of area '1' differs from that in the lower portion. (The procedure described to define area '1' is also applied to the thermographs in Figures 3.17(b) and 3.17(c)).

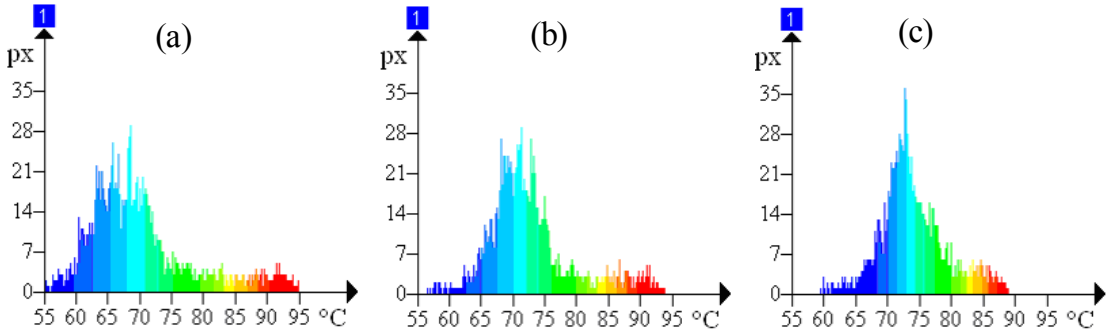

Figure 3.18 Variation of number of pixels (px) with temperature in area '1' (a) 1st (b) 2nd (c) 3rd image

Figures 3.18(a)-(c) show respectively the number of pixels associated with various temperatures within area '1' in Figures 3.17(a)-(c). A comparison of Figure 3.18(a) and Figure 3.18(b) reveals that all the temperatures lie between 55°C and 95°C; however, the temperature corresponding to the largest number of pixels increases from Figure 3.18(a) to Figure 3.18(b), indicating a general increase in temperature after 1ms. This is attributed to heat flow from the hotter interior of the specimen to the surface. In Figure 3.18(c), the temperature range encapsulated by all the pixels in area '1' shrinks from both ends compared with Figures 3.18(a) and 3.18(b), and the temperature distribution becomes narrower, indicating a progression towards

equalization between the low and high temperature areas on the surface, as well as between the surface and interior of the specimen. It is envisaged that a uniform temperature will emerge with time and Figure 3.18(c) would tend towards a narrow column at the average temperature of the entire specimen.

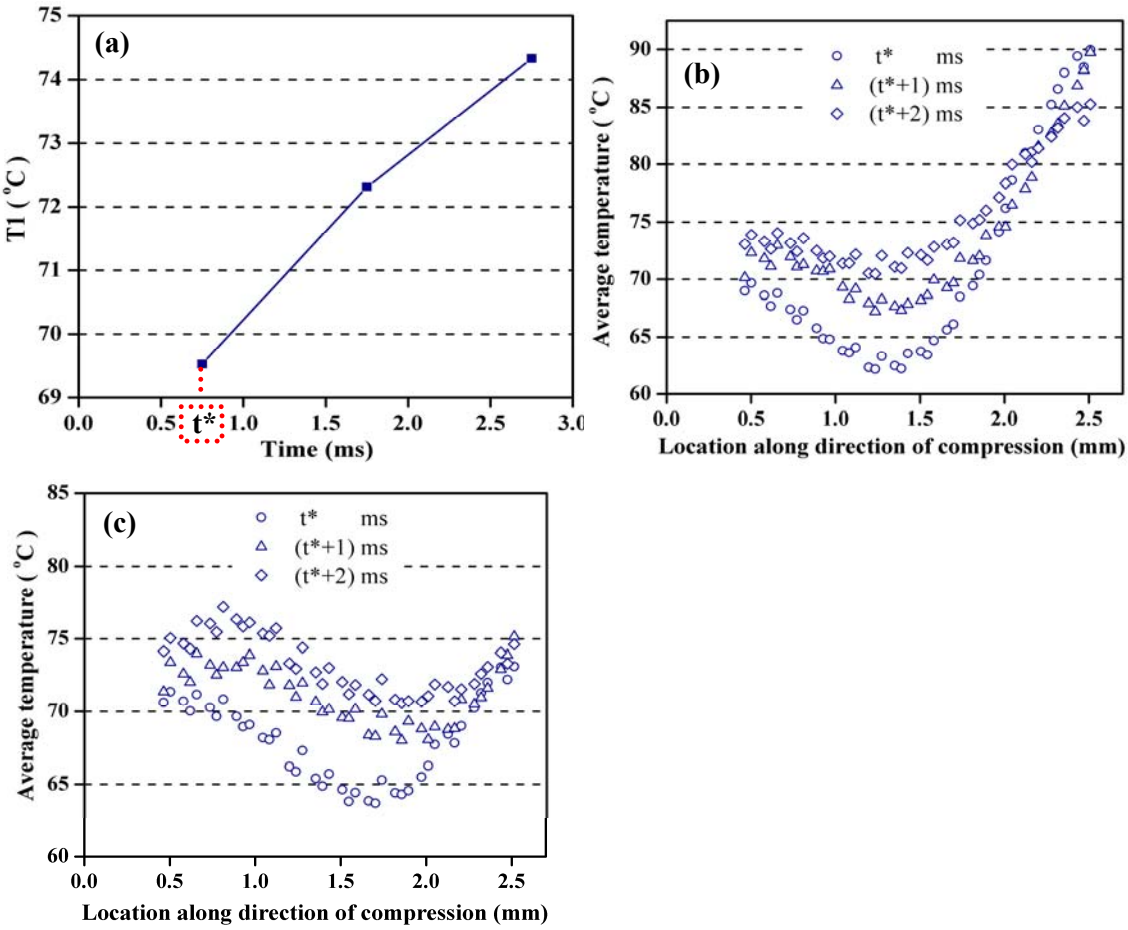

Figure 3.19 (a) Variation of T1 with time (b) Distribution of average temperature in upper-half (c) Distribution of average temperature in lower-half

The mean temperature in area '1' is obtained by considering all the pixels and their associated temperatures, as depicted in Figure 3.18. Denoting the commencement of deformation by t=0 in Figure 3.19(a), t*, which represents the instant the first image is captured (identification of t* is discussed later), should be less than 1ms, since the IR camera works at a framing rate of 1,000 pps. Consequently, the second and third images correspond to t*+1 ms and t*+2 ms respectively. Figure 3.19(a) depicts the

variation of the mean temperature in area '1' (T1) with time and shows that T1 continues to rise after deformation has been completed. This indicates the conduction of heat from the interior of the specimen to the surface, confirming that the temperature inside is higher. The second feature in Figure 3.19(a) is the decrease in the slope of T1 with time, which is a result of the reduction in temperature gradient between the interior of the specimen and the surface as the entire specimen progresses towards a common temperature.

The average surface temperature distributions for the upper and lower halves of area '1' are plotted respectively in Figures 3.19(b) and 3.19(c), whereby each data point represents the average temperature at that position (relative to the left interface between the sample and the fixed bar). The portion without data points corresponds to the width of the double-sided tape that covers the sample surface, as shown in Figure 3.17(g). The presence of interfacial friction causes an increase in temperature near the interfaces, which is more significant than the heat generated by plastic work in those regions, shown previously in Figure 3.12(b). This is because in the absence of friction, the temperature at the two ends of the sample is only about 0.5^{o}C higher, as indicated in Figure 3.12(c), whereas Figures 3.19(b) and 3.19(c) show a temperature difference of several degrees. The lowest temperatures are located approximately 1.3mm and 1.7mm from the interface with the fixed bar, in the upper and lower halves respectively, and they grow fastest with time due to the influx of heat from higher temperature regions. However, the rate of temperature change decreases from t^* to (t^*+1), because of the reduction in temperature gradient; this correlates with the variation of the average temperature in area '1', as shown in Figure 3.19(a). At time (t^*+2), there is a drop in temperature at the two ends of the specimen, which results

from heat loss through the interfaces. This is not obvious before time (t^*+1), indicating the reasonableness of the assumption of adiabatic deformation.

The IHF value can be calculated from the temperature rise using Equation (3.4). Simulations are undertaken to determine its value by matching the predicted average temperature with experimental results. In the FEM model (Figure 3.8), the striker is assigned a diameter of 12mm, a length of 498mm and an impact speed is 11.3 m/s, in accordance with experiments. At interfaces '1' and '2', a friction coefficient of 0.13 and an interfacial tangential stress of 10 MPa are prescribed as respective boundary conditions. It is assumed that no heat transfer across these interfaces occurs within 2ms after commencement of impact, in accordance with the experimental observations in Figures 3.19(b) and 3.19(c). Figure 3.20(a) shows how the kinetic energy (KE) of the striker varies with time from commencement of impact. As with

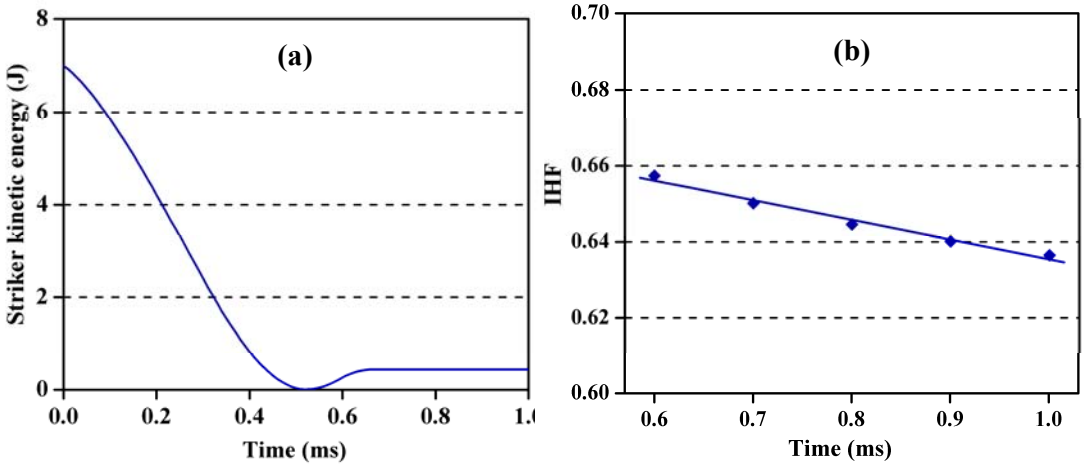

Figure 3.20 (a) Variation of striker kinetic energy (KE) with time (b) Variation of calculated IHF with time

the interpretation of Figure 3.12(a), maximum strain (comprising elastic and plastic components) is induced 0.52ms after impact commences (the change in sample strain after this is associated with elastic recovery). However, the elastic component is negligible compared to the plastic strain of 57.5%. Therefore, deformation is considered to be completed 0.52ms after commencement of impact, according to

Figure 3.20(a). t^* represents the instant the first thermographic image is captured after completion of impact, but is difficult to identify exactly because of the relatively coarse time interval between successive images at the framing rate the IR camera operates at. Consequently, by assuming different values of t^*, the IHF determined from FEM simulation varies a little because of the increase in the surface temperature with time arising from heat flow from the specimen interior to the surface. Since it takes 0.52ms to deform the sample, t^* lies in the range from 0.52-1ms. Figure 3.20(b) shows the IHF value calculated at 0.6, 0.7, 0.8, 0.9 and 1ms, and it decreases approximately linearly. Although the variation of around 0.02 within 0.4ms is small, an effort is made to find the most appropriate value by evaluating the difference in temperature distribution between experiment and simulation for different times.

Figure 3.21(a) shows a comparison of the distribution of average temperature from experiments with simulation results for different times. According to the processing of experimental data described earlier, area '1' in the thermographic images is divided into upper and lower halves and the temperature distributions along the axis of deformation plotted. The discrete data points denote experimental results while the solid and dashed lines represent the computed temperatures in the upper and lower halves respectively. A least-squares approach is adopted to assess the difference between experimental data and simulation results at various instants of times. Figure 3.21(b) depicts the absolute difference. A third-order polynomial is fitted, and shows that the smallest difference occurs at 0.81ms. Consequently, the instant that the first image is captured is taken to be 0.81 ms after commencement of deformation (to 57.5% engineering strain at a strain rate of 1,100/s). By identifying t^*=0.81ms and referring to Figure 3.20(b), the IHF value determined is 0.644 (This value has three decimal places because the neighbouring data points in Figure 3.20(b) differs by less

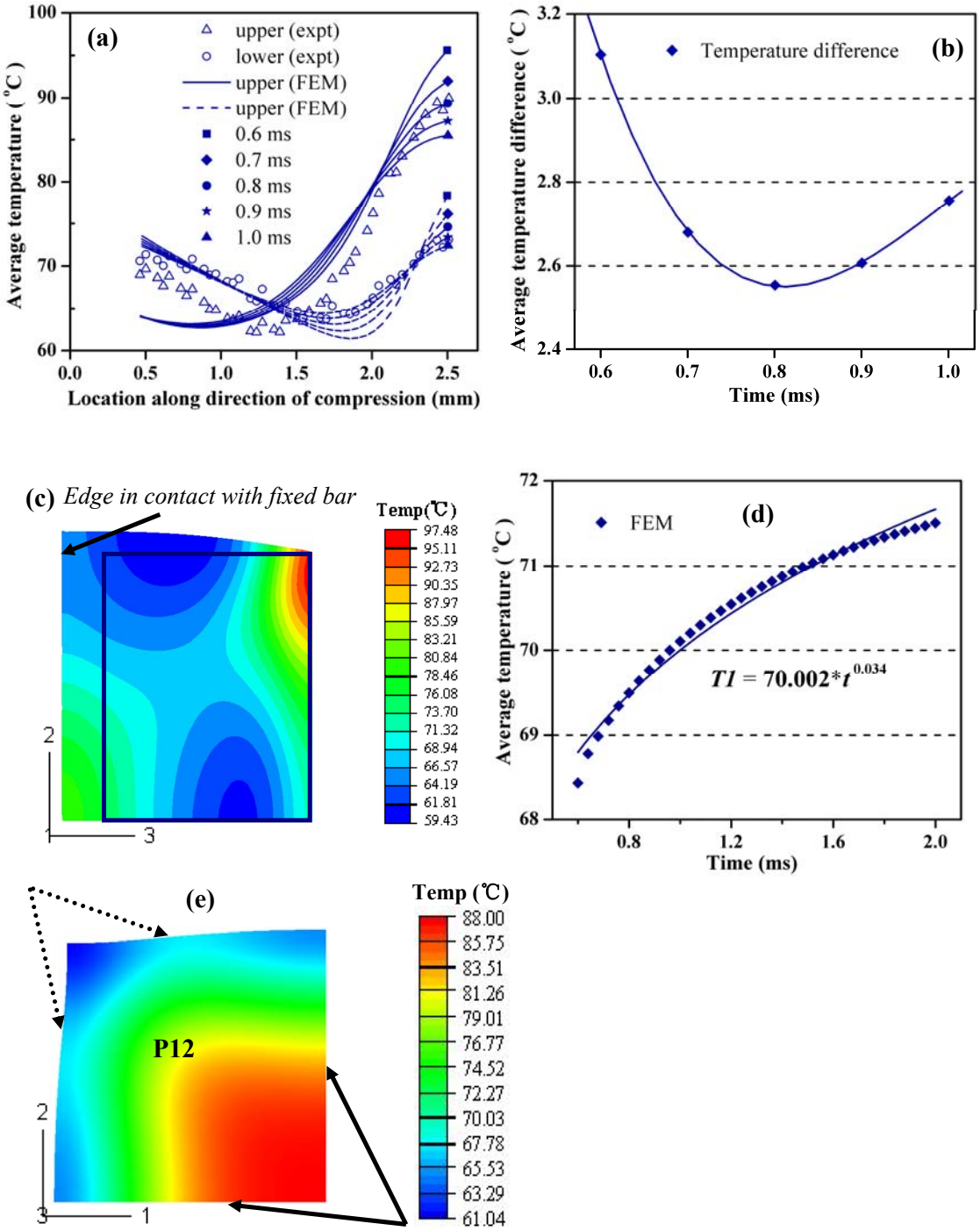

Figure 3.21 (a) Variation of temperature distribution with time (b) Variation of temperature difference with time (c) Surface temperature at 0.81 ms after impact (from simulation) (d) Variation of T1 with time (e) Temperature of sample face normal to the direction of compression (3-axis)

than 0.01 in terms of the IHF). It is noted that the value of μ in the current FE model is determined using the arrangement in Figure 3.14, whereby the contact conditions

(normal force, relative motion speed, etc.) leading to μ are likely to be somewhat different from those during actual impact of a specimen. However, the temperature distribution from FEM calculations differs from that of experiments by ~3^{o}C, as evident from Figure 3.21(b). This difference is considered acceptable, bearing in mind that the measured temperature is ~70^{o}C; hence the estimate of μ used in the FE model is also deemed acceptable.

Using the IHF value (0.644) thus obtained, the rate of change of surface temperature ($dT1/dt$) from FEM simulation is further analyzed by comparison with experimental data. Figure 3.21(c) shows the computed surface temperature 0.81ms after commencement of impact. The area enclosed by the blue outline corresponds to area '1' in the thermographs in Figures 3.17(a)-(c). The average temperature within this outline (average of all nodal temperatures in the area) is calculated and the square data points in Figure 3.21(d) show that the surface temperature increases with time. This is because the interior of the sample is hotter, resulting in heat flux towards the surface. Figure 3.21(e) depicts a typical set of temperature contours for a sample face (denoted as P12) perpendicular to the direction of compression (3-axis), corresponding to the same instant of time (0.81 ms) as Figure 3.21(c). The straight borders, indicated by the solid arrows, define the axes of symmetry corresponding to the FEM model in Figure 3.8, while the curved edges, indicated by the dashed arrows, are the sides of the specimen. It is obvious that the temperature decreases from the centre (bottom right corner) to the outer surfaces. The rate of temperature rise decreases with time, as shown in Figure 3.21(d). This decreasing temperature gradient is a result of the heat flow from the sample interior to the surface. A power-law relationship is fitted to compute the average temperatures within the outlined area and this facilitates determination of dT1/dt at any instant between 0.6 and 2 ms. At t=0.81,

the value of $dT1/dt$ is 2.917°C/millisecond; while experimental data from Figure 3.19(a) indicates the corresponding values to be 2.783°C /millisecond. This corresponds to a relative difference of 4.8%, which seems reasonable, indicating that simulation is able to estimate heat conduction as well as temperature rise due to plastic work. Equation (3.15) highlights that the IHF value obtained from FEM simulation based on the J-C model should be multiplied by the factor W_j/W_e. Taking into consideration that the strain rate associated with Figure 3.17(a) is in the order of 1,000/s, a value of 1.03 for W_j/W_e is adopted, according to Figure 3.10. Consequently, the IHF value is determined to be 0.663.

3.6 Variation of IHF with strain

The variation of the IHF value with specimen strain is further investigated by exploiting the full working range of the infrared camera, from 35-100°C. By varying the length and initial velocity of the striker, different final engineering plastic strains (ε_p) were induced in specimens at an average stain rate ($\dot{\varepsilon}_p$) of around 1,000/s. Table 3.3 lists the conditions for the various tests and Figure 3.22 shows thermographs of

Table 3.3 Striker parameters; strain and strain rate induced

Strikers				ε_p (%)	$\dot{\varepsilon}_p$ (/s)	v_0 (m/s)
Length (mm)	Diameter (mm)	ρ(tonne/mm^3)	E (MPa)			
302	12	7.8e-9	1.93e5	44.5	1110	12.1
498				46	867	9.3
453				50	1000	10.2
498				53.2	1005	10.5
605				56.3	1000	10.6
756				59.4	943	9.9

specimens deformed to 44.5-59.4% strain, and the distribution of the temperature enclosed in area '1'. All the images exhibit a higher temperature at the two ends, and

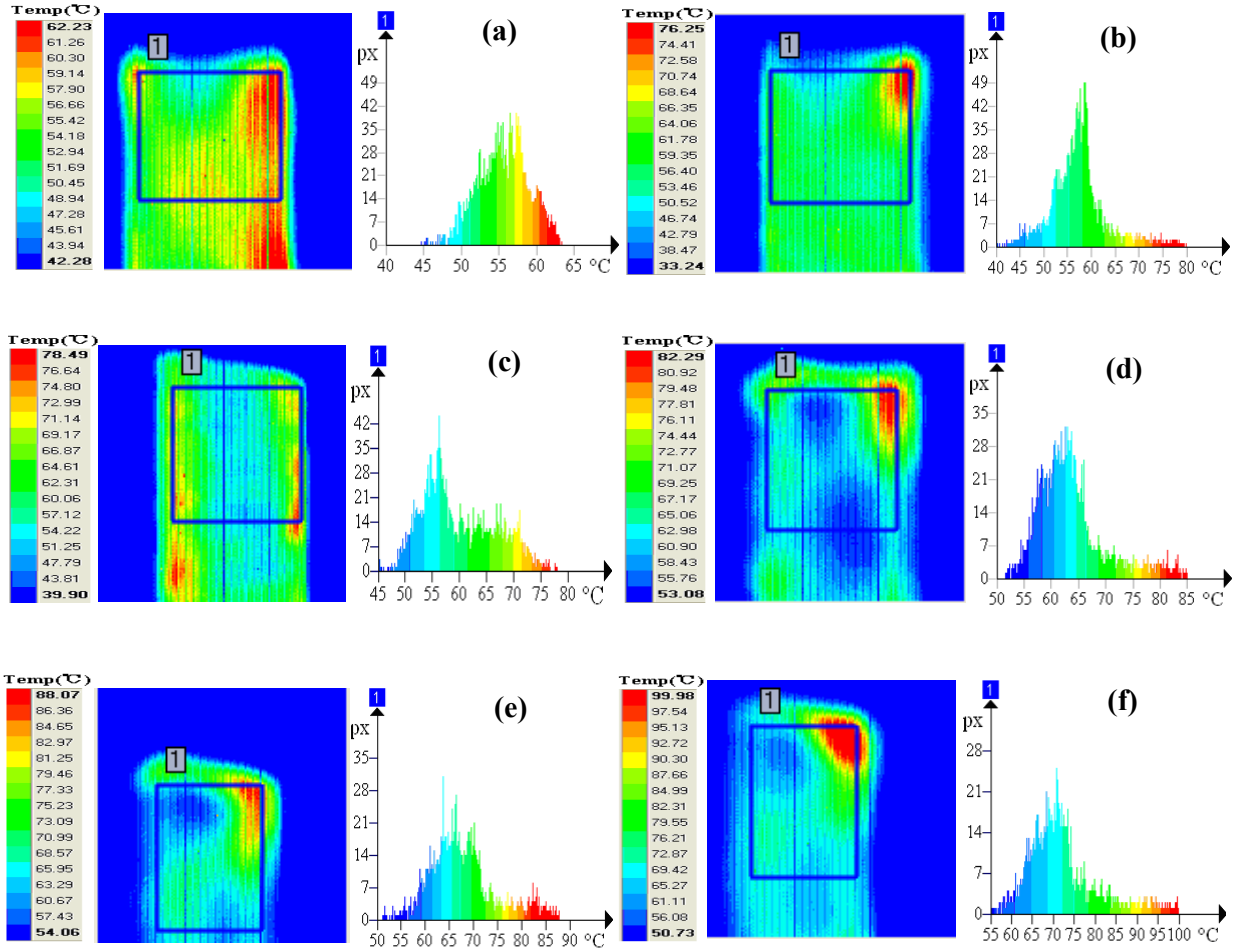

Figure 3.22 Thermal images and temperature pixel distribution in area '1' for different final strains: (a) 44.5% (b) 46% (c) 50% (d) 53.2% (e) 56.3% (f) 59.4%

the highest temperatures usually occur at the top right corner, possibly as a result of stress concentration there. Figure 3.22(a) shows that the temperature in area '1' ranges from 40°C to ~65°C. However, with larger final strains, the temperature range tends to increase, with the lower and upper bounds assuming values of 55°C and 100°C respectively for deformation to 59.4% strain, as shown in Figure 3.22(f). A comparison of Figure 3.22(a) with Figure 3.22(b) shows that the maximum temperature generated increases from about 63°C to 80°C when the final strain is increased from 44.5% to 46%. Such a rise in maximum temperature per unit increment of final strain is rather large in contrast to that observed in the other thermographs of Figure 3.22. Noting that Figure 3.22(c) shows a maximum

temperature of only around 80°C, it appears that Figure 3.22(b) displays a higher than expected maximum temperature if the maximum temperatures in Figures 3.22(c)-3.22(f) are analysed in conjunction with Figure 3.17. Note also that the maximum temperature in Figure 3.22(b) appears at the top right corner of the sample. This suggests that the higher temperature there possibly results from highly localised contact between the sample corner and the striker at the very beginning of impact, arising from either imperfect machining of the specimen edge or a minute mismatch in the angular alignment of the axes of the fixed bar and the striker. However, the number of pixels corresponding to this high temperature is small in comparison with the total number of pixels in area '1'. Therefore, it does not affect the overall distribution of temperature pixels, as can been seen from Figure 3.22(b). (One feature is that the total number of temperature-related pixels enclosed in area '1' decreases for higher final strains; this is because the area of the specimen side reduces with a larger deformation). For each final strain, at least two tests were undertaken, and comparisons between the results from similar tests show that the difference in temperatures is around 1°C, demonstrating consistency in the results. Figure 3.23 shows that the average surface temperature T1 increases with final engineering strain (ε_p). A straight line is fitted to the experimental data, and this indicates that every 1% increment in plastic strain generates an average surface temperature rise of 1.23°C.

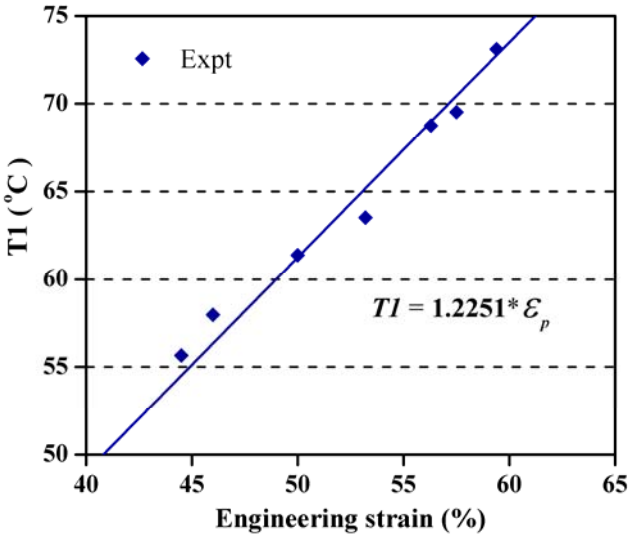

Figure 3.23 Variation of T1 with final strain

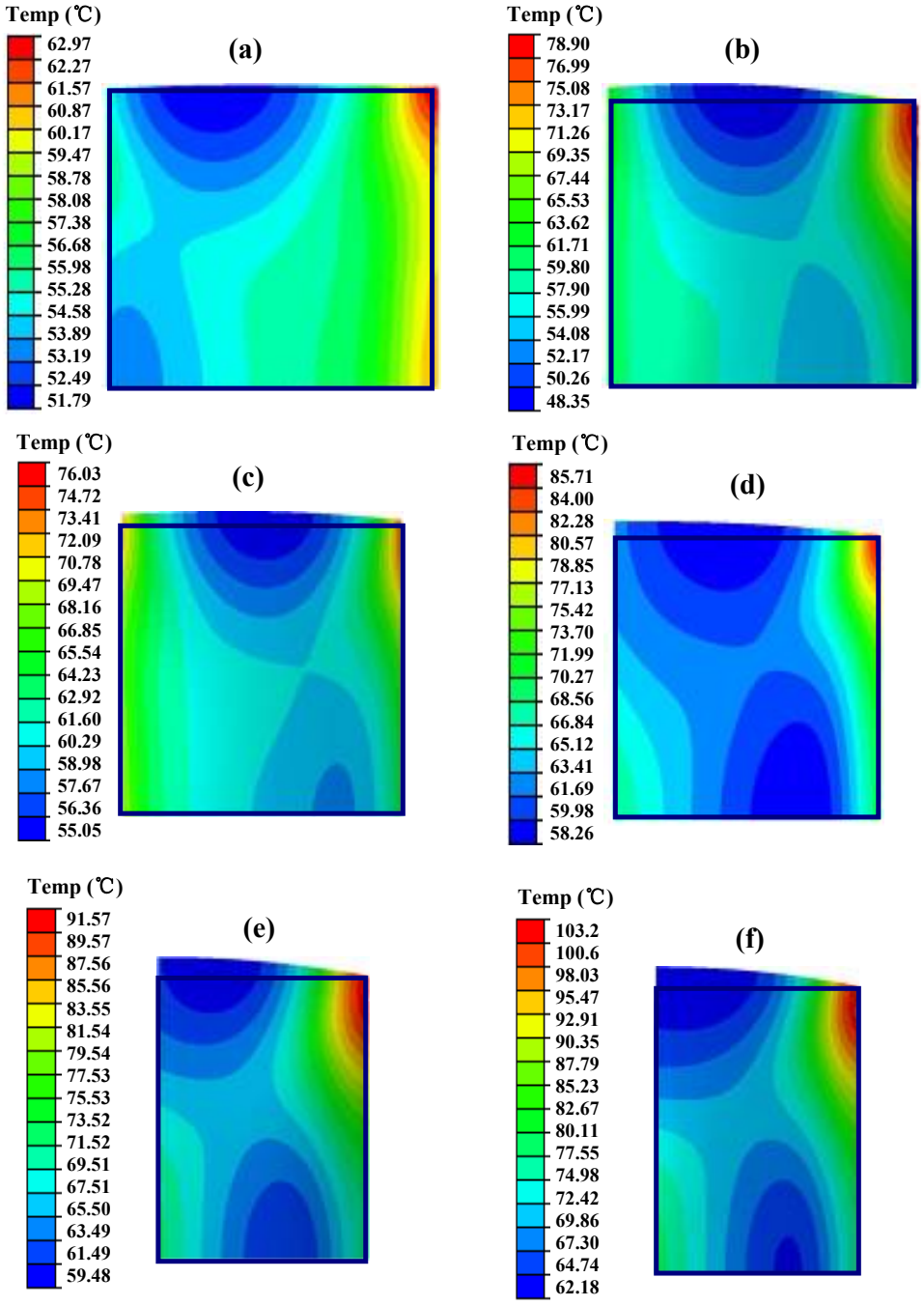

Figure 3.24 Surface temperatures of area '1' from simulations for various final strains (a) 44.5% (b) 46% (c) 50% (d) 53.2% (e) 56.3% (f) 59.4%

Simulations were undertaken to determine the IHF value for different final strains corresponding to the images in Figure 3.22, following the procedure described for Figures 3.20 and 3.21. Figure 3.24 shows the computed surface temperatures, excluding the region shielded by the double-sided tape. Each rectangular outline

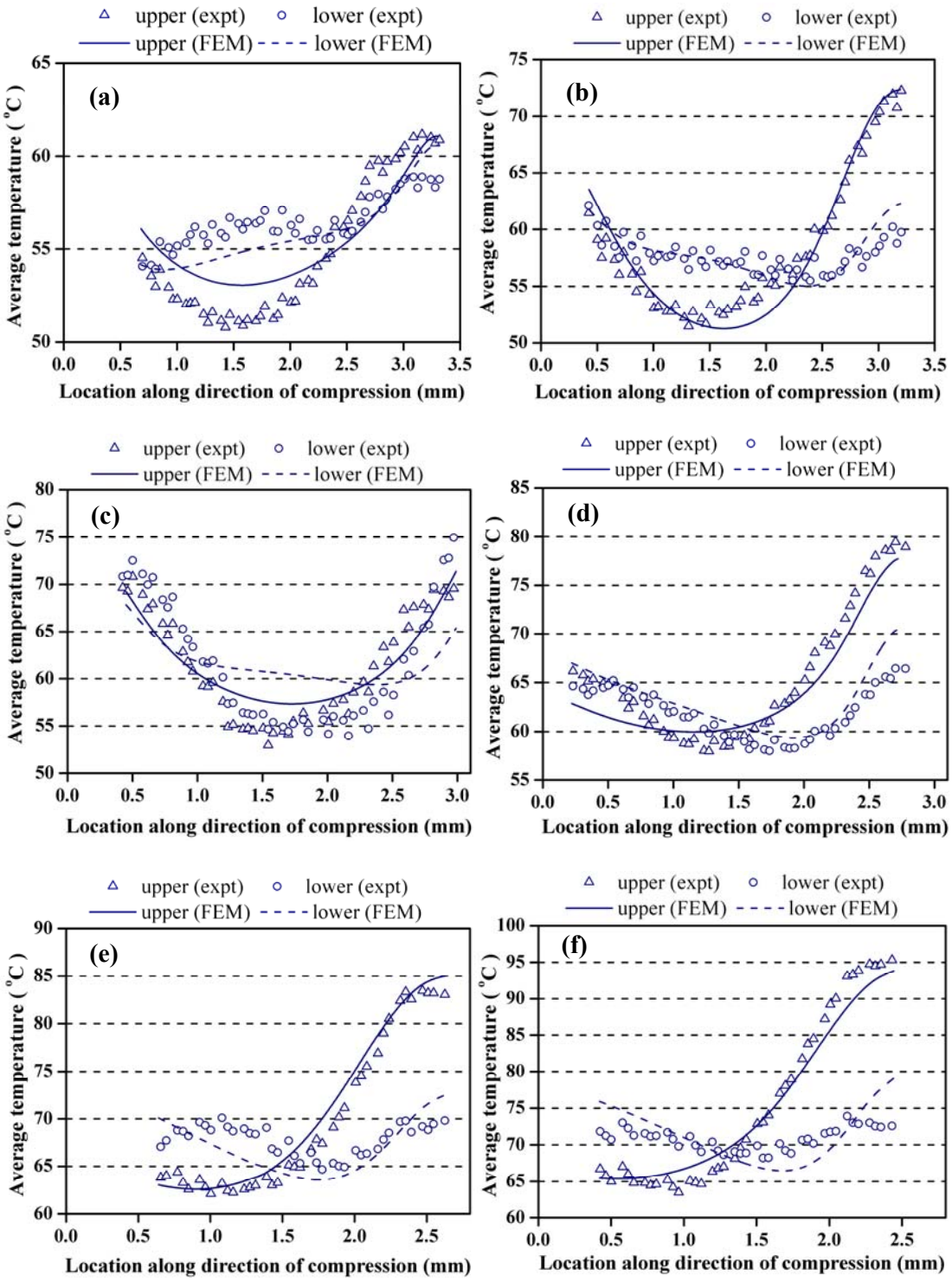

Figure 3.25 Average temperature distributions along direction of compression, in upper- and lower-halves for different final strains: (a) 44.5% (b) 46% (c) 50% (d) 53.2% (e) 56.3% (f) 59.4%

represents the corresponding area '1' in Figure 3.22, and the average temperature within it is plotted in Figure 3.23. In addition to matching the average temperature in area '1' determined from FEM simulations with experiments, the distribution of average temperature along the axis of deformation is also compared. As with the procedure applied to obtaining Figure 3.19, area '1' in the thermographs and simulations are divided into upper and lower halves, and the respective temperature distributions plotted in Figure 3.25 (the data points and lines represent respectively the experimental and simulation results). For all the six cases, the difference between the simulation and experimental results is around 3^{o}C, further confirming the acceptability of the IHF value obtained. Figure 3.26 shows IHF values calculated for different final strains, with the adjustment factor of 1.03 (according to Equation (3.15) and Figure 3.10) incorporated. An increase in final strain from 0.445 to 0.594 results in a decrease in the IHF from 0.696 to 0.655; this difference of 0.04 is insignificant for a strain increase of 0.15. Consequently, an average of the seven cases is taken, resulting in an IHF value of 0.68 for final strains of 0.445-0.60.

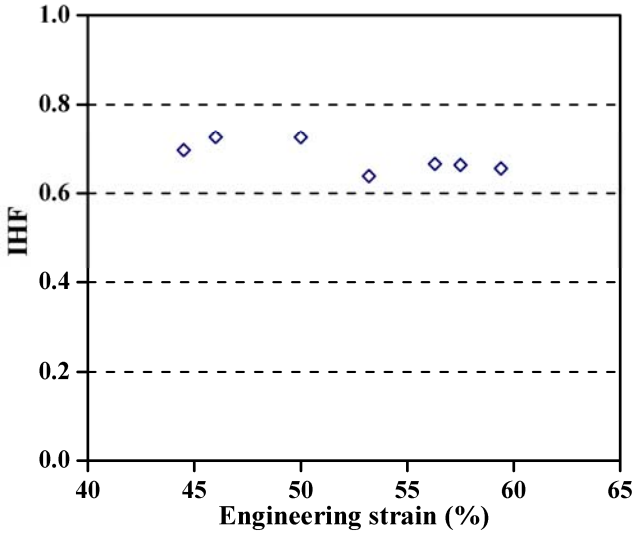

Figure 3.26 Variation of IHF with final engineering strain

3.7 Prediction of surface temperature and temperature within specimen

Consider a cuboid OFHC copper sample measuring $3.9 \times 3.9 \times 5.9$mm, dynamically compressed to 50% engineering strain by a striker with a length of 125 mm and an initial velocity of 20.2 m/s. This deformation process is simulated with an IHF value of 0.68 and the computed surface temperature at 1ms after commencement of impact is shown in Figure 3.27(a). The surface temperature recorded from experiments is also presented in Figure 3.27(b) for comparison with simulation results. As discussed previously, the sample surface near the interface with the fixed bar is shielded by double-sided tape, so this area is not considered in calculation of the average surface temperature. Half of the specimen side profile, represented by area '1' is outlined in Figure 3.27(b), and the variation of the number of pixels associated with each temperature is given in Figure 3.27(c), from which the average temperature is found to be 66.3^{o}C. The region corresponding to area '1' in the simulation is enclosed by the blue frame in Figure 3.27(a) and the average temperature within it is 66^{o}C, a difference of only about 0.4% with experiments. In addition to the average temperature, the temperature distributions from experiments and FEM simulation are also examined in the same way as that for Figure 3.25, and this is shown in Figure 3.27(d). The two arrows correspond to the left and right boundaries of area '1' in Figure 3.27(b). The region between 0 (the fixed bar-striker interface) and ~0.3mm has no data, as this is portion is shielded by double-sided tape. The difference between FEM prediction and experimental data in Figure 3.27(d) is evaluated by a least-squares approach and found to be only about 2^{o}C, indicating favourable agreement.

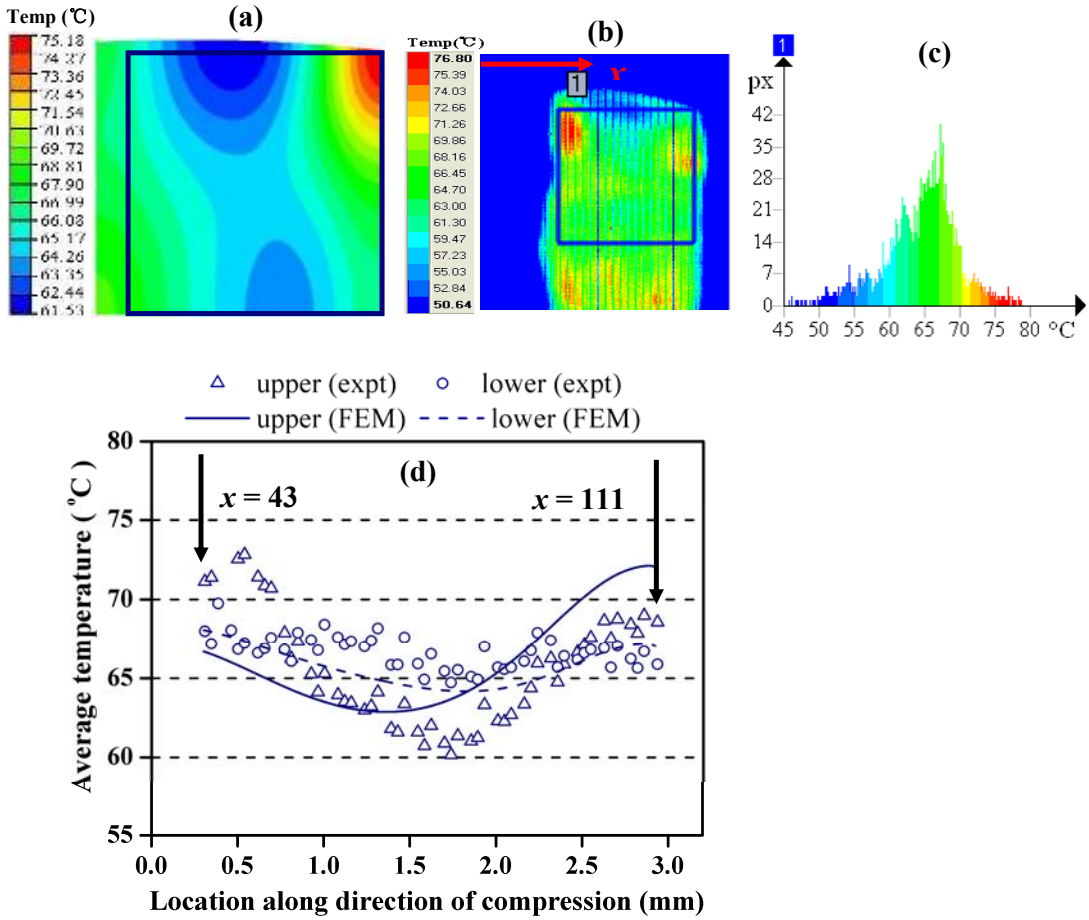

Figure 3.27 (a) Surface temperature from simulation (b) Surface temperature from experiments (c) Variation of number of pixels (px) with temperature in area '1' (d) Distribution of average temperature in upper- and lower- halves along direction of compression

3.8 Summary

An approach that combines dynamic gross plastic deformation with FEM simulation is proposed for determination of the IHF value for metals, whereby an infrared camera operating at a framing rate of 1,000 pictures per second is employed to capture the surface temperature of OFHC copper samples compressed by impact. The IHF value input into simulations is adjusted until the predicted surface temperature matches experimental results in terms of average surface temperature and temperature distribution. It is noted that the measured temperature distributions do not

match the calculated ones exactly, and that temperature distributions can be affected by other parameters apart from the IHF. Nevertheless, the present method constitutes a reasonable approach to addressing the complex problem of estimating IHF values. With respect to OFHC copper, the following are identified:

(1) In terms of temperature distribution, the regions adjacent to the interfaces with the striker and fixed bar exhibit higher temperatures. This is mainly attributed to friction between the specimen and the striker and fixed bar. The average surface temperature continues to increase after impact, indicating heat flux from the interior of the sample, confirming that the temperature inside is higher. The region with the lowest surface temperature displays the largest rate of temperature increase because of heat flux from the interior, but the rate of temperature change decreases with time. Two milliseconds after commencement of deformation, the surface temperature near the interfaces with the striker and fixed bar begins to drop because of heat loss through the interfaces. As the duration of specimen deformation is less than 1ms, the deformation process can be considered adiabatic.

(2) The computed surface temperature changes with time, leading to some variation in the calculated IHF value. Consequently, the IHF value for various deformation conditions is obtained from the instant the difference in temperature distribution between the experimental results and the simulation is smallest. For a final strain of 57.5% and a strain rate of 1,100/s, the value of the IHF is found to be 0.663. The predicted rate of surface temperature change also agrees closely with experiments, indicating that simulation can be employed to estimate temperature changes in the specimen.

(3) For strain rates of 867-1,110/s, the average surface temperature increases with final strain; every 1% increment in plastic strain causes an increase of 1.23^{o}C. The

IHF exhibits negligible variation over the range of 44.5-60% in final strain values. Consequently, the overall average value of the IHF is concluded to be 0.68. Based on this value, the surface temperature of a sample deformed to 50% strain at a strain rate of 2,000/s was simulated. The results match experimental data closely, demonstrating the validity of the IHF obtained for deformation of OFHC copper at such strain rates, and indicating that for the material studied, the value is lower than 0.9, which is commonly assumed.

Chapter 4 – Microstructure resulting from quasi-static and dynamic deformation at RT and LNT

In Chapter 2, it was highlighted that in contrast to quasi-static plastic deformation (Section 2.2) carried out primarily at strain rates below 10^0 /s and at RT to refine the grain structure of metallic materials, dynamic deformation at RT (Section 2.3.1) or quasi-static deformation in an environment colder than RT (Section 2.4.1) leads to a finer grain structure. This motivates the coupling of dynamic loading with a low ambient temperature environment to produce a grain structure finer than that obtained either by dynamic deformation at RT or quasi-static deformation at temperatures below RT. In the present study, dynamic loading is imposed using a gas gun, and a low ambient temperature achieved by immersing the sample in liquid nitrogen. To highlight the combined effects of high strain rate (dynamic loading) and low temperature on the microstructure of a deformed sample, comparisons are made with samples deformed quasi-statically and at RT. Quasi-static deformation is applied using a Shimadzu Universal testing machine (SUTM) and RT is defined as 298K. Unlike processes that are characterized by repeated deformation passes, such as those discussed in Section 2.2, uniaxial single compression (USC) is the deformation mode employed and examined.

4.1 Introduction

Severe plastic deformation (SPD) is a well-accepted approach to synthesize ultrafine or nano-grained metals and alloys, and possesses advantages in overcoming difficulties associated with other techniques, such as the introduction of porosity from

inert gas condensation and impurities from mechanical alloying [12]. Equal-channel angular pressing (ECAP) [30], high-pressure torsion (HPT) [31], accumulative roll-bonding (ARB) [32] and multiple forging (MF) [33] are typical SPD techniques that lead to significant grain refinement. However, these approaches have two limitations: firstly, the processing time needed is protracted because of the generally low strain rates (< 1 /s) applied during deformation of a sample, and repeated deformation is required to reduce the grain size to the ultrafine 100-1000 nanometer (*nm*) or nano-(<100 *nm*) range, e.g. eight passes and four full rotations are needed respectively for ECAP and HPT to generate a structure with grain sizes of 0.25-0.26 μm in copper [34, 35]. Secondly, the grains produced by these techniques, usually at room temperature (298K), display a minimum size limit, regardless of the processing method – viz. unidirectional and multidirectional deformation [23]. By employing high strain-rate compression (~ 10^4/s) on hat-shaped specimens at room temperature (RT), the microstructure of copper and zirconium have been successfully refined by a single impact, but still corresponds to the ultrafine regime [66, 67]. At a lower temperature (195 K) and low strain rate (10^{-3}/s), the grain size obtained in copper is 0.16 μm after multiple-forging (MF) [75]; this is smaller than the saturation value of 0.2 μm for RT deformation [19]. However, multiple forging still involves repeated deformation. High strain rate (10^2 ~2×10^3/s) can be combined with low temperature (77 K) to yield nano-grains in copper, but this still necessitates a multiple deformation process [79].

The aim of the present work is to explore the possibility of generating nano-grained structures by a single deformation process. Uniaxial single compression (USC), which is much simpler to execute and requires less complex equipment compared to ECAP, HPT, etc, is selected as the deformation mode. Pure copper,

which displays a saturation minimum grain size of 0.2 μm based on conventional SPD (cSPD) – i.e. processing at a low strain rate (< 1/s) and RT – is the target material investigated. As highlighted in literature [36], the saturation grain size decreases with an increase in the dislocations that can be stored in a deformed material. Therefore, the dislocation storage capacity required to facilitate the generation of nano-grains should be higher than that associated with the saturation grain size resulting from cSPD. Since material hardness increases with dislocation density, as described by the Taylor model [97], this parameter is used for comparison with the value for cSPD samples comprising saturation-sized grains; consequently, it is also regarded as a preliminary indicator of the formation of nano-grains. It is noted that the saturation (Vickers) hardness of severely deformed copper lies within a wide range (100-150) as reported by various researchers (Figure 1 of [69]). This study is directed at investigating the hardness that can be achieved by a single deformation process – uniaxial compression – in relation to the hardness associated with saturation-sized grains generated by multiple forging. The approach adopted in this study focuses on enhancement of dislocation storage by compressing samples at high strain rates (10^4 – 10^5 /s) and/or at a low temperature, both of which are considered effective in suppressing dislocation recovery, and hence may elevate dislocation density. Uniaixal single compression of samples is conducted at two temperatures – RT and liquid nitrogen temperature (77K); for both, samples are deformed quasi-statically and dynamically, and the resulting microstructure and strength examined. For plastic deformation at RT, Andrade et al. [66] found that the initial state of a sample (i.e. annealed or initially work hardened to different degrees) affects the final microstructure and mechanical properties after it is subjected to subsequent impact, whereas Mishra et al. [69] reported that for samples subjected to ECAP, the initial

state has no influence. This motivates the accompanying objective of investigating whether USC leads to a difference in the microstructure (and mechanical properties) arising from different initial states. Two initial conditions are examined – annealed copper and samples work hardened via compression in two directions.

4.2 Modes of Deformation

4.2.1 Compression in two and three directions

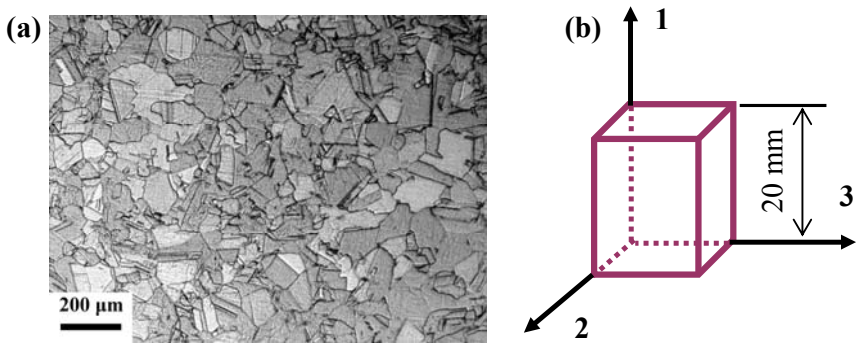

Figure 4.1 (a) Optical micrograph showing microstructure of annealed copper.

As-received polycrystalline OFHC copper (99.99% purity) in the form of 35mm diameter rods were used to fabricate 12×12×20mm cuboid samples by means of wire-cutting. The samples were then heat treated to 450^{o}C for 3 hours, and the grain structure after annealing is shown in Figure 4.1(a). As depicted schematically in Figure 4.1(b), annealed samples were compressed sequentially along mutually orthogonal axes (1, 2 and 3); this was repeated several times to yield a refined structure for comparison with uniaxially compressed samples. Sequential compression in two-directions (2DC) was also conducted along the 2- and 3- axes to produce hardened samples that were subsequently subjected to USC. MF and 2DC at room temperature were both performed using a Shimadzu Universal Testing Machine (SUTM), shown schematically in Figure 4.2(a), at a loading rate of 0.5 mm/min to

induce a final true strain $\varepsilon_f = \ln(L_0/L_f)$ of 0.69 (corresponding to 50% engineering strain) for each axial compression, where L_0 and L_f are respectively the initial and final length of the sample.

4.2.2 Uniaxial single compression (USC)

USC is performed respectively at RT and a reduced temperature of 77K. Figure 4.2(a) is a schematic drawing for quasi-static compression at RT. The sample is placed on a platen while the cross-head moves downwards to compress the sample at a constant speed v_0. This speed determines the strain rate ($\dot{\varepsilon}$), which is defined in the present study as:

$$t = \frac{L_0 - L_f}{v_0}$$
$$\dot{\varepsilon} = \frac{\varepsilon_f}{t} \tag{4.1}$$

where t is the duration of the compression. Figure 4.2(b) is a schematic drawing of a gas gun for dynamic compression at RT. A cylindrical projectile is propelled by pressurized helium through the barrel to impact the sample adhered to an anvil. The initial speed (v_0) of the projectile is determined by the time taken by the projectile to cut the beams of two laser emitters in its path. The average speed of the projectile during compression of the sample is estimated to be $v_0/2$, and thus the strain rate is:

$$t = \frac{L_0 - L}{(v_0/2)}$$
$$\dot{\varepsilon} = \frac{\varepsilon_f}{t} \tag{4.2}$$

Alternatively, the duration of the sample compression t, can be obtained from high-speed photography, which records visual images of the deformation process. This enables evaluation of the strain rate $\dot{\varepsilon} = \varepsilon_f / t$. In the present study, the strain rate for

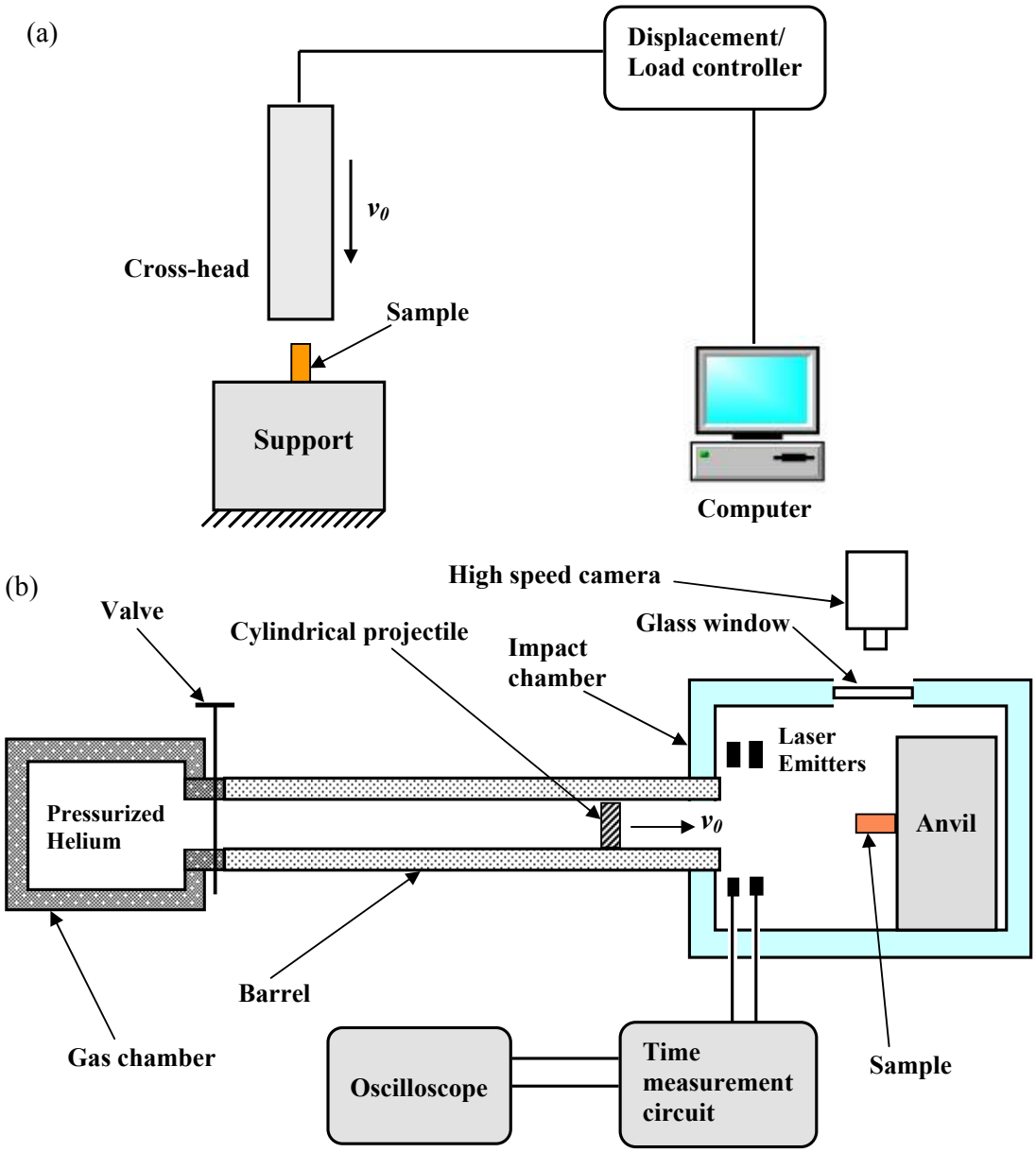

Figure 4.2 Schematic drawing of: (a) SUTM; (b) gas gun arrangement

deformation at RT is calculated by employing a high speed camera to evaluate the deformation time t, whereas for deformation at a reduced temperature, it is estimated using equation 4.2. This is because for tests at reduced temperatures, the sample is enclosed by a temperature chamber, which prevents capturing of visual images. This experimental setup for deformation at reduced temperatures is now described. To generate an ambient temperature lower than RT, additional fixtures are used in

conjunction with the Shimadzu Universal Testing Machine and the gas gun. Figure 4.3 illustrates schematically the fixture for the Shimadzu Universal Testing Machine.

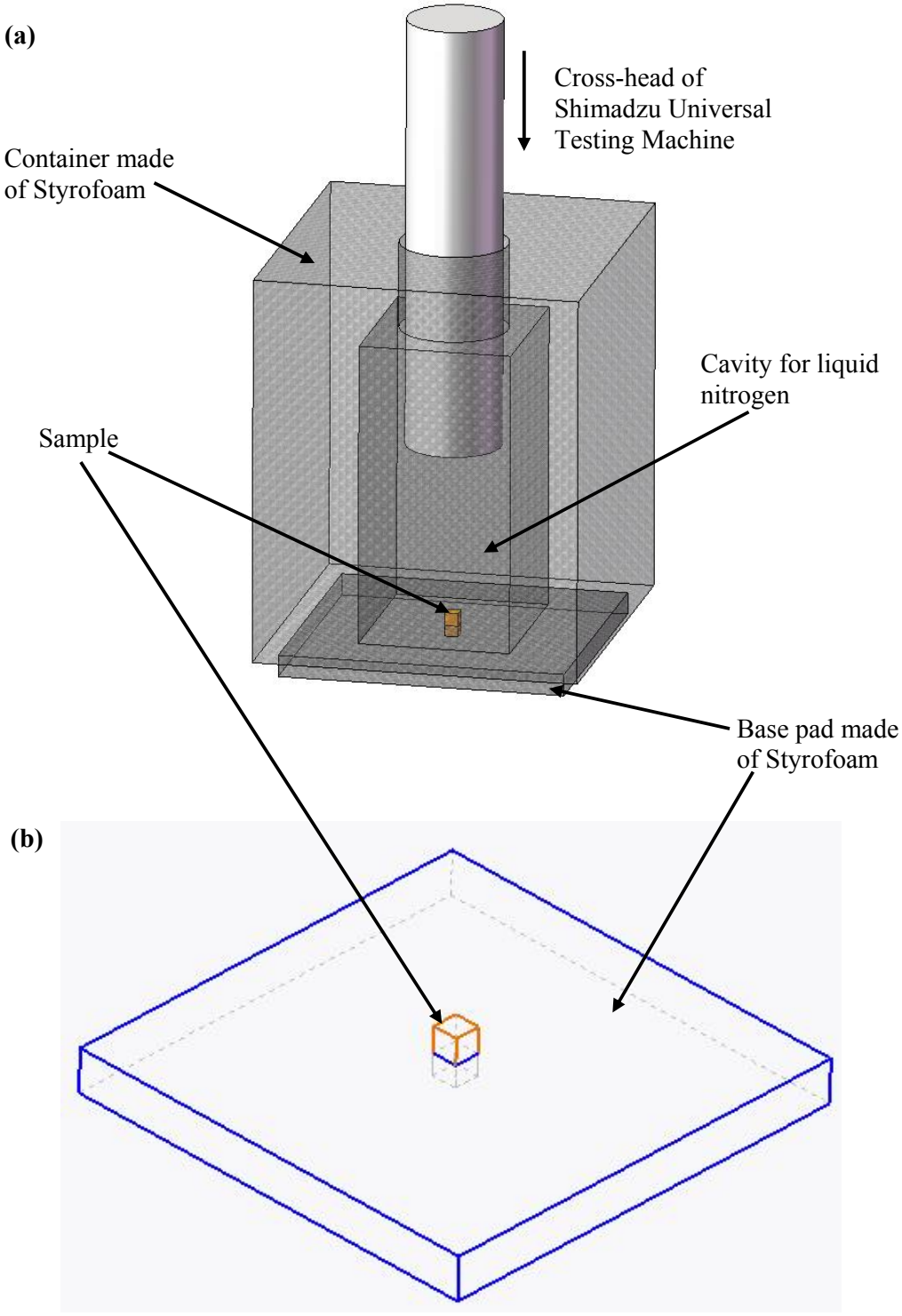

Figure 4.3 Components of additional fixture for Universal Testing Machine (a) chamber to cool samples; (b) mounting of sample on base pad

An enclosure made of Styrofoam is stuck to the base plate by adhesive (Figure 4.3(a)), then stored in a refrigerator for fifteen minutes to solidify the adhesive. Subsequently, liquid nitrogen is poured into the container to cool the sample, which is then compressed by the cross-head of the universal testing machine. Location of the sample in the base pad is shown in Figure 4.3(b); a cavity with a depth of 2mm is created in the centre of the pad, which has a thickness of 9mm. The sample is the placed in the cavity and lightly tapped several times by a rod to ensure that it is vertically aligned before compression commences. Figure 4.4 shows the additional fixtures used in conjunction with the gas gun. As with the description for Figure 4.3, the sample is positioned on the styrofoam plate, and the liquid nitrogen to cool the sample is poured into the styrofoam container. The striker, propelled by pressurized helium, breaks the styrofoam plate sealing the container as shown in Figure 4.4(a) and impacts the sample. After compression of the specimen, a hole is created in the styrofoam plate, as shown in Figure 4.4(b). The styrofoam container remains intact and can be reused. The striker employed in the present study comprises a steel disc and a hollow polymeric rod attached to it, to increase the length without adding significant mass, as shown in Figure 4.4(c). The steel disc makes direct contact with the sample and compresses it, while the hollow rod is helps to maintain the trajectory of the projectile. Without the polymeric rod extension, the steel disc will spin about its diametral axis so that its edge rather than its surface strikes the sample, as illustrated in Figure 4.5(b). In some cases, the steel disc misses hitting the sample because of deviation of its trajectory after breaking the Styrofoam plate. Addition of the rod extension facilitates contact between the free surface of the steel plate and the sample; the pits induced by the deformed samples on the steel plates demonstrate this, as indicated by the arrows in Figure 4.5(c). For a given pressure of the propelling helium

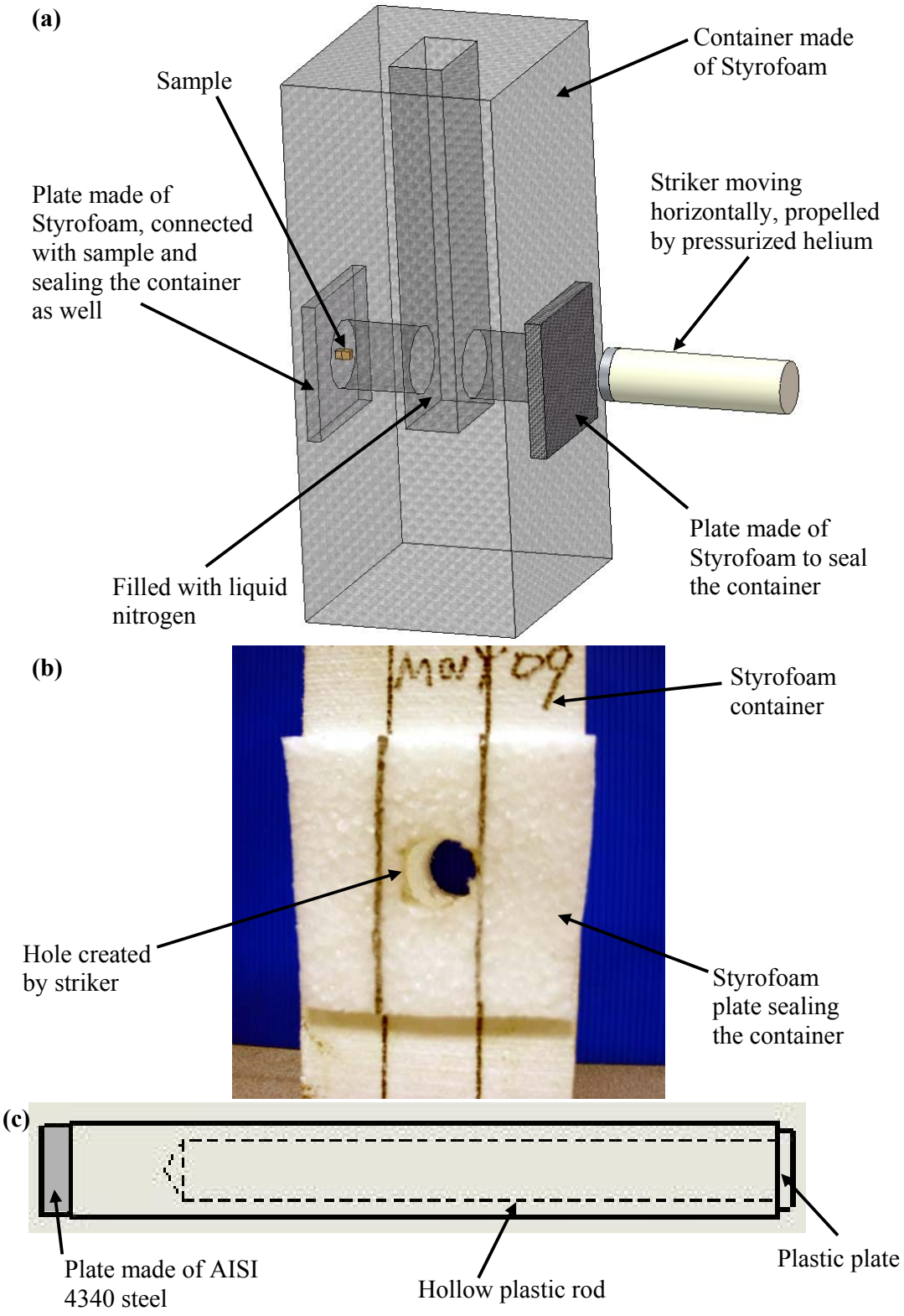

Figure 4.4 Components added to gas gun (a) Setup used to cool samples; (b) Photo showing the hole created by striker on the Styrofoam plate; (c) Striker

gas, the speed of the striker can be increased by reducing the striker weight. This is achieved by drilling a hole into the polymer rod (Figure 4.4(c)) and reducing the thickness of the steel disc. However, it is noted that if the steel disc is too thin, e.g. 3mm, it is deformed after impacting the sample as schematically depicted in Figure 4.5(d). The curvature induced in the impact surface of the steel disc determines the smallest final thickness a sample can be deformed to (δ in Figure 4.5(d)). Moreover, the deformed sample exhibits a non-uniform thickness, being thicker in the central region and thinner at the edge. To overcome these undesirable outcomes, the thickness of the steel disc is set at 6mm, resulting in a striker weight of 54.5 grams (Figure 4.4(c)).

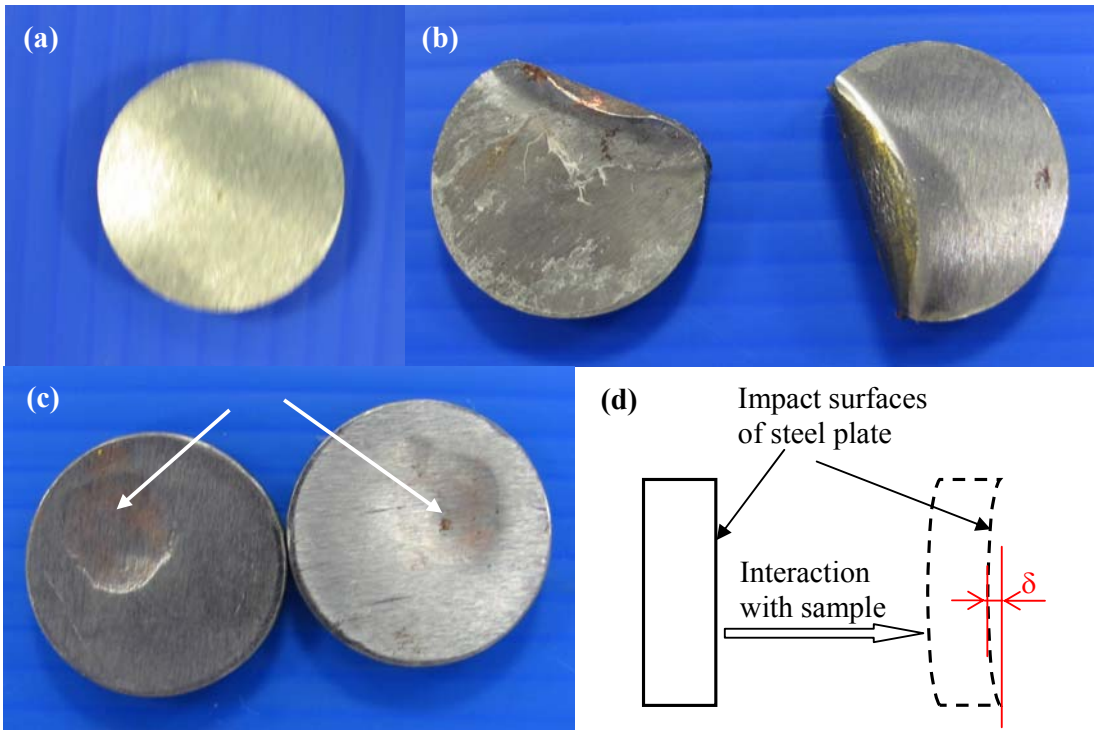

Figure 4.5 (a) Steel disc before impact; (b) Steel disc after impact, without polymer rod attached; (c) Steel disc after impact, with polymer rod attached (see Figure 4.3(c)); (d) Sketch of deformed thin steel plate after impact

The test fixtures in Figures 4.3 and 4.4 are adopted to cool the sample, and the sample temperature is measured using a FLUKE K-type thermocouple with a measuring range of 73-1643K. Before taking measurements, accuracy of the

thermocouple is checked by measuring the temperature of boiling water, an ice-water mixture, and liquid nitrogen. The measured temperatures of these three substances, together with accepted values, are listed in Table 4.1. It is observed that the temperatures measured by the thermocouple agree with the accepted values, confirming its reliability.

Table 4.1 Theoretical and measured temperatures

Substances	Boiling water	Ice water mixture	Liquid nitrogen
Theoretical temperature (K)	373	273	77
Measurements by thermocouple (K)	373.3±0.2	273	79±0.3

Figure 4.6 is a schematic diagram depicting measurement of the sample temperature. As with the illustrations in Figures 4.3 and 4.4, part of the sample is surrounded by Styrofoam while the rest is immersed in liquid nitrogen. Since a small hole has been created at the bottom of the Styrofoam container (Figure 4.6) to allow connection of the sample to the thermocouple, adhesive is introduced into the gap between the sample and the Styrofoam and allowed to solidify to prevent leakage of the liquid nitrogen. This results in a measured sample temperature of 80K, which is

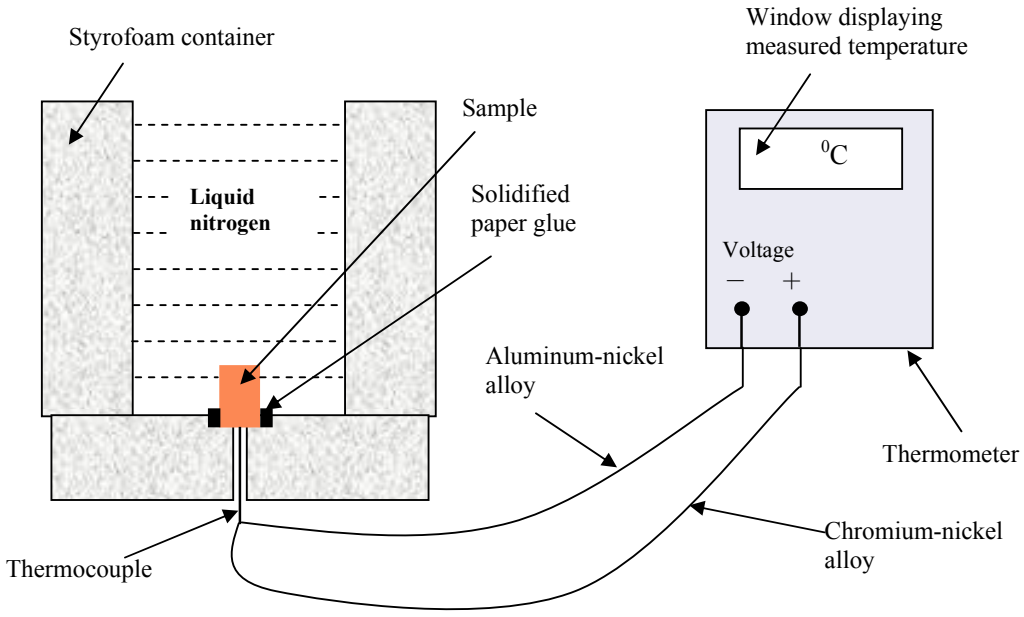

Figure 4.6 Schematic diagram of sample temperature measurement

one degree higher than the measured temperature of liquid nitrogen (Table 4.1). This difference is small and it can be assumed that the temperature in the sample is uniform and equal to that of the liquid nitrogen. It is also noted that the measured temperature of liquid nitrogen (Table 4.1) is two degrees higher than its commonly accepted value. This may be the result of experimental error. Rather than examining the cause of the negligible difference between the commonly-accepted and measured temperatures of liquid nitrogen, it is assumed that the temperature of liquid nitrogen and the sample is 77K. The final issue that needs to be clarified prior to compression tests is how long a sample should be immersed in liquid nitrogen before its temperature drops to 77K. Figure 4.6 shows that the temperature reading from thermometer stabilizes ~20 seconds after liquid nitrogen is poured into the styrofoam container; however, the response time of the thermocouple is 3-4s, which is obtained by direct measurement of the temperature of liquid nitrogen. Therefore, the process corresponding to the cooling of sample to 77K takes ~16s. The time required for a sample to cool to the expected 77K can also be estimated by analyzing the heat transfer between the sample and the liquid nitrogen. For a sample surrounded by liquid nitrogen, heat transfer within the sample is very rapid compared to that at the interface between the sample and the liquid nitrogen, because OFHC copper possesses a very high conductivity. Consequently, it is reasonable to assume a uniform temperature within the sample. Based on this assumption, the change in sample temperature (ΔT) arising from heat transfer between the sample and liquid nitrogen can be determined by applying the lumped-heat-capacity method [107] which relates ΔT to time (t) by:

$$\Delta T = \frac{\chi S_A t}{c \rho_C V} \tag{4.3}$$

where χ represents the heat flux at the interface between the sample and liquid nitrogen, S_A, c, ρ_C and V are respectively the sample surface area in contact with the liquid nitrogen, and the specific heat, density and volume of the sample. The specific heat c depends on temperature (T) and varies significantly when the temperature is below 300K. Marquardt et al. [111] and Banerjee [95] proposed their respective models describing the variation of c with T for T<300 K. Although different in how c varies with T, they converge as the temperature increases, as shown in Figure 4.7. In this study, the model by Banerjee [95] is adopted and this has the following form:

$$c = \begin{cases} 0.0000416T^3 - 0.027T^2 + 6.21T - 142.6 & \text{for } T < 270K \\ 0.1009T + 358.4 & \text{for } T \geq 270K \end{cases} \quad (4.4)$$

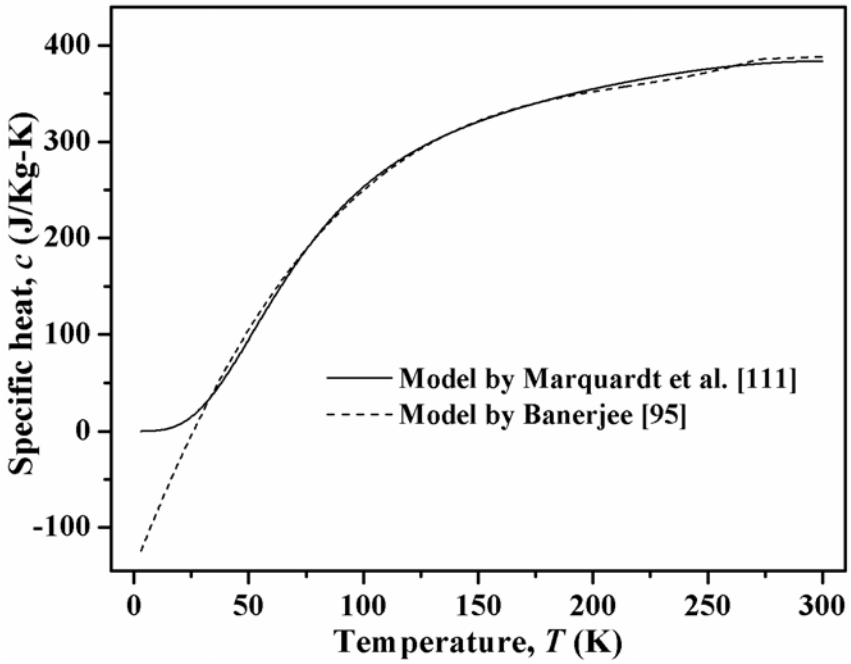

Figure 4.7 Convergence in the value of specific heat based on two models for 30K<T<300K

Denoting the initial temperature of the sample by T_i, the instantaneous temperature ($T(t)$) after immersion in liquid nitrogen for a duration t is calculated from:

$$T(t) = T_i + \Delta T \quad (4.5)$$

Clearly, determination of $T(t)$ requires quantification of χ, which varies with sample temperature in excess of the boiling point of liquid nitrogen, and the mechanism (i.e. convection, nucleate boiling, film boiling) accounting for heat transfer at the interfaces. Investigations [108-110] have shown that χ lies within a range bounded by a maximum (χ_{max}) and minimum (χ_{min}) heat flux, which are defined by:

$$\chi_{max} = \overline{E} h_{fg} \rho_v \left[\frac{g\varpi(\rho_l - \rho_v)}{\rho_v^{\,2}} \right]^{1/4}$$
$$\chi_{min} = 0.09 h_{fg} \rho_v \left[\frac{g\varpi(\rho_l - \rho_v)}{(\rho_l + \rho_v)^2} \right]^{1/4} \tag{4.6}$$

where h_{fg}, ρ_v, ρ_l and ϖ are parameters for nitrogen at $77K$, and represent respectively the latent heat of vaporization, vapor density, liquid density and surface tension; g is gravitational acceleration and $\overline{E}$ is a constant. Table 4.2 lists the values of parameters in equation 4.6 for quantification of χ_{max} and χ_{min}.

Table 4.2 Values of parameters in equation 4.6

Parameters	h_{fg} (J/Kg)	ρ_v (Kg/m^3)	ρ_l (Kg/m^3)	ϖ (N/m)	g (m/s^2)	$\overline{E}$
Values	1.99e5	4.66	806	8.93e-3	10	0.19

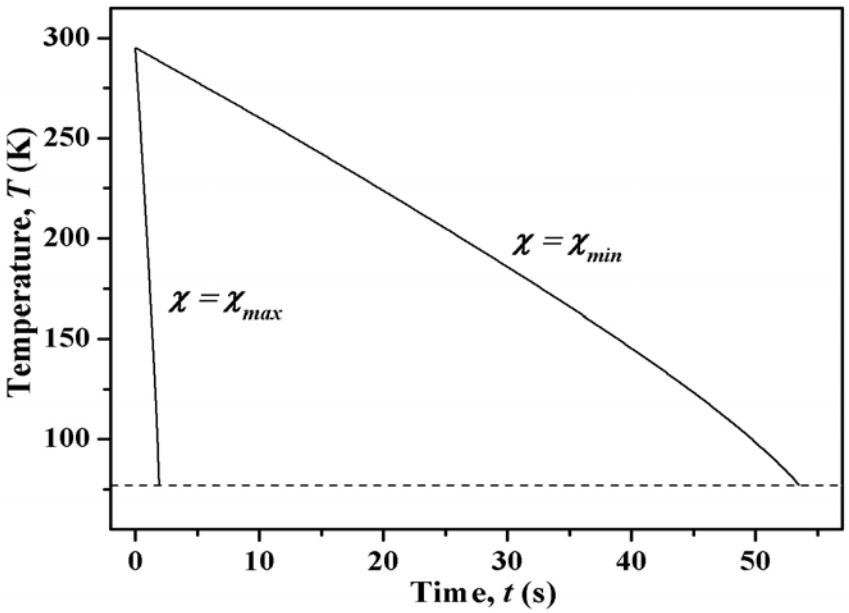

Figure 4.8 Variation of sample temperature with cooling time for $\chi = \chi_{max}$ and χ_{min}

Combining equations 4.3-4.6, the variation of sample temperature with cooling time is shown in Figure 4.8. With χ made equal respectively to χ_{max} and χ_{min}, the times taken for the sample temperature drop to 77K (dashed line in Figure 4.8) are respectively 2s and 53s. These two values define the limits of the duration a sample should be immersed in liquid nitrogen. The earlier experimentally-determined cooling time of 16s lies within these two limits and thus is reasonable. It is therefore concluded that the sample should be immersed in the liquid nitrogen for more than 16s before deformation commences. For the containers shown in Figures 4.3 and 4.4, it takes 40 minutes for 150ml of liquid nitrogen to completely evaporate, because the Styrofoam provides good heat insulation. This means that the experimental arrangement employed provides sufficient time for the sample to cool to 77K. Figure 4.9(a) is a photograph of a copper sample cooled by liquid nitrogen before compression. The compressed sample, shown in Figure 4.9(b), is a disk of uniform thickness, and its strength and microstructure are subsequently analysed.

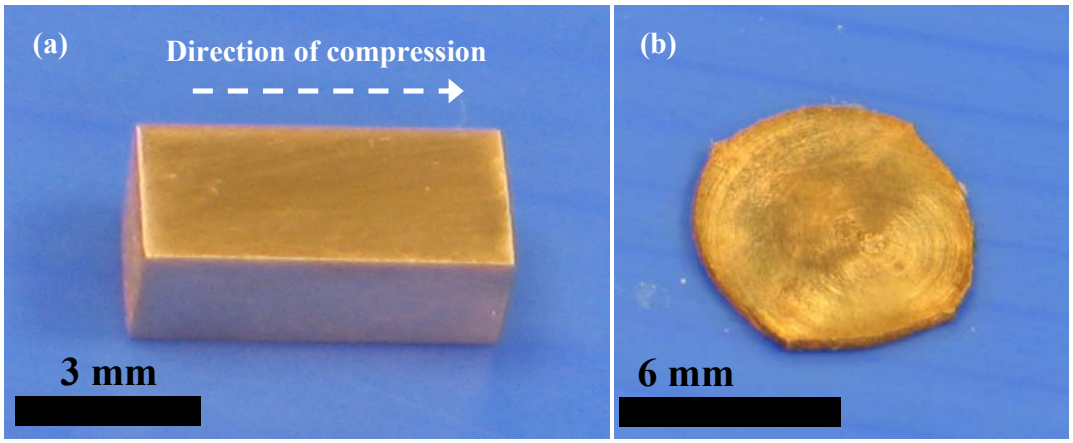

Figure 4.9 Photos of sample (a) before compression; (b) after compression at 77K

In summary, Table 4.3 lists the initial conditions of USC samples, as the final strain ε_f imposed and the true strain rate ($\dot{\varepsilon}$) during compression (The annealed samples listed in Table 4.3 were cut from the large sample shown in Figure 4.1(b),

taking into consideration the loading capacity of the Universal Testing Machine and the maximum allowable diameter of projectiles launched by the gas gun).

Table 4.3 Initial condition of samples; ε_f and $\dot{\varepsilon}$ induced during USC

Initial temperature	Initial state	Initial size (Axis '2' ×'3'×'1')	Direction of compression	Equipment			
				SUTM		Gas gun	
				ε_f	$\dot{\varepsilon}$ (/s)	ε_f	$\dot{\varepsilon}$ (/s)
RT (298K)	Hardened by 2DC	2.1×2.1×5.7mm	Axis 1	2.7	4×10^{-3}	2.7	1.3×10^{5}
	Annealed						
LNT (77K)	Annealed			2.3	9.4×10^{-2}	2.3	6.9×10^{4}

4.3 Processing of deformed samples

4.3.1 Tests on microhardness and stress-strain behavior

Deformed samples were polished using 800 grit SiC abrasive paper, followed by another polishing sequence using 5, 1 and 0.3μm aluminum oxide abrasive in a water suspension. Subsequently, the Vickers microhardness was measured using a Matsuzawa Seiko tester model MXT50, which applied a load of 50gf for 15s. Care was taken to ensure that the diagonal length of each indentation was no larger than 1/5 the sample size, and that all indentations were located sufficiently far from each other and from the sample edge. Stress-strain characteristics were derived using an Instron servo-hydraulic testing machine to elicit the quasi-static behaviour, and a Split Hopkinson Pressure Bar was employed to determine the dynamic responses. The surfaces of samples in contact with the test machines were polished and coated with molybdenum disulfide grease to reduce friction.

4.3.2 Microstructure characterization

Metallographic analysis was carried out based on observations made via an Olympus optical microscope (model BH2). Prior to examination, sample surfaces were polished and etched with a solution comprising a mix of HNO_3, H_3PO_4 and $C_2H_4O_5$ in a 9:2:9 volume ratio. The microstructure was examined by means of a JEM-2010F transmission electron microscope (TEM) operating at 200 KV. Samples for TEM observation were in the form of 3mm diameter discs punched from deformed test samples; the discs were mechanically ground to a thickness of around 25 μm, and the resulting foil further thinned by ion milling until perforation at the center was achieved.

4.4 Microhardness of multiple-forged (MF) and two-direction compression (2DC) samples

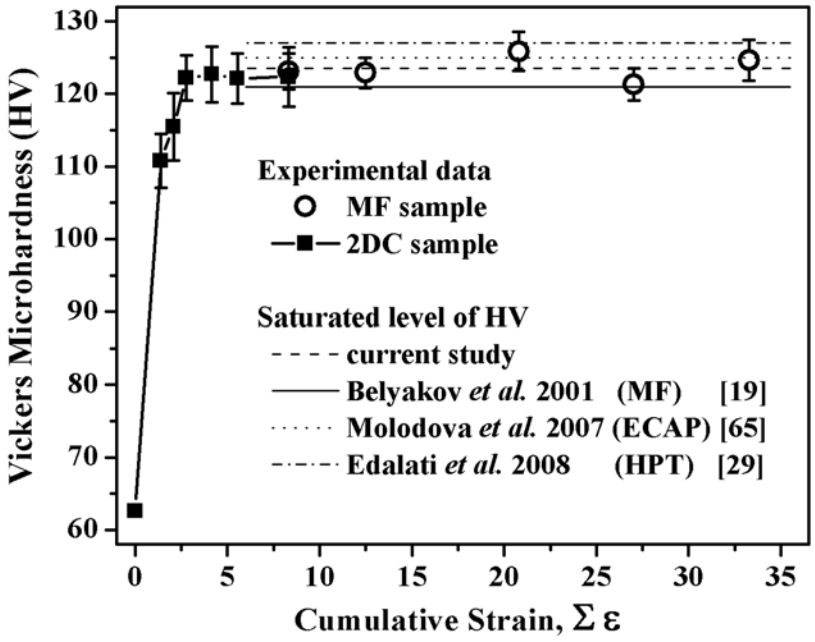

Figure 4.10 Variation of HV with cumulative true strain for MF and 2DC copper samples

Figure 4.10 shows the variation of the Vickers microhardness (HV) with cumulative strain for MF and 2DC samples. A pronounced increase in hardness with

cumulative strain is observed up to a true strain of 2.8, after which the hardness appears to fluctuate around a constant value, irrespective of the sequence and mode of deformation, viz. MF and 2DC. This suggests a saturation value for the HV, which remains essentially unchanged with further strain. The dashed line in Figure 4.10 marks the saturation level of the microhardness, which is obtained by averaging the HV values of MF samples corresponding to different amounts of cumulative strain. For comparison, the saturation HV levels for pure copper studied by others (Belyakov *et al.* [19]), whereby the HV shown is converted from stress by multiplying a factor of 3/10) or other techniques (ECAP [65]; HPT [29]) are also shown, and this demonstrates close correlation with results from the current study. Saturation of the HV indicates the occurrence of dynamic recovery, whereby dislocation annihilation accompanies dislocation generation during plastic deformation. Despite saturation in the HV, the microstructure does evolve with increasing strain. Figures 4.11(a) and 4.11(b) show TEM bright field (BF) images of MF samples that correspond respectively to cumulative true strains of 12.5 and 27 (Figure 4.10). As can be seen, the (sub)grain structure is finer for larger cumulative strains; this results from further

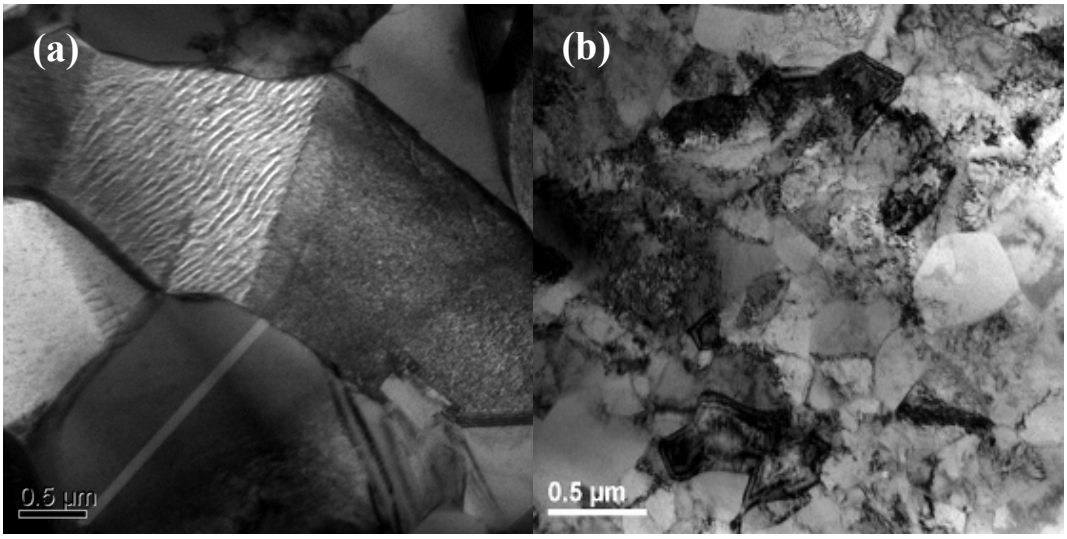

Figure 4.11 Bright field TEM images of samples after multiple forging: (a) $\sum\varepsilon = 12.5$; (b) $\sum\varepsilon = 27$.

subdivision of existing grains with increasing strain. However, subdivision does not occur when the grain size has been reduced to a critical value, as pointed out by Humphreys *et al.* [18]; this defines the existence of a saturation minimum grain size.

4.5 Evolution of mechanical properties and microstructure of uniaxial single compression (USC) samples at 298K

Quasi-statically deformed 2DC samples (Figure 4.10) with a cumulative true strain of 8.3 (sum of uniaxially-applied true strains) were subjected to subsequent uniaxial single compression (USC); this was done at quasi-static rates for some samples and under impact loading for others. After six cycles of 2DC (Section 4.2.1), the samples (denoted as 2D6C samples) assume a geometry similar to that of a rod with a square cross-section of about 2mm. The resulting rod was then cut into several shorter lengths, measuring 5.7mm each. These were then deformed by quasi-static and impact compression along their longer length. (Details of the test samples are given in Table 4.3.)

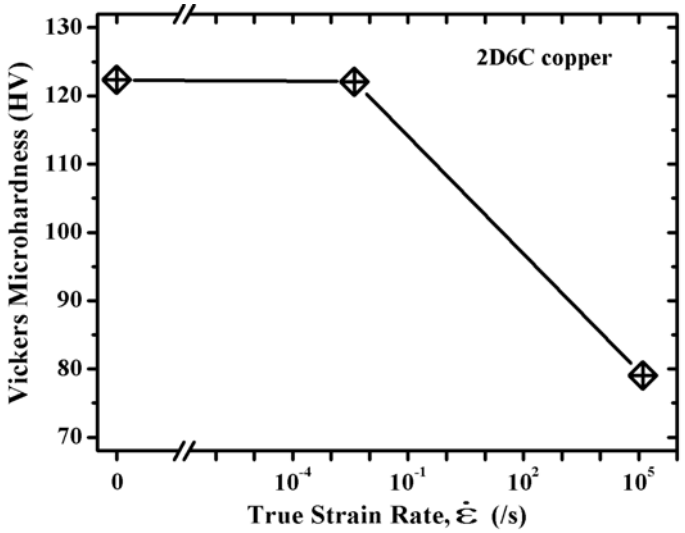

Figure 4.12 Variation of HV with strain rate for compression of 2D6C copper

Figure 4.12 shows how the resulting HV of 2D6C samples varies with the strain rate imposed during the final uniaxial compression. For low strain-rates, there is

negligible change in the HV, which is consistent with the results in Figure 4.10; however, the hardness decreases significantly for samples deformed by impact. This observation suggests that high-rate deformation affects the microstructure, and therefore warrants investigation. Figure 4.13 shows the microstructure of a 2D6C sample before and after impact; Figure 4.13(a) depicts elongated grains, while twins (indicated by arrows) and newly-formed equiaxed grains are observed in Figure 4.13(b). The significant drop in the HV (Figure 4.12) and the difference in microstructures between Figures 4.13(a) and 4.13(b) point to the occurrence of recrystallization (RX).

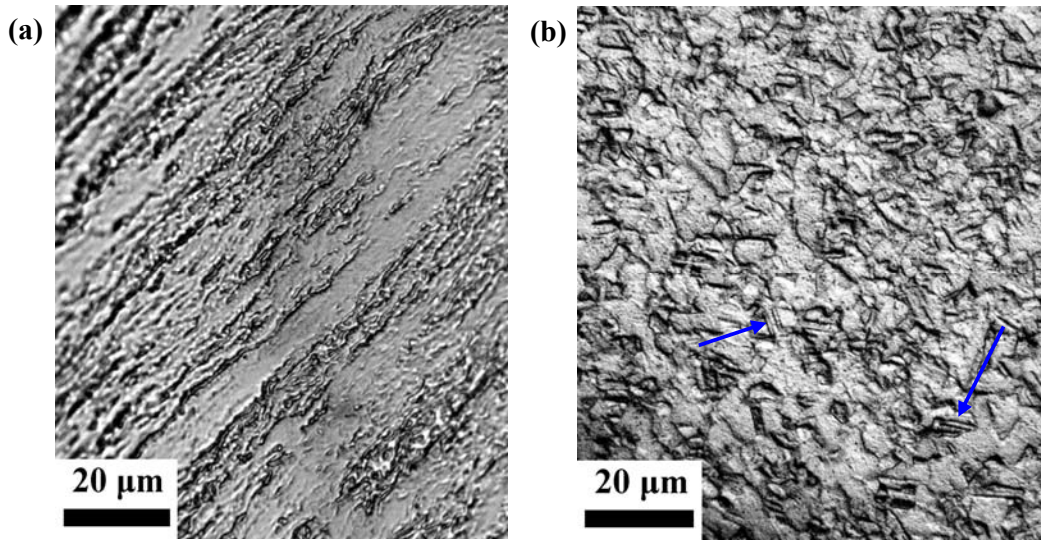

Figure 4.13 Optical images showing microstructure of 2D6C copper: (a) before impact; (b) after impact

The generation of deformation twins is a typical characteristic of high strain-rate deformation, which has been reported for oxygen free electronic copper [91] and copper alloys [98]. As discussed in some literature [99], the thickness of twins measured using optical microscopy is overestimated compared to values derived from TEM. Current TEM measurements show that the thickness of twins ranges from 60 nm to a few µm. A noteworthy feature of the twins generated in the present study is their intersections at various angles (e.g. TW_1 and TW_2 in Figure 4.14). Figure 4.14(a)

shows that dislocations are present at the boundaries of twins, a typical characteristic of deformation twins, whereas annealing twins usually display dislocation-free boundaries [78]. The boundary defining the intersection between TW_1 and TW_2 comprises straight lines. Another result of the interaction between TW_1 and TW_2 is the generation of a short third twin (TW_3), which does not align with either TW_1 or TW_2. Figures 4.14(b) and 4.14(c) show respectively the diffraction patterns of TW_2 and TW_3; the diffraction spots associated with the matrix surrounding the twin and that of the twin are denoted respectively by the subscripts 'M' and 'T', and are symmetric with respect to the {1 1 1} plane, indicating a typical {1 1 1}/[1 1 2] type twin relationship.

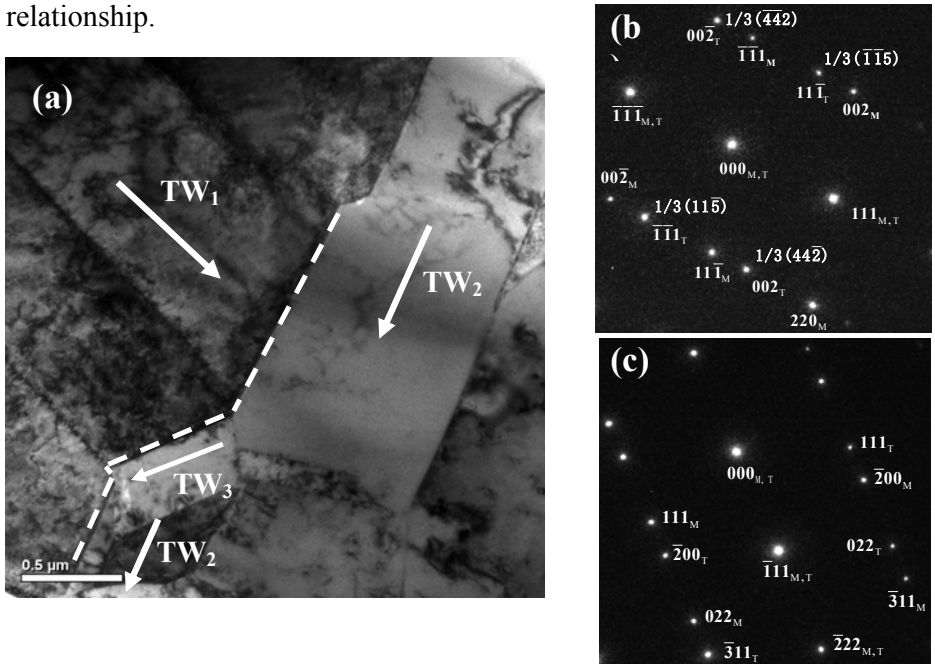

Figure 4.14 (a) Bright field TEM image showing intersection of TW_1 and TW_2 and twinning at a third orientation (TW_3). (b) (1 $\bar{1}$ 0) diffraction pattern of TW_2. (c) (0 $\bar{1}$ 1) diffraction pattern of TW_3.

With regard to the occurrence of RX, the challenge is to determine the instant it initiates – i.e., during or after impact. To clarify this, the temperature history of samples during impact is estimated using the Johnson-Cook (J-C) phenomenological constitutive model [100], expressed as:

$$\sigma = \left(\sigma_0 + B\varepsilon^n\right)\left(1 + C\,log\,\frac{\dot{\varepsilon}}{\dot{\varepsilon}_0}\right)\left[1 - \left(\frac{T - T_r}{T_m - T_r}\right)^m\right] \tag{4.7}$$

where σ, ε , $\dot{\varepsilon}, \dot{\varepsilon}_0$ are respectively the stress, strain, current and reference strain rates; T, T_r and T_m represent respectively the current, reference, and melting temperatures; σ_0, B, n, C and m are experimentally-determined parameters and their values for 2D6C copper samples are determined. Figure 4.15 shows the compressive stress-strain responses of 2D6C samples, together with those of samples initially annealed.

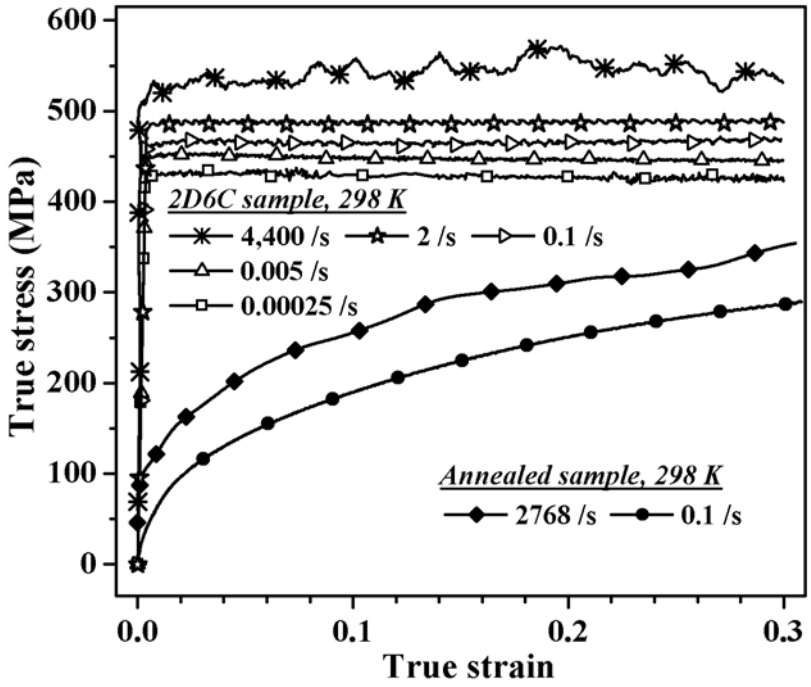

Figure 4.15 Stress-strain response of 2D6C and annealed samples at $T=T_r=298K$

Compared to annealed samples that display strain-hardening, the flow stress of 2D6C samples varies little with strain, which is consistent with the hardness measurement presented in Figures 4.10 and 4.12. Therefore, for 2D6C samples, the work hardening coefficient n can be assumed to be zero, and then the term within the leftmost parentheses in equation (4.7) becomes $\sigma_0 + B$. Taking the reference strain rate to be $\dot{\varepsilon}_0 = 2.5 \times 10^{-4}$ /s and fitting equation (4.7) to the flow stress at $\dot{\varepsilon}_0$, the relationship $\sigma_0 + B = 429.5$ MPa is obtained. The parameter defining strain rate sensitivity, C, is

determined by a linear fit to the yield stress in Figure 4.15; this results in $C = 1.33 \times 10^{-2}$. For a constant strain rate, equation (4.7) can be re-expressed to yield m:

$$m = \frac{\ln\left(1 - \sigma_T / \sigma_{T_r}\right)}{\ln\left((T - T_r)/(T_m - T_r)\right)}, \tag{4.8}$$

where σ_T, σ_{Tr} represent respectively the stress at T and T_r.

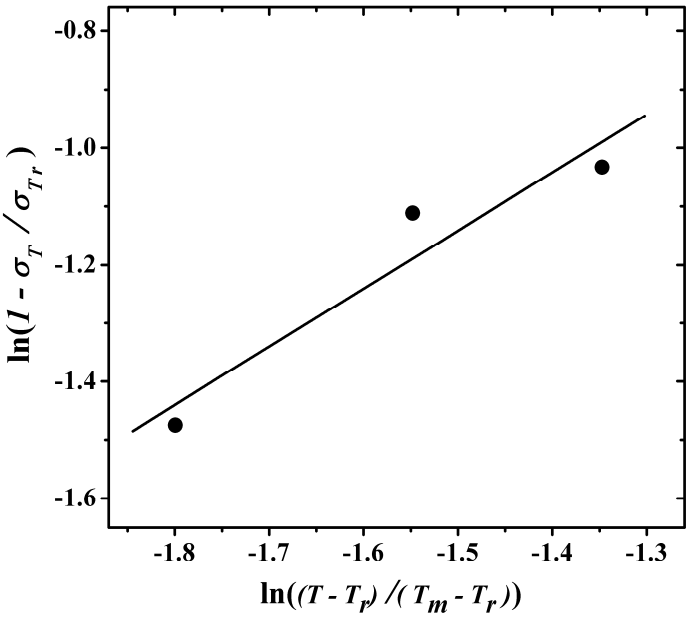

Figure 4.16 Determination of m

At $\dot{\varepsilon} = 5 \times 10^{-3}$ /s, the flow stresses (σ_T) of 2D6C copper at 0.1% strain are experimentally determined for three temperatures, namely 473K, 523K and 573K. According to equation (4.8), m is the slope of the straight line fit to the experimental data shown in Figure 4.16, and a value of 0.994 is obtained. The instantaneous temperature during deformation is estimated from:

$$T = T_i + \frac{\beta}{\rho_C c} \int \sigma \, d\varepsilon \tag{4.9},$$

where β, T_i, c and ρ_C represent respectively the fraction of plastic work transformed into heat, the initial temperature, and the specific heat and density of copper. β is experimentally determined as 0.7 from uniaxial single compression tests [101] (see

Chapter 3), which is similar to values obtained by others for tension and compression, whereas the often-assumed value of $\beta = 0.9$ has been reported for samples subjected to torsion [93]. Figure 4.17 depicts the variation of temperature in 2D6C samples during impact. The curve corresponding to β=1.0 indicates the upper limit for the

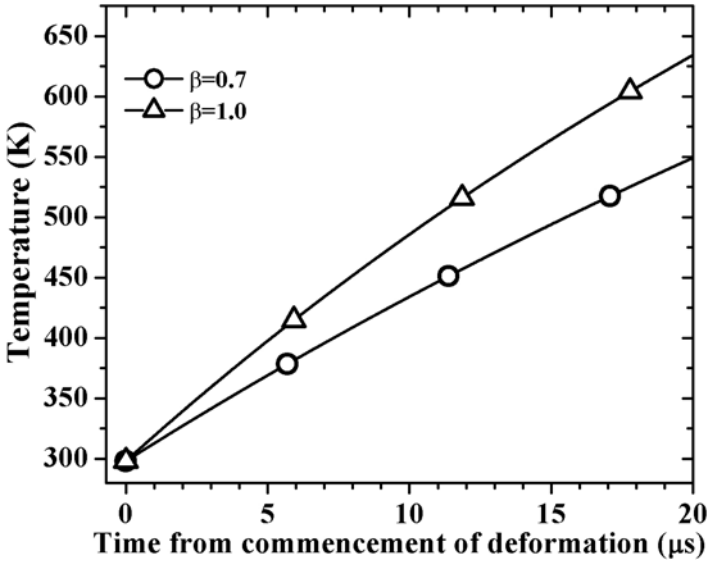

Figure 4.17 Variation of temperature during impact

sample temperature and displays a maximum of 634K at the end of deformation (20μs). To assess the kinetics of static RX, a 2D6C sample was first quasi-statically compressed to a true strain of 2.7, equivalent to the strain induced under impact deformation, and then annealed at 634K. Figure 4.18 shows the variation of the HV with annealing dwell time; this indicates that softening of the sample consists of three stages. In the early stage, the HV varies negligibly with dwell time; this corresponds to recovery. Upon further annealing, there is a sharp drop in the HV, arising from the occurrence of RX. In the third stage, the HV again appears insensitive to dwell time, and this is attributed to the occurrence of grain growth. It is noted from Figure 4.18 that a period of 200s is required before the HV drops to that corresponding to the impacted samples, i.e. HV = ~80. However, measurements from thermocouples show that 30-40s after commencement of impact, the sample temperature has attained

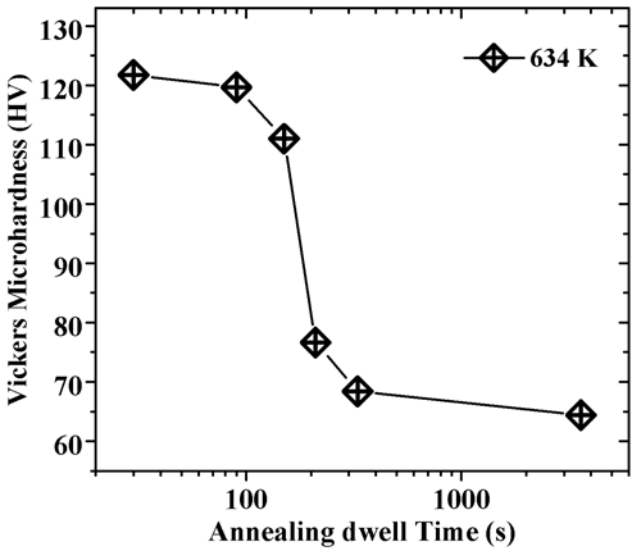

Figure 4.18 Variation of HV with annealing duration at 634K

equilibrium with the ambient temperature. This implies that static RX cannot fully account for the formation of new grains in the impacted samples. Instead, the most probable mechanism is that new grains nucleate during impact, then subsequently grow when the sample is gradually cooled. This is reasonable for two reasons: (i) the temperature of the sample during impact, shown in Figure 4.17, has reached that for the onset of RX, i.e. ~500K [66], so that nucleation during impact is possible; (ii) Figure 4.18 demonstrates that a significant drop in the HV by RX can occur within several seconds, which is similar to the cooling time of the impacted sample. Therefore, the grains shown in Figure 4.13(b) are a result of DRX during impact and static RX during subsequent cooling of the samples. Figures 4.19(a) and 4.19(b) show respectively, examples of typical dislocation cells and grain boundary characteristics in 2D6C samples. Some of these cells, indicated by arrows in Figure 4.19(a), are around 0.2 μm in size; the grain boundary defined by the dashed line in Figure 4.19(b) is characterized by kinks (indicated by the arrows) where there appear to be a high concentration of dislocations. The dislocation energy stored both at the cell walls and in the vicinity of grain boundaries provides the driving force for RX.

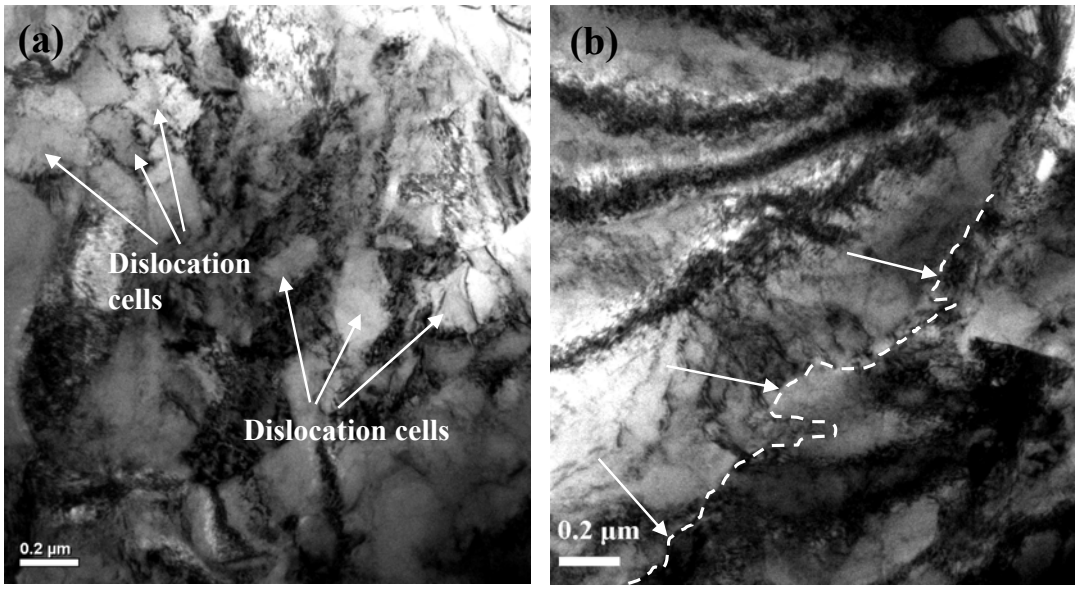

Figure 4.19 Bright field TEM images of 2D6C copper: (a) typical dislocation cells; (b) grain boundary characteristics

The HV of initially annealed samples compressed at low and high strain rates are respectively 121.2 and 71.3. The former is consistent with Figure 4.10, while the latter indicates the occurrence of RX, similar to that for 2D6C samples subjected to impact.

4.6 Evolution of mechanical properties and microstructure of samples subjected to uniaxial single compression at 77K

Unlike the USC tests at 298K, in which both initially hardened and annealed samples are used (Table 4.3), the tests at 77K involve only annealed samples, because the results in Section 4.5 have demonstrated that a difference in the initial state (i.e. work hardened vis-à-vis annealed) yields negligible differences in the mechanical properties (and the grains) of deformed samples. Figure 4.20 shows the HV of copper after compression at a common initial temperature (77K) but at different strain rates. The average HV of quasi-statically deformed samples is slightly higher than the

saturation HV of samples prepared at RT, while that of dynamically deformed samples exceeds the saturation HV by 16%.

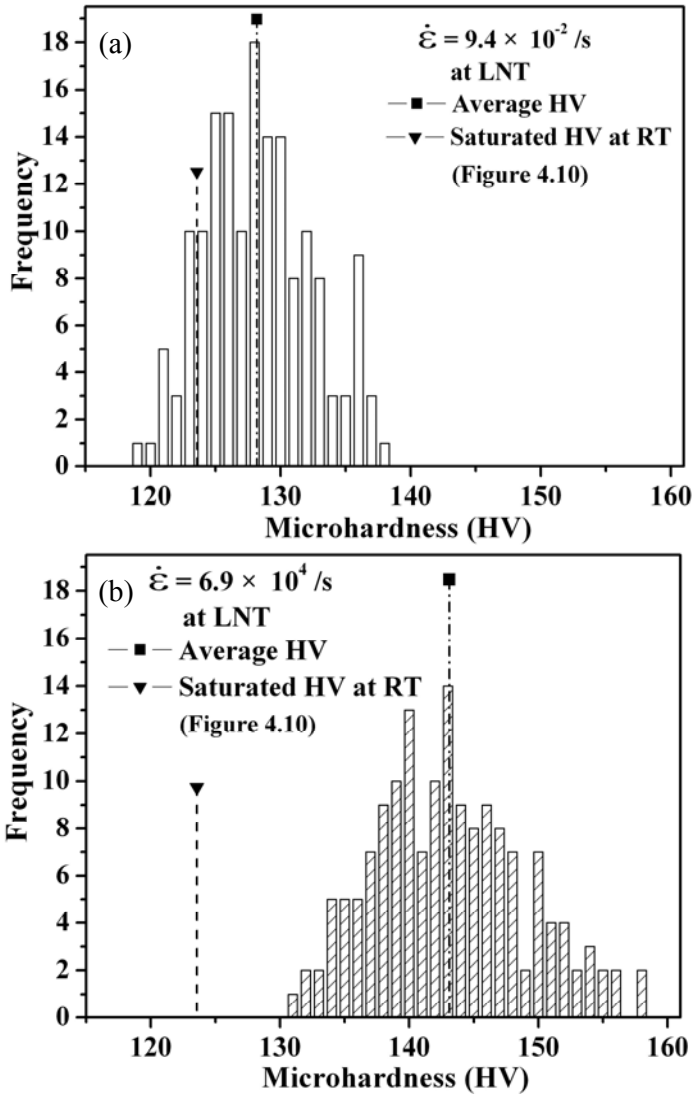

Figure 4.20 HV values of samples deformed at different strain rates: (a) 9.4 $\times 10^{-2}$ /s; (b) 6.9 $\times 10^{4}$ /s

Figure 4.21 shows TEM bright field images of quasi-statically deformed samples. The roughly homogenous distribution of dislocations, identified by arrows, indicates the suppression of dynamic recovery because of the low temperature, which retards the formation of low-energy cells in these regions. This maintains a higher dislocation density compared to cases where recovery occurs at RT, and thus may account for the slight increase in the HV compared to quasi-statically deformed specimens. In

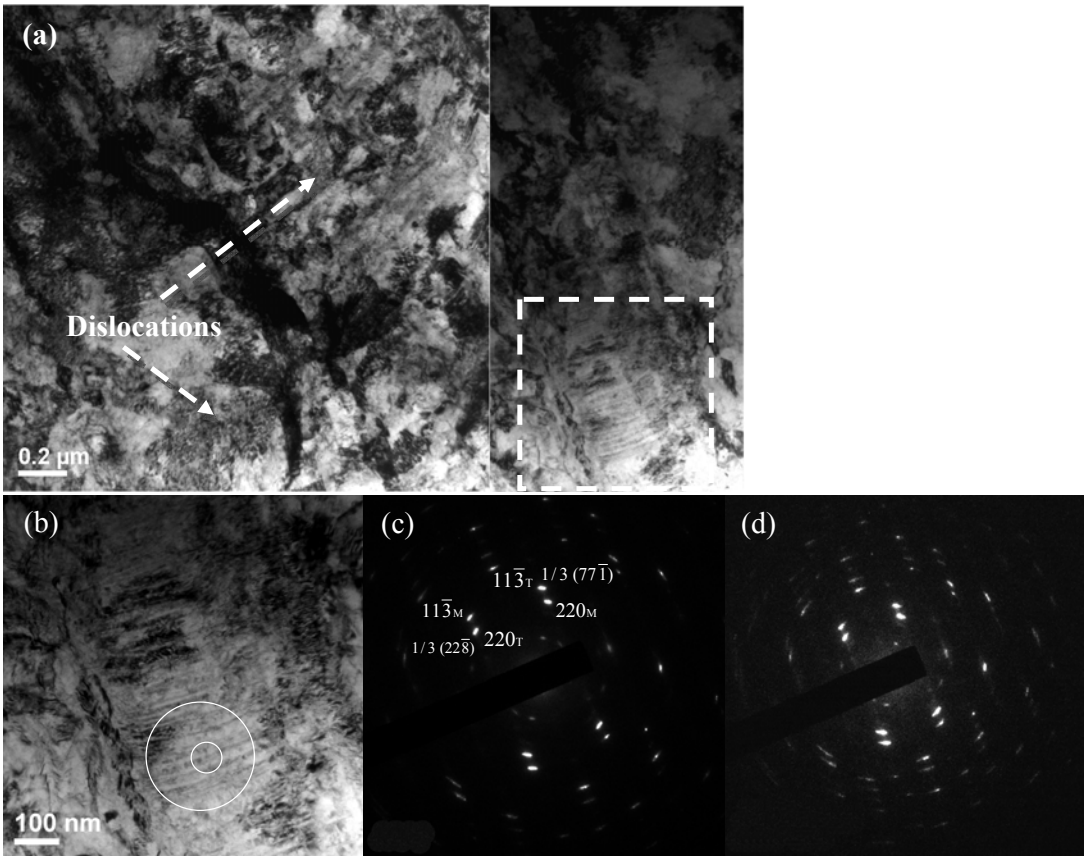

Figure 4.21 (a) Bright field TEM images of quasi-statically deformed samples; (b) Magnification of area outlined in (a); (c) and (d) are the respective SAED patterns of the areas in the small and large circles in (b)

addition, a structural feature of significance is the aggregation of bands of nano-sized width within the dashed frame in Figure 4.21(a); this is discernible by the varying contrast defining the bands. A higher magnification image of the outlined region is given in Figure 4.21(b), and selected area electron diffraction (SAED) patterns are shown in Figures 4.21(c) and 4.21(d), which correspond respectively to the areas bounded by the small and big circles in Figure 4.21(b). Figures 4.21(c) and 4.21(d) display identical diffraction spots, which reveal a twin-relationship among the bands, as can be seen from the indices in Figure 4.21(c). These nano-sized multiple twins are comparable in size with those produced by dynamic plastic deformation at strain rates of 10^3/s [102, 103], though smaller in quantity. This generation of twins reflects localized deformation in regions where the stress is sufficiently high to nucleate them.

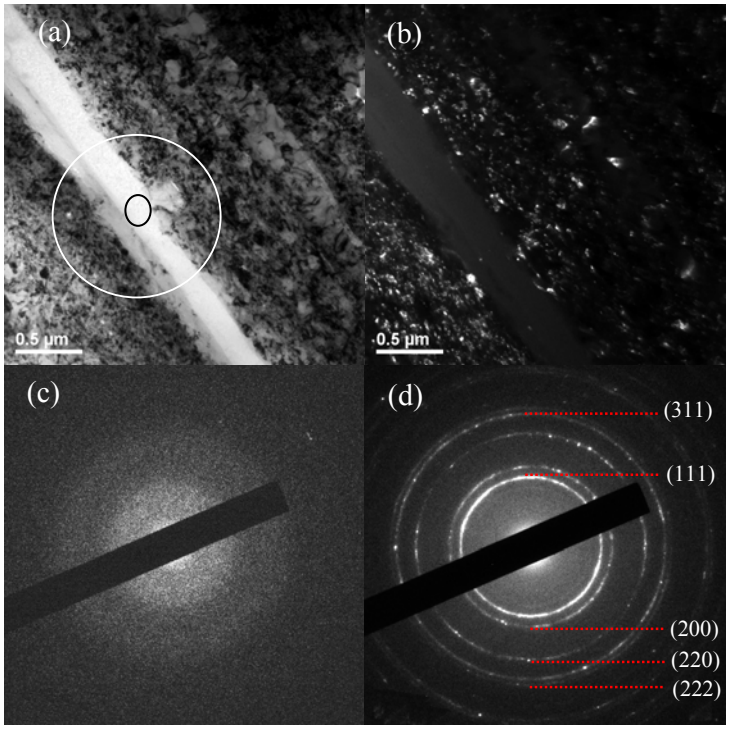

Figure 4.22 TEM images of dynamically deformed samples: (a) BF image; (b) DF image; (c) SAED pattern corresponding to small circle in (a); (d) SAED pattern corresponding to large circle in (a)

Figure 4.22 shows typical TEM images of dynamically deformed samples (DDS). Figure 4.22(a) is a bright field image, whereby a white band is surrounded by nano particles identified by a distinct contrast, whereas Figure 4.22(b) is the dark field image corresponding to Figure 4.22(a). SAED patterns are obtained respectively for areas outlined by the small and big circles in Figure 4.22(a), and these are shown in Figures 4.22(c) and 4.22(d). The uniform colour intensity of the band in Figures 4.22(a) and 4.22(b), as well as the diffused halo rings in Figure 4.22(c), indicates the formation of an amorphous structure in the band. The SAED pattern in Figure 4.22(d) is characterized by the overlapping of two patterns that correspond respectively to an amorphous and a poly-crystalline structure, with their indices annotated. This suggests that in the vicinity of the amorphous band, nano-sized grains with a wide range of misorientation angles are generated.

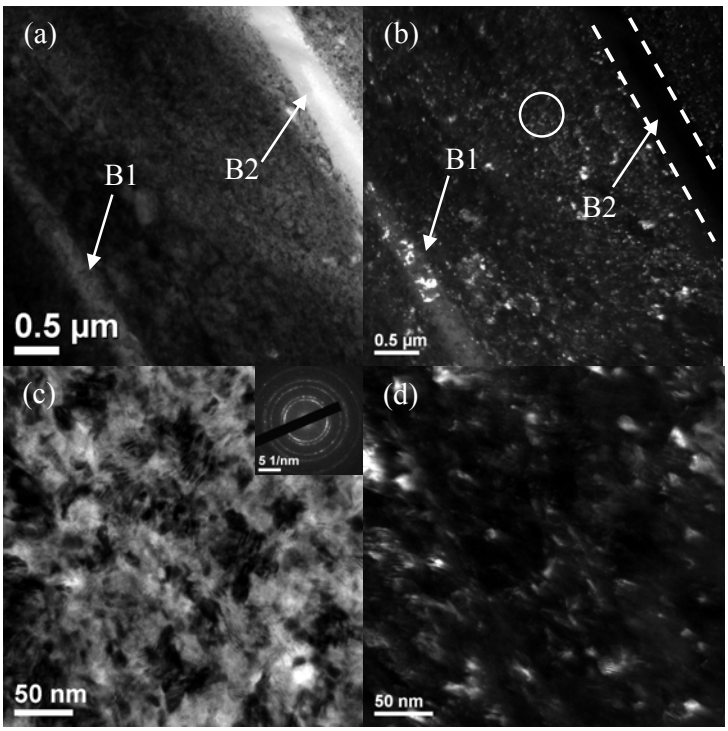

Figure 4.23 TEM images showing area with two shear bands: (a) BF image; (b) DF image; (c) BF image corresponding to circle in (b); (d) DF image of (c)

The amorphous bands in DDS, usually 20-500 nm in thickness, either cut across the crystalline area with a nearly straight boundary, or form an area surrounded by crystalline regions; they occur at random distances from one another. Figure 4.23(a) shows a region in which two bands, denoted by 'B1' and 'B2', are close to each other. These two bands are similar in shape to that in Figure 4.22. However, a dark field image of B1 in Figure 4.23(b) displays a few regions which are notably whiter, indicating the diffraction of electron beams there, possibly due to the presence of crystals. In contrast, B2 and the band in Figure 4.22 are totally dark. (The possible coexistence of amorphous and crystalline structures in the band is discussed later.) The microstructure in the region between B1 and B2 is analogous to that around the band in Figure 4.22. A magnified bright field image of the area circled in Figure 4.23(b) is shown in Figure 4.23(c), while Figure 4.23(d) is the dark field image corresponding to Figure 4.23(c). The continuous rings of the SAED pattern, depicted

by the inset of Figure 4.23(c), demonstrate the formation of a polycrystalline structure with random crystallographic orientations. The grain size, as seen from Figures 4.23(c) and 4.23(d), is of the order of several nanometers.

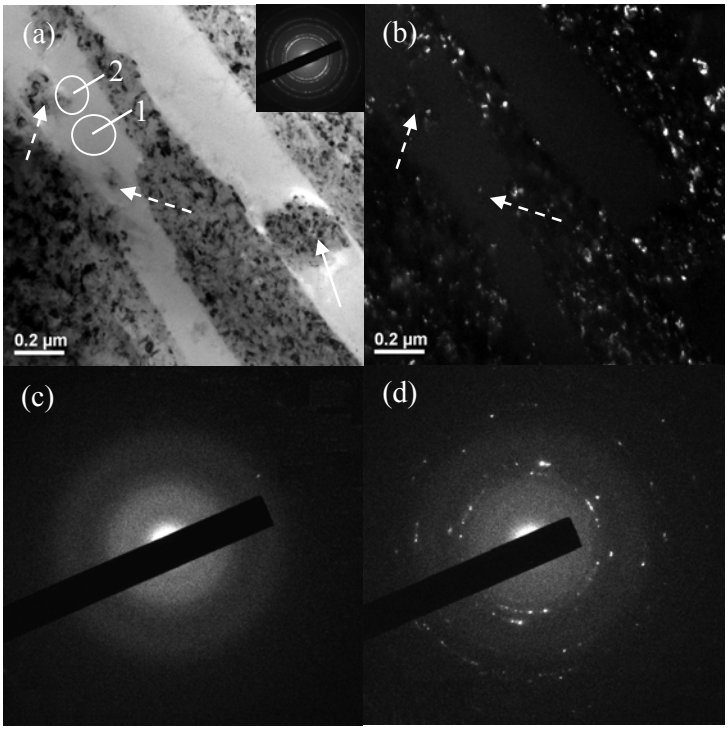

Figure 4.24 (a) Bright field TEM image; (b) Dark field TEM image corresponding to (a); (c) SAED pattern of area '1' in (a); (d) SAED pattern of area '2' in (a)

Figure 4.24(a) depicts bands, discernible by their contrast. The inset in Figure 4.24(a) is the corresponding SAED pattern, and indicates the presence of both amorphous and polycrystalline structures. A comparison of Figures 4.24(a) and 4.24(b) reveals regions (indicted by dashed arrows) within a band that exhibit significant contrast with the band, but are similar in appearance to areas outside the bands. This feature of the bands is identical to that of B1 in Figure 4.23. Figures 4.24(c) and 4.24(d) show respectively, SAED patterns of areas '1' and '2' in Figure 4.24(a). In contrast to Figure 4.24(c), a number of diffraction spots emerge in Figure 4.24(d) and tend to form rings corresponding to those for polycrystalline copper. This confirms that the regions indicated by the arrows in Figure 4.24(a) maintain a crystalline

microstructure. The existence of crystals within the amorphous bands indicates that the strain or strain rate is non-uniform, even within a band, and that a critical strain is required to transform the crystalline structure into an amorphous one; a strain lower than this leads only to the generation of smaller grains but no amorphization. The crystalline region, indicted by the solid arrow in Figure 4.24(a), separates that particular band into two parts. This is possibly the location where the two separated bands initiate or terminate, or a localized area of relatively small strain within a band like those marked by the dashed arrows.

Figure 4.25(a) shows a region with multiple bands. The SAED patterns of the narrowest and thickest bands, indicated by solid arrows, are shown respectively in Figures 4.25(b) and 4.25(c), and demonstrate the formation of an amorphous structure there. The area outlined in Figure 4.25(a) is examined in detail, and Figures 4.25(d) and 4.25(e) are respectively the bright- and dark-field images of this area at higher magnification. The SAED pattern of the region circled in Figure 4.25(d) is shown in Figure 4.25(f), and indicates the generation of fine polycrystalline grains between the two amorphous bands. However, the grains located at a location relatively remote from the amorphous bands, such as those bounded by the dashed lines in Figure 4.25(e), are larger than those nearer the bands. This is different from Figure 4.23, where the grain size is roughly uniform in the region between shear bands, and the difference is accounted for as follows: The shear strain decreases with distance from a shear band (this is indicated by an increase in grain size), and the direction of shearing follows that of the shear band. When two shear bands which have the same direction of shear occur in close proximity to each other, the superposition of their influence on the region between them is constructive, resulting in a smaller variation of strain (i.e. more uniform small grains). The converse takes place when the directions of shearing

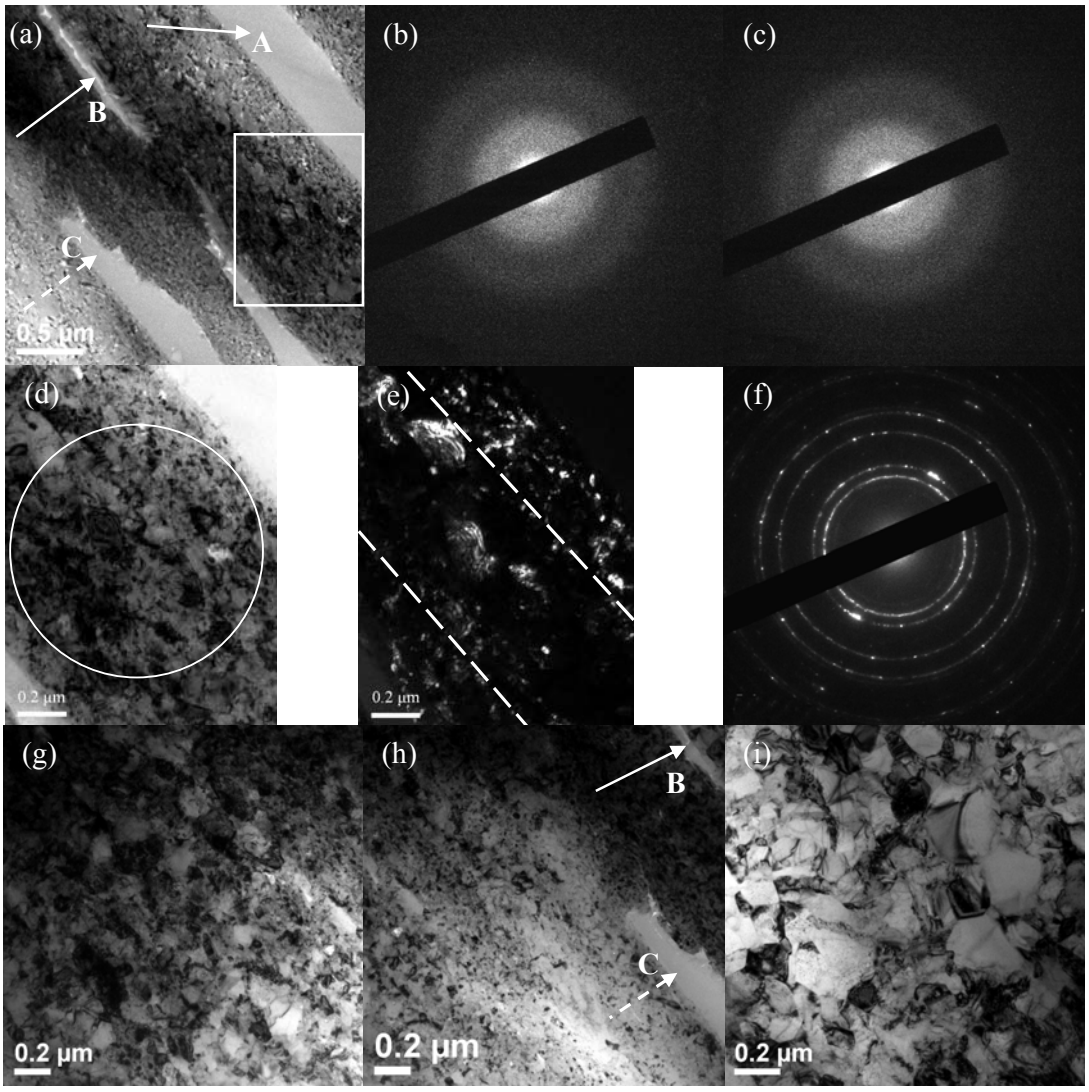

Figure 4.25 (a) Bright field TEM image showing multiple bands; (b) and (c) are respective SAED patterns corresponding to the narrowest and thickest bands in (a); (d) Magnification of bright field image of area outlined in (a); (e) Dark field image of (d); (f) SAED pattern of circle in (d); (g) Bright field image of area adjoining that in (h); (h) region left of B and C in (a); (i) Bright field image of area remote from the bands.

in neighbouring shear bands oppose each other; this produces an increased variation in the shear strain between the bands, and thus a noticeable variation in grain size, as shown in Figure 4.25(e). The assumption that regions closer to a shear band have larger local strains is supported by Figures 4.25(g)-4.25(i)**.** The shear bands indicated by B and C in Figure 4.25(h) correspond respectively to the bands with the same labels in Figure 4.25(a), and the region shown in Figure 4.25(g) connects to the left of

that in Figure 4.25(h). It is observed that the size of crystalline grains increases with distance from a band, reflecting a decrease in localized strain. Figure 4.25(i) shows an area relatively distant (about 10 μm) from a band, where the grains are noticeably larger. These results indicate that deformation inside the sample is heterogeneous, and that the generation of nanograins is associated with the formation of amorphous bands.

With regard to the bands mentioned, which display SAED patterns corresponding to an amorphous structure, it could be postulated that they were formed during the thinning of samples by ion milling for TEM observation. However, amorphous regions that are associated with TEM sample preparation usually exist at the edge of hole in the sample. The amorphous regions such as those shown in Figures 4.22-4.25 are not at the periphery of the hole. Furthermore, the diffused ring SAED patterns, such as those in Figures 4.22(c) and 4.24(c), correspond only to the shear bands, whereas the regions adjacent to the bands show SAED patterns comprising continuous rings (e.g. Figures 4.23(c) and 4.25(f)), which are characteristic of a polycrystalline structure. This indicates that the amorphous phase of the shear bands originates from plastic deformation rather than post-deformation sample treatment, such as ion milling; if it were the latter, there would not be such distinct differences between an amorphous band and its adjacent regions. Figure 4.26 shows a typical high-resolution TEM (HRTEM) image of a shear band displaying a diffused ring SAED pattern. Although a crystal lattice (marked by the solid arrow) is discernible, the dominant structure within the band comprises a disordered arrangement of atoms, as indicated by the dashed arrows. This gives rise to SAED patterns characteristic of an amorphous state. Bearing in mind that the purity of the OFHC copper samples in this study is rated at 99.99%, it is reasonable to assume that inclusions, and therefore

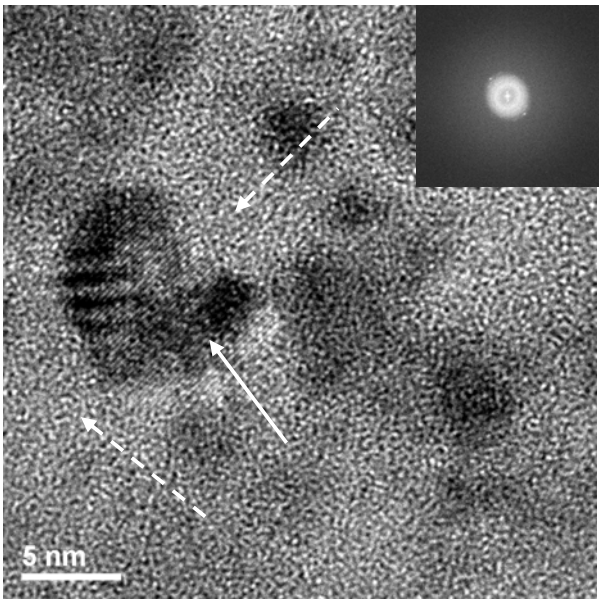

Figure 4.26 HRTEM image of a shear band displaying a diffused ring pattern (inset is the live FFT view of the entire image)

their possible participation in precipitating amorphous phases during plastic deformation, are negligible. Moreover, the diffraction spots corresponding to a generic area in the band, shown in Figure 4.24(d), are indicative solely of copper, confirming the absence of inclusions in contributing to the formation of the amorphous phase. Therefore, the generation of the amorphous regions arises from localised deformation at high strain rates rather than the possibility of inclusions being present and playing a part in this. It is noted that the amorphous phases are found in only some of the shear bands (others comprised solely ultrafine and nano-grains, similar to the observations of [66, 106, 116]); in general, they do not occur on their own, but together with nanograins (e.g. Figures 4.24(a) and 4.26). This indicates that these amorphous structures emerge after grains within the bands have been reduced below a critical size. The critical grain size and thus the localised strain corresponding to the generation of amorphous phases within shear bands cannot be deduced from the current study. Consequently, the localised temperature and strain rate at which amorphization takes place, as well as the duration of this process (which is definitely

shorter than that of the entire deformation), are unknown and constitute a topic for future consideration. Nevertheless, the current work substantiates the results of previous molecular dynamics simulation [104], which show that amorphization is a mechanism associated with plastic deformation of pure copper.

The microstructure of dynamically-deformed specimens can be summarized as follows: (1) amorphous bands form in regions where the localized strain is large, whereas in other regions, a crystalline structure is preserved; (2) nano-grains generally occur near the amorphous bands, but in regions sufficiently far from the amorphous bands the grain size increases and exceeds 100 nm; (3) the distribution of nano-grains between amorphous bands is related to the direction of shearing by which the bands are formed. Twinning is an important mechanism to accommodate plastic deformation, as concluded by Tao and Lu [80]. However, they are rarely found in DDS in the current study. Instead, amorphous bands are readily observed. This is consistent with simulation results that point to amorphization playing a role in accommodating plastic deformation at high strain rates, in the same way twinning does at low strain rates [104]. It appears that imposition of a strain rate in the order of 10^4/s in a 77K temperature environment is able to produce amorphous regions in polycrystalline copper.

4.7 Nanograins in dynamically-deformed samples

Grain refinement in the vicinity of amorphous bands indicates a RX process associated with impact deformation. Although the Johnson-Cook (JC) model described in Section 4.5 has a simple form and is accurate for deformation at RT, its predictions do not match experimental data that well for deformation at LNT [95]. Therefore, the modified Steinberg-Cochran-Guinan-Lund (SCGL) constitutive model,

predicting the stress-strain response for annealed OFHC copper deformed at 77K and high strain rates more accurately than the frequently-used Johnson-Cook, Zerilli-Armstrong, Mechanical Threshold Stress and Preston-Tonks-Wallace models, [95], is adopted to calculate the change in temperature during impact. The modified SCGL model is defined as:

$$\sigma(\varepsilon, \dot{\varepsilon}, T) = [\sigma_{Athermal} f(\varepsilon) + \sigma_{Thermal}(\dot{\varepsilon}, T)] \frac{\mu^M(p,T)}{\mu_0{}^M} \tag{4.10}$$

where $\sigma_{Athermal}$ and $\sigma_{Thermal}$ are respectively the athermal and thermally-activated components of the flow stress, $f(\varepsilon)$ represents the strain hardening, $\mu^M(p, T)$ is the shear modulus dependent on pressure p and temperature T, and $\mu_0{}^M$ is a constant. $f(\varepsilon)$ is related to the strain ε by:

$$f(\varepsilon) = [1 + \overline{\beta}(\varepsilon + \varepsilon_i^{equi})]^{\overline{n}} \tag{4.11}$$

where $\overline{\beta}$ and $\overline{n}$ are work hardening parameters, and ε_i^{equi} is the initial equivalent plastic strain. The thermal component of the flow stress $\sigma_{Thermal}$ is calculated from a bisection algorithm, as defined by the following equation:

$$\dot{\varepsilon} = [\frac{1}{C_1} \exp[\frac{2U_k}{\kappa_b T}(1 - \frac{\sigma_{Thermal}}{\sigma_{Peierls}})^2] + \frac{C_2}{\sigma_{Thermal}}]^{-1} \tag{4.12}$$

where $\sigma_{Peierls}$, κ_b and $2U_k$ are respectively the Peierls stress, the Boltzmann constant and the energy to form a kink-pair in a dislocation segment; C_1 and C_2 are constants. The Steinberg-Cochran-Guinan (SCG) shear modulus model [95, 112-113], shown in equation 4.13, describes the relationship between $\mu^M(p, T)$ and p and T and is adopted in the present study.

$$\frac{\mu^M(p,T)}{\mu_0{}^M} = 1 + \frac{1}{\mu_0{}^M}\frac{\partial \mu^M}{\partial p}\frac{p}{\overline{\eta}^{1/3}} + \frac{1}{\sigma_{y0}}\frac{\partial \sigma_y}{\partial T}(T - 300) \tag{4.13}$$
$$\overline{\eta} = \rho / \rho_0$$

where ρ, σ_y and σ_{y0} represent respectively the current density of copper, the yield stress at a strain of 0.2 and the value of σ_y at 300K; ρ_0 is the initial density and taken as 8,930kg/m^3. The values of the parameters in equations 4.10-4.13 are listed in Table 4.4.

Table 4.4 Values of parameters in the modified SCGL constitutive model and the SCG shear modulus model

Parameter	$\sigma_{Athermal}$ (MPa)	$\sigma_{Peierls}$ (MPa)	U_k (eV)	$\overline{\beta}$	$\overline{n}$	C_1 (/s)	C_2 (MPa-s)
Value	125	20	0.31	36	0.45	7.1e5	0.012
Parameter	ε_i^{equi}	$\mu_0{}^M$ (GPa)	$\partial\mu^M/\partial p$	σ_{y0} (MPa)	$\partial\sigma_y/\partial T$ (MPa/K)		κ_b (J/K)
Value	0.0	47.7	1.3356	330	-0.25		1.38e-23

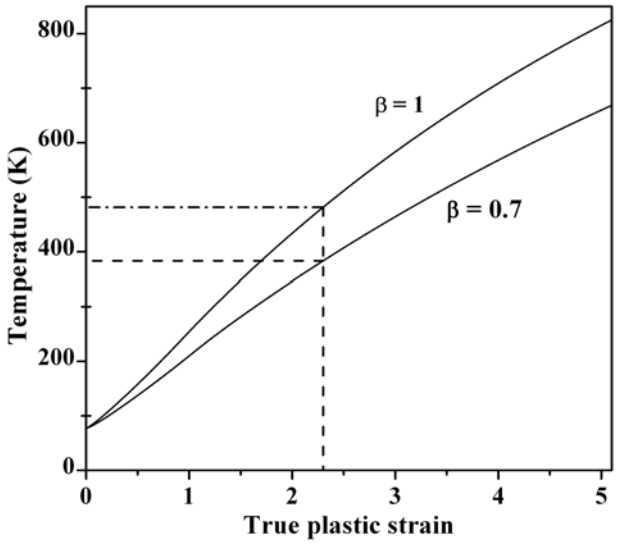

Figure 4.27 Variation of predicted temperature with strain, based on modified SCGL model

Based on equation (4.9), the change in sample temperature with respect to plastic strain is calculated and presented in Figure 4.27. The dashed vertical line defines the final strain of the impacted samples. It can be seen that the temperature at the conclusion of deformation does not reach that required for initiation of RX, i.e. 500K, even if β is assigned a large value of unity. The strain is not uniformly distributed within the sample, thus generating a spatial variation in temperature. In the shear bands, the localized strain is as large as 10^1 for OFHC copper [105]. Therefore, the localized strain around these amorphized shear bands should also exceed the overall

macroscopic plastic strain of 2.3. Moreover, a comparison with the findings of Belyakov et al. [19] and Kobayashi et al. [75] suggests the generation of finer grains if a larger strain is imposed, and for generation of grains with sizes of 0.16 μm, a cumulative strain of at least 5 is required. Noting the nano-grains generated in the current study, it is envisaged that the localized strain in regions containing nano-grains should be much larger. Nevertheless, assuming that the localized strain in regions near the shear bands is only 1.5 times that of the overall final strain (i.e. 1.5 x 2.3 = 3.45), then the respective final temperatures are 512.4 K and 642.4K for β=0.7 and β=1, according to the curves in Figure 4.27. These two temperatures exceed the critical temperature for initiation of RX. However, investigations [66, 106] have demonstrated that for metals, the heat generated in small localized regions after deformation will be rapidly conducted into their surroundings, so that RX is unable to occur via conventional nucleation and grain growth, but rather by rotational DRX. Rotational DRX is a process in which dislocation cells gradually transform into subgrains and then into high angle grains because of minimization of the interfacial energy; the kinetics for rotational DRX follow a function of temperature and time, as defined by the following equation [69]:

$$\frac{3\tan\theta - 2\cos\theta}{3 - 6\sin\theta} + \frac{2}{3} - \frac{4\sqrt{3}}{9} ln\frac{2+\sqrt{3}}{2-\sqrt{3}} + \frac{4\sqrt{3}}{9} ln\frac{\tan(\theta/2) - 2 - \sqrt{3}}{\tan(\theta/2) - 2 + \sqrt{3}} = \frac{4\gamma_{GB}\delta_{GB}D_{GB}}{L_1 k_b T} t \quad (4.14)$$

where θ, γ_{GB}, δ_{GB}, D_{GB}, Q_b, T, L_1, k_b and t represent respectively the subgrain misorientation, grain boundary energy, grain boundary thickness, grain boundary diffusion coefficient, activation energy for grain-boundary diffusion, temperature, average subgrain size, Boltzmann constant and time. The product of δ_{GB} and D_{GB} is a function of Q_b and T and experimentally determined to be [69, 114]:

$$\delta_{GB} D_{GB} = 3.9 \times 10^{-16} \exp[\frac{-Q_b}{RT}] \quad (4.15)$$

where R is the universal gas constant. The values of γ_{GB}, Q_b and R are listed in Table 4.5, while L_1= 20 nm corresponds to the current study. According to the mechanism of rotational DRX, a rotation angle of 0.52 radians is required for the formation of recrystallized grains. Figure 4.28 shows the variation of grain misorientation with time for two temperatures, and indicates that the higher the sample temperature, the shorter the time needed for accomplishment of RX. Moreover, for both the temperatures in Figure 4.28, the time for RX is less than that for deformation (33 μs). This supports the proposition of rotational DRX accounting for the formation of nano-grains in the current study.

Table 4.5 Values of parameters in equations 4.14 and 4.15

Parameter	γ_{GB} (J/m^2)	Q_b (kJ/mol)	R (J/(K-mol))
Value	0.625 [115]	72.5 [114]	8.314

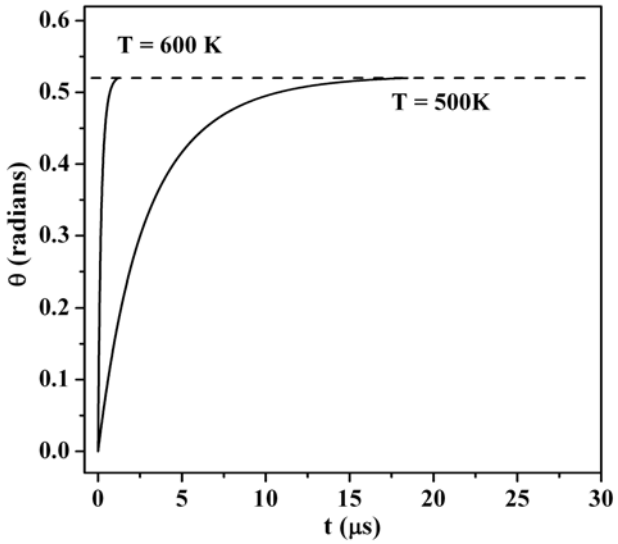

Figure 4.28 Variation of angle of rotation of subgrain boundary with time

A comparison of properties such as the HV and microstructure of samples deformed under different conditions (Table 4.3) indicates that nano-grains are only generated in samples subjected to low temperatures (77K) and high-strain-rate deformation, and occur in regions of large localized strain. The effects of large strain, high strain rate and low temperature on the process of nano-grain formation are

interpreted as follows: (1) dislocations are generated during plastic deformation; (2) with a reduced temperature (77K) and high strain rate, the capacity for dislocation storage is enhanced, compared to that of deformation at lower strain rates and higher temperatures; this leads to smaller dislocation cells bounded by a network of dislocations, especially in regions of large strains; (3) when the temperature increase with plastic strain exceeds the critical value for initiation of RX, rotational DRX takes place, resulting in randomly-orientated grains. Figures 4.25 and 4.27 indicate that a true strain in excess of 2.3 is necessary for both the generation of a nano-sized structure and for sufficient temperature elevation to trigger RX.

4.8 Summary and conclusions

The microstructure and strength of OFHC copper subjected to uniaxial single compression at 298K and 77K were investigated. For quasi-static deformation at 298K, the hardness reaches a saturation value of 123.6 HV when a cumulative strain of 2.8 is imposed; further deformation by multiple forging causes substructure refinement. This saturation HV value of the hardness is consistent with that reported for samples subjected to ECAP and HPT. Samples subjected to high-strain-rate uniaxial single compression at 298K exhibit a decrease in hardness compared with those deformed quasi-statically; this is the case for both initially hardened and annealed samples. The microstructure of impacted sample is characterized by the formation of deformation twins either individually, or intersecting one another, as well as equiaxed micron-sized grains. The temperature rise predicted using the modified J-C model in this study and an analysis of the kinetics of RX suggest that nucleated grains form during impact and grow subsequently, leading to softening of the material. For an ambient temperature of 77K, the hardness of quasi-statically-

deformed samples is slightly higher than the saturation HV value. This is attributed to the suppression of dynamic recovery. Nano-scale twins are observed, but the number is small compared to that produced by dynamic compression (10^3/s) at 77K [102]. The hardness of dynamically-deformed samples at 77K exceeds the saturation HV value by 16%, and the resulting microstructure includes nano and ultrafine grains, as well as shear bands with a composite structure comprising amorphous and crystalline phases, while twins are scarce. Formation of these shear bands results from the occurrence of very high localized strains, and grains measuring several nanometers in size are commonly found near the bands. The variation in grain size between neighbouring bands is associated with the direction of shear that initiates the bands. The nano-grains observed are deduced to have been evolved through rotational DRX and a true strain exceeding 2.3 is required for the formation of such fine grains.

Chapter 5 – Effect of strain rate on microstructure of materials subjected to uniaxial single compression at liquid nitrogen temperature (LNT)

In Chapter 4, differences in the microstructure and mechanical properties of materials resulting from deformation at different ambient temperatures were demonstrated and discussed. The dramatic strengthening of materials deformed at LNT, in contrast to the lower strength or even softening of materials deformed at RT, demands that attention be focused on LNT deformation, because improvement in material strength in a key concern of this study. The difference in microstructure associated with the difference in strain rate, described in Chapter 4 – e.g. the presence and absence of localized deformation bands and nanometer grains in materials deformed at strain rates respectively in the order of 10^{-2} /s and 10^{4} /s – reveals the dependence of microstructure on strain rate. Thus, a more comprehensive investigation into the effects of strain rate is instructive. To enable this, the strain rates imposed on the specimens described in this chapter deal span more orders of magnitude than those discussed in Chapter 4. Also, other microstructural characterization techniques, such as X-ray diffraction (XRD) profile analysis, are employed in conjunction with TEM to observe the microstructure more fully, in contrast to the sole use of TEM in Chapter 4.

5.1 Introduction

Investigations pertaining to large plastic deformation have been summarized in Chapter 2. It has been highlighted that systematic investigations into how strain rate

affects the resulting microstructure of samples deformed to large strains at low temperature are lacking. This issue is now addressed by examining the effect of strain rate on the microstructure of OFHC copper severely deformed at LNT (77K). Characterization of material microstructure is often performed using transmission electron microscopy (TEM) or X-ray diffraction (XRD). Although TEM enables direct observation of the microstructure, only a miniscule volume of the specimen is examined. In contrast, XRD involves scanning a much larger volume of the specimen, leading to more representative statistics of the microstructure, and is thus utilized in conjunction with TEM in this study for more comprehensive observation. In XRD, microstructural characteristics such as dislocation density and crystallite size can be extracted from the peaks in the XRD scan outputs by applying evaluation techniques, such as the Warren-Averbach analysis (WAA) [117], Williamson-Hall plot (WHP) [118] and the variance method [119]. Recently, the WAA and WHP have been upgraded by the introduction of a parameter called the "contrast factor of dislocations" and these are referred to respectively as the modified WAA (MWAA) and the modified WHP (MWHP) techniques [120]. The MWAA and MWHP have been verified as being reliable and precise in evaluating dislocation density, grain size, density of twinning boundaries, etc. [121-123], and are hence adopted in the current analysis. Differential scanning calorimeter (DSC) [124], which is usually utilized for analyzing the thermal stability of a microstructure, is also employed. The procedures of cooling a sample down to LNT, TEM examination and micro-hardness testing of deformed samples, are similar to those described in Chapter 4, and are thus not described again.

5.2 Methodology/Techniques

5.2.1 Deformation of material

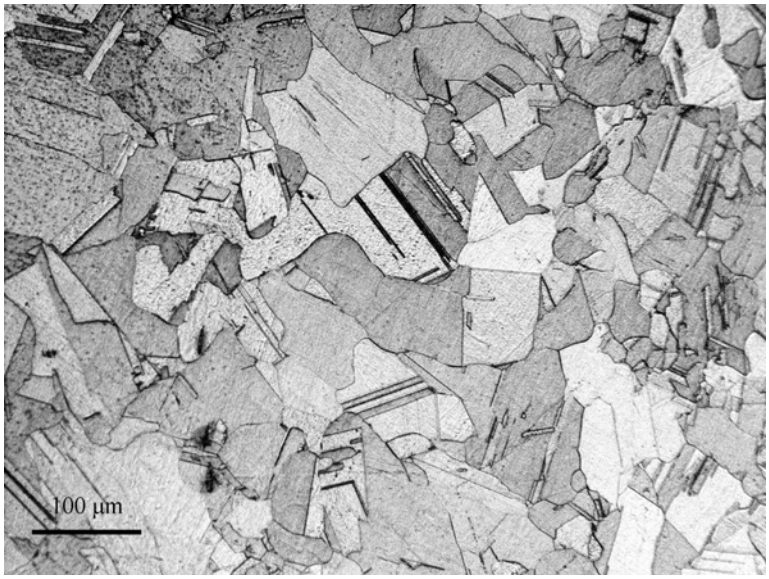

Figure 5.1 Optical micrograph showing microstructure of annealed samples

Cuboid samples of oxygen-free high conductivity copper (OFHC) are fabricated by wire-cutting them from a rod which has been annealed, and they possess a microstructure characterized by grains ~100 μm in size, as well as annealing twins (Figure 5.1). Samples are immersed in a liquid nitrogen bath for a duration sufficient to cool them down to LNT, and then compressed in an atmosphere of liquid nitrogen. Compressive deformation at various strain rates are performed using a Shimadzu Universal Testing Machine (SUTM), drop tester, split Hopkinson pressure bar (SHPB) and gas gun, and the respective true strain and strain rate induced are given in Table 5.1, in which ε and $\dot{\varepsilon}$ are defined respectively as:

$$\begin{aligned} \varepsilon &= \ln(L_0 / L_f) \\ \dot{\varepsilon} &= \varepsilon / t \end{aligned} \qquad (5.1),$$

L_0 and L_f represent respectively the initial and final length of a sample, and t is the duration of compression. The deformed samples are kept in a refrigerator prior to subsequent analysis.

Table 5.1 Parameters for compression tests

Equipment	Temperature	True strain, ε	True strain rate (/s), $\dot{\varepsilon}$
SUTM	LNT (77K)	2.3	9.4×10^{-2}
SUTM			1.9
Drop tester			4.8×10^{2}
SHPB			5.7×10^{3}
Gas gun			6.9×10^{4}

5.2.2 XRD profile analysis of microstructure

A Shimadzu 6000 X-ray diffractometer with Cu Kα radiation was used to collect XRD data. The voltage and current at which the diffractometer works are respectively 40 KV and 30 mA. Scanning was carried out in a continuous mode at a speed of 0.01^0/s and ranged from 40-$122^0$2θ, with a step size ($(2\theta)_s$) of 0.01^0. The Cu Kα radiation used is a doublet, consisting of Kα1 and Kα2, which respectively correspond to wavelengths of 1.54060nm (λ_1) and 1.54439nm (λ_2). Bragg's law, expressed in equation 5.2, relates wavelength (λ) to the interplanar spacing (d_{hkl}) of crystallographic planes with Miller indices (*hkl*) and a diffraction angle (θ). If Cu Kα radiation is incident on a sample, the diffraction lines associated with the Kα1 and Kα2 radiation for a particular reflection index (*hkl*) will be located at two different angles. This leads to angular dispersion of the diffractometer. The magnitude of angular dispersion ($\mathrm{d}\theta/\mathrm{d}\lambda$) is assessed by differentiating Bragg's law, as shown in equation 5.3.

$$\lambda = 2d_{hkl}\sin\theta \tag{5.2}$$

$$\frac{\mathrm{d}\theta}{\mathrm{d}\lambda} = \frac{1}{2d_{hkl}\cos\theta} \tag{5.3}$$

Equation 5.3 shows that $d\theta/d\lambda$ increases with θ; this indicates a possible separation of the diffraction lines corresponding respectively to Kα1 and Kα2 radiation at high values of 2θ . However, at low 2θ angles, the two lines are often superimposed and unresolved. This gives rise to difficulty in interpreting the diffractions lines for two reasons: firstly, the diffractions lines are distorted due to their mutual superposition; secondly, the diffraction angle corresponding to maximum intensity of one line is displaced due to the presence of the other diffraction line. Therefore, separation of the two lines associated respectively with Kα1 and Kα2 radiation is necessary. Figure 5.2 is an example showing the experimentally-observed diffraction line corresponding to

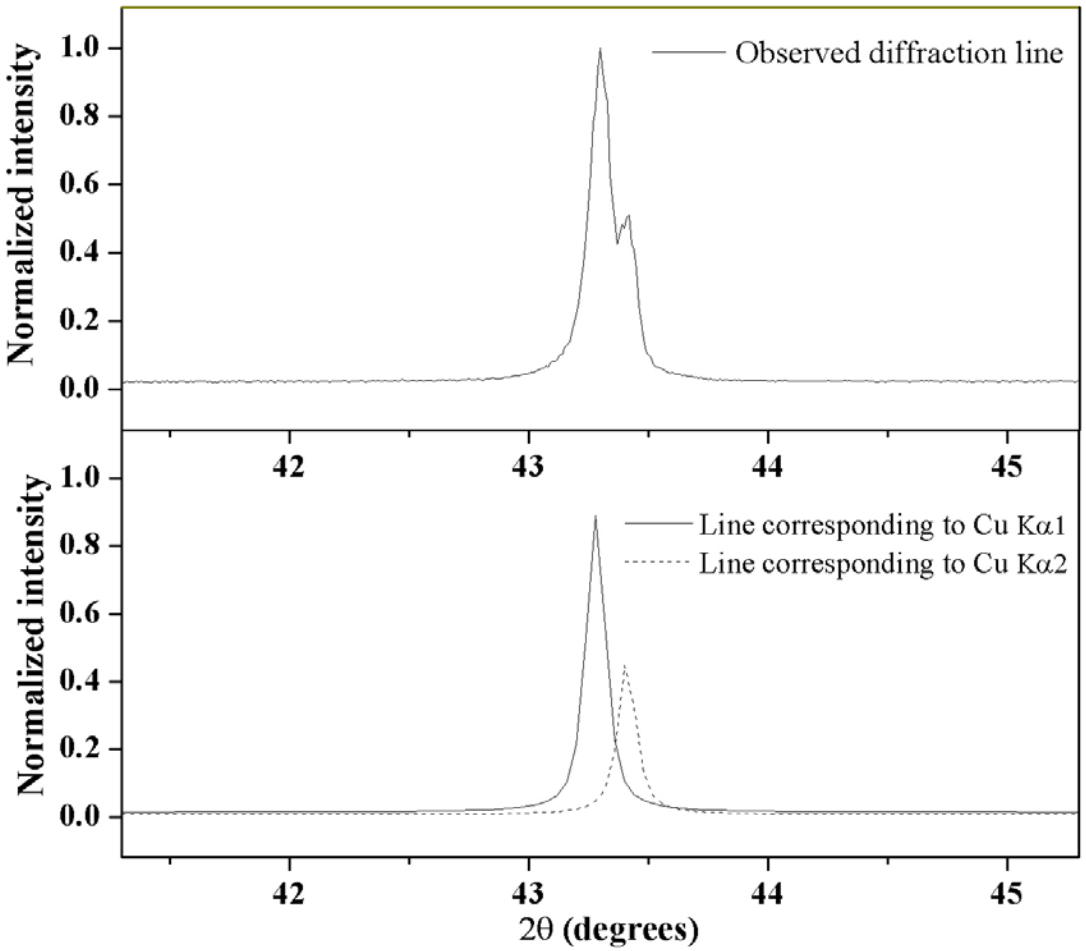

Figure 5.2 Experimentally-observed diffraction line of annealed copper and lines contributed respectively by Cu Kα1 and Cu Kα2

(111) reflection of annealed copper, as well as the lines contributed by Kα1 and Kα2 after separation. In contrast to the experimentally-observed line, which is the superposition of the lines associated with Kα1 and Kα2 radiation, the line from either Kα1 or Kα2 (the intensity of Kα1 is double that of Kα2) is simpler to interpret. In practice, the Cu Kα2 line component is stripped from the experimentally-observed line, whereas the diffraction line corresponding to Kα1 radiation is preserved for microstructural analysis. The stripping away of the Cu Kα2 line component in the present study is performed using the software that accompanies the Shimadzu 6000 X-ray diffractometer.

After eliminating the effect of Cu Kα2 radiation as described above, the observed line is further processed by removing the background intensity and the effect of instrumental broadening on the observed line, to obtain the diffraction line associated with the microstructure of the material investigated. Mathematically, the observed line, $h(2\theta)$ can be expressed as [125]:

$$h(2\theta) = g(2\theta) \otimes f(2\theta) + bg(2\theta) \tag{5.4}$$

where $g(2\theta)$ and $f(2\theta)$ represent the diffraction lines broadened respectively because of the characteristics of a particular instrument and the microstructure of the material investigated; $\otimes$ denotes convolution of $g(2\theta)$ with $f(2\theta)$, and $bg(2\theta)$ defines the background intensity in the observed diffraction pattern, as a result of scattering from the sample holder, sample mount substrate, air, etc. $bg(2\theta)$ is not a constant over the 2θ range under examination and is usually modeled by a polynomial [126-129]. As

with [129], a second order polynomial is used to describe $bg(2\theta)$ in the present study. The broadening of $g(2\theta)$ arises from wavelength dispersion and the geometry [126] of the diffractometer, whereas $f(2\theta)$ is broadened generally because of lattice imperfection and the presence of crystallite domains scattering X-rays incoherently in the material. To identify the microstructure of a material, $f(2\theta)$ must be deconvoluted from $h(2\theta)$. The deconvolution method employed in the present study is based on integral breadths of $h(2\theta)$ and $g(2\theta)$ by applying equation 5.5 [130].

$$\beta_{fL} = \beta_{hL} - \beta_{gL}$$

$$(\beta_{fG})^2 = (\beta_{hG})^2 - (\beta_{gG})^2 \qquad (5.5)$$

where β_L and β_G represent respectively the integral breadths of the Lorentzian and Gaussian components of a profile, and the subscripts f, h and g denote respectively $f(2\theta)$, $h(2\theta)$ and $g(2\theta)$. β_{hL} and β_{hG} are evaluated by fitting a Voigt function to $h(2\theta)$. (Prior to fitting, components of $h(2\theta)$ contributed by $K\alpha 2$ radiation are stripped away as mentioned). The Voigt function has been theoretically justified [131, 132] and verified to be amenable for implementation [133] in terms of describing the diffraction lines. It is a convolution of Gaussian and Lorentzian functions [134] and can be expressed in the form shown in equation 5.6:

$$V(2\theta) = \frac{\Theta \Gamma_L \sqrt{\ln 2}}{\Gamma_G \pi^{3/2}} \int_{-\infty}^{\infty} \frac{\exp[-(2x\sqrt{\ln 2} / \Gamma_G)^2]}{[(2\theta - 2\theta_0) - x]^2 + (\Gamma_L / 2)^2} \, \mathrm{d}x + bg(2\theta) \qquad (5.6)$$

Θ, $2\theta_0$, Γ_G and Γ_L represent respectively the integrated intensity, peak position, full width at half maximum (FWHM) of the Gaussian and Lorentzian components of a diffraction line. The fitting of $V(2\theta)$ to $h(2\theta)$ leads to determination of Θ, $2\theta_0$, Γ_G and Γ_L, of which Γ_G and Γ_L can be converted respectively to β_{hG} and β_{hL} using equation 5.7:

$$\beta_{hG} = \frac{\Gamma_G}{2}\sqrt{\frac{\pi}{\ln 2}}$$
$$\beta_{hL} = \frac{\pi\Gamma_L}{2} \tag{5.7}$$

The values of β_{gG} and β_{gL} at $2\theta_0$ are determined after scanning a standard silicon sample that contributes no microstructure defect related broadening. The values of β_{hG} and β_{hL} for diffraction lines of silicon, represented respectively by β_{hG}^{Si} and β_{hL}^{Si}, are also determined on the basis of equations 5.6 and 5.7. From β_{hG}^{Si} and β_{hL}^{Si}, the value of the integral breadth β_h^{Si}, as well as the shape factor of the diffraction lines, Φ_h^{Si}, can be obtained from equation 5.8 [135]:

$$\beta_h^{\mathrm{Si}} = \beta_{hG}^{\mathrm{Si}}\frac{\exp\{-[\beta_{hL}^{\mathrm{Si}}/(\sqrt{\pi}\beta_{hG}^{\mathrm{Si}})]^2\}}{1-\mathrm{erf}[\beta_{hL}^{\mathrm{Si}}/(\sqrt{\pi}\beta_{hG}^{\mathrm{Si}})]}$$
$$\Phi_h^{\mathrm{Si}} = \frac{2\sqrt{\ln 2/\pi}\{1+0.9039645[\beta_{hL}^{\mathrm{Si}}/(\sqrt{\pi}\beta_{hG}^{\mathrm{Si}})]+0.7699548[\beta_{hL}^{\mathrm{Si}}/(\sqrt{\pi}\beta_{hG}^{\mathrm{Si}})]^2\}}{1+1.364216[\beta_{hL}^{\mathrm{Si}}/(\sqrt{\pi}\beta_{hG}^{\mathrm{Si}})]+1.136195[\beta_{hL}^{\mathrm{Si}}/(\sqrt{\pi}\beta_{hG}^{\mathrm{Si}})]^2} \tag{5.8}$$

Since broadening of the diffraction lines of silicon is contributed only by instrument sources, β_h^{Si} and Φ_h^{Si} essentially demonstrate the characteristics of instrumentally broadened lines ($g(2\theta)$). However, the peak positions for silicon do not coincide with those of copper, the material studied. This gives rise to difficulty in determining the values of β_g at angles corresponding to the diffraction peaks of copper, which need to be known, according to equation 5.5. Therefore, the Caglioti relation [136], which facilitates determination of β_g at any given angles, is utilized. It describes the angular dependence of β_g and has the following form:

$$[\beta_g(2\theta)]^2 = U_g(\tan\theta)^2 + V_g \tan\theta + W_g \tag{5.9}$$

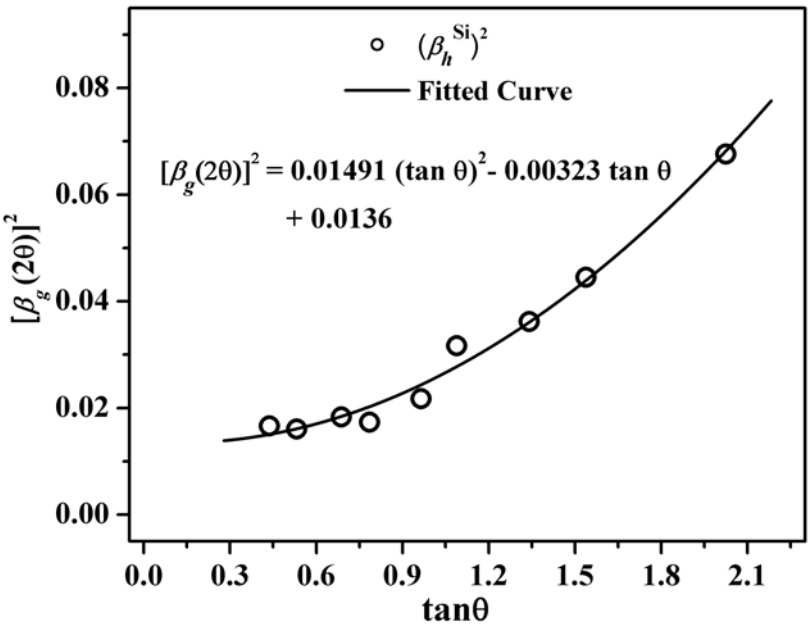

Figure 5.3 Determination of U_g, V_g and W_g for the instrument used in the present study

U_g, V_g and W_g are characteristic parameters of the instrument used, and determined by fitting the Caglioti relation to the values of β_h^{Si}. The values of U_g, V_g and W_g for the instrument used in the present study are determined, as shown in Figure 5.3, and they lead to evaluation of β_g at $2\theta_0$ corresponding to copper.

In addition to the integral breadth, the shape of $g(2\theta)$ is also angle dependent. As with [129], the shape factor of $g(2\theta)$, Φ_g, can be described by:

$$\Phi_g(2\theta) = A_g(2\theta)^2 + B_g(2\theta) + C_g \tag{5.10}$$

As with U_g, V_g and W_g, A_g, B_g, and C_g are determined by fitting equation (5.10) to Φ_h^{Si} and this is demonstrated in Figure 5.4. A knowledge of U_g, V_g, W_g, A_g, B_g, and C_g enables determination of β_g and Φ_g, the characteristic parameters of $g(2\theta)$, at angles corresponding to the diffraction peak positions of copper. This in turn leads to determination of β_{gG} and β_{gL} using equation 5.11 [135].

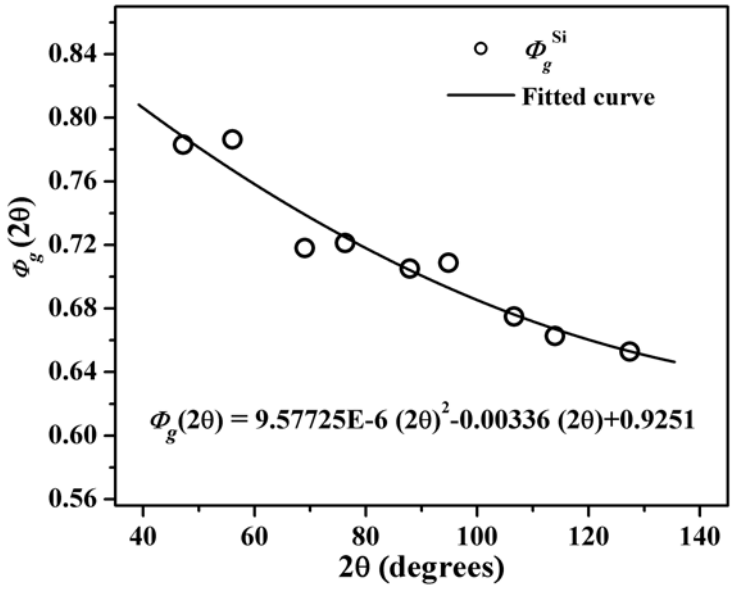

Figure 5.4 Determination of A_g, B_g and C_g for instrument used in the present study

$$\bar{\kappa} = \frac{(1.452163\Phi_g - 0.9039645) + (-3.040869\Phi_g{}^2 + 5.490729\Phi_g - 2.262667)^{1/2}}{2(0.7699548 - 1.209442\Phi_g)}$$

$$\beta_{gG} = \beta_g \exp(\bar{\kappa}^2)[1 - \mathrm{erf}(\bar{k})] \qquad (5.11)$$

$$\beta_{gL} = \sqrt{\pi}\bar{\kappa}\beta_g \exp(\bar{\kappa}^2)[1 - \mathrm{erf}(\bar{k})]$$

By substituting equations 5.7 and 5.11 into equation 5.5, the values of β_{fL} and β_{fG} can be determined. A knowledge of β_{fL} and β_{fG} enables construction of the physically broadened profile $f(2\theta)$, from which characteristic parameters of the profile such as the full width at half maximum (FWHM), the diffraction angle and the Fourier coefficients required in the MWHP and MWAA can be determined.

With regard to the deconvolution method elaborated above, the use of the Voigt function is necessary to determine the β_{hG} and β_{hL} values of the observed profile $h(2\theta)$. However, the Voigt function is only able to model profiles with a shape factor within the range of 0.6366-0.9394 – the lower and upper limits which correspond respectively to the shape factor of the Lorentzian and Gaussian function. Therefore,

for observed profiles that cannot be described by the Voigt function, the Stokes method [137] is employed to deconvolve the physically broadened profile $f(2\theta)$. The Stokes method involves Fourier analysis of $h(2\theta)$ and $g(2\theta)$. The real and imaginary Fourier coefficients of $h(2\theta)$ and $g(2\theta)$, represented respectively by subscripts 'r' and 'i', are calculated using equation 5.12:

$$\begin{aligned} H_r(t) &= \frac{1}{a}\sum_{-a/2}^{a/2} h(2\theta)\cos\frac{2\pi t(2\theta - 2\theta_0)}{a(2\theta)_s} \qquad G_r(t) = \frac{1}{a}\sum_{-a/2}^{a/2} g(2\theta)\cos\frac{2\pi t(2\theta - 2\theta_0)}{a(2\theta)_s} \\ H_i(t) &= \frac{1}{a}\sum_{-a/2}^{a/2} h(2\theta)\sin\frac{2\pi t(2\theta - 2\theta_0)}{a(2\theta)_s} \qquad G_i(t) = \frac{1}{a}\sum_{-a/2}^{a/2} g(2\theta)\sin\frac{2\pi t(2\theta - 2\theta_0)}{a(2\theta)_s} \end{aligned} \quad , \tag{5.12}$$

where a is the number of data point intervals for a profile under Fourier analysis. For $f(2\theta)$, its Fourier coefficients can be obtained indirectly by equation 5.13:

$$\begin{aligned} F_r(t) &= \frac{H_r(t)G_r(t) + H_i(t)G_i(t)}{[G_r(t)]^2 + [G_i(t)]^2} \\ F_r(t) &= \frac{H_i(t)G_r(t) - H_r(t)G_i(t)}{[G_r(t)]^2 + [G_i(t)]^2} \end{aligned} \tag{5.13}$$

Using the values of $F_r(t)$ and $F_i(t)$ from equation 5.13, $f(2\theta)$ can be synthesized from equation 5.14:

$$f(2\theta) = \sum_t F_r(t)\cos\frac{2\pi t(2\theta - 2\theta_0)}{a(2\theta)_s} + \sum_t F_i(t)\sin\frac{2\pi t(2\theta - 2\theta_0)}{a(2\theta)_s} \tag{5.14}$$

The Stokes method provides an alternative approach to obtain $f(2\theta)$. However, it is usually used to process $h(2\theta)$ that is 2-6 times broader than $g(2\theta)$ at $2\theta_0$, because the Stokes method is most suited for this [138]. Therefore, in the present study, the observed diffraction lines that can be modeled with the Voigt function are subjected to the algorithm described by equation 5.5, whereas the others are processed by the Stokes method to extract $f(2\theta)$ from $h(2\theta)$.

After obtaining $f(2\theta)$, the next step is to assess the microstructure of the material by applying the MWHP and MWAA evaluation techniques. As mentioned earlier, the

dislocation contrast factor ($\overline{C}$) is introduced into the MWHP and MWAA and expressed in the form of equation 5.15 for copper [122]:

$$\overline{C} = 0.304(1 - qH^2) \tag{5.15}$$

where q depends on the edge and/or screw character of dislocations, and $H^2 = (h^2k^2+h^2l^2+k^2l^2)/(h^2+k^2+l^2)^2$, where h, k, l are the Miller indices of a particular reflection.

The MWHP and MWAA are formulated respectively, according to the following equations [121, 139]:

$$(\Delta K)^2 \cong (0.9/D)^2 + (\pi A_0{}^2 b^2 / 2)\rho(K^2\overline{C}) \tag{5.16}$$

$$\ln A(L) \cong \ln A^S(L) - (\pi\rho b^2 L^2 / 2)\ln(R_e/L)(K^2\overline{C}) \tag{5.17}$$

where $K = 2\sin\theta_0 / \lambda_1$, $\Delta K = \cos\theta_0[\Delta(2\theta)]/\lambda_1$; θ_0 and $\Delta(2\theta)$ are respectively the Bragg angle and FWHM of a profile; A_0 is a constant depending on R_e - the effective outer cutoff radius of dislocations. D, b, ρ, $A(L)$ and $A^S(L)$ represent respectively the volume averaged crystallite size, dislocation Burgers vector, dislocation density, Fourier cosine coefficients of a profile, and Fourier size coefficients; L is the Fourier length defined by $L = na_3$, with $a_3 = \lambda/[2(\sin\theta_2 - \sin\theta_1)]$ and n, θ_1 and θ_2 are an integer and the lower and upper limits of an angular range corresponding to the measured diffraction profile.

The dislocation arrangement parameter M, which characterizes the extension of the strain field of dislocations relative to the mean dislocation spacing ($1/\sqrt{\rho}$), is defined by [140]:

$$M = R_e\sqrt{\rho} \tag{5.18}$$

A smaller value of M indicates stronger mutual screening of dislocation strain fields, and vice versa. It should be mentioned that although ρ is present in both MWHP and

MWAA, its value can only be determined by MWAA, as explained in [121]. In this study, two samples were used for XRD analysis for each strain rate.

5.2.3 Thermal analysis

The samples studied were polished and treated with dilute nitric acid to remove damaged surfaces that may cause preferential recrystallization, and they eventually weighed 30-50mg. A differential scanning calorimeter (DSC), TA Instruments Model DSC-2910, was calibrated using a standard indium sample and utilized for thermal analysis. The deformed sample and a reference sample (annealed copper), were placed in separate aluminum pans, heated at a constant rate of 20^0C/min up to 400^0C in an argon flow environment of 100 ml/min, then cooled to RT. Following this, a second thermal analysis was undertaken to obtain the baseline from which the exothermic peak in a DSC curve corresponding to the heat release of the sample studied can be determined. One set of measurements was taken for each of the three samples deformed at a common strain rate.

5.3 Results

5.3.1 Microstructural examination using TEM

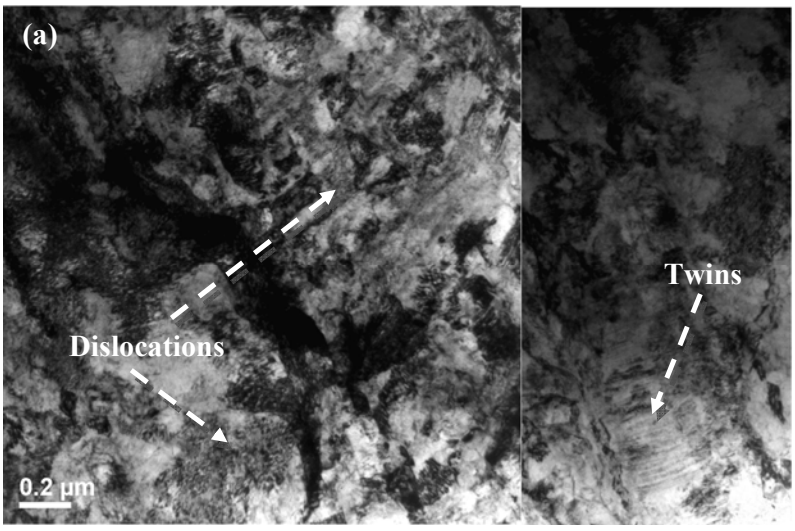

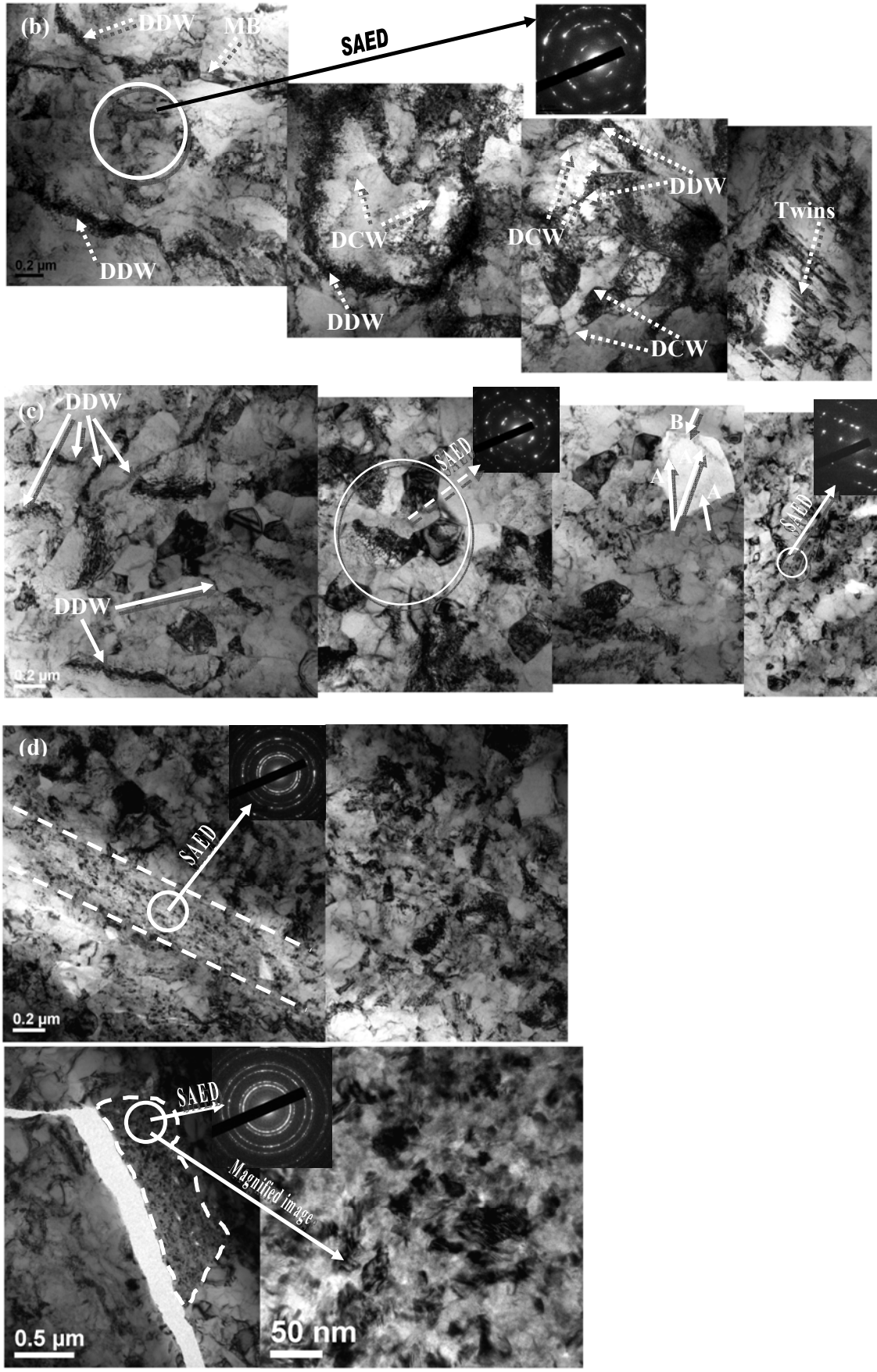
(b)
DDW
MB
SAED
DDW
0.2 μm
DCW
DDW
DCW
DDW
DCW
Twins
(c)
DDW
DDW
0.2 μm
SAED
B
A
SAED
(d)
SAED
0.2 μm
SAED
Magnified image
0.5 μm
50 nm

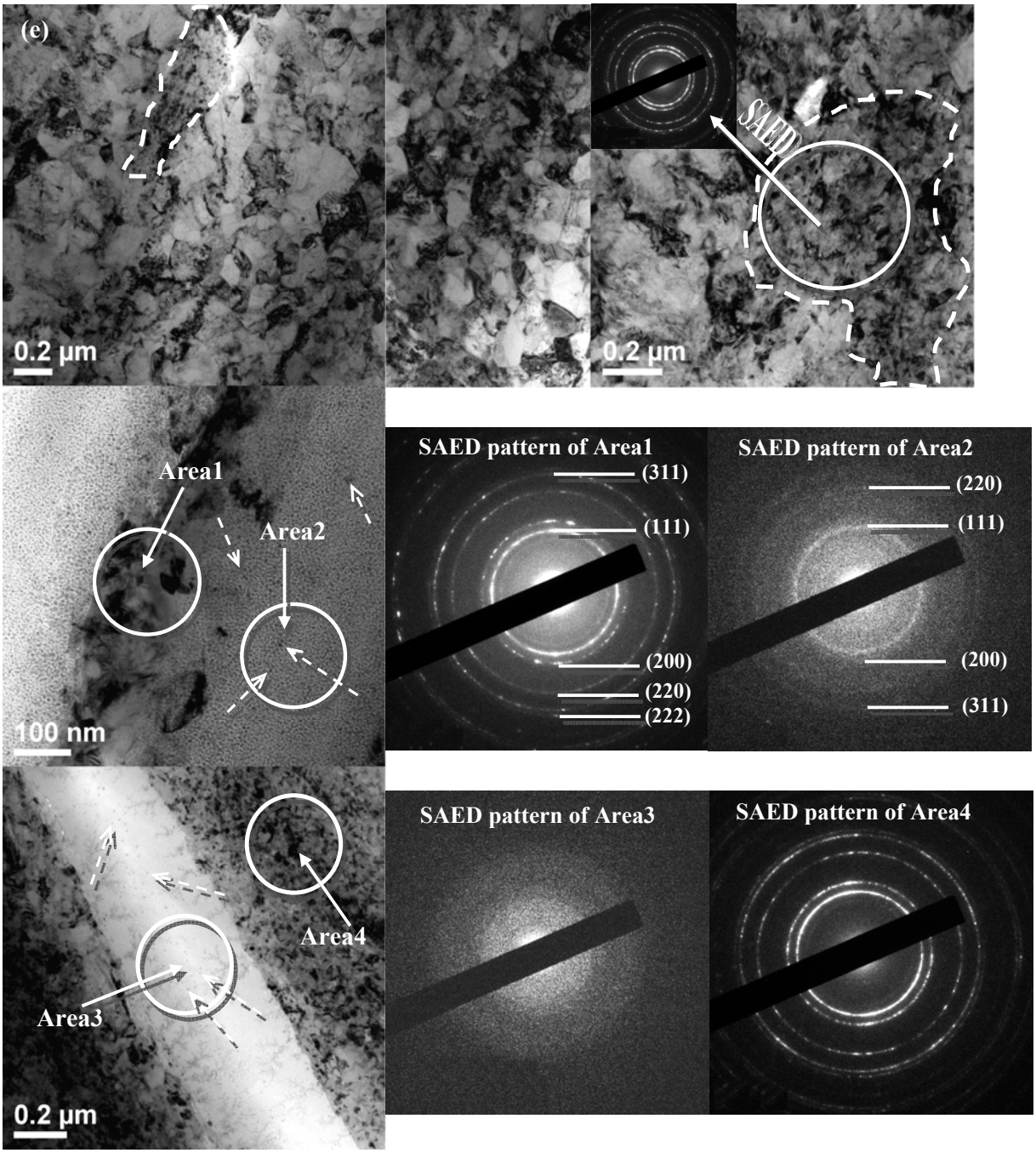

Figure 5.5 Bright-field TEM images of samples deformed at various strain rates (a) 9.4×10^{-2} /s (SUTM) (b) 1.9/s (SUTM) (c) 4.8×10^{2}/s (Drop tester) (d) 5.7×10^{3}/s (SHPB) (e) 6.9×10^{4}/s (Gas gun)

Figure 5.5 shows typical bright-field TEM images of samples deformed at various strain rates. At the lowest strain rate, the microstructure is characterized by the presence of forest dislocations and twins, as indicated by the dashed arrows in Figure

5.5(a). At higher strain rates, dislocations become entangled and form dense dislocation walls (DDWs) which divide the originally coarse grains into sub-micrometer/micrometer domains. Dislocation cell walls (DCWs) further subdivide each domain into smaller regions, and twins are also formed (Figure 5.5(b)). The circle in Figure 5.5(b) contains a few dislocations cells (DCs) and the corresponding electron diffraction (SAED) pattern of the area enclosed by the circle is characterized by elongated spots, indicating the presence of subgrains. The microstructural configuration in Figure 5.5(b) is similar to those of fcc metals deformed at similar strain rates but at RT, wherein geometrically necessary boundaries, including DDWs and micro-bands (MB in Figure 5.5(b)), demarcate cell blocks consisting of groups of DCs [5, 141]. As the strain rate is increased to the order of 10^2/s, DDWs are still observable, as shown in Figure 5.5(c), but thinner than those in Figure 5.5(b), whereas the sizes of cell blocks bounded by DDWs appear smaller. In addition, the fact that the black regions within the circle exhibit a striking contrast with the grey background indicates the formation of grains there and this is confirmed by the SAED pattern of the encircled area. Moreover, tangled dislocations are observed in the newly formed submicrometer grains; some (labeled 'A') divide the grain while others (labeled 'B') accumulate at the grain boundary. Nano-sized twins also exist, and this is confirmed by the SAED pattern located at the top right corner. At a higher strain rate (Figure 5.5(d)), DCs and (sub)grains dominate the microstructure and their sizes appear generally smaller than those in Figure 5.5(c). Apart from this, a notable feature is the presence of deformation bands, such as those defined within the dashed lines. The magnified image, as well as the continuous SAED ring patterns for the areas within the circles, reveals that these deformation bands are composed of nanometer grains with random crystallographic orientations. This generation of a region that contains

grains with sizes about one order smaller than the DCs and (sub)grains in the surrounding area points to the occurrence of deformation localization. At the highest strain rate, of the order of 10^4 /s (Figure 5.5(e)), the majority of DCs and (sub)grains formed exhibit sizes smaller than 0.2μm. As with samples deformed at a lower strain rate (in the order of 10^3 /s), nanometer-sized grains are produced in localized regions and these regions assume arbitrary shapes, such as those bounded by the dashed lines. For samples deformed at the highest strain rate, a small fraction of the regions with highly localized strains assume the form of bands and display the characteristics of an amorphous structure not observed in samples deformed at lower strain rates. For example, in Figure 5.5(e), diffused halo rings in the SAED pattern of Area3 indicate the formation of an amorphous phase in the deformation bands; whereas the Debye-Scherrer SAED ring pattern of Area1 are typical of polycrystalline copper. In contrast to Area1 or Area3, the SAED pattern of Area2 is a superposition of patterns corresponding to polycrystalline and amorphous structures; this implies that Area3 has a higher degree of amorphization than Area2. In line with this, the size of the grains in Area3 is also smaller, as is the fraction of the area comprising grains (indicated by dashed arrows). In the vicinity of the deformation band, like the one that encompasses Area3, nanometer grains are generated as revealed from the SAED pattern of Area4. A notable feature is that twins are hardly found in samples deformed at strain rates above $10^3 s^{-1}$, although they are readily observed in samples deformed at lower strain rates.

5.3.2 XRD profile analysis of microstructure

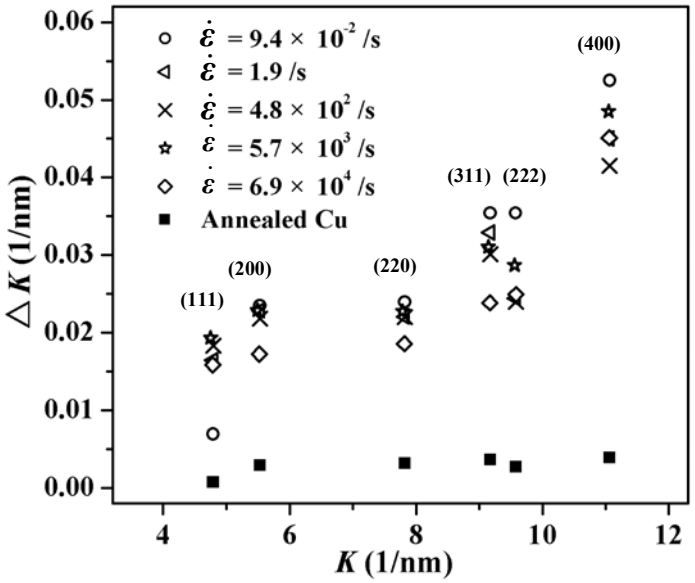

Figure 5.6 Conventional Williamson-Hall plot of the FWHM versus K, for annealed copper and copper samples deformed at various strain rates (numbers in parentheses are Miller indices of reflections).

Figure 5.6 shows typical FWHM values of peak profiles for initially annealed copper and copper samples subjected to plastic deformation at various strain rates (Table 5.1). Compared with samples that are annealed, the ones that are deformed, regardless of strain rate, exhibit much broader peak profiles for all the six reflections, indicating an evolution of microstructure via plastic deformation. Determination of the q value and the respective fractions of screw and edge dislocations stored in a sample is carried out following the procedures introduced in [121]. For annealed copper, numerical calculations result in q = 2.23, which corresponds to screw and edge dislocation fractions of 81.1% and 18.9% respectively. This is consistent with existing reports [47, 139] that there is a higher fraction of screw dislocations compared to edge dislocations in annealed metals and alloys. For samples deformed at different strain rates, the values of q and screw/edge dislocation fractions are shown in Figure 5.7. The value of q, as well as the fraction of screw dislocations, decreases, whereas the fraction of edge dislocations increases with stain rate. It is also noted that a sharp change in the value of each parameter occurs in the strain rate range of 10^2-

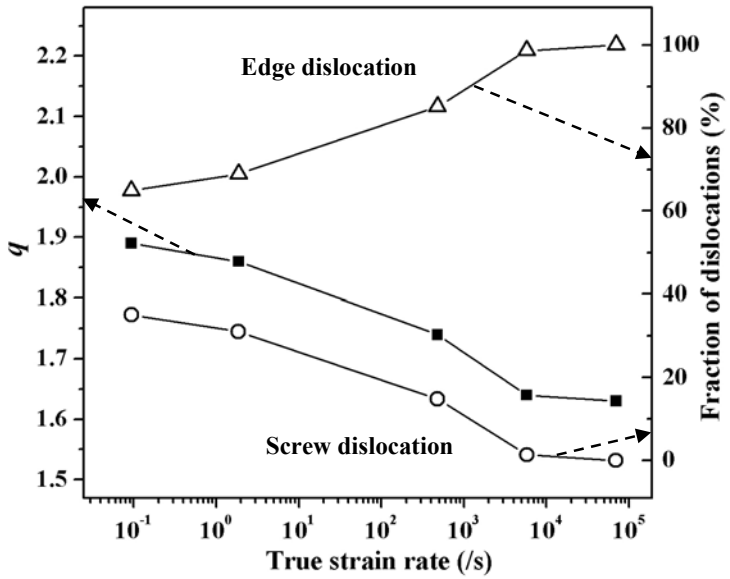

Figure 5.7 Variation of q and fraction of screw/edge dislocations with strain rate

10^3/s. The crystallite size, D, determined from equation (5.16) is depicted in Figure 5.8 as a function of strain rate, and a decrease of D with strain rate is observed. The

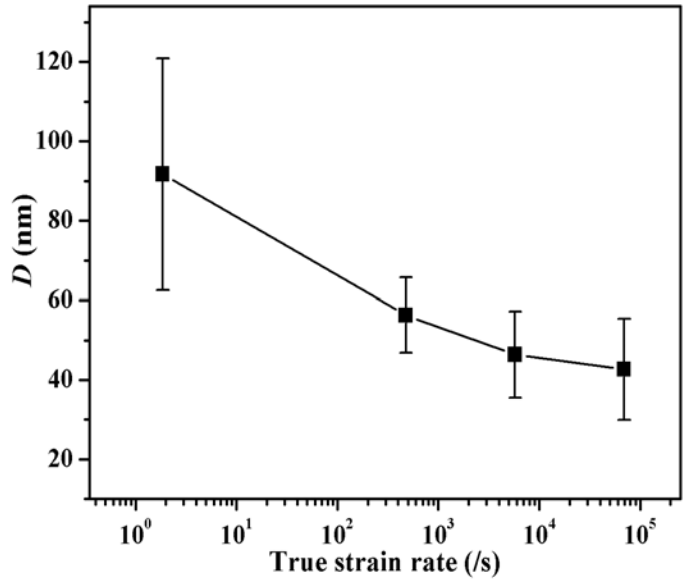

Figure 5.8 Variation of crystallite size (D) with strain rate

density (ρ) and effective outer cutoff radius of dislocations (R_e) are evaluated from equation (5.17) and shown in Figure 5.9. Compared with annealed copper, which has a dislocation density of only $(2.11 \pm 0.02) \times 10^{13} m^{-2}$ (not indicated in Figure 5.9), the samples deformed regardless of strain rate exhibit significantly enhanced dislocation

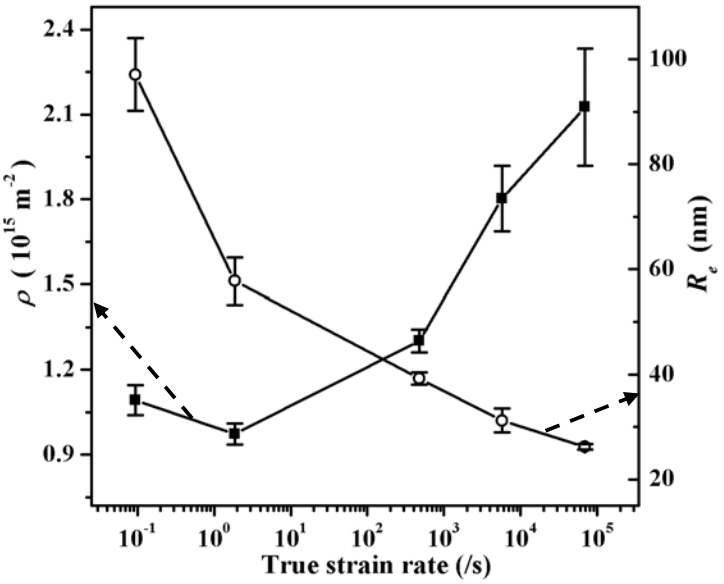

Figure 5.9 Variation of dislocation density (ρ) and effective outer cutoff radius (R_e) with strain rate

storage by an approximate factor of two orders of magnitude. Although ρ decreases slightly when the strain rate increases from ~0.1/s to ~2/s, it keeps increasing with strain rate thereafter. Nevertheless, *Re*, which represents the extent of a dislocation strain field, decreases monotonously with strain rate, whereby there is a sharp decrease for strain rates below ~2/s. The dislocation arrangement parameter *M*, defined by equation (5.18), also decreases with strain rate, as shown in Figure 5.10,

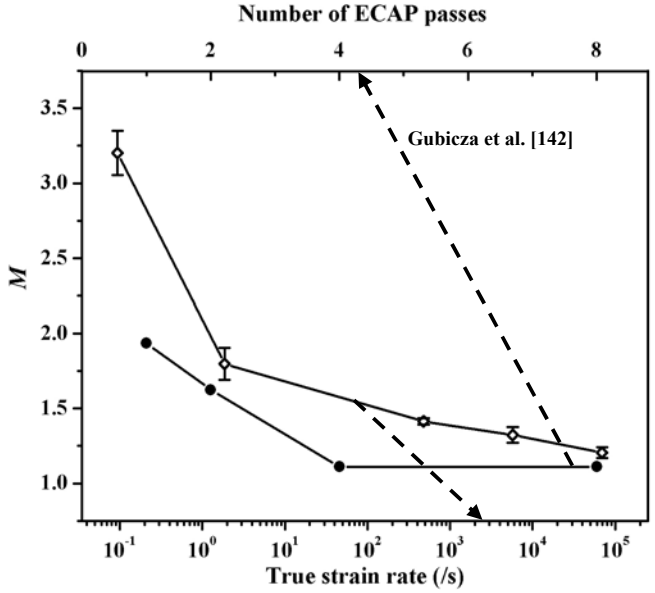

Figure 5.10 Variation of dislocation arrangement parameter (M) with strain rate

and varies in a manner similar to R_e; this implies a stronger screening of the dislocation strain field with increasing strain rate. Moreover, it is noted that the values of M corresponding to strain rates between 10^0-10^5/s lie in a range similar to that exhibited by copper samples subjected to 1-8 passes of deformation by equal-channel angular pressing (ECAP) [142], and that the effect of a higher strain rate on the variation of M resembles that of a greater strain during ECAP.

5.3.3 Thermal analysis of microstructure

Figure 5.11 shows DSC curves for samples deformed at different strain rates. The peaks in the curves correspond to the generation of heat in deformed samples, originating from an exothermic reaction such as recrystallization. The temperature that signifies the onset of RX is determined according to [143] and defined by the temperature associated with each peak; this corresponds to the occurrence of 50% recrystallization [144]. The stored energy (E_s) in the deformed sample is calculated from the area under the heat flow curves and shown in Figure 5.12. For samples

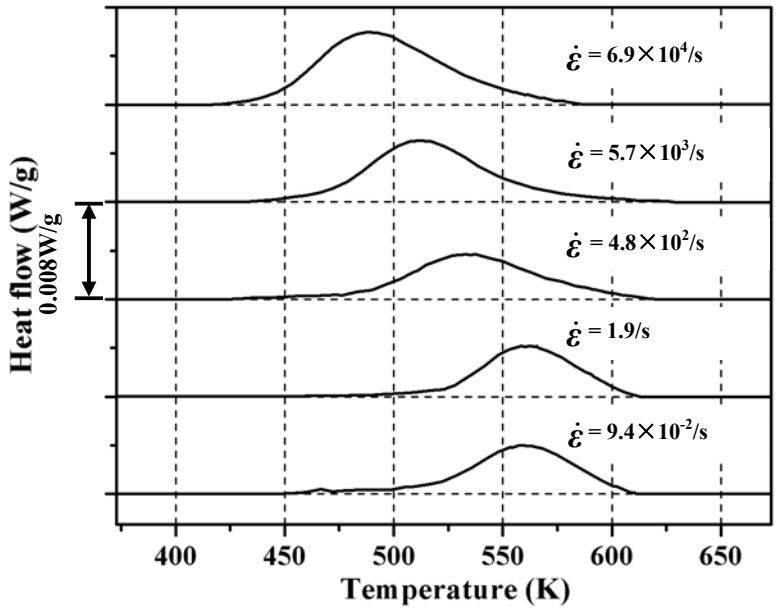

Figure 5.11 DSC curves for samples deformed at various strain rates

deformed at a relatively low strain rate, i.e. $\dot{\varepsilon}$ <10/s in the current case, E_s is close to but lower than the saturation E_s, which defines the maximum defect energy that can be stored in a deformed sample; this is obtained for samples (of purity similar to the material in this study) processed by cold-rolling (CR) at RT [145]. However, the saturation E_s is exceeded when the strain rate rises above 10^2/s. Furthermore, at strain rates higher than ~3×10^3/s in the present study, E_s exceeds the saturation E_s [146] reported for samples deformed via ECAP at RT to a strain of ~4, which exceeds the strain induced in samples in this study. The onset of RX and the RX temperatures in Figure 5.12 vary with strain rate in a trend opposite to that of the stored energy. This is because an increase in stored energy enhances the driving force for RX, so that nucleation and growth of new strain-free grains take place at lower temperatures.

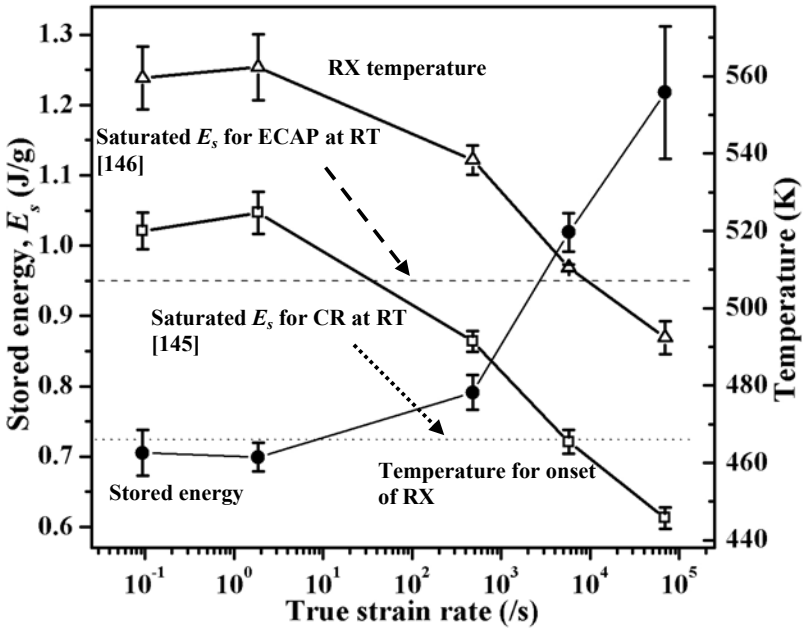

Figure 5.12 Stored energy, onset of and RX temperatures for samples deformed at various strain rates

5.3.4 Micro-hardness

Figure 5.13 shows the variation of hardness with strain rate. It is observed that, a higher strain rate leads to strengthening of the deformed sample, although this is not significant at strain rates lower than 10/s.

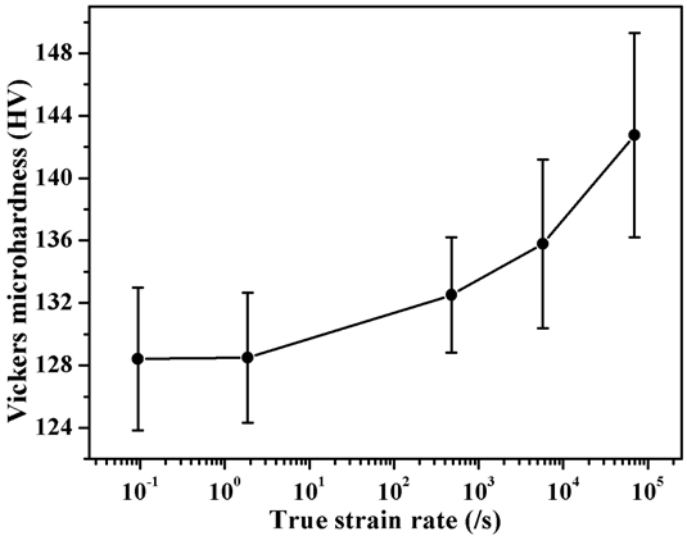

Figure 5.13 Variation of micro-hardness with strain rate

5.4 Discussion

5.4.1 Deformation mechanism

It is well known that dislocation glide is the dominant mechanism for plastic strain in metals, whereas deformation twinning is an alternative that plays a noticeable role, particularly at low temperatures, whereby the high stresses required to nucleate twins are available. This general perspective of deformation mechanisms is applied to the current investigation, wherein substructures such as DCs and DDWs defined by groups of dislocations, as well as twins, constitute the deformed microstructure shown in Figure 5.5. However, it is noted from TEM examinations that very few twins are observed in samples deformed at strain rates as high as 10^3-10^5/s, and this is confirmed by XRD and DSC analysis, as illustrated in Figure 5.14. The dislocation density corresponding to DSC analysis in Figure 5.14 is calculated

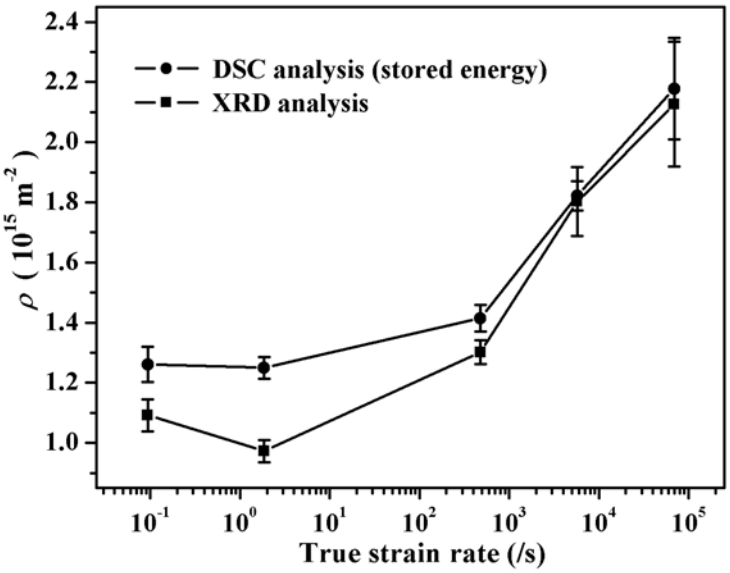

Figure 5.14 Dislocation density (ρ) calculated respectively from DSC and XRD analysis

from $\rho = \rho_C * E_s / E^d$, where ρ_C and E^d represent respectively the density of copper and the energy per unit length of a dislocation, assuming that the defect energy stored is contributed only by dislocations. The fact that the dislocation density obtained from DSC calculations exceeds that from XRD analysis implies that other types of defects contribute to the stored energy. Based on TEM examination and earlier analysis that the contribution of point defects is negligible [143], it is reasonable to assume that the stored energy corresponding to the difference between the calculated dislocation density from DSC analysis and the value from XRD measurements is contributed by the boundaries of deformation twins. Consequently, Figure 5.14 indicates that the number of twins declines significantly when the deformation strain rate exceeds 10^3/s, which concurs with TEM observations. However, published experimental results have shown that a high strain rate favors the formations of twins [99, 143, 147]. Therefore, the mechanism leading to fewer twins at high strain rates observed in the present study might arise from fragmentation of deformation twins as reported in [148, 149], which resembles the breakup of coarse grains into ultrafine ones during severe plastic deformation. The fragmentation of twins arises from interaction between twin

boundaries and dislocations. The enhanced storage of dislocations at high strain rates, as revealed by reduced dislocation cell sizes (Figure 5) and directly by XRD (Figure 5.9), points to the probability of dislocations subdividing twins, resulting in the smaller number of twins observed in the post-deformation microstructure. In addition to dislocation glide and twinning, amorphization is observed to play a role in deformation at the highest strain rates, in the order of 10^4 /s. This is consistent with results from molecular dynamics simulation of the deformation mechanism in single copper crystals, which indicates that amorphization is a means of accommodating plastic deformation at high strain rates, in the same way twinning does at low strain rates [104]. A detailed discussion on the initiation and propagation of amorphization is presented later.

5.4.2 Comparison of general microstructure for deformation at different strain rates

Since temperature elevation is a key factor affecting the microstructure, this is estimated for samples deformed at each strain rate before the microstructure is discussed.

5.4.2.1 Temperature of deformed samples

During deformation, there are two primary sources of temperature change in a sample. One is the partial transformation of plastic work into heat, and the other is heat transfer at the interface between the sample and the liquid nitrogen the sample is immersed in.

For the former, the temperature rise can be calculated from the following:

$$\Delta T_r = \frac{\beta}{c\rho_C}\int \sigma d\varepsilon \tag{5.19}$$

where β, c and σ represent respectively the fraction of plastic work converted into heat, and the specific heat and flow stress of the sample. β has been experimentally determined to have a value of 0.7 from uniaxial single compression tests [101] (see Chapter 3), which is similar to values obtained by others for tension and compression, whereas the commonly-assumed value of β = 0.9 has been reported for samples subjected to torsion [93]. c is temperature dependent [95, 111], and the variation of c with T assumed in this study has the following form [95]:

$$c = \begin{cases} 0.0000416T^3 - 0.027T^2 + 6.21T - 142.6 & \text{for } T < 270K \\ 0.1009T + 358.4 & \text{for } T \geq 270K \end{cases} \tag{5.20}$$

The plastic flow of copper is described by the Preston-Tonks-Wallace model defined by equation (5.21), which appears to predict the compressive stress-strain response more accurately than the frequently-used Johnson-Cook, Zerilli-Armstrong and Mechanical Threshold Stress models [95] (note that the modified Steinberg-Cochran-Guinan-Lund constitutive model used in Chapter 4 is not employed here because it is not suitable for deformation at low strain rates such as those performed on an SUTM).

$$\sigma(\varepsilon, \dot{\varepsilon}, T) = \begin{cases} 2\left[\tau_s + \alpha' \ln\left[1 - \varphi \exp\left(-\beta' - \frac{\theta\varepsilon}{\alpha'\varphi}\right)\right]\right]\mu(p,T) & \text{thermal regime} \\ 2\tau_s \mu(p,T) & \text{shock regime} \end{cases} \tag{5.21}$$

where $\alpha' = (s_0 - \tau_y)/d$, $\beta' = (\tau_s - \tau_y)/\alpha'$, $\varphi = \exp(\beta') - 1$ and τ_s, s_0, τ_y, d and θ are respectively the normalized work-hardening saturation stress, the value of τ_s at 0K, the normalized yield stress, a dimensionless parameter modifying the Voce hardening law and the hardening constant. $\mu(p, T)$ is the shear modulus defined by the Nadal-Le Poac model and varies with hydrostatic pressure p and temperature T.

With regard to heat transfer between the sample and the surrounding liquid nitrogen, the sample cooling rate is analyzed using a lumped-heat-capacity method [107], which assumes a uniform temperature distribution throughout the sample. Such an assumption is reasonable because of the high conductivity and fairly small volume (~25 mm^3) of copper samples used in this study. Consequently, the variation in sample temperature is defined as:

$$\Delta T_c = \frac{\chi S_A t}{c\rho_C V} = \frac{\chi S_A \varepsilon}{c\rho_C V \dot{\varepsilon}} \tag{5.22}$$

where χ, S_A and V are respectively the heat flux at the interfaces between a sample and the liquid nitrogen, surface area of sample in contact with liquid nitrogen and sample volume. χ varies with sample temperature above the boiling point of liquid nitrogen, and the heat transfer mechanism (i.e. convection, nucleate boiling, film boiling) at the interfaces. Existing reports [108-110] state that for copper, the value of χ lies within a range bounded by the minimum (χ_{min}) and maximum (χ_{max}) heat fluxes, which are calculated from equation (5.23):

$$\begin{aligned} \chi_{max} &= \overline{E} h_{fg} \rho_v \left[\frac{g\varpi(\rho_l - \rho_v)}{\rho_v^{\,2}} \right]^{1/4} \\ \chi_{min} &= 0.09 h_{fg} \rho_v \left[\frac{g\varpi(\rho_l - \rho_v)}{(\rho_l + \rho_v)^2} \right]^{1/4} \end{aligned} \tag{5.23}$$

where h_{fg}, ρ_v, ρ_l and ϖ are parameters for nitrogen at $77K$, and represent respectively the latent heat of vaporization, vapor density, liquid density and surface tension of the liquid; g is gravitational acceleration and $\overline{E}$ is a constant assumed to be 0.19 in this study.

$$T = 77 + \Delta T_r - \Delta T_c \tag{5.24}.$$

In summary, the instantaneous temperature of a sample during deformation can be estimated from equation (5.24), which relates temperature to strain and strain rate.

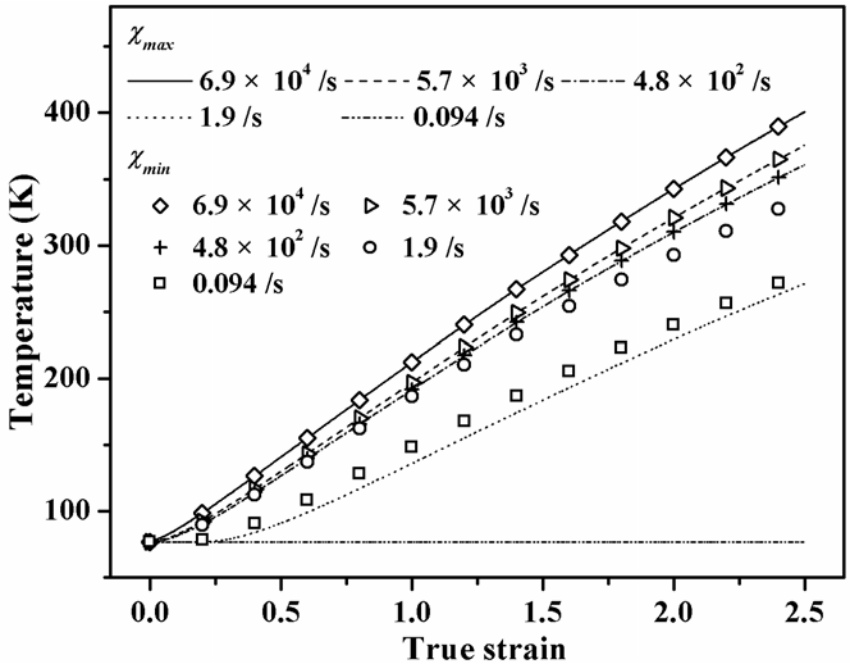

Figure 5.15 Variation of temperature with strain at different strain rates

Figure 5.15 shows the variation of the calculated temperature with strain at different strain rates. With the values of χ_{max} and χ_{min} assigned, both computed temperatures exhibit a monotonous increase with strain and strain rate. The difference between χ_{max} and χ_{min} does cause a difference in the temperature-strain curves for strain rates lower than 10^2 /s. However, at higher strain rates, curves for the two limits converge because of the short deformation duration that makes heat transfer at the interfaces insignificant. More importantly, it is noted that the sample temperature after deformation at all the strain rates imposed is lower than the recrystallization temperature of copper, i.e. ~500K [66]. Underestimation of temperature arising from use of equation (5.24) is suspected, because some investigations (e.g. [88, 150]) have claimed α to be variable, rather than assuming it to be a constant in the present instance. To address this, a large value of unity is assigned to α to determine the maximum attainable temperature of a deformed sample. At the highest strain rate of 6.9×10^4 /s, the calculated temperature is ~470K for a final true strain of 2.3. This

suggests that although a sample undergoes a temperature rise during deformation, the process of thermally activated recrystallization via nucleation and growth of new strain-free grains will not occur within samples deformed at all the strain rates imposed in this study.

5.4.2.2 General microstructure

In contrast with the almost homogeneous distribution of dislocations shown in Figure 5.5(a), the dislocations in Figures 5.5(b)-5.5(e) accumulate to form dislocation walls, wherein the strain fields of dislocations are mutually screened. This transformation of dislocation arrangement is also captured by the parameter M, which decreases dramatically when the strain rate increases beyond 10^0/s (Figure 5.10), indicating a stronger screening of dislocation strain fields. Compared with Figure 5.5(a), the dislocation structures in Figures 5.5(b)-5.5(e) lead to a reduction in the free energy of dislocations and are thus favored. Therefore, the dislocation configuration in Figure 5.5(a) implies suppression of dislocation mobility because of the low temperature, whereas such suppression is not as strong for samples deformed at higher strain rates because of the significant rise in sample temperature (Figure 5.15). The evolution of microstructure from Figure 5.5(a) to Figure 5.5(b) is accompanied by a slight drop in ρ and E_s (Figures 5.9 and 5.12 respectively), indicating the occurrence of dynamic recovery in samples deformed at a strain rate of 1.9/s. However, both ρ and E_s are elevated when the strain rate is increased beyond 10^2/s; this is attributed to the enhanced rate of dislocation generation at higher strain rates. In summary, the microstructure of samples deformed at strain rates of 10^0-10^5/s is characterized by the presence of irregularly shaped cell blocks and approximately equiaxed (sub)grains, schematically shown in Figure 5.16. Cell blocks dominate the

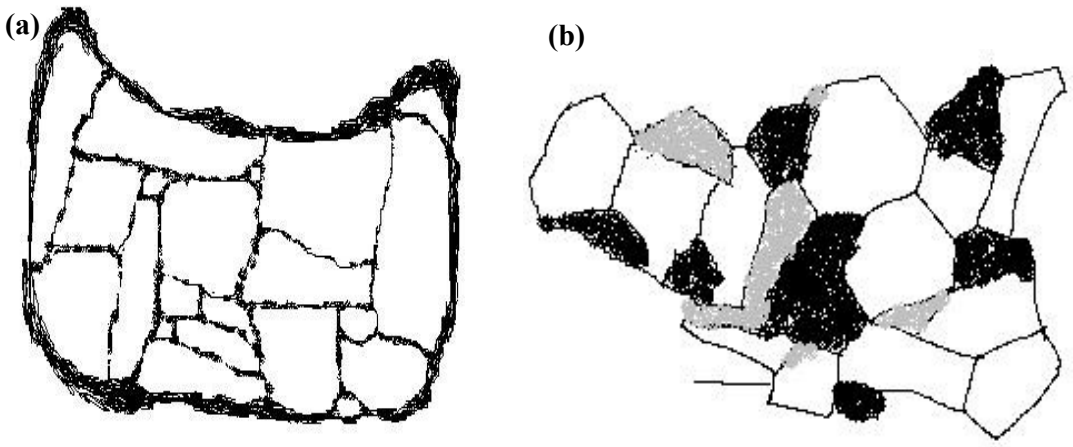

Figure 5.16 Schematic drawing of (a) cell block (b) (sub)grains

microstructure of samples deformed at $\dot{\varepsilon}$=1.9/s and shrink with increasing strain rate while (sub)grains start to emerge and prevail respectively at $\dot{\varepsilon}$=480/s and $\dot{\varepsilon}$=5700/s; they also decrease in size with strain rate. This qualitative observation of microstructure refinement with increasing strain rate is consistent with the XRD results in Figure 5.8 (the crystallite size *D* indicated appears lower than the sizes of the DCs and (sub)grains in Figure 5.5 because for XRD measurements, *D* is equivalent to the mean size of domains coherently scattering X-rays, and is thus able to distinguish between DCs with an angular orientation difference of less than 1^0). The current observation of reduction in the size of DCs and (sub)grains with increasing strain rate agrees with results of previous studies respectively on nickel [151], electrical conductor grade aluminum [152] and OFHC copper [153] at strain rates ranging from 10^{-5}-10^{-1} /s, and supports the conclusions of earlier investigations involving deformation at higher strain rates, i.e. 10^0-10^5 /s. The observed effect of strain rate on the size of DCs/subgrains can be explained by the principle of similitude [154-156], which states an inverse relationship between the DC/subgrain size and the square root of dislocation density. Since the density of dislocations obtained at higher strain rates (Figure 5.9) is larger, it is not unexpected that smaller DCs/subgrains are formed. The enhancement of dislocation storage with increasing strain rate is

presumably caused by two effects: firstly, the generation of dislocations during deformation is elevated by a higher strain rate, as implied by Orowan's equation [157] which relates strain rate $\dot{\varepsilon}$ to the density of mobile dislocations ρ_m (i.e. dislocations contributing to plastic strain) by $\dot{\varepsilon} = \rho_m b v^d$ (v^d represents the velocity of mobile dislocations); secondly, annihilation of dislocations is suppressed at higher strain rates because recovery is a time-dependent process [158]. Despite the consistency between the present and earlier studies [e.g. 153] in characterizing the effect of strain rate on the size of DCs, the earlier study reported insensitivity of DC size to strain rate at strains above 30% because of saturation in the size of DCs, whereas the present study demonstrates that for a large strain of 90%, the size of DCs remains variable and not directly related to strain rate. This dichotomy is considered to be the result of the difference in the ambient temperatures at which the present and earlier studies were carried out. Owing to the low ambient temperature in the present study, thermally-activated recovery is reduced compared to that in the earlier work mentioned [153], which was conducted at RT. Consequently, for the present study, the balance between the generation and annihilation of dislocations which leads to saturation in the size of DCs is not attained at strains corresponding to that for saturation in the DC size in the earlier study. This implies that a decrease in the ambient temperature of deformation causes an increase in the strain corresponding to the saturation size of DCs, which concurs with earlier experimental results [75].

The significant reduction in the thickness of dislocation cell walls shown in Figures 5.5(c)-5.5(e), compared to that in Figure 5.5(b), indicates a higher recovery efficiency at higher strain rates. Although the shorter deformation duration associated with a higher strain rate hinders the process of recovery, as mentioned above, the generation of more well-defined cell walls at higher strain rates implies a higher

degree of recovery, which is associated with the higher temperature generated (Figure 5.15) that promotes recovery. This indicates that recovery is influenced more by temperature than time. It must be noted that even though the extent of recovery is enhanced at higher strain rates, the density of stored dislocations does increase with strain rate (Figure 5.9), pointing to the dominant role of strain rate in stimulating the generation of dislocations. Figure 5.7 suggests that the recovery process progresses mainly via the annihilation of screw segments of dislocations, which results in an increase in the fraction of edge dislocations with strain rate. This supports the deformation model based on relatively low strain rate experiments, proposed in [16, 17], which shows that for f.c.c. metals severely deformed at temperatures below $0.5T_m$ (T_m being the melting temperature), it is primarily screw dislocations that are involved in annihilation. The reason why screw dislocation annihilation predominates in the present study may be linked to the low ambient temperature. It is well accepted that screw dislocations annihilate one another by cross slip, and that formation of a constriction in a screw dislocation is a necessary condition for cross slip. Li et al. [159] found that at a temperature as low as 30K, constriction of screw dislocation is achieved. As the formation of such constriction is aided by thermal activation, it is reasonable to assume in the present study that screw dislocations can be constricted and that cross slip can occur, leading to annihilation of dislocations of opposite signs. The annihilation of edge dislocations, however, requires dislocation climb, which is difficult to achieve at low temperatures because of difficulty in the diffusion of vacancies. Therefore, the dislocations stored in deformed samples exhibit characteristics more akin to edge dislocations, and this increases with strain rate. The grains generated (e.g. Figure 5.5(c)) display curved boundaries and a non-uniform contrast within the interior, which indicates severe distortion of the crystal lattice;

these are characteristic of grains generated by severe plastic deformation. It is therefore concluded that the grains thus formed have evolved from dislocation cells through the accumulation of dislocations at cell boundaries. Schafler et al. [11] found that the progression of cells into sub-grains accompanied the evolution of dislocation structures from a PDW (polarized dipolar walls) at the cell walls to PTW (polarized tilt walls) at subgrain boundaries, which is reflected by the decrease in the value of the dislocation arrangement parameter *M*. Note in Figure 5.10 that *M* decreases with the number of ECAP passes [142] and Mishra et al. [69] have shown that an increase in the number of ECAP passes contributes to the transformation of dislocation cells into subgrains, and then grains, implying an increase in the misorientation angle. This means that *M* is possibly linked to the misorientation angle of domains (DCs, subgrains and grains) and a smaller *M* indicates a larger misorientation angle. Bearing in mind the values of *M* obtained in the present study, the decrease of *M* with strain rate (Figure 5.10) suggests an increase in the degree of transformation of DCs into (sub)grains with strain rate. This is reasonable if one considers the higher temperatures (Figure 5.15) generated at higher strain rates favoring the formation of subgrains through recovery, and the higher density of dislocations produced at higher strain rates which accumulate at subgrain boundaries leading to an increase in the misorientation angle.

5.4.3 Formation of nanometer grains

The deformation bands signify instability of the lattice orientation in the material and appear in samples deformed at strain rates above 10^3/s. These bands are a consequence of deformation localization that leads to localized heat generation, which softens the material and in turn accelerates deformation localization. The formation of

these deformation bands initiates the generation of nanometer grains, either within (Figure 5.5(d)) or in the vicinity of the deformation bands (Figure 5.5(e)). Apart from deformation bands, nanometer grains are also found in regions with microstructures not corresponding to a band, such as those outlined by the dashed line in Figures 5.5(d) and 5.5(e). Whatever the geometry of regions containing nanometers grains is, the continuous rings of the SAED patterns indicate the generation of nanometer grains as a result of recrystallization. Recrystallization within the localized regions has been reported earlier for Cu [66] and other fcc, bcc and hcp metals [106, 147, 160-161] severely deformed at high strain rates. However, compared with the 0.1-0.2μm ultrafine grains obtained previously at RT [66], the grains formed in the present study are smaller by almost one order. This is attributed to the lower initial temperature of the sample, which allows a higher level of straining and thus a higher density of dislocations, resulting in smaller DCs being generated within localized regions before the final temperature rises to the threshold for the onset of recrystallization – a consequence of conversion of plastic work into heat. Based on equation (5.24), a strain of 3.5 must be induced in these localized regions to attain the critical recrystallization temperature of 500K. Due to the short deformation duration as well as the rapid cooling of the localized regions, recrystallization cannot arise from grain boundary migration. Instead, a 'rotational dynamic recrystallization' (RDRX) mechanism has been proposed to account for the formation of new grains [69, 106]. The kinetics of RDRX has been established as a function of temperature (T) and sub-grain diameter (L_1) [67, 69]:

$$t_R = \frac{L_1 \kappa T}{4\gamma' \delta D_{0b} \exp(-Q_b / RT)} \left(\frac{3\tan\theta_R - 2\cos\theta_R}{3 - 6\sin\theta_R} + \frac{2}{3} - \frac{4\sqrt{3}}{9} \ln \frac{2+\sqrt{3}}{2-\sqrt{3}} + \frac{4\sqrt{3}}{9} \ln \frac{\tan(\theta_R/2) - 2 - \sqrt{3}}{\tan(\theta_R/2) - 2 + \sqrt{3}} \right) \quad (5.25)$$

where t_R, γ', δ, D_{0b}, Q_b, R and κ represent respectively the time required to induce a rotation of θ_R to the subgrains, grain boundary energy, grain boundary thickness, a constant related to grain boundary diffusion, grain boundary activation energy, the gas constant and the Boltzmann constant. Using the values $\gamma'=6.25\times10^{-4}$ J/m^2, Q_b=7.25 $\times$ 10^4 J/mol, R=8.314 J/(mol-K), κ=1.38·10^{-23} J/K and $\delta D_{0b}=3.9\times10^{-16}\exp(-Q_b/RT)$ [69], the variation of θ_R with t_R is shown in Figure 5.17. It is observed that, for a rotation of ~0.52 radians (horizontal dotted line in Figure 5.17) which is required for the formation of new grains, the time required decreases with increasing temperature and decreasing subgrain size. At the critical recrystallization temperature, i.e. 500K, 20 μs is needed to transform a 20nm subgrain into grains. Considering that the deformation durations are respectively 404 μs and 33μs for tests done on a SHPB and a gas gun, the plots in Figure 5.17 indicate that nanometer grains can be formed during deformation via the mechanism of RDRX.

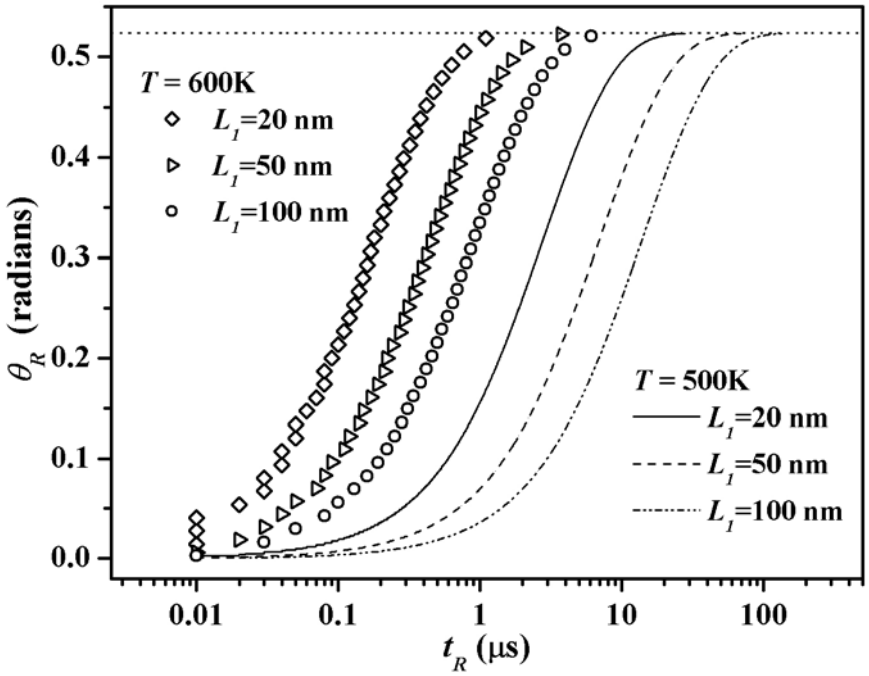

Figure 5.17 Variation of rotated angle with time at different values of T and L_1

5.4.4 Amorphization within localized bands

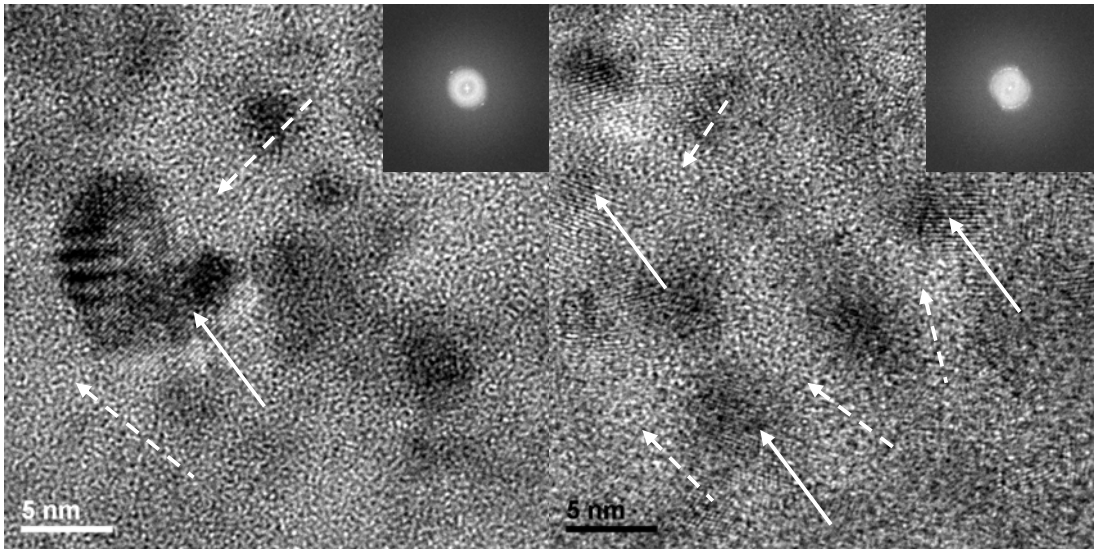

Figure 5.18 HRTEM images showing typical feature of microstructure in the localized bands (insets are live FFT views of images)

When the strain rate increases to the order of 10^4/s, amorphization occurs within the localized bands. However, these bands are not fully amorphized but display a composite structure comprising crystalline and amorphous phases. Such characteristics are typically depicted by high-resolution TEM (HRTEM) images, shown in Figure 5.18, in which grains of a few nanometers (marked by solid arrows) are surrounded by wide amorphized regions (marked by dashed arrows). The initiation and development of amorphization are related to the extreme localized strain induced at high strain rates, and this is depicted schematically in Figure 5.19. In stage I, localized deformation results in the generation of nanometer grains in an originally coarse-grained structure, as discussed in Section 5.4.3. With progressive straining, the grains are further refined and this leads to the advent of stage II, where amorphous structures start to emerge at grain boundary regions. The grain size associated with stage II is estimated to be ~13nm, from comparison of the different microstructures in

the two regions represented respectively by Area1 and Area2 in Fig. 5.5(e); the exact value is difficult to determine from the current study.

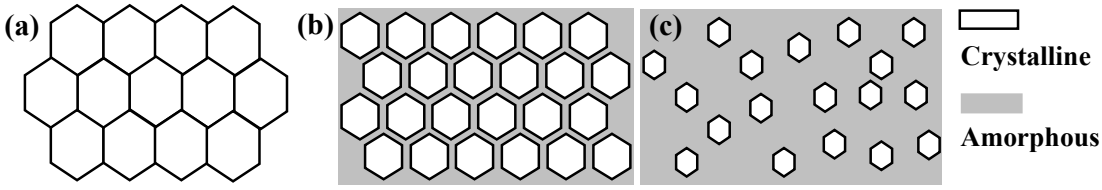

Figure 5.19 Schematic drawing showing the initiation and development of amorphized region (a) stage Ⅰ (b) stage Ⅱ (c) stage Ⅲ

The amorphous phase in stage II might be pseudo and a result of severe distortion of crystal lattices at regions near the grain boundary due to excessive dislocations there, leading to the loss of lattice periodicity, as pointed out in [12]. However, the observation of an increase in regions characterized by disordered arrangement of atoms and a reduction in grain size in contrast to stage II, as typified by Area3 in Figures 5.5(e) and 5.18, points to amorphization being responsible for evolution of the microstructure from stage II to stage III (Figure 5.19(c)). Typical HRTEM images shown in Figure 5.20 reveal two locations where amorphization takes place – one is the boundary between two adjacent grains (marked by solid arrows) and the other is the region close to the connection between two crystalline domains (marked by solid arrows) with a small orientation mismatch, as indicated respectively by the dashed arrows in Figures 5.20(a) and 5.20(b). These two locations are where plastic deformation is dominant; this is because the size of grains in Figure 5.20 lies in a range, specifically <15nm for copper [162, 163], where dislocation slip within individual grains to accommodate plastic deformation ceases to operate and thereby grain boundaries become the means of plastic deformation, via grain boundary sliding [164] or movement of disclination dipoles along grain boundaries causing crystal lattice rotation [165]. The occurrence of crystal lattice rotation resulting from

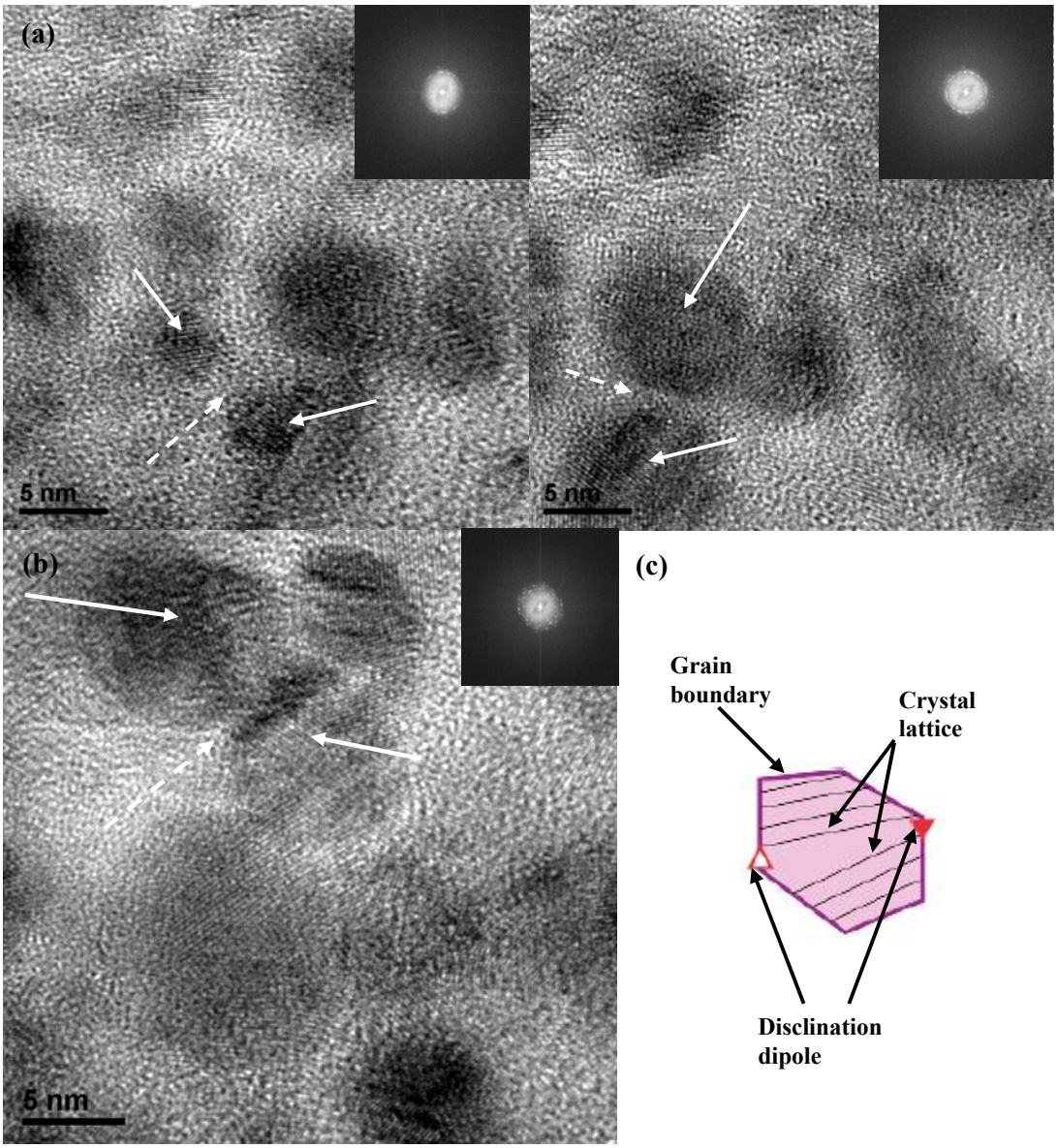

Figure 5.20 Location of amorphization (a) boundary between adjacent grains (b) region around adjoining point of two domains with small orientation mismatch (c) schematic showing rotation of crystal lattice resulting from motion of disclination dipole along grain boundary [165] (insets in Figs. (a) and (b) are live FFT views of the images)

movement of disclination dipoles along grain boundaries is shown schematically in Figure 5.20(c) and considered to account for the formation of the misorientated crystals indicated by solid arrows in Figure 5.20(b). Therefore, the observation of amorphous phases in Figures 5.20(a) and 5.20(b) provides direct proof that amorphization is a consequence of plastic deformation and thus acts as a deformation

mechanism in copper with grain sizes less than ~13nm, i.e. after stage II. The mechanism of amorphization offers an explanation for the experimentally observed 'inverse Hall-Petch effect' (or 'negative Hall-Petch effect') [166, 167], which pertains to a decrease in material strength with decreasing grain size, contrary to the traditionally-accepted strengthening effect due to grain refinement, as described by the well-known Hall-Petch relation [51, 168]. The area of grain boundaries increases with decreasing grain size; hence, upon yielding, the volume fraction of atoms associated with the amorphized zones around grain boundaries is higher for material initially composed of smaller grains. According to the model by Nieh and Wadsworth [169], metals in an amorphous state are weaker than their crystalline counterparts. Hence, a lower strength is exhibited by metals with a finer grain structure. It should be mentioned that although several mechanisms (e.g. grain boundary migration [170], grain boundary diffusion creep [171], and atomic shuffling across grain boundaries [172]) have been proposed for accommodation of plastic deformation at grain boundaries, these are based on computer simulations. On the other hand, the present study has identified from experimental observations, amorphization as a deformation mechanism. The occurrence of amorphization is attributed to the high localized strain rate within the band structures generated by high speed deformation, which definitely exceeds $10^5 s^{-1}$ (based on the localized strain calculated in Section 5.4.3), since at low strain rates, deformation is accomplished through Coble creep [173, 174], i.e. diffusion of atoms along grain boundaries. This concurs with simulation results [104] revealing amorphization as a deformation mechanism at high strain rates. However, the exact strain rate at which amorphization takes place is difficult to assess from the current study and constitutes a topic for future investigation. From the perspective of energy conservation, the work associated with plastic deformation is partially

converted into heat, while the rest is stored in the amorphous structure. With a sudden temperature rise within localized bands, the amorphous structure may crystallize to lower its Gibbs free energy. However, this seems to be absent in present observations, and may be attributed to the rapid cooling of the bands by the surrounding zones, which results in insufficient time for crystallization of the amorphous structure to occur. Therefore, the amorphous phase formed during deformation is preserved in post-deformation samples, as shown in Figures 5.5(e), 5.18, 5.20 from the current work and in Figures 9-12 from a previous publication [175] (Figures 4.22-4.25 in Chapter 4 of this thesis). It is known that localized bands provide preferential sites for crack nucleation. However, no crack was found in the present study. It appears that the localized bands exhibit super-plastic behavior and such behavior is reasonable because the characteristics of the bands, which include grains as small as a few nanometers, high localized temperatures, as well as deformation characterized by amorphization of crystals, favors super-plastic flow.

5.4.5 Strengthening effect

The dislocation density and hardness (Figures 5.8 and 5.12 respectively) exhibit similar trends with strain rate, suggesting a close correlation between dislocation storage and material strength. Quantitatively, the yield strength (σ^y) can be calculated from the dislocation density (ρ) by the Taylor equation:

$$\sigma^y = \sigma_0 + \overline{\alpha} M^\sigma G b \rho^{1/2} \tag{5.26}$$

where σ_0, M^σ and G are respectively the friction stress, the Taylor factor (M^σ = 3 for polycrystalline materials) and the shear modulus. $\overline{\alpha}$ is a proportionality constant of the order of 10^{-1} and usually taken as 0.33. For copper, σ_0 = 20 MPa, G = 42 GPa, and

the yield strength calculated using equation (5.26) is shown in Figure 5.21. For comparison, the measured hardness has been converted to yield strength values (denoted by 'σ_H^y') by multiplying a factor of 10/3 and included in Figure 5.21. It is

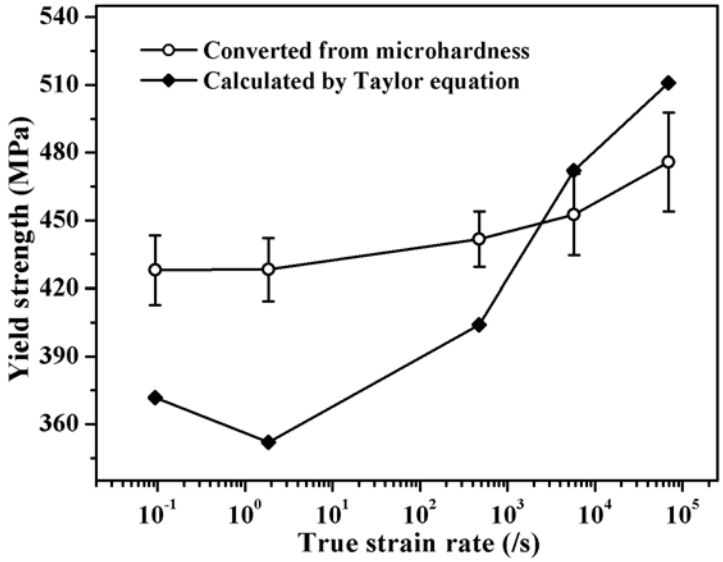

Figure 5.21 Variation of yield strength with strain rate

observed that the yield strengths obtained respectively from calculations based on dislocation density do not match very well with values derived from experimental measurements of hardness. The lower values of σ^y relative to σ_H^y at strain rates below 10^3 /s imply contributors to sample strength other than dislocations. With reference to TEM observations, it is reasonable to attribute such a discrepancy in yield strength to the presence of twin boundaries, which act as obstacles to dislocation motion and hence contribute to sample strengthening [99, 176]. Another factor leading to the mismatch in yield strength may be the variation of $\bar{\alpha}$. Experimental results by Schafler et al. [11] have shown that $\bar{\alpha}$ depends on the arrangement of dislocations and decreases from 0.28 to 0.17, when the dislocation arrangement parameter (M) decreases from 0.8 to 0.5. Figure 5.10 suggests that $\bar{\alpha}$ should be a variable rather than a constant for deformation at different strain rates. Therefore, adoption of a constant value of $\bar{\alpha}$ of 0.33 in the preceding calculations causes the

difference between the calculated and experimentally-measured (converted from hardness) yield strength values. An estimation of the value of $\bar{\alpha}$ for the samples studied was obtained by equating σ^{y} to $\sigma_H{}^{y}$ in equation (5.26). This generates values of $\bar{\alpha}$ that decrease from 0.4 to 0.3, which corresponds to an increase in the strain rate from $0.094s^{-1}$ to $6.9\times10^{4}s^{-1}$. The estimated values of $\bar{\alpha}$ herein are larger than those for single crystal copper in [11], but lie within the range of 0.26 to 0.46, which was reported for polycrystalline copper [177]. It should be emphasized that although the amorphous phase formed in samples deformed at the strain rate of $6.9\times10^{4}s^{-1}$ causes softening, as discussed in Section 5.4.4, it does not really weaken the bulk deformed material, because its volume is very small.

5.4.6 Considerations in application to metal forming

5.4.6.1 Zener-Hollomon parameter

This study has demonstrated that at 77K, material strength can be elevated through deformation by increasing the strain rate. However, at RT (see Chapter 4), high-strain-rate (~10^{5} /s) compression leads to significant softening of samples that are subjected to strains similar to that induced in the current study [175], owing to the occurrence of thermally activated recrystallization. This indicates that the resulting strength of a deformed material is affected by both strain rate and temperature. To describe the combined effects of strain rate and temperature on material strength, the Zener-Hollomon parameter *Z*, which incorporates strain rate and temperature in a single expression, is adopted. *Z* is defined as:

$$Z = \dot{\varepsilon}\exp(Q_b/RT) \tag{5.27}$$

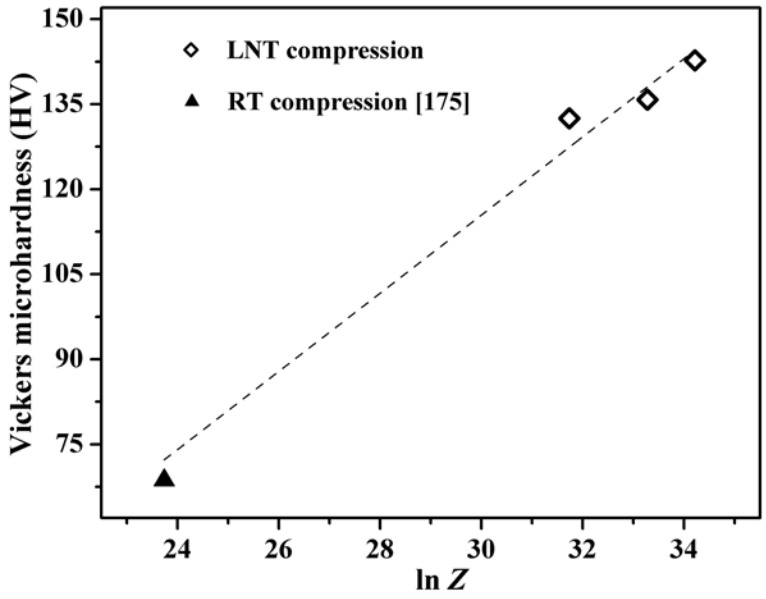

Figure 5.22 Variation of microhardness with the logarithm of Z

Figure 5.22 shows the variation of hardness with Z, using a logarithmic scale (values of Z corresponding to LNT deformation at strain rates lower than 10^2 /s are not indicted because of difficulty in determining the sample temperature, which is determined from Figure 5.15). It is noted that although the samples deformed respectively at LNT and RT consist of grains evolved via different mechanisms – the former are gradually transformed from dislocation cells while the latter experience nucleation and grain growth – their hardness values follow a common tendency, whereby an increase in Z causes an increase in material strength, as indicated by the dashed line. Z increases with a decrease in T; therefore, for samples deformed at a particular strain rate to a common final strain, a higher value of Z will be obtained if the sample undergoes more stages of deformation, i.e. a smaller amount of strain induced in each stage, leading to a lower sample temperature. This is why the copper samples deformed by multiple impacts at LNT [178] are stronger than those formed in this study by single impact to an equivalent final strain. From the tendency shown in Figure 5.22, it appears that material strength can be achieved by controlling the value

of *Z,* by varying the strain rate, the deformation environment temperature, and the strain induced during each stage of deformation.

5.4.6.2 Selection of strain rate

Nano-grained materials prepared by severe plastic deformation (SPD) techniques should posses a few key characteristics before they are utilized in engineering applications. These include: (i) uniform microstructure (ii) absence of cracks (iii) prevalence of high angle grain boundaries [12]. Although increasing the strain rate leads to enhanced storage of dislocations, as shown in Figure 5.9, inhomogeneity of deformation, typically represented by the presence of localized bands, emerges and causes significant non-uniformity of the microstructure when the strain rate increases to and above the order of 10^3/s. These localized bands provide potential sites for the nucleation of cracks. Therefore, it is suggested that strain rates in the order of 10^2/s be applied to deform samples. For SPD techniques, an important role of dislocations is to convert the boundaries of DCs and subgrains to high angle ones. To sequentially generate dislocations that contribute to an increase in the fraction of high angle boundaries, repetition of deformation should be undertaken. Since more dislocations are stored at higher strain rates for the same amount of strain, it is envisaged that fewer repetitions of deformation are needed if the strain rate is elevated from commonly applied values of around 1/s to the order of 10^2/s. In this study, the generation of nanograins within or in the vicinity of the localized deformation bands, as shown in Figures 5.5(d) and 5.5(e), implies a higher dislocation storage capacity at LNT than at RT, which corresponds to a saturation grain size of ~0.2 μm. Therefore, if multiple compressions [19, 75] applied at RT to generate ultrafine grains in copper

are carried out at LNT using a drop tester which is capable of imposing a strain rate in the order of 10^2/s, nano-sized grains would be produced.

5.5 Summary and conclusions

The aim of this study is to investigate how strain rate affects the resulting microstructure of metals deformed at LNT. Polycrystalline OFHC copper is selected as the material for investigation. Initially annealed copper samples are subjected to uniaxial single compression at strain rates of 10^{-2}-10^5 /s to a final common true strain of 2.3. The microstructure of deformed samples is characterized using TEM, XRD and DSC. For samples compressed at all strain rates, dislocation glide is the main mechanism for plastic deformation. Twinning also contributes to accommodation of plastic deformation, but the quantity of twins seems to drop dramatically when the strain rate exceeds 10^3 /s, possibly due to their break-up at higher strain rates. Amorphization is also a deformation mechanism and is activated in microstructures with grain sizes smaller than ~13nm; this offers an explanation for the 'inverse Hall-Petch effect'. Amorphous phases are only observed within localized bands in samples deformed at the highest strain rate of 6.9×10^4 /s. The occurrence of amorphization accompanies relative displacement between adjacent grains at grain boundaries, as well as rotation of individual grains to accommodate plastic deformation. It is characteristic of deformation at high strain rates. In general, the increase in strain rate leads to two effects – enhancement of dislocation storage and a rise in temperature. The former contributes to a reduction in the size of (sub)grains and an increase in the misorientation angle of dislocation cells, while the latter favors the initiation of recovery leading to a change in the character and arrangement of dislocations with strain rate. A threshold strain rate of $10^3 s^{-1}$ is identified for the formation of localized

deformation bands, which characterizes heterogeneity of deformation at high strain rates. These bands are composed of grains that are significantly smaller than those outside them, as well as those obtained at strain rates lower than $10^3 s^{-1}$. Under particular conditions, grains as small as several nanometers can be generated in the vicinity of these bands. Calculations show that the nanograins generated within or in the vicinity of localized bands in deformed samples are formed via RDRX. The strengthening of samples with increasing strain rate is attributed to the increase in dislocation density. However, the relationship between strength and dislocation density does not follow the Taylor equation closely. There are two reasons for this: (a) besides dislocations, deformation twins also contribute to sample strength; (b) the value of $\bar{\alpha}$ in the Taylor equation is not a constant for the samples studied, which are prepared at different strain rates, but varies between 0.3 and 0.4. The variation of sample strength with the Zener-Hollomon parameter Z shows that a higher value of Z corresponds to a higher strength of the deformed sample. Based on experimental results, it is suggested that a stain rate in the order of $10^2 s^{-1}$ should be adopted in SPD techniques to produce nanocrystalline metals.

Chapter 6 – Conclusions and Recommendations for future work

This study has focused on the effect of varying strain rate and ambient temperature on the resulting microstructure of materials deformed to large strains. The strain rates imposed differ in terms of order of magnitude and lie within a range of 10^{-3}-$10^{6}s^{-1}$; this is achieved by using different facilities, i.e. a Shimadzu Universal Testing machine, drop tester, split Hopkinson Pressure bar and gas gun. The ambient temperatures include room temperature (RT) and liquid nitrogen temperature (LNT), which are defined respectively as 298K and 77K. Oxygen-free high conductivity (OFHC) copper is used as the material for this study and subjected to uniaxial single compression. The microstructure of deformed materials is characterized using optical microscopy, TEM, XRD and DSC, whereas their mechanical properties are elicited predominantly by measurement of Vickers microhardness. In the event that the stress-strain behavior of deformed materials needs to be clarified, an Instron servo-hydraulic testing machine and a Split Hopkinson Pressure Bar are respectively utilized to characterize the quasi-static and dynamic responses.

6.1 Conclusions

In order to determine the temperature increase resulting from plastic deformation, which potentially affects evolution of microstructure, an approach that combines dynamic deformation, infrared (IR) photography and finite element simulation is established to determine the inelastic heat fraction (IHF) value of metals by uniaxial single compression. This is applied to OFHC copper. OFHC copper specimens are dynamically compressed and infrared thermographs captured at a rate of 1,000

images/s. FEM simulation of the deformation using ABAQUS is undertaken and the initial IHF value input adjusted until the computed average surface temperature, as well as the temperature distribution, matches the experimental data. An IHF value of 0.7 for OFHC copper is identified. It differs from the commonly-assumed value of 0.9, but is similar to values obtained experimentally by others for tension and compression [93]. This value is subsequently used to calculate the temperature rise and to analyze the associated microstructural change.

The microstructure and strength of OFHC copper deformed at RT and LNT are investigated. At RT, samples quasi-statically deformed via multiple forging and two-direction compression exhibit a saturation hardness value at 123.6 HV when a cumulative strain of 2.8 is imposed; further deformation by multiple forging causes substructure refinement. This saturation hardness value is consistent with that reported for samples subjected to ECAP and HPT, and corresponds to a microstructure comprising grains with a saturation size of 0.2-0.3 μm. Attempts at generating nano-grains through uniaxial single compression are made by deforming copper samples at RT and LNT. At RT, dynamically-deformed samples become softer, in contrast to quasi-statically deformed samples, which show a hardness close to the saturation value; this is the case for both initially hardened and annealed samples. The microstructure of impacted sample is characterized by the formation of deformation twins, either individually or intersecting one another, as well as equiaxed micron-sized grains. The temperature rise predicted using the modified J-C model in this study and an analysis of RX kinetics suggest that nucleated grains form during impact and subsequently grow, leading to softening of the material. At LNT, the hardness of quasi-statically-deformed samples is slightly higher than the saturation HV value. This is attributed to the suppression of dynamic recovery. Nano-scale twins are

observed, but the number is small compared to that produced by dynamic compression (10^3/s) at LNT [102]. The hardness of dynamically-deformed samples at LNT exceeds the saturation HV value by 16%, and the resulting microstructure includes nano and ultrafine grains, as well as shear bands with a composite structure of amorphous and crystalline phases, while twins are scarce. The nano-grains observed are deduced to have been evolved through rotational DRX, and a true strain exceeding 2.3 is required for formation of such fine grains. Formation of shear bands results from very high localized strains, and the variation in gain size between neighbouring bands is associated with the direction of shear that initiates the bands. The generation of nanograins implies a higher dislocation storage capacity at LNT than at RT.

The effect of strain rate on the resulting microstructure of materials subjected to uniaxial single compression at LNT is elaborated. For samples deformed at all strain rates, dislocation glide is the main mechanism for plastic deformation. Twinning also contributes to accommodation of plastic deformation, but the quantity of twins seems to drop dramatically when the strain rate exceeds 10^3 /s, possibly due to their break-up at higher strain rates. Amorphization is also a deformation mechanism and is only observed within localized bands in samples deformed at the highest strain rate of 6.9 $\times 10^4$ /s imposed. A difference in strain rate leads to a change in the density, character and arrangement of dislocations, as well as the size and configuration of dislocations cells/(sub)grains in deformed samples. At the lowest strain rate, of the order of 10^{-2} /s, dislocations are almost homogeneously distributed. When the strain rate is increased to the range of 10^0-10^5 /s, dislocations group and arrange themselves at the walls of dislocation cells. In general, the increase in strain rate leads to two effects – enhancement of dislocation storage and a rise in temperature. The former contributes

to a reduction in the size of (sub)grains and an increase in the misorientation angle of dislocation cells, while the latter favors the initiation of recovery leading to a change in the character and arrangement of dislocations with strain rate. A threshold strain rate of $10^3 s^{-1}$ is identified for the formation of localized deformation bands, which characterizes heterogeneity of deformation at high strain rates. These bands are composed of grains that are significantly smaller than those outside them, as well as those obtained at strain rates lower than $10^3 s^{-1}$. Under particular conditions, grains as small as several nanometers can be generated in the vicinity of these bands. A model that illustrates the initiation and propagation of an amorphous phase during deformation is proposed. It consists of three stages and offers an explanation for the 'inverse Hall-Petch effect'. The strengthening of samples with increasing strain rate is attributed to the increase in dislocation density. However, the relationship between strength and dislocation density does not follow the Taylor equation closely. There are two reasons for this: (a) besides dislocations, deformation twins also contribute to sample strength; (b) the value of $\bar{\alpha}$ in the Taylor equation is not a constant for the samples studied, which are prepared at different strain rates, but varies between 0.3 and 0.4. The strength of deformed samples exhibits the tendency to increase with the value of the Zener-Hollomon parameter, which captures both strain rate and temperature rise during deformation. From this study, it is suggested that a strain rate in the order of 10^2/s should be adopted in severe plastic deformation techniques to produce nanometer-sized grains.

6.2 Recommendations for future work

The work described in Chapter 3 resulted in determination of the IHF value for OFHC copper. However, the strain rate imposed is confined to the order of $10^3 s^{-1}$. As

discussed in Chapter 5 and in references [88, 150], the IHF value may vary with strain rate. Therefore, determination of IHF values corresponding to strain rates corresponding to other orders of magnitude deserves investigation. Figure 3.2 shows an experimental arrangement for determination of the IHF value for stain rates beyond $10^3 s^{-1}$, whereby the striker velocity can be increased and its mass reduced to maintain the same kinetic energy and achieve approximately similar final strains. To prevent tilting of a very fast but short striker before impact with the specimen, it could be adhesively connected to a light polymeric tube, as shown in Figure 6.1(a), which only emerges from the barrel just before complete compression of the sample.

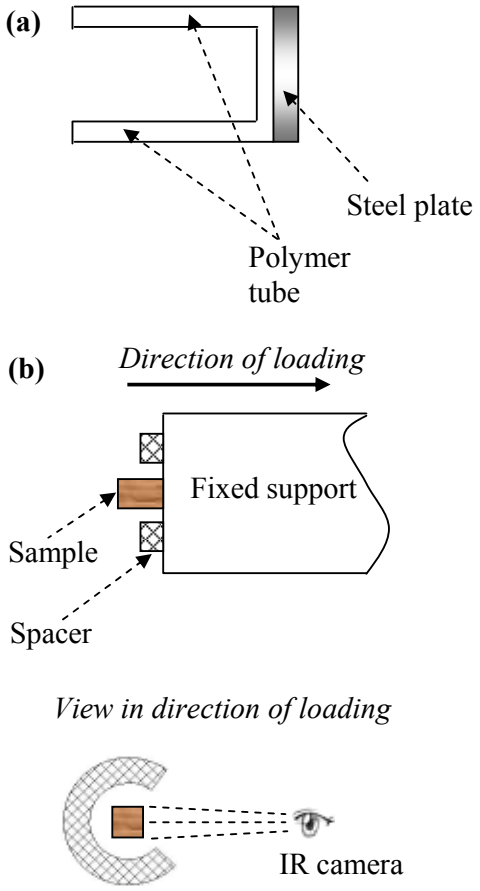

Figure 6.1 (a) Projectile for high strain rate compression (b) Spacer to limit amount of compression

For even higher strain rates, the velocity of the projectile can be increased, but its length cannot be decreased further. In such cases, a semi-annular circular spacer made of high-strength material can be mounted onto the fixed support, as shown in Figure 6.1(b). This will limit the deformation imposed on the specimen. The gap in the spacer facilitates capture of infra-red radiation emitted from the sample by an IR camera. In addition, the approach proposed in Chapter 3 can be extended for application to other materials to determine their IHF values.

Chapter 4 reports the observation of amorphous phases within the shear bands generated in materials deformed dynamically using a gas gun. However, the localized strain corresponding to initiation of this amorphous phase is unknown. This can be addressed by the use of a hat-shaped specimen deformed in a manner similar to that for the samples described in Chapter 4. The hat-shaped specimen was introduced in Section 2.3.1 of Chapter 2 and is reiterated here. Figures 6.2(a) and 6.2(b) are respectively configurations of the hat-shaped specimen before and after compression. The shear strain (γ) within the shear region is controlled by the spacer ring and can be calculated from:

$$\gamma = \frac{\delta}{w_s} \tag{6.1}$$

where w_s is the width of the shear region.

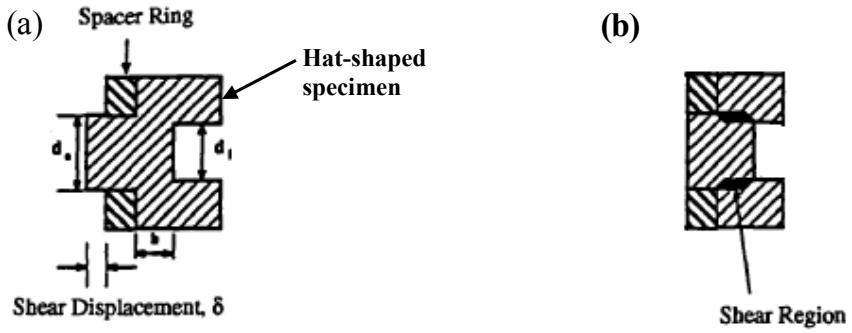

Figure 6.2 Hat-shaped specimen (a) before compression (b) after compression [66]

By adjusting the values of δ, strains of different magnitude can be induced in the region of shear. Examination of the microstructure there by TEM will lead to determination of the strain corresponding to initiation of amorphization, as well as an estimation of the temperature and strain rate at which amorphization takes place.

In Chapter 5, the suggestion of deforming material at strain rates in the order of $10^2 s^{-1}$ and ambient temperatures lower than RT was made. It is envisaged that nanograins can be generated, and the limit of a 0.2 μm minimum saturation grain size associated with conventional quasi-static severe plastic deformation (cSPD) of copper at RT be overcome. It is also expected that for a resulting microstructure characterised by a particular grain size, the adoption of dynamic deformation at a reduced ambient temperature will lead to a decrease in number of deformation repetitions required, compared to cSPD. These expectations could be verified via multiple compression at LNT using a drop tester. In this study, only the micro-hardness of the deformed material was measured because of the small sample size. Deformation of specimens using a drop tester can yield much larger samples and this facilitates testing for other mechanical properties, such as the yield strength, tensile strength, ductility and strain-rate sensitivity.

Stacking fault energy (SFE) is an important parameter that influences deformation mechanisms and the mechanical response of a material. For example, twins are formed in materials with low SFE, such as Cu-Zn alloys [179], to accommodate plastic deformation, while they are hardly observed in materials with high SFE, such as Al [180]. For Cu-Al alloys [99] with different concentration of Al, and thus different values of SFE, the alloys with a high SFE exhibit greater shock-strengthening and possess higher defect energy storage and dislocation density, compared to those with low SFE but deformed identically. Since amorphization has

been identified as a deformation mechanism, as discussed in Chapters 4 and 5, it is of interest to investigate whether the occurrence of amorphization depends on the SFE and whether parameters such as strain, strain rate and temperature at which amorphizaiton takes place change with SFE. This can be addressed by subjecting materials with different SFEs to the same deformation and comparing the resulting microstructures. Since the microstructure of pure copper has now been examined, future investigations could involve copper alloys (e.g. Cu-Zn, Cu-Al) with different SFE values, for comparison with results from the present study. Published SFE values for pure copper, as well as Cu-Zn and Cu-Al alloys are given in Table 6.1 for reference.

Table 6.1 Values of SFE for Cu, Cu-Al alloys and Cu-Zn alloys [176, 103]

Pure Cu [176]	Cu-Al alloys [176, 103]		Cu-Zn alloys [176]	
SFE (mJ/m^2)	Al content (Wt. Pct)	SFE (mJ/m^2)	Zn content (Wt. Pct)	SFE (mJ/m^2)
80	0.5 [103]	61	6	50
	1 [103]	50	8	38
	2 [176]	37	10	36
	2.2 [103]	25	16	23
	4.5 [176]	7	20	18
	8 [176]	4	24	16
			30	14

References

[1] Taylor GI, Proc R Soc Lond 1934; 145:362.

[2] Hirsch PB. Phil Mag 1962; 7:67.

[3] Zerilli FJ, Armstrong RW. J Appl Phys 1987; 61:1816.

[4] Follansbee PS, Kocks UF. Acta Metall 1988; 36:81.

[5] Bay B, Hansen N, Hughes DA, Kuhlmann-Wilsdorf D. Acta Metall Mater 1992; 40:205.

[6] Kuhlmann-Wilsdorf D, Hansen N. Scripta Metall Mater 1991; 25:1557.

[7] Estrin Y, Toth LS, Molinari A, Brechet Y. Acta Mater 1998; 46:5509.

[8] Kuhlmann-Wilsdorf D. Philos Mag A 1999; 79:955.

[9] Muller M, Zehetbauer M, Borbely A, Ungar T. Scripta Mater 1996; 35:1461.

[10] Ungar T, Zehetbauer M. Scripta Mater 1996; 35:1467.

[11] Schafler E, Simon K, Bernstorff S, Hanak P, Tichy G, Ungar T, Zehetbauer MJ. Acta Mater 2005; 53:315.

[12] Valiev RZ, Islamgaliev RK, Alexandrov IV. Prog Mater Sci 2000; 45:103.

[13] Kumar KS, Swygenhoven HV, Suresh S. Acta Mater 2003; 51:5743.

[14] Meyers MA, Mishra A, Benson DJ. Prog Mater Sci 2006; 51:427.

[15] Argon AS, Haasen P. Acta Mater 1993; 41:3289.

[16] Zehetbauer M, Seumer V. Acta Metall Mater 1993; 41:577.

[17] Zehetbauer M. Acta Metall Mater 1993; 41:589.

[18] Humphreys FJ, Prangnell PB, Bowen JR, Gholinia A, Harris C. Phil Trans R Soc Lond A 1999; 357:1663.

[19] Belyakov A, Sakai T, Miura H, Tsuzaki K. Philos Mag A 2001; 81:2629.

[20] Belyakov A, Tsuzaki K, Miura H, Sakai T. Acta Mater 2003; 51:847.

[21] Han BJ, Xu Z. Mater Sci Eng A 2007; 447:119.

[22] Han BJ, Xu Z. J Alloys Compd 2008; 457:279.

[23] Belyakov A, Tsuzaki K, Kimura Y, Kimura Y, Mishima Y. Mater Sci Eng A 2007; 456:323.

[24] Guo Q, Yan HG, Chen ZH, Zhang H. Mater Character 2007; 58:162.

[25] Kilmametov AR, Vaughan G, Yavari AR, LeMoulec A, Botta WJ, Valiev RZ. Mater Sci Eng A 2009; 503:10.

[26] Lugo N, Llorca N, Cabrera JM, Horita Z. Mater Sci Eng A 2008; 477:366.

[27] Lewandowska M, Swiatnicki W, Piatkowski A, Jasienski Z. J Microscopy 2006; 223:275.

[28] Su CW, Lu L, Lai MO. Mater Sci Eng A 2006; 434:227.

[29] Edalati K, Fujioka T, Horita Z. Mater Sci Eng A 2008; 497:168.

[30] Iwahashi Y, Wang JT, Horita Z, Nemoto M, Langdon TG. Scripta Mater 1996; 35:143.

[31] Alexandrov IV, Zhu YT, Lowe TC, Islamgaliev RK, Valiev RZ. NanoStruct Mater 1998; 10:49.

[32] Tsuji N, Saito Y, Utsunomiya H, Tanigawa S. Scripta Mater 1999; 40:795.

[33] Richert J, Richert M. Aluminium 1986; 62:604.

[34] Zhang Y, Wang JT, Cheng C, Liu JQ. J Mater Sci 2008; 43:7326.

[35] Schafler E, Kerber MB. Mater Sci Eng A 2007; 462:139.

[36] Tao NR, Lu K. J Mater Sci Technol 2007; 23**:**771.

[37] Christian JW, Mahajan S. Prog Mater Sci 1995; 39:1.

[38] Gottstein G. Metal Forming (Cold): Dislocation Mechanisms and Microstructural Changes; In: Encyclopedia of Materials Science and Technology, ISBN 0-08-0431526, pp 5394-5401.

[39] Hull D and Bacon DJ, Introduction to dislocations, Fourth Edition 2001.

[40] Prinz F, Argon AS. Acta Metall 1984; 32:1021.

[41] Nix WD, Gibeling JC, Hughes DA. Metall Trans 1985; 16A:2215.

[42] Kocks UF. J Engng Mater Technol 1976; 98:76.

[43] Mecking H, Kocks UF. Acta Metall 1981; 29:1865.

[44] Estrin Y, Mecking H. Acta Metall 1984; 32:57.

[45] Klepaczko JR, Chiem CY. J Mech Phys Solids 1986; 34:29.

[46] Zehetbauer M, Ungar T, Kral R, Borbely A, Schafler E, Ortner B, Amenitsch H, Bernstorff S. Acta Mater 1999; 47:1053.

[47] Zhong Y, Yin F, Sakaguchi T, Nagai K, Yang K. Acta Mater 2007; 55:2747.

[48] Artz E. Acta mater 1998; 46:5611.

[49] Birringer R. Mater Sci Eng A 1989; 117:33.

[50] Palumbo G, Thorpe SJ, Aust KT., Scripta Metall Mater 1990; 24:1347-1350.

[51] Hall EQ, Proc Soc London 1951; B64:747

[52] Ashby MF. Philos Mag 1982; A46:737.

[53] Yamakov V, Wolf D, Phillpot SR, Mukherjee AK, Gleiter H. Nature Materials 2002;1: 1.

[54] Gleiter H., nanocrystalline materials, Prog Mater Sci 1989; 33:223-315.

[55] Suryanarayana C. Orog mater Sci 2001; 46:1-184.

[56] Eckert J, Holzer JC, Krill ⅢCE, Johnson WL., J Mater Res 1992; 7:1751.

[57] Erb U., Nanostruct Mater 1995; 6:533-538.

[58] Lu L., Shwaiger R., Shan ZW, Dao M, Lu K., Suresh S., Acta Mater 2005; 53:2169.

[59] Shen YF, Lu L, Lu QH, Jin ZH, Lu K., Scripta Mater 2005; 52:989.

[60] Lu K., Mater Sci Eng 1996; R16: 161-221.

[61] Scott MG, Amorphous metallic alloys, In: Luborsky FE; 1988, p. 144.

[62] Valiev RZ, Ivanisenko YuV, Rauch EF, Baudelet B. Acta Mater 1996; 44:4705.

[63] Korznikov AV, Ivanisenko YuV, Laptionok DV, Safarov IM, Pilyugin VP, Valiev RZ. Nanostructured Mater 1994; 4:159.

[64] Stolyarov VV, Latysh VV, Shundalov VA, Salimonenko DA, Islamgaliev RK, Valiev RZ. Mater Sci Eng 1997: A234-236:339.

[65] Molodova X, Gottstein G, Winning M, Hellmig RJ. Mater Sci Eng A 2007; 460-461:204.

[66] Andrade U, Meyers MA, Vecchio KS, Chokshi AH. Acta Metall Mater 1994; 42:3183.

[67] Kad BK, Gebert JM, Perez-Prado MT, Kassner ME, Meyers MA. Acta Mater 2006; 54:4111.

[68] Meyers MA, Subhash G, Kad BK, Prasad L. Mech Mater 1994; 17:175.

[69] Mishra A., Kad BK, Gregori F, Meyers MA. Acta Mater 2007; 55:13.

[70] Kiritani M, Sota T, Tawara T, Arimura H, Yasunaga K, Matsukawa Y, Komatsu M. Rad Eff and Defects in Solids 2002; 157:53.

[71] Kiritani M, Satoh Y, Kizuka Y, Arakawa K, Ogasawara Y, Arai S, Shimomura Y. Philos Mag Letters 1999; 79:797.

[72] Kiritani M, Yasunaga K, Matsukawa Y, Komatsu M. Rad Eff and Defects in Solids 2002; 157:3.

[73] Tawara T, Matsukawa Y, Kiritani M. Mater Sci Eng A 2003; 350:70.

[74] Yasunaga K, Iseki M, Kiritani M. Mater Sci Eng A 2003; 350:76.

[75] Kobayashi C, Sakai T, Belyakov A, Miura H. Philos Mag Letters 2007; 87:751.

[76] Han K, Walsh RP, Ishmaku A, Toplosky V, Brandao L, Embury JD. Philos Mag 2004; 84:3705.

[77] Leprince-Wang Y, Han K, Huang Y, Yu-Zhang K. Mater Sci Eng 2003; 351:214.

[78] Lu L, Shen YF, Chen XH, Qian LH, Lu K. Science 2004; 304:422.

[79] Li WL, Tao NR, Lu K. Scripta Mater 2008; 59:546.

[80] Tao NR, Lu K. Scripta Mater 2009; 60:1039.

[81] Langford G., Cohen M., Trans ASM 1969; 62-623.

[82] Meyers MA, Dynamic Behavior of Materials, John Wiley & Sons, Inc., New York, 1994.

[83] McQueen RG, Marsh SP, Taylor JM, Frits JN, Carter WJ. High-Velocity Impact Phenomena, Academic Press, New York, 1970.

[84] Chaboche JL. Continuum thermomechanics, 87-100, 2000.

[85] Kay G. US department of Transportation, Federal Aviation Administration, September, 2003.

[86] Poizat C, Campagne L, Daridon L, Ahzi S, Husson C, Merle L. J Forming Processes 2005; 8:29.

[87] Woznica K, Klepaczko JR. J Mechanical Sci 2003; 45:359.

[88] Ravichandran G, Roaskis AJ, Hodowany J, Rosakis P. 2002 American Institute of Physics 0-7354- 0068-7/02.

[89] Thomas JE, Kinast J, Turlapov A. Virial Theorem and Universality in a Unitary Fermi Gas. PRL 95, 120402 (2005).

[90] Pettifor DG. The virial theorem and binding in transition metals. J. Phys. F: Met. Phys. 1 L62-L66.

[91] Lassila DH, Shen T, Cao BY, Meyers MA. Metall and Mater Trans A 2004; 35A: 2729.

[92] Zubelewicz A, Zurek AK, Potocki ML. J Phys IV France 2006; 134:23.

[93] Macdougall D. Exp Mech 2000; 40:298.

[94] Bouferra R, Pron H, Henry JF, Bissieux C, Beaudoin JL. J Thermal Sci 2005; 44:115.

[95] Banerjee B. ArXiv:cond-mat/0512466 v1, 19 Dec 2005.

[96] Finkbeiner JR, Dunlap PH, Steinetz BM. NASA/TM-2004-213204, AIAA-2004-3891.

[97] Ribárik G, Gubicza J, Ungár T. Mater Sci Engng A 2004; **387-389:**343.

[98] Wright RN, Mikkola DE. Mater Sci Engng 1982; **53:**273.

[99] Rohatgi A, Vecchio KS, Gray III GT. Acta mater 2001; **49:**427.

[100] Johnson GR, Cook WH. Engng Fracture Mech 1985; **21:**31.

[101] Zhang B, Shim VPW. Intern J Impact Engng 2010; **37:**50.

[102] Qin EW, Lu L, Tao NR, Lu K. Scripta Mater 2009; **60:** 539.

[103] Zhang Y, Tao NR, Lu K., Scripta Mater 2009; **60:** 211.

[104] Wu HA, Soh AK, Wang XX, Sun ZH. Key Engng Mater 2004; **261-263:** 33.

[105] Batra RC, Kim CH. Intern. J. plasticity 1992; **8:** 425.

[106] Nesterenko VF, Meyers MA, LaSalvia JC, Bondar MP, Chen YJ, Lukyanov YL. Mater Sci Eng A 1997; 229:23.

[107] Holman JP, White PRS. Heat Transfer, *7th edition;* p. 137.

[108] Kida M, Kikuchi Y, Takahashi O, Michiyoshi I. J Nuclear Sci Tech 1981; 18(7):501.

[109] Incropera F, DeWitt D. Fundamentals of Heat and Mass Transfer, 3rd edition, 1990, John Wiley & Sons, New York.

[110] Lienhard JH. A Heat Transfer Textbook, 1981, Prentice Hall.

[111] Marquardt ED, Le JP, Radebaugh R. Cryogenic material properties database. In: 11th international cryocooler conference 2000, edited by Ross RG.

[112] Steinberg DJ, Cochran SG, Guinan MW. J Appl Phys 1980; 51:1498.

[113] Zocher MA, Maudlin PJ, Chen SR, Flower-Maudlin EC. In: Proc, European Congress on Computational Methods in Applied Sciences and Engineering 2000; Barcelona, Spain.

[114] Surholt T, Herzig C. Acta Mater 1997; 45:3817.

[115] Murr LE. Interfacial phenomena in metals and alloys. Reading (MA): Addison-Wesley; 1975.

[116] Xiao GH, Tao NR, Lu K. Mater Sci Engng A 2009; 513-514:13.

[117] Warren BE, Averbach BL. J Appl Phys 1952; 23:1059.

[118] Williamson GK, Hall WH. Acta Metall 1953; 1:22.

[119] Wilson AJC. Proc Phys Soc 1962; 80:286.

[120] Ungar T, Borbely A. Appl Phys Lett 1996; 69:3173.

[121] Ungar T, Tichy G. Phys Stat Sol (a) 1999; 171:425.

[122] Ungar T, Dragomir I, Revesz A, Borbely A. J Appl Cryst 1999; 32:992.

[123] Ungar T, OTT S, Sanders PG, Borbely A, Weertman JR. Acta Mater 1998; 46:3693.

[124] Balogh L, Gubicza J, Hellmig RJ, Estrin Y, Ungar T. Z Kristallogr Suppl 2006; 23:381.

[125] Taupin D. J Appl Cryst 1973; 6:266.

[126] Jenkins R, Snyder RL. Introduction to Powder Diffractometry.

[127] Dong YH, Scardi P. J Appl Cryst 2000; 33:184.

[128] Ribarik G, Ungar T, Gubicza J. J Appl Cryst 2001; 34:669.

[129] Soleimanian V, Aghdaee SR. Powder Diffraction 2008; 23:41.

[130] Louer D. Defect and Microstructure Analysis by Diffraction, ed by Snyder RL, Fiala J, Bunge HJ; 1999. p. 673.

[131] Langford JI, Cernik RJ, Louer D. J Appl Cryst 1991; 24:913.

[132] Louer D, Langford JI. J Appl Cryst 1988; 21:430.

[133] Delhez R, De Keijser TH, Mittemeijer EJ. Fresenius Z Anal Chem 1982; 312:1.

[134] Di Rocco HO, Iriarte DI, Pomarico J. Appl Spectroscopy 2001; 55:822.

[135] Langford JI. Defect and Microstructure Analysis by Diffraction, ed by Snyder RL, Fiala J, Bunge HJ; 1999. p. 59.

[136] Caglioti G, Paoletti A, Ricci FP. Nuclear Instruments 1958; 3:223.

[137] Stokes AR. Proc Phys Soc Lond 1948; 61:382.

[138] Balzar D. Defect and Microstructure Analysis by Diffraction, ed by Snyder RL, Fiala J, Bunge HJ; 1999. p. 94.

[139] Schafler E, Zehetbauer M, Ungar T. Mater Sci Eng A 2001; 319-321:220.

[140] Wilkens M. Phys Status Solidi 1970; 2:359.

[141] Hughes DA, Hansen N. Metall Trans A 1993; 24A: 2021.

[142] Gubicza J, Nam NH, Balogh L, Hellmig RJ. J Alloys Compd 2004; 378:248.

[143] Rohatgi A, Vecchio KS. Mater Sci Eng A 2002; 328:256.

[144] Mandal D, Baker I. Scripta Metall Mater 1995; 33:645.

[145] Liu L, Baker I. Scripta Metall Mater 1993; 28:197.

[146] Cao WQ, Gu CF, Pereloma EV, Davies CHJ. Mater Sci Eng A 2008; 492:74.

[147] Kennedy C, Murr LE. Mater Sci Eng A 2002; 325:131.

[148] Li YS, Tao NR, Lu K. Acta Mater 2008; 56:230.

[149] Wang K, Tao NR, Liu G, Lu J, Lu K. Acta Mater 2006; 54:5281.

[150] Hodowany J, Ravichandran G, Rosakis AJ, Rosakis P. Experimental Mechanics 2000; 40:113.

[151] Chao YY, Varma SK. Scripta Metall 1990; 24:1665.

[152] Chao YY, Varma SK. J Mater Sci Letters 1991; 10:630.

[153] Thiagarajan S, Varma SK. J Mater Sci Letters 1992; 11:692.

[154] Sevillano JG, Aernoudt E. Mater Sci Eng 1987; 86:35.

[155] Holt DL. J Appl Phys 1970; 41:3137.

[156] Staker MR, Holt DL. Acta Metall 1972; 20:569.

[157] Orowan E. Dislocation is Metals, Edited by Cohen M; Met Soc AIME, Warrendale, PA; 1954, p. 152.

[158] Korbel A, Swiatkowski K. Met Sci J 1972; 6:60.

[159] Li M, Chu WY, Gao KW, Qiao LJ. J Phys Condens Matter 2003; 15:3391.

[160] Wang BF, Yang Y. Mater Sci Eng A 2008; 473:306.

[161] Chichili DR, Ramesh KT, Hemker K. Acta Mater 1998; 46:1025.

[162] Van Swygenhoven H, Spaczer M, Caro A; Acta Mater 1999; 47:3117.

[163] Sanders PG, Eastman JA, Weertman JR. Acta Mater 1997; 45:4019.

[164] Schiotz J, Di Tolla FD, Jacobsen KW. Nature 1998; 391:561.

[165] Ovid'ko IA. Science 2002; 295:2386.

[166] Chokshi AH, Rosen A, Karch J, Gleiter H. Scripta Metall 1989; 23:1679.

[167] Conrad H, Narayan J. Scripta Mater 2000; 42:1025.

[168] Petch NJ. J Iron Steel Inst 1953; 174:25.

[169] Nieh TG, Wadsworth J. Scripta Metall 1991; 25:955.

[170] Hasnaoui A, Van Swygenhoven H, Derlet PM. Phys Rev B 2002; 66:184112.

[171] Yamakov V, Wolf D, Phillpot SR, Gleiter H. Acta Mater 2002; 50:61.

[172] Van Swygenhoven H, Derlet PM. Phys Rev B 2001; 64:224105.

[173] Cai B, Kong QP, Lu L, Lu K. Scripta Mater 1999; 41:755.

[174] Cai B, Kong QP, Cui P, Lu L, Lu K. Scripta Mater 2001; 45:1407.

[175] Zhang B, Shim VPW. Philos Mag 2010; 90:3293.

[176] Rohatgi A, Vecchio KS, Gray GT Ⅲ. Metall Mater Trans A 2001; 32A:135.

[177] Biermann H, Ungar T, Pfannenmuller T, Hoffmann G, Borbely A, Mughrabi H. Acta Metall Mater 1993; 41:2743.

[178] Zhao WS, Tao NR, Guo JY, Lu QH, Lu K. Scripta Mater 2005; 53:745.

[179] Danaf EE, Kalidindi SR, Doherty RD. Metall Mater Trans A 1999; 30A:1223.

[180] Gray III GT. Acta Metall 1988; 36:1745.

Appendix A

TEM images

(A1) Multiple forged samples (cumulative strain $\sum\varepsilon = 27$)

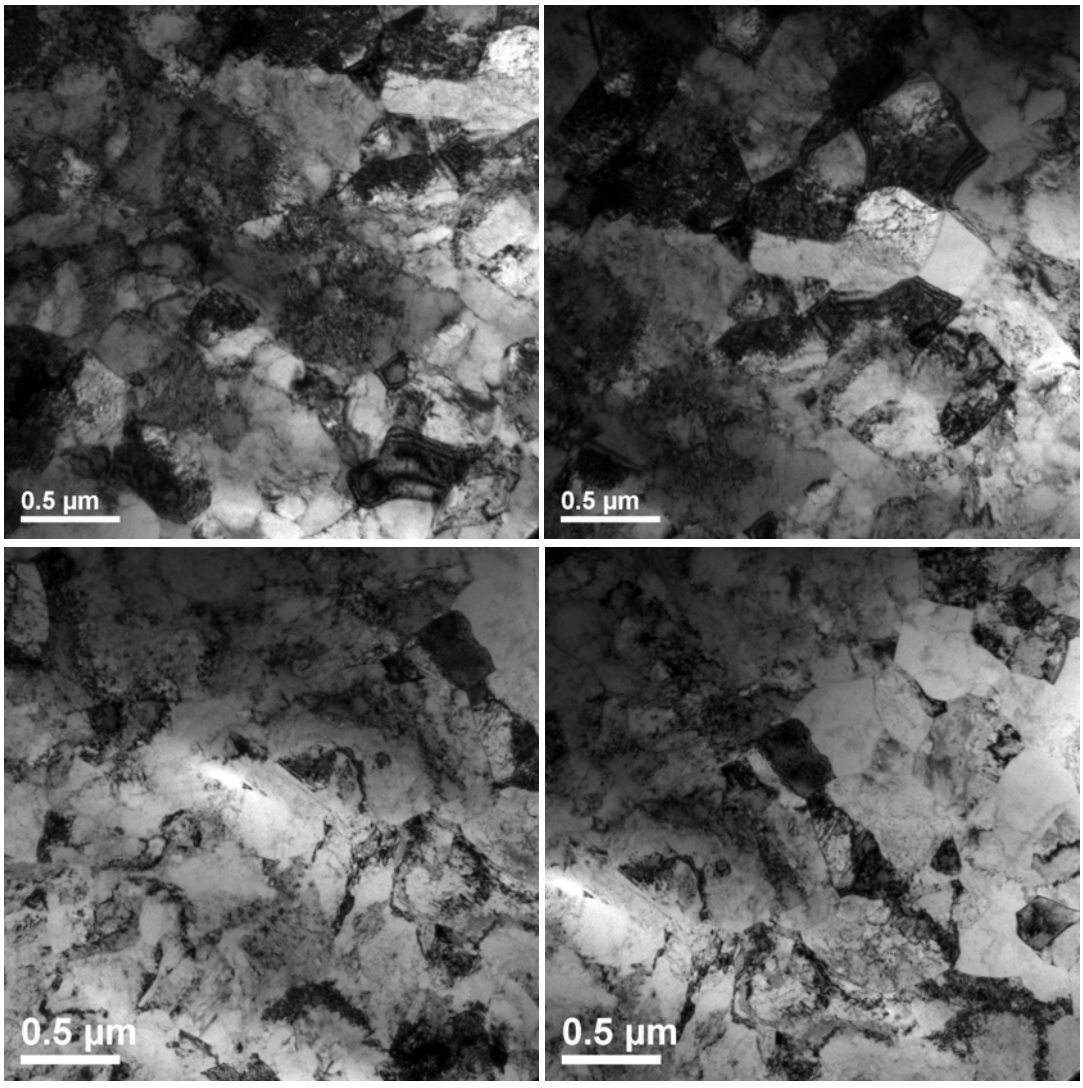

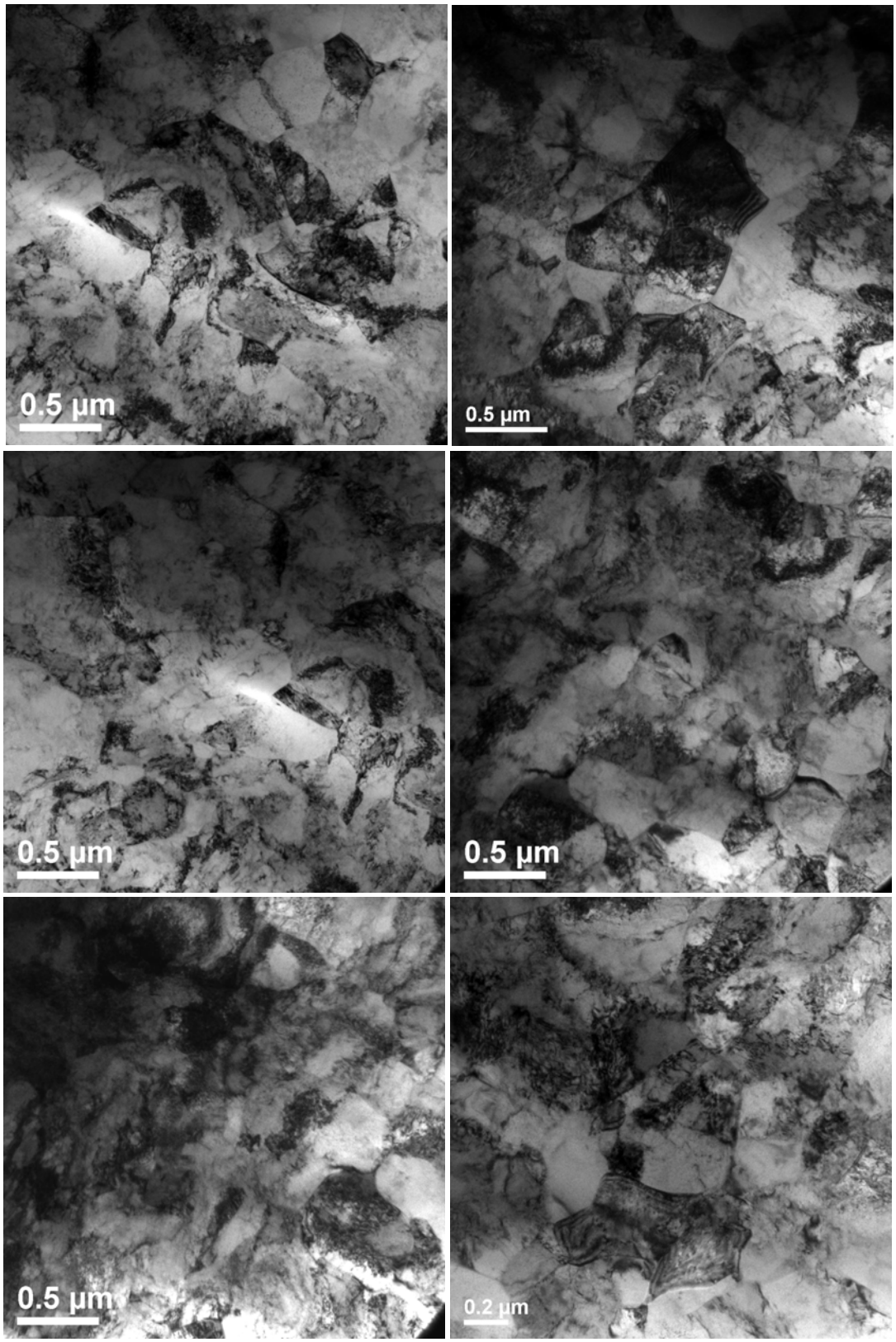
0.5 µm
0.5 µm
0.5 µm
0.5 µm
0.5 µm
0.2 µm

(A2) Multiple forged samples (cumulative strain $\sum\varepsilon = 12.5$)

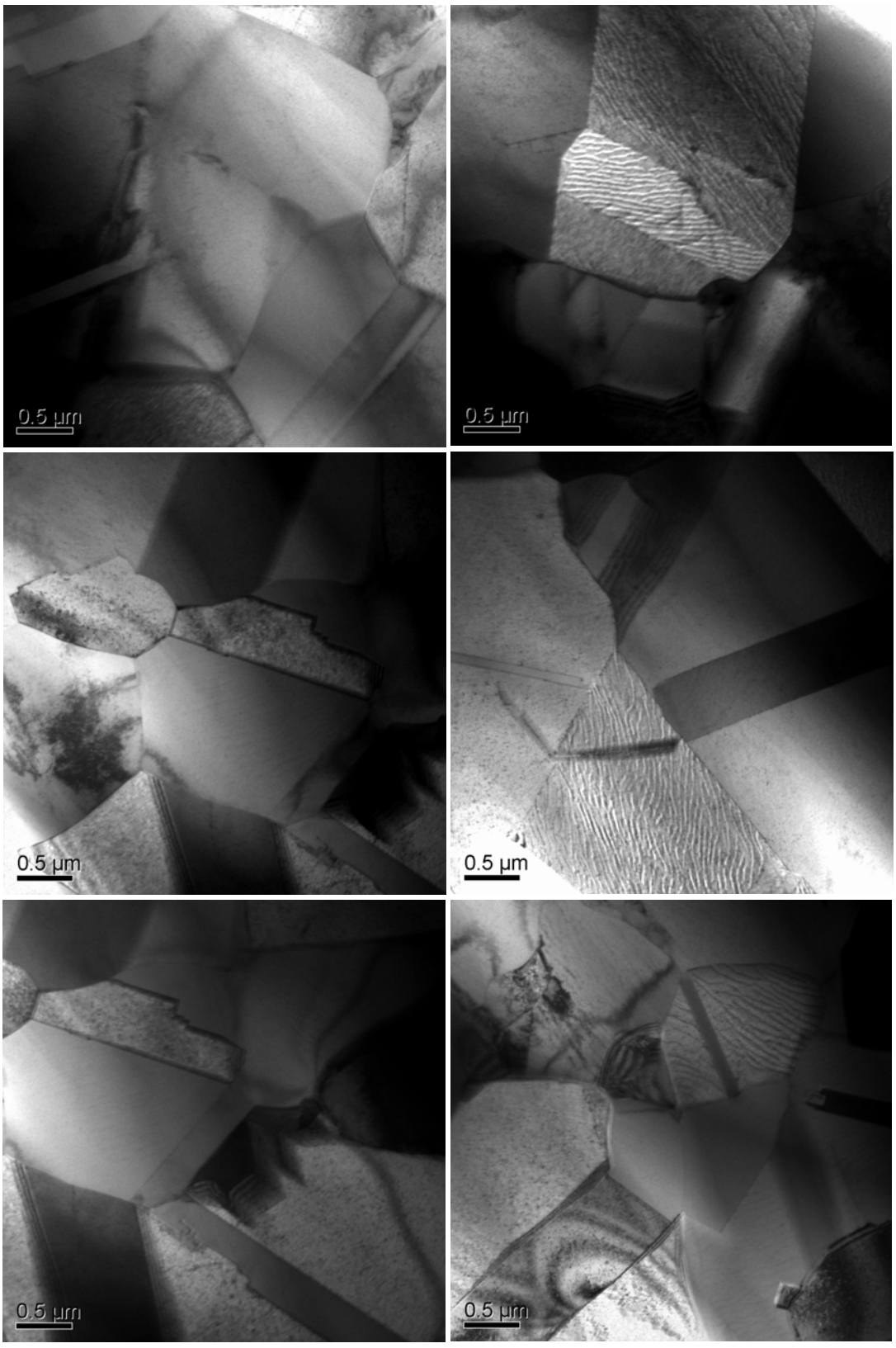

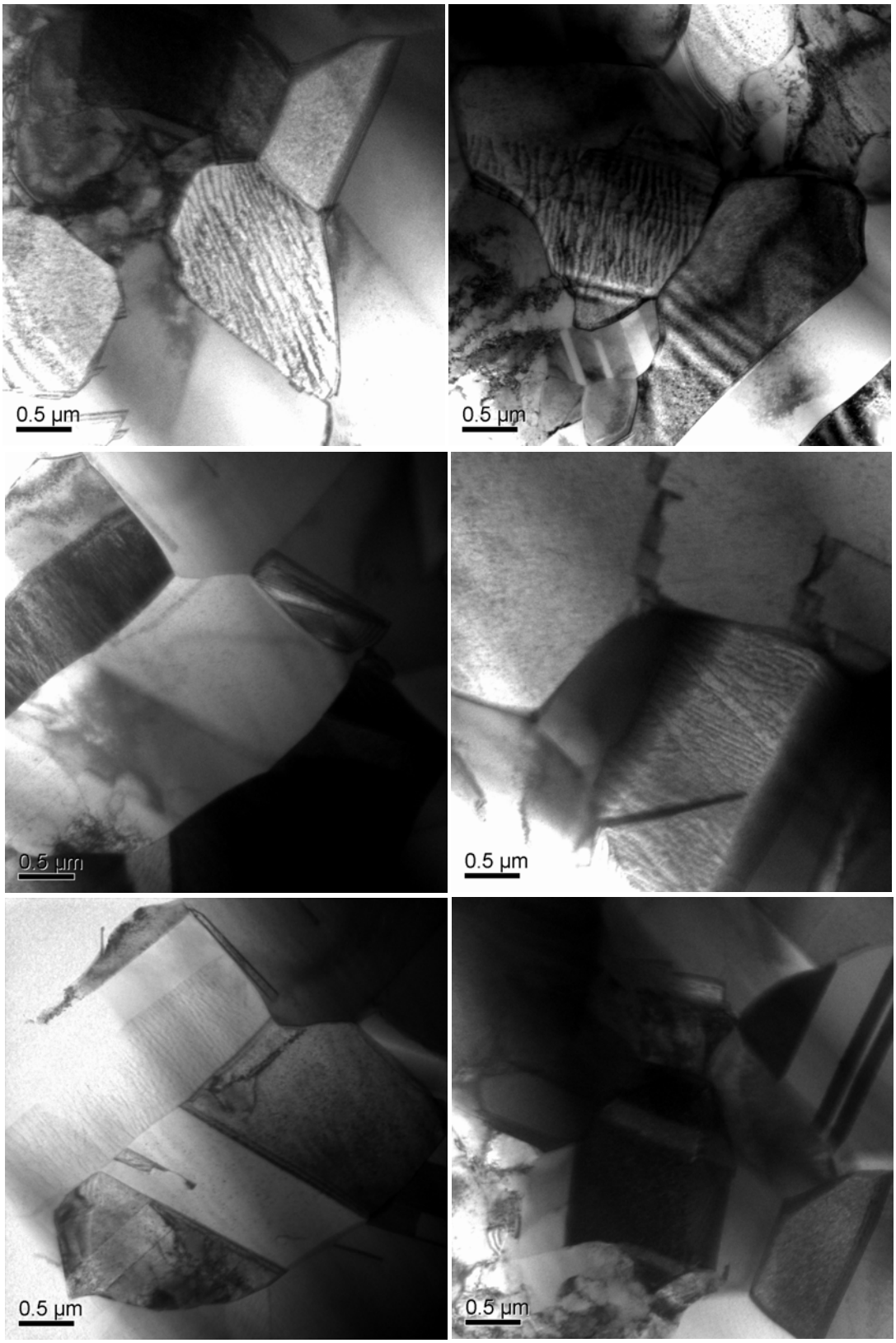
0.5 µm
0.5 µm
0.5 µm
0.5 µm
0.5 µm
0.5 µm

(A3) Samples subjected to LNT compression on Shimadzu Universal Testing Machine ($\dot{\varepsilon} = 9.4 \times 10^{-2} s^{-1}$)

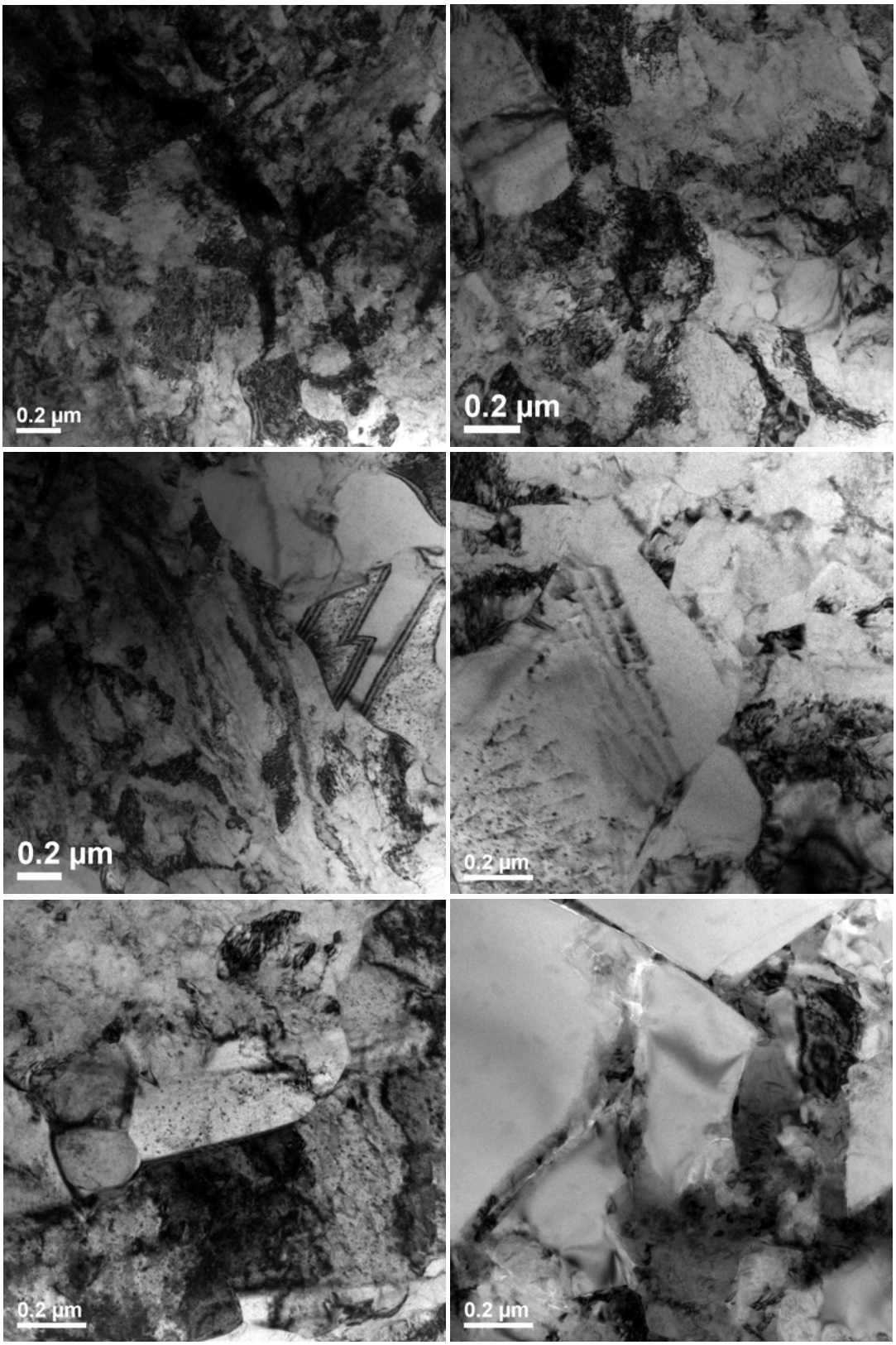

(A4) Samples subjected to LNT compression on Shimadzu Universal Testing Machine ($\dot{\varepsilon} = 1.9s^{-1}$)

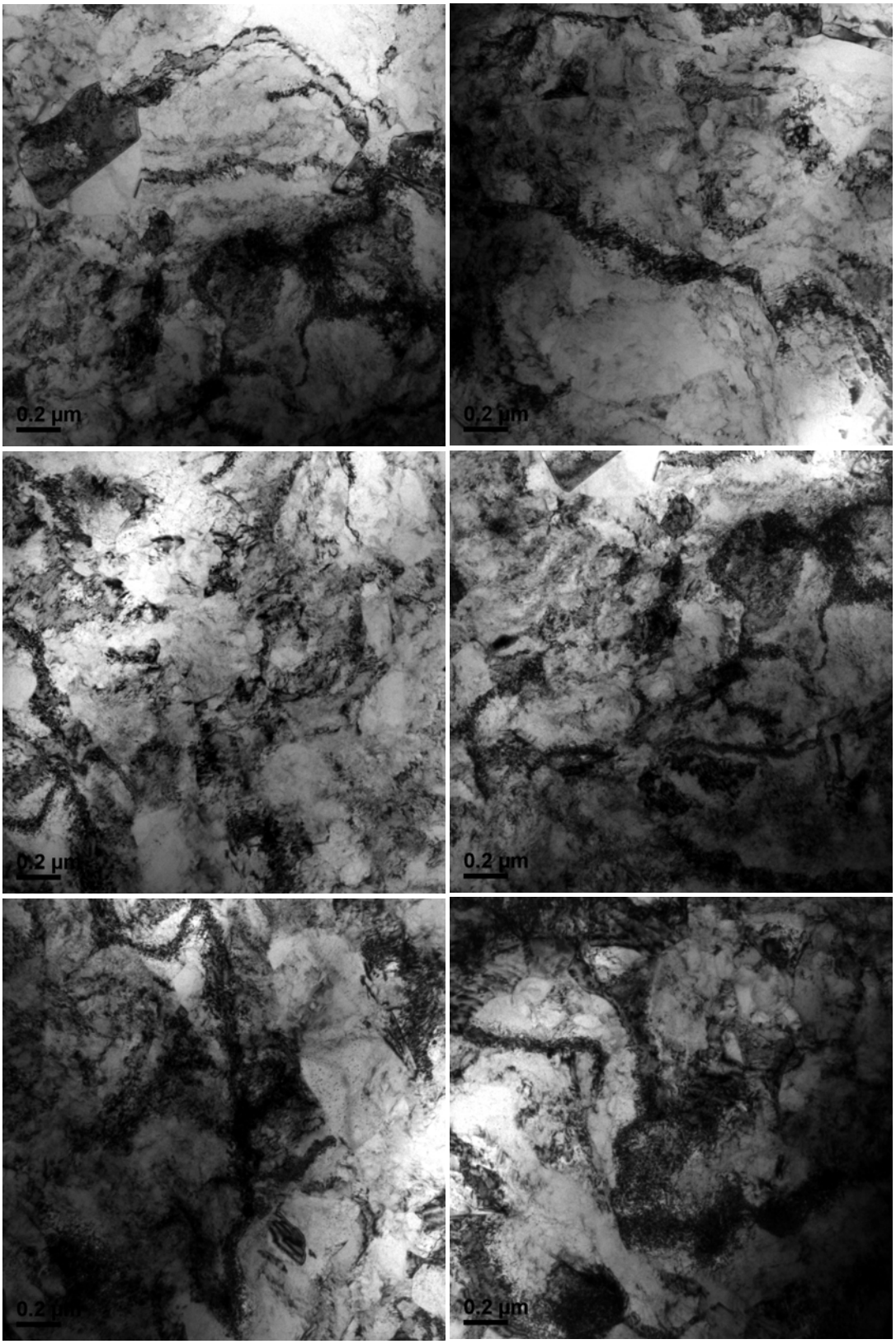

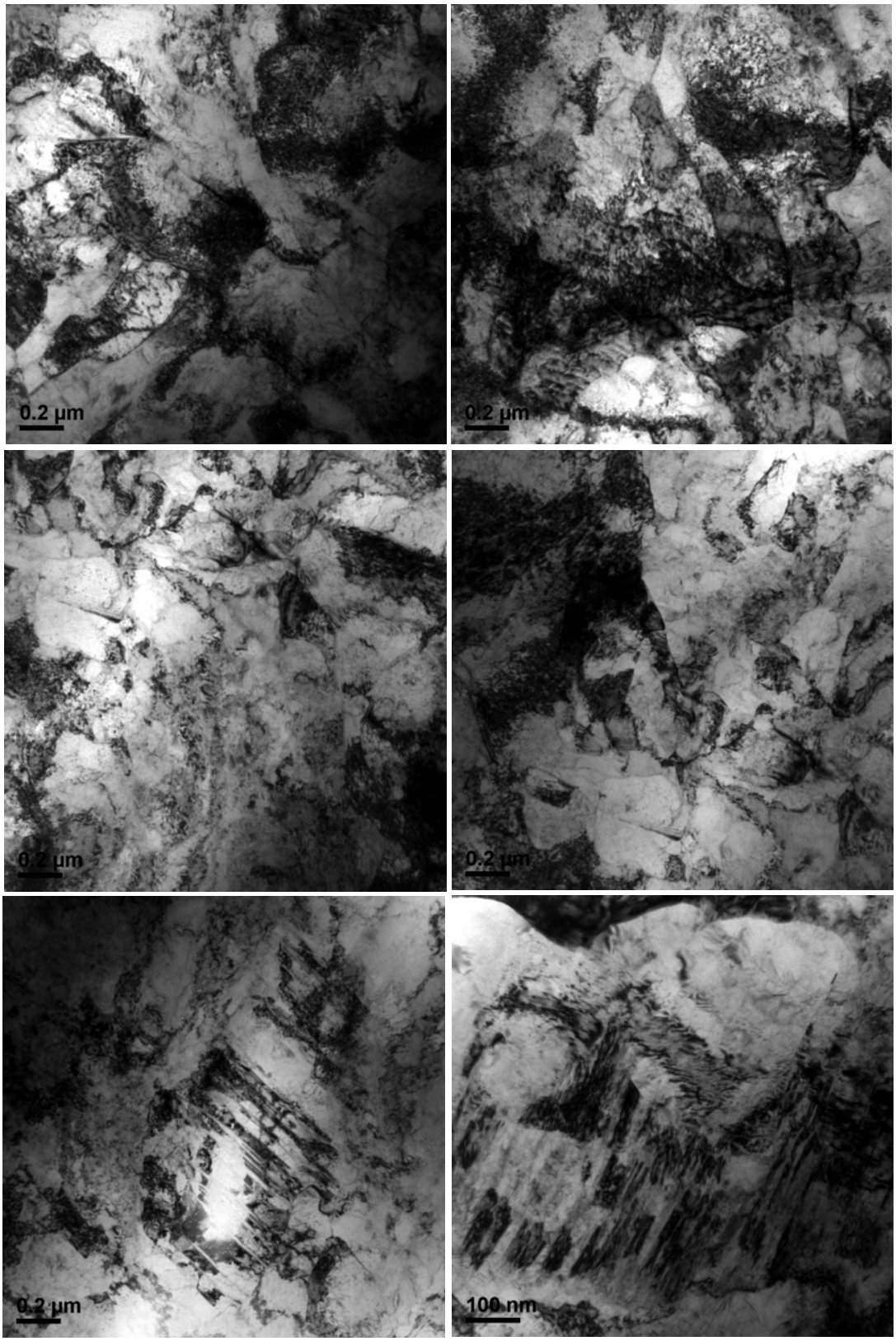
0.2 µm
0.2 µm
0.2 µm
0.2 µm
0.2 µm
100 nm

(A5) Samples subjected to LNT compression on a drop tester ($\dot{\varepsilon} = 4.8 \times 10^{2} s^{-1}$)

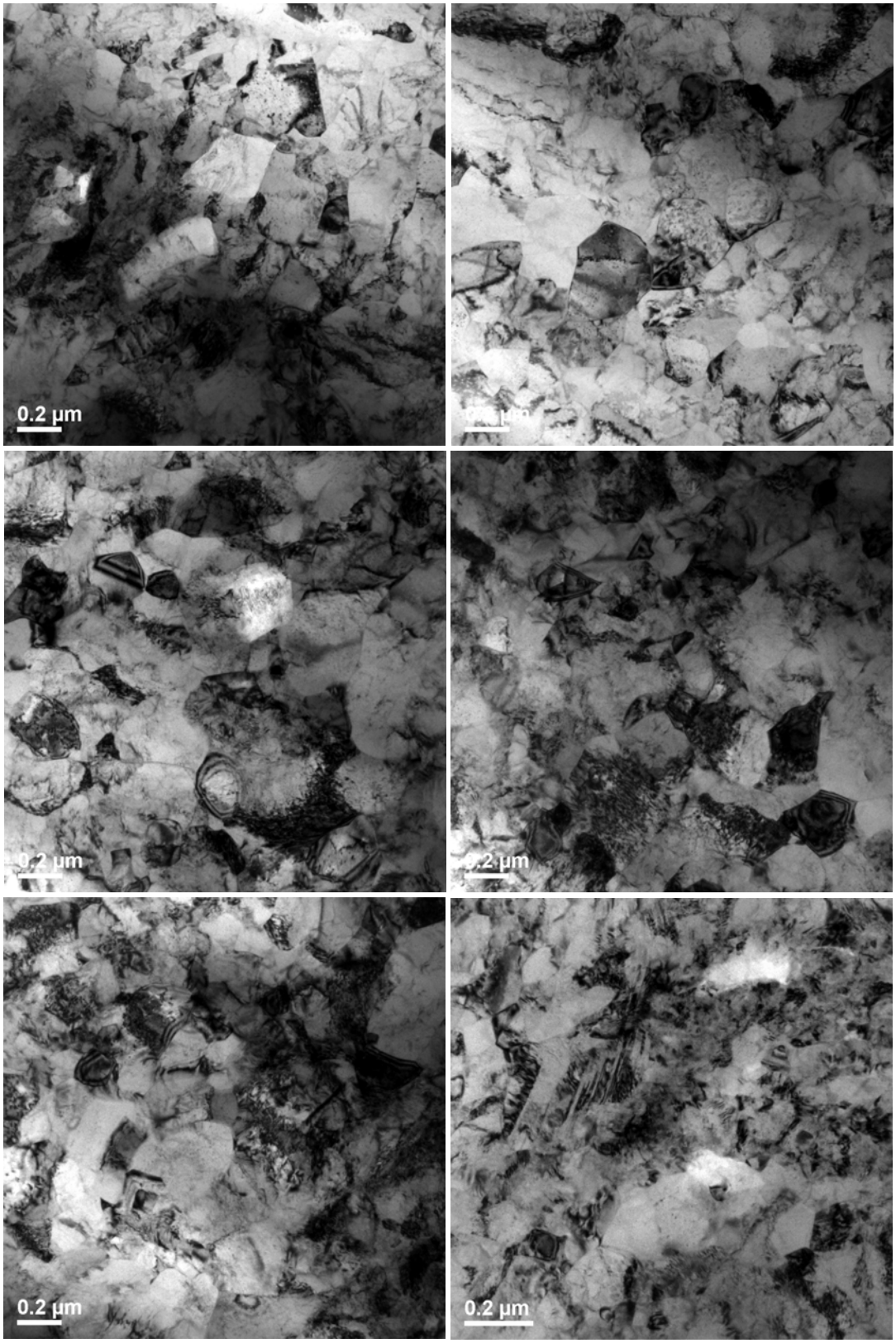

(A6) Samples subjected to LNT compression on a Split Hopkinson Pressure Bar

($\dot{\varepsilon} = 5.7 \times 10^{3} s^{-1}$)

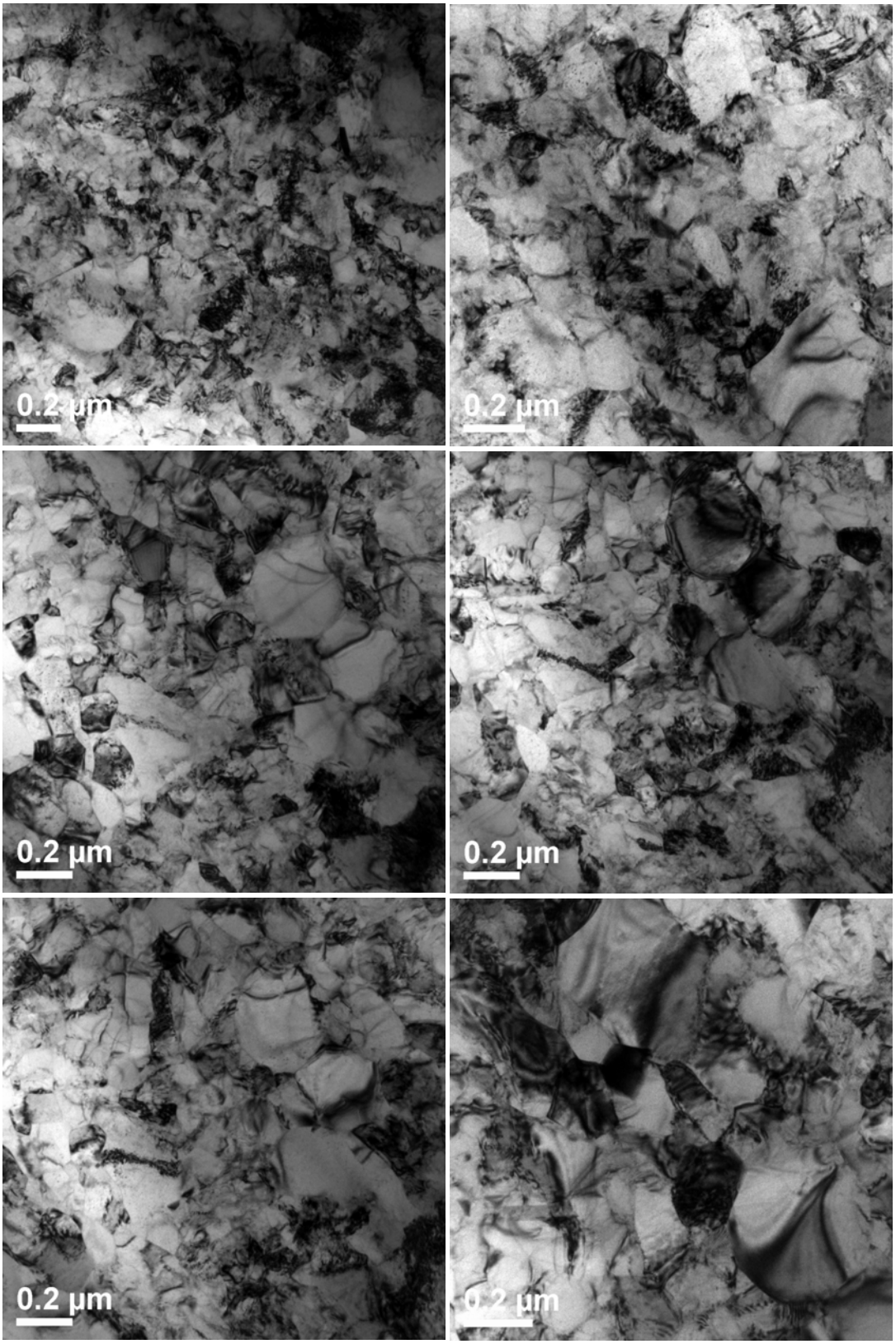

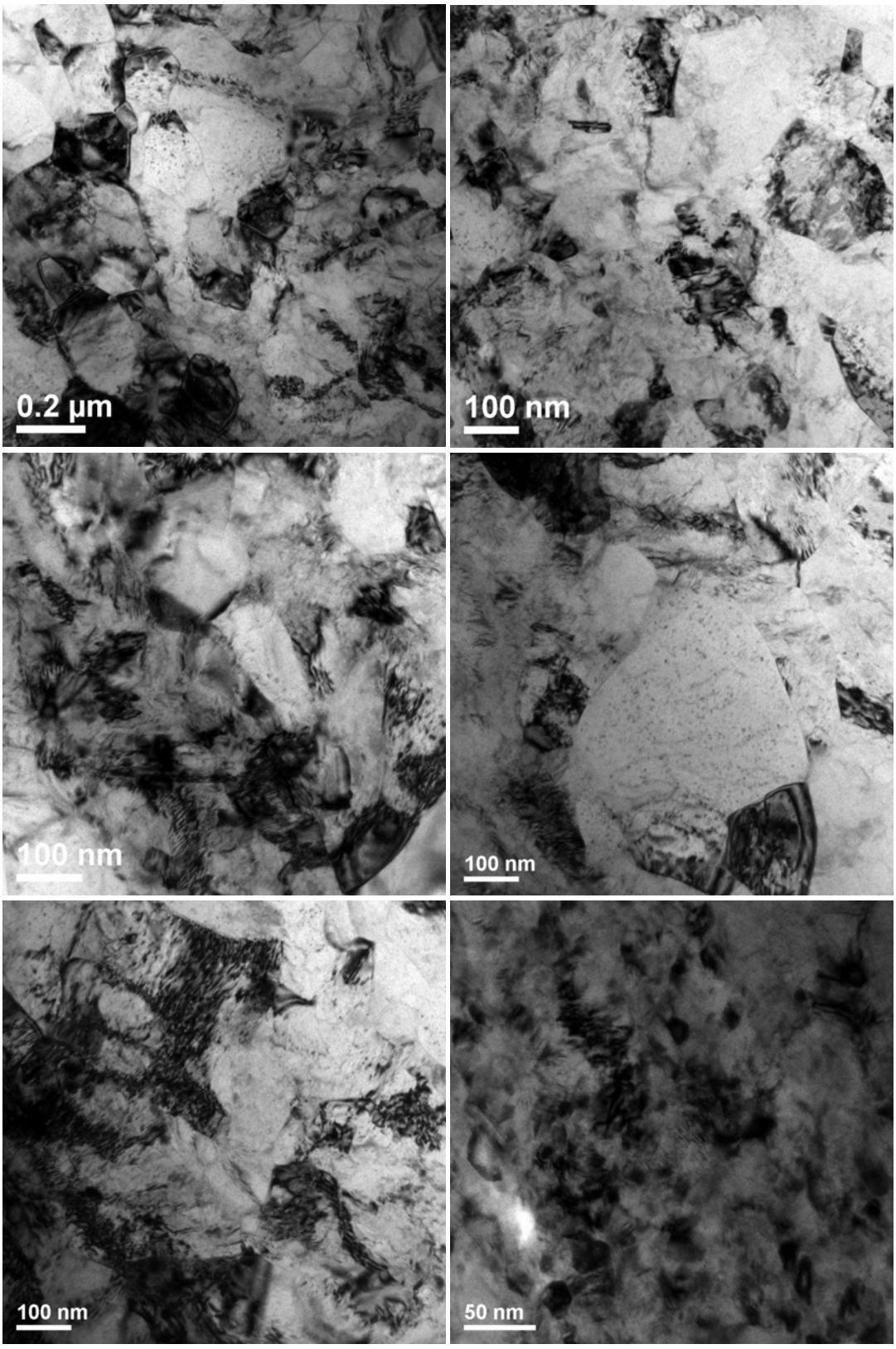
0.2 µm
100 nm
100 nm
100 nm
100 nm
50 nm

(A7) Samples subjected to LNT compression on a gas gun apparatus

($\dot{\varepsilon} = 6.9 \times 10^4\ s^{-1}$)

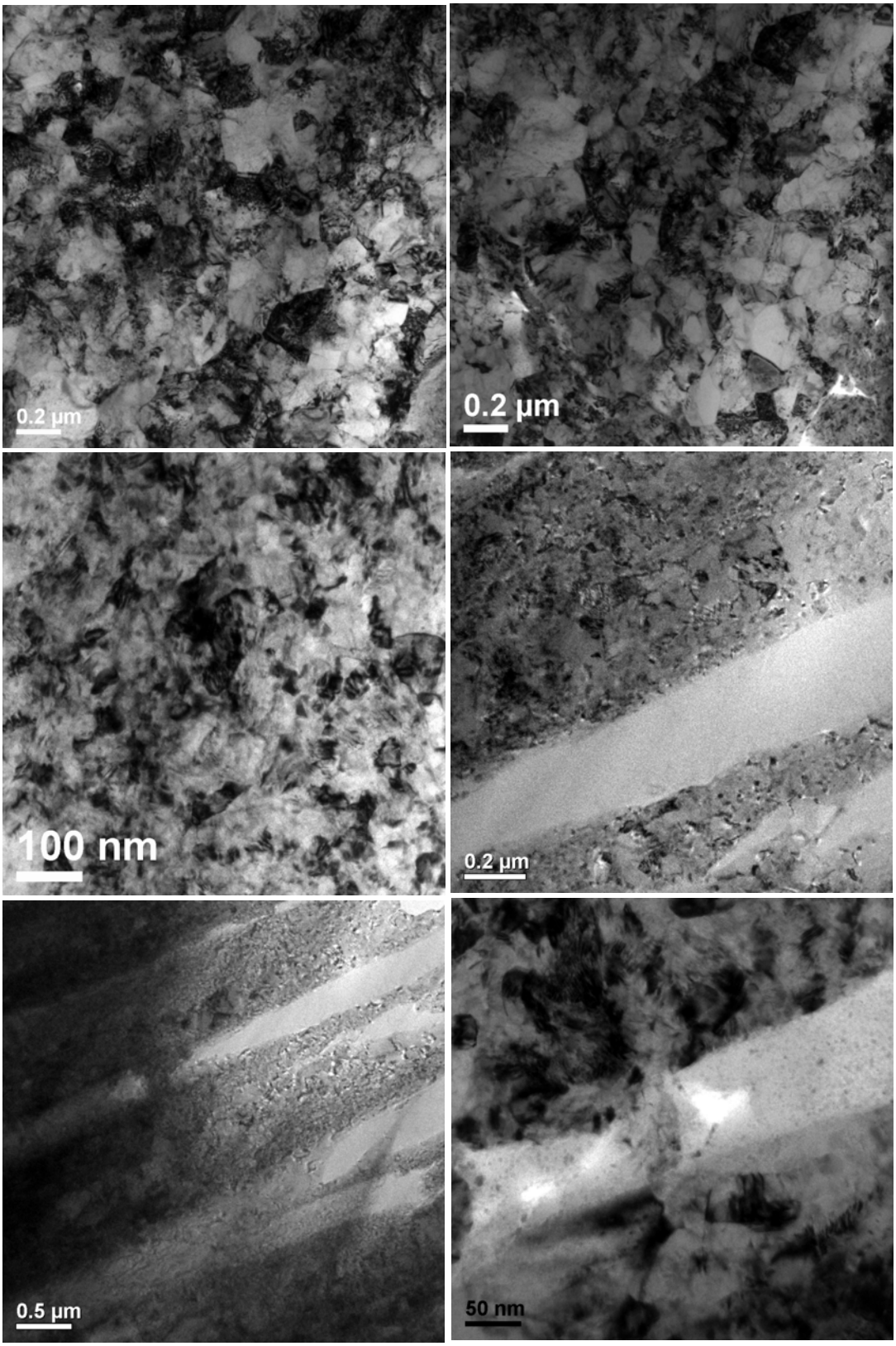

Appendix B

XRD line profile analysis

(B1) Observed XRD line profiles

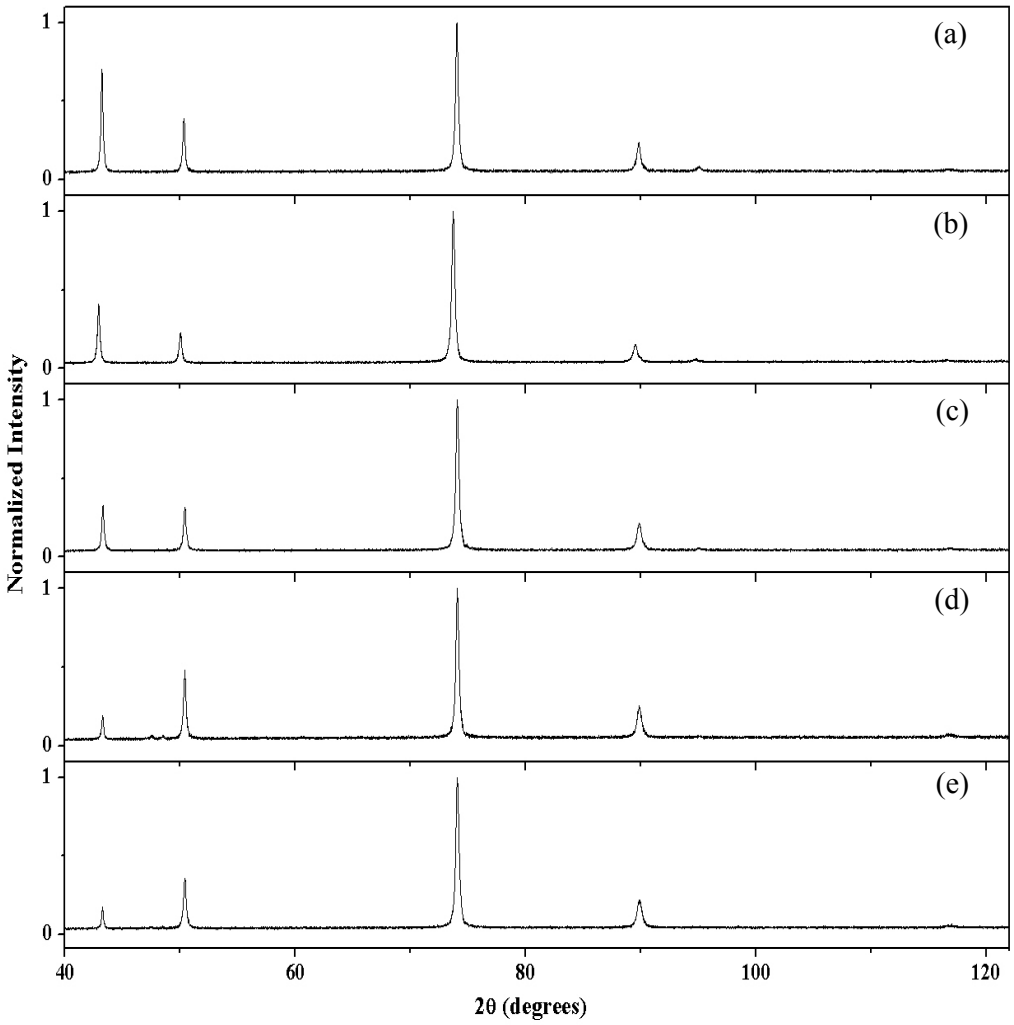

Figure B1 Observed XRD line profiles of samples deformed at different strain rates: (a) $6.9\times10^{4}s^{-1}$ (gas gun) (b) $5.7\times10^{3}s^{-1}$ (split Hopkinson pressure bar) (c) $4.8\times10^{2}s^{-1}$ (drop tester) (d) $1.9s^{-1}$ (Shimadzu universal testing machine) (e) $9.4\times10^{-2}s^{-1}$ (Shimadzu universal testing machine)

(B2) Determination of *q* (Chapter 5) that is related to the type (i.e. edge and/or screw) of dislocations; according to [121, 122], *q* is determined as the slope of the linear line fitted to data points that are obtained from experiments and shown in the graphs below. This enables determination of the dislocation contrast factor, expressed by equation 5.15. Figures (a), (b), (c), (d) and (e) correspond respectively to samples deformed at the strain rates of $6.9\times10^{4}s^{-1}$, $5.7\times10^{3}s^{-1}$, $4.8\times10^{2}s^{-1}$, $1.9s^{-1}$ and $9.4\times10^{-2}s^{-1}$.

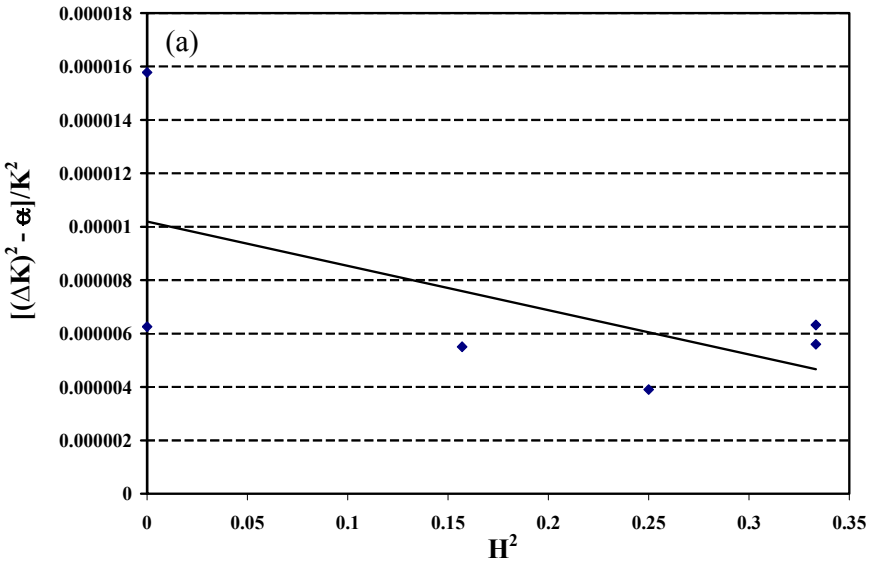

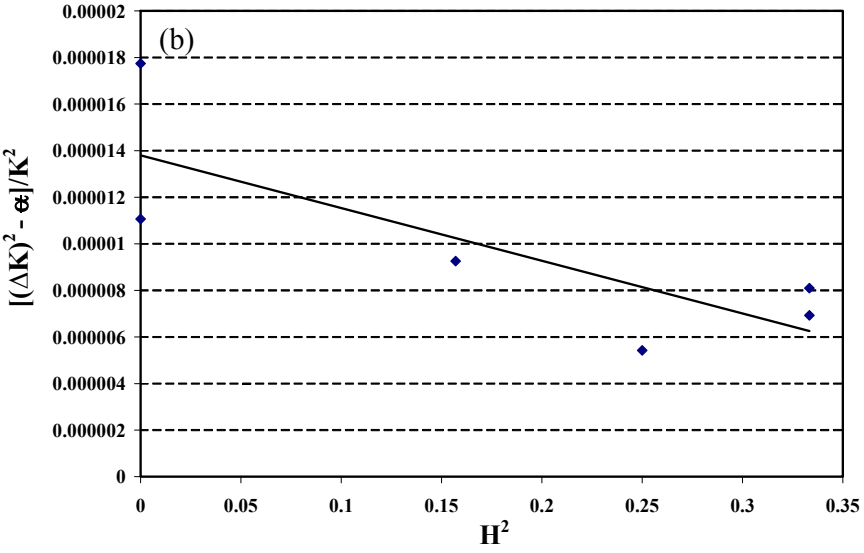

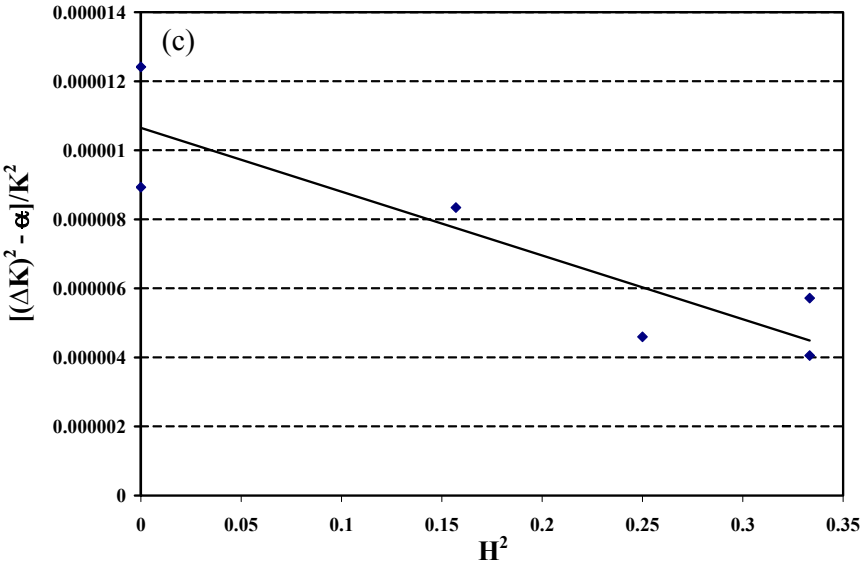
(c)
0.000014
0.000012
0.00001
0.000008
0.000006
0.000004
0.000002
0
[(ΔK)² - ε]/K²
0
0.05
0.1
0.15
0.2
0.25
0.3
0.35
H²

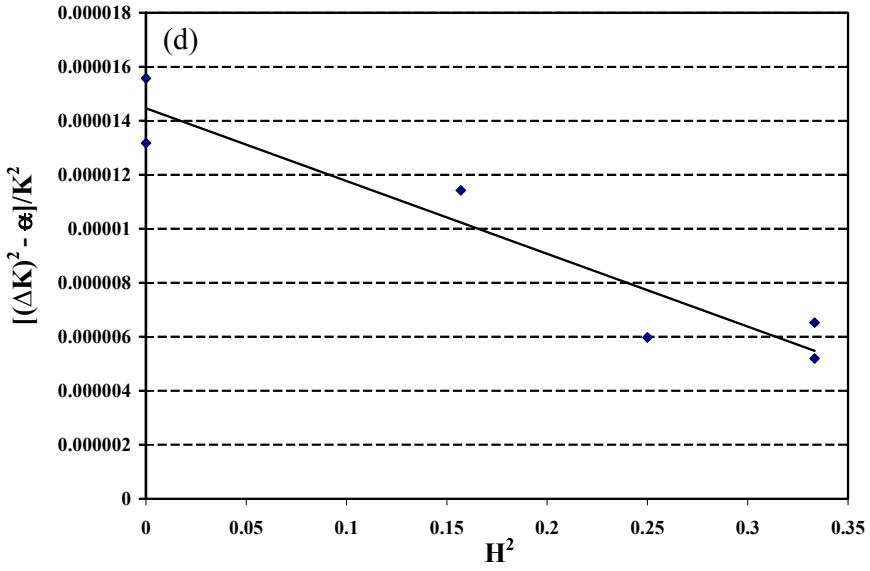
(d)
0.000018
0.000016
0.000014
0.000012
0.00001
0.000008
0.000006
0.000004
0.000002
0
[(ΔK)² - ε]/K²
0
0.05
0.1
0.15
0.2
0.25
0.3
0.35
H²

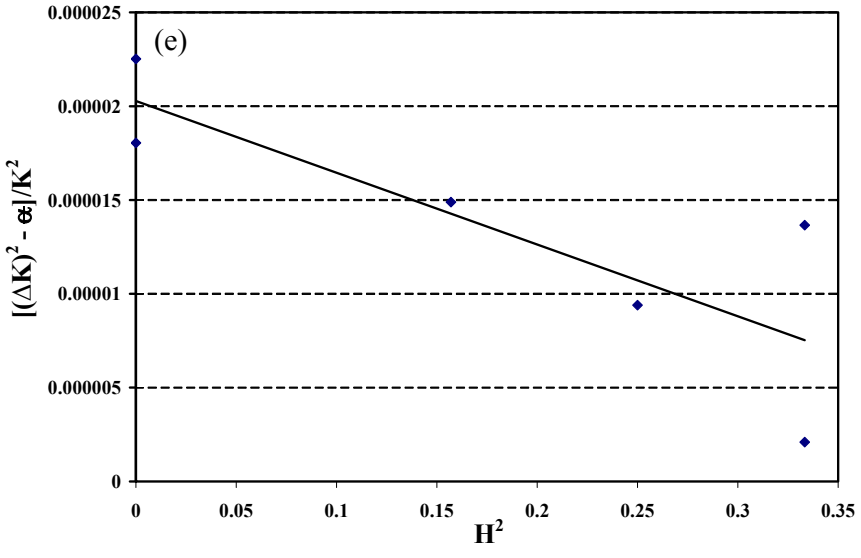
(e)
0.000025
0.00002
0.000015
0.00001
0.000005
0
[(ΔK)² - ε]/K²
0
0.05
0.1
0.15
0.2
0.25
0.3
0.35
H²

Appendix C

DSC curves

Figures (a), (b), (c), (d) and (e) correspond respectively to samples subjected to LNT compression at the strain rates of $6.9\times10^{4}s^{-1}$, $5.7\times10^{3}s^{-1}$, $4.8\times10^{2}s^{-1}$, $1.9s^{-1}$ and $9.4\times10^{-2}s^{-1}$. The three samples used for measurement corresponding to a particular strain rate are distinguished by the difference in line types.

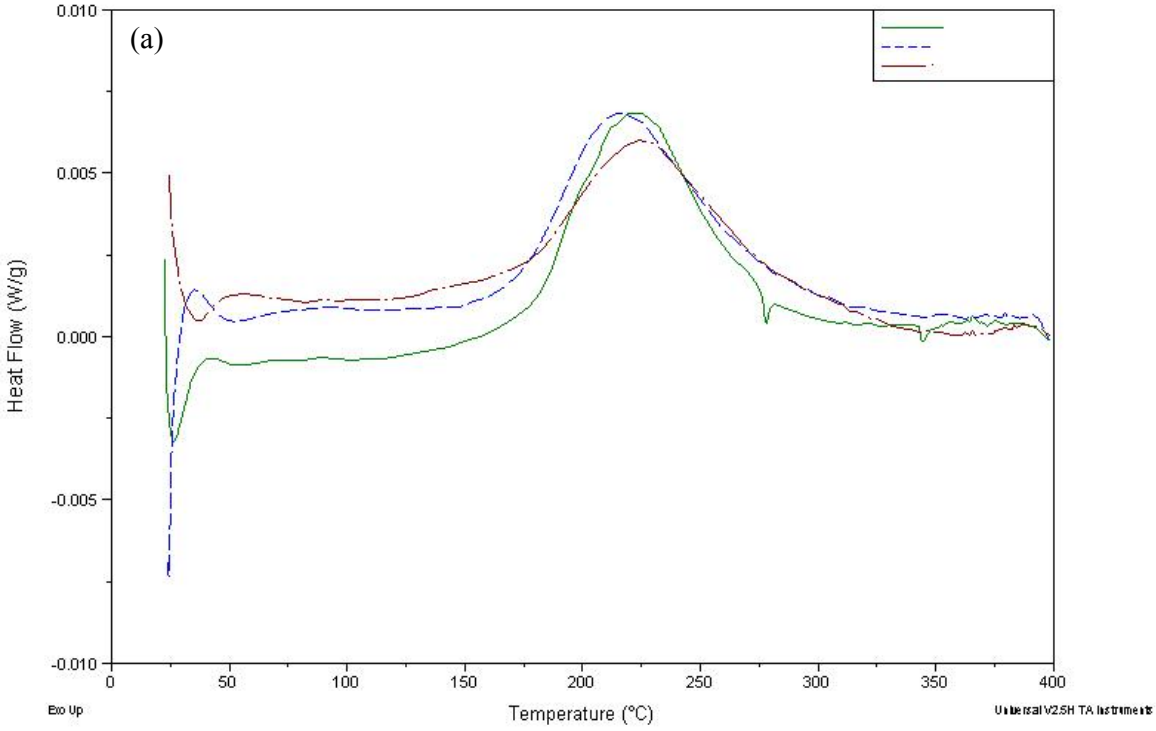

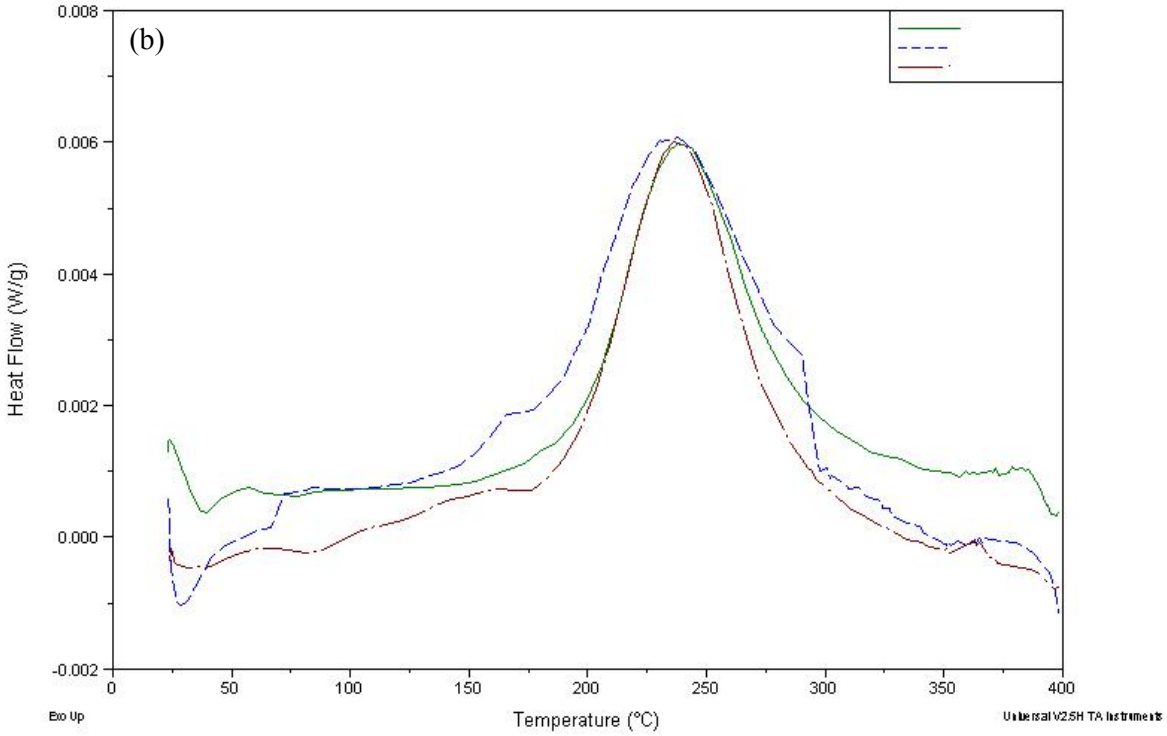
(b)
0.008
0.006
0.004
0.002
0.000
-0.002
Heat Flow (W/g)
0
50
100
150
200
250
300
350
400
Temperature (°C)
Exo Up
Universal V2.5H TA Instruments

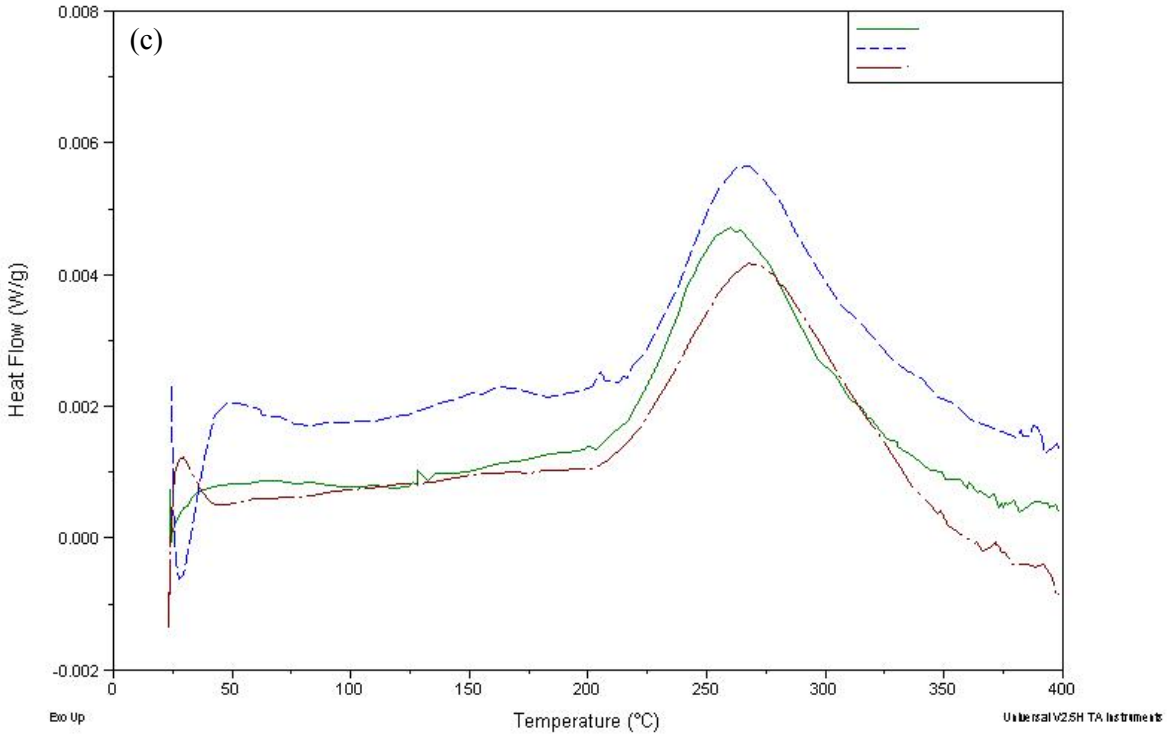
(c)
0.008
0.006
0.004
0.002
0.000
-0.002
Heat Flow (W/g)
0
50
100
150
200
250
300
350
400
Temperature (°C)
Exo Up
Universal V2.5H TA Instruments

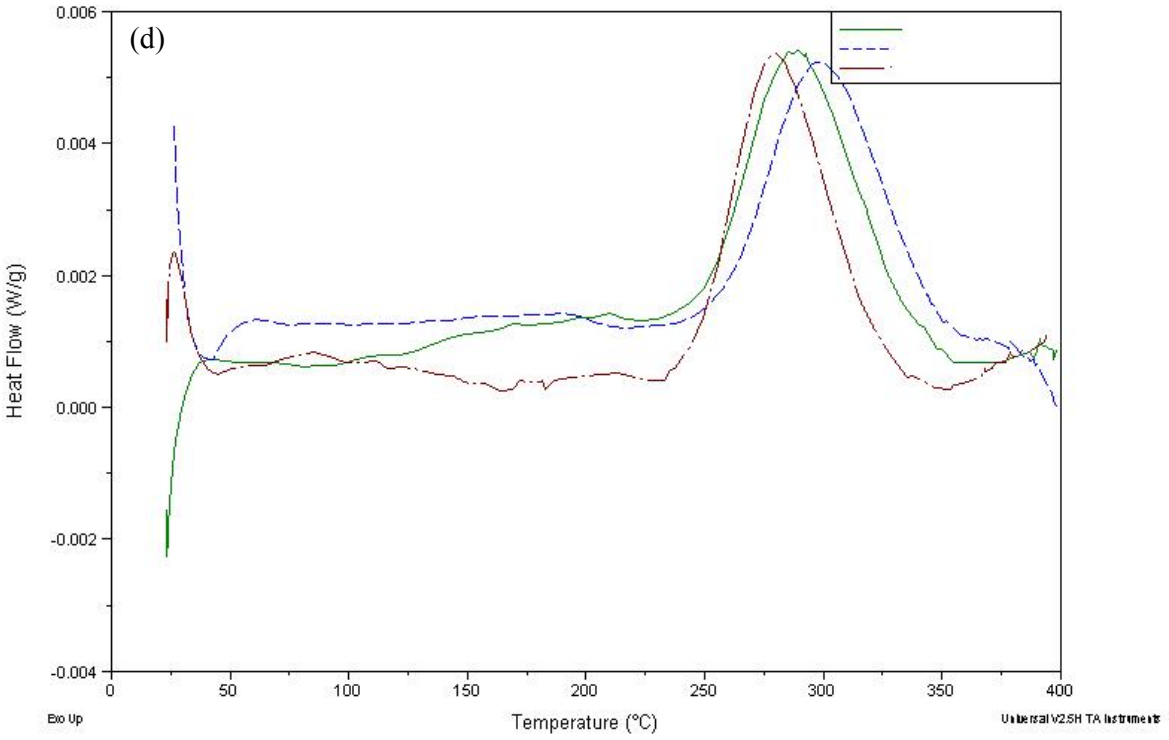
(d)
0.006
0.004
0.002
0.000
-0.002
-0.004
Heat Flow (W/g)
0
50
100
150
200
250
300
350
400
Temperature (°C)
Exo Up
Universal V2.5H TA Instruments

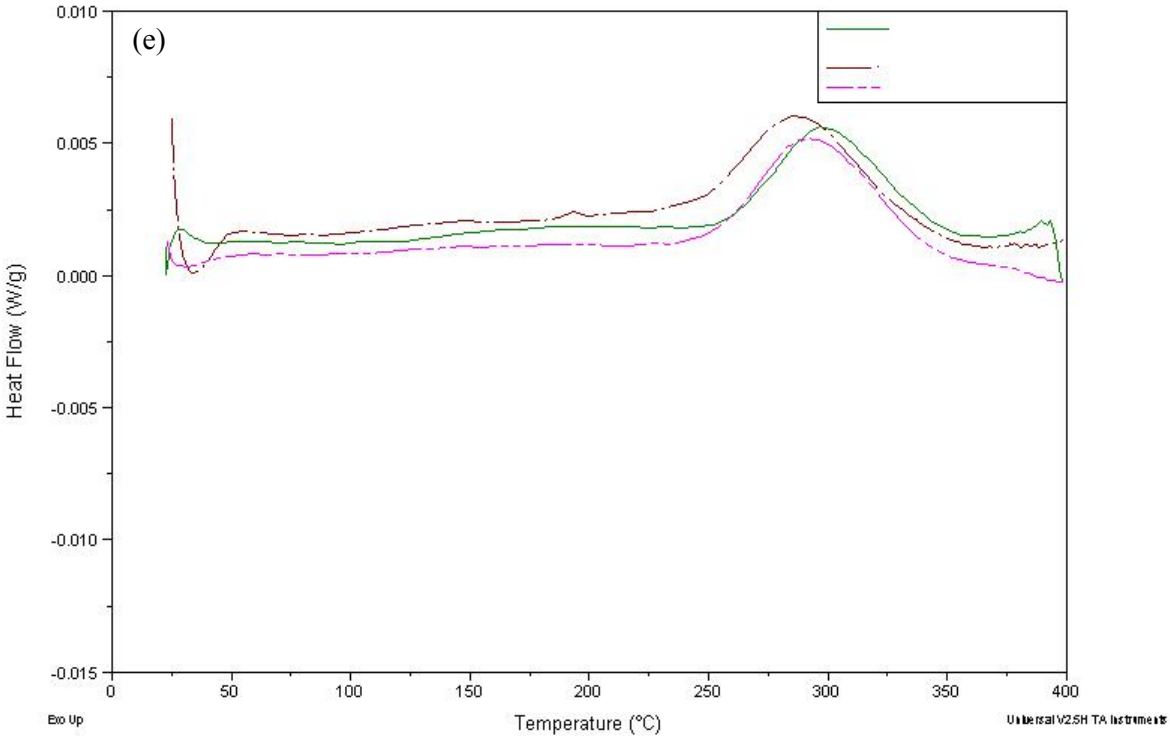
(e)
0.010
0.005
0.000
-0.005
-0.010
-0.015
Heat Flow (W/g)
0
50
100
150
200
250
300
350
400
Temperature (°C)
Exo Up
Universal V2.5H TA Instruments

Appendix D

Micro-hardness test readings

Reading of Vickers micro-hardness value (HV) corresponding to an individual indentation made on samples prepared under a particular condition is listed in the tables below.

(D1) Samples subjected to 2DC at RT (∑ε denotes cumulative strain)

HV (∑ε = 1.39)		HV (∑ε = 2.08)		HV (∑ε = 2.77)		HV (∑ε = 4.16)		HV (∑ε = 5.55)		HV (∑ε = 8.32)	
107	113	119	118	121	121	127	121	121	124	119	118
111	108	113	115	124	128	120	123	117	122	116	129
113	102	117	119	117	124	127	125	122	125	125	123
106	116	114	118	119	122	128	128	118	123	119	122
108	110	109	121	123	127	127	116	123	115	121	119
109	110	112	119	122	123	121	124	129	119	119	119
111	112	112	119	122	124	124	121	121	123	118	127
110	116	110	120	118	125	125	121	125	118	122	122
112	114	112	122	115	121	122	118	124	122	123	130
105	115	117	119	123	117	118	121	119	125	124	133
112	111	109	116	120	123	123	122	126	119	120	120
116	109	109	115	123	122	128	115	125	122	118	119
111	115	121	110	121	125	128	119	123	116	120	127
103	112	118	123	127	121	118	127	129	122	126	124
110	116	104	114	127	121	125	119	122	125	125	123

(D2) Samples multiple forged at RT (∑ε denotes cumulative strain)

HV (∑ε = 8.32)		HV (∑ε = 12.5)		HV (∑ε = 20.8)		HV (∑ε = 27)		HV (∑ε = 33.3)	
120	124	125	124	126	120	121	119	123	128
122	123	122	121	127	130	122	120	120	125
121	120	124	122	126	129	120	123	120	122
119	122	125	123	128	127	120	119	122	125
120	124	124	123	127	128	119	120	130	125
124	122	128	123	128	128	123	123	126	128
121	123	121	125	125	124	125	119	127	126
126	127	126	123	129	122	120	121	126	123
124	125	127	123	126	123	121	124	128	120
127	126	119	124	126	126	120	121	126	120
123	123	122	120	129	123	120	119	124	126
124	126	123	121	125	127	120	126	124	128
122	123	121	119	124	129	120	126	125	126
120	126	123	122	123	128	120	123	121	128
124	129	122	122	123	120	120	126	122	125

(D3) Samples subjected to dynamic uniaxial single compression at RT (Chapter 4)

Initially hardened by 2D6C					**Initially annealed sample**					
92.9	76	83.6	77.5	73.9	77.5	72.7	74.1	74.7	82.5	70.3
80.8	76.5	85.7	76.9	79.3	65.8	68.9	74.8	74.9	66.1	78.8
80.8	81.2	75.7	81.9	78.8	67.5	69.4	70.2	73	70	67.3
80.7	77.1	80.1	74.4	81.2	69.2	71	74.1	78.2	68	67.4
78.7	75.5	78.8	75.4	81.7	77.6	65.9	70.5	62.8	69.5	68.6
78.6	82.1	74.6	77.4	74.3	75.6	78.3	69	73.5	70.6	65.1
77.3					65.3	71.9				

(D4) Samples subjected to LNT compression on a gas gun apparatus

($\dot{\varepsilon} = 6.9 \times 10^{4}\ s^{-1}$)

144	142	134	143	139	134	139	150	155	144	150	135	129	131	154
140	152	141	140	136	134	139	156	148	151	140	137	130	133	149
140	144	143	145	145	141	147	147	148	150	133	145	143	154	144
139	137	147	139	132	138	142	140	146	147	143	139	146	146	140
151	121	138	134	141	138	135	139	143	151	144	143	140	140	146
142	142	141	146	142	137	158	136	144	150	142	141	148	135	145
155	154	128	148	143	137	158	142	150	149	137	143	139	137	153
146	151	136	147	140	140	152	148	153	147	145	138	136	143	138
150	148	139	139	140	145	145	134	156	146	141	138	143	146	143
163	144	144	152	147	138	148	135	152	145	143	135	137	138	143
130	132	150	146	143	142	140	142	147	142	144	141	138	136	140

(D5) Samples subjected to LNT compression on a Split Hopkinson Pressure Bar

($\dot{\varepsilon} = 5.7 \times 10^{3} s^{-1}$)

137	149	130	147	143	134	125	141	138	131	140	131	129	138	132
137	155	137	148	140	137	143	139	136	127	135	132	128	129	136
141	134	138	142	131	134	135	138	138	135	136	125	128	142	138
137	136	138	129	152	139	132	130	145	138	146	128	126	128	132
137	131	135	131	136	140	132	137	134	131	146	133	135	134	136
127	151	134	130	145	130	134	138	137	133	133	130	134	134	140
128	145	133	134	141	140	135	135	136	133	134	130	133	132	140
139	135	133	139	135	128	139	141	133	133	141	133	135	129	134
145	140	132	140	134	123	138	139	130	133	144	137	132	134	141
140	129	148	133	135	130	131	135	134	137	135	131	130	132	139
139	135	134	132	134	143	136	139	129	133	134	127	128	143	

(D6) Samples subjected to LNT compression on a drop tester ($\dot{\varepsilon} = 4.8 \times 10^{2} s^{-1}$)

135	139	136	134	128	123	128	128	132	131	132	135	139	133	134
132	131	132	131	129	132	133	133	127	137	135	136	133	133	132
139	128	132	130	130	132	141	133	127	139	136	133	132	132	130
129	127	127	129	130	135	132	133	132	136	133	135	130	134	128
132	129	127	133	130	141	139	137	126	129	134	134	154	128	133
130	129	130	129	134	128	134	127	133	136	129	132	135	133	132
135	133	129	137	134	142	125	128	127	137	137	138	137	132	132
130	134	128	127	136	136	134	134	130	135	136	128	141	131	131
133	133	132	132	129	135	131	128	132	135	137	131	136	130	141
137	134	127	132	131	137	123	127	129	131	133	137	144	130	131
132	125	127	133	128	133	133	135	133	133	136	138	133	129	

(D7) Samples subjected to LNT compression on Shimadzu Universal Testing Machine ($\dot{\varepsilon} = 1.9 s^{-1}$)

130	134	133	126	133	127	131	132	129	133	131	132	125	124	130
125	126	130	128	125	131	126	129	132	129	131	132	124	132	126
135	130	127	120	117	131	128	131	133	129	130	131	129	133	129
130	135	132	119	126	129	125	131	133	138	128	131	127	134	130
127	132	126	118	126	127	124	132	129	131	132	128	136	131	129
128	128	123	117	128	127	127	129	126	134	125	129	127	128	126
126	129	135	125	120	130	126	128	130	128	126	128	128	132	124
134	129	123	123	120	127	127	135	127	127	130	136	127	135	
134	134	127	121	123	124	127	132	127	124	132	137	126	138	
134	134	117	118	120	126	126	124	127	128	127	130	134	133	
132	136	123	122	123	128	128	128	126	129	129	129	129	134	
130	130	120	125	125	135	125	128	130	127	133	128	130	131	
133	130	127	126	129	130	130	132	129	126	132	124	131	127	

(D8) Samples subjected to LNT compression on Shimadzu Universal Testing Machine ($\dot{\varepsilon} = 9.4 \times 10^{-2} s^{-1}$)

129	128	128	126	129	135	129	128	123	126	127	124	128	127	130
126	128	125	126	125	136	129	128	128	130	130	123	124	125	125
128	121	126	130	124	128	121	128	118	124	128	130	141	133	128
135	128	129	124	127	132	133	133	123	136	133	132	136	128	129
138	125	125	127	126	132	125	125	128	132	125	124	121	136	136
131	132	120	124	130	127	129	127	125	131	131	126	133	134	131
129	140	124	123	135	131	129	131	123	130	125	130	137	137	127
126	127	118	127	119	133	126	136	124	123	129	122	137	136	123
133	129	125	124	130	130	130	125	126	132	130	134	129	125	126
129	132	122	132	131	134	123	123	126	128	136	123	122	141	130
126	133	121	127	131	132	129	121	125	126	126	130	128	136	128
132														

Appendix E

MATLAB files

(E1) Determination of XRD line profile at diffraction angle xc due to instrumental broadening

```
clear all;

% input center of peak profile-xc
xc=116.62;      % unit:degree,2theta

% step for angles and number of data intervals
step=0.01; % unit:degree,fixed in the current case
N=600 ; % number of data intervals,fixed in the current case

% parameters regarding instrumental broadening IB (integral breadth)-
--------U,V,W
U=0.0149117527;
V=-0.0032277796;
W=0.0135977333;

% parameter regarding angular dependence of SF (shape
factor=FWHM/IB)--------a,b,c
a=0.0000095772;
b=-0.0033554762;
c=0.9250988407;

% calculation of tan_th
tan_th=tan((xc/2)*pi/180);

% calculation of IB and SF
IB=sqrt(U*tan_th^2+V*tan_th+W);
SF=a*xc^2+b*xc+c;

%calculation of Voigt parameter---------k
A0=0.9039645;
B0=0.7699548;
C0=1.364216;
D0=1.136195;
E0=0.9394372;
k=((E0*A0-SF*C0)+sqrt(((SF*C0-E0*A0)^2)-4*(SF*D0-E0*B0)*(SF-
E0)))/(2*(SF*D0-E0*B0));

%calculation of Gauss and Cauchy component of integral breadth
IB_G=IB*exp(k^2)*(1-erf(k)); % Gauss component
IB_C=IB_G*k*sqrt(pi);        % Cauchy component

%calculation of HWHM (half width at half maximu) of Gauss and Cauchy
%components
```

```
HWHM_G=IB_G/sqrt(pi/log(2)); % Gauss component
HWHM_C=IB_C/pi;

%calculation of the voigt profile at the angle of xc, showing the
%instrumental broadeing at that angle
 min_angle=-step*(N/2);
 max_angle=step*(N/2);
 x=[min_angle:step:max_angle];
 y=[2*min_angle:step:2*max_angle];
 c_l=0; %center of profile,set to zero
 BKG=0; %background level, set to zero for the current case
 Im=1; %peak maximum intensity, set to unity for the current case
 g_f=BKG + Im.*exp(-(log(2))*((x-c_l).^2)/(HWHM_G^2)); %Gaussian
function
 c_f=BKG + Im./(1+((x-c_l)./HWHM_C).^2);                %Cauchy
function
 v_f=100*conv(g_f,c_f)/max(conv(g_f,c_f)); %Voigt profile,
convolution of gauss and cauchy functions,normalized with maximum
intensity of 100
 plot(x,g_f,'c',x,c_f,'g',y,v_f,'r')

%print out data characterizing intrumental broadeing at a certain
angle,described by the voigt function
voigt=fopen('intrument_broadening.txt','w');
for i=1:length(y)
    fprintf(voigt,'%20.15f %20.15f %20.15f\n',y(i)+xc,-N+i-1,v_f(i));
end
```

(E2) Calculation for the variation of sample temperature during uniaxial single compression; the sample has been cooled to liquid nitrogen temperature

```
% this program is to calulate the temperature rise of sample immersed
in LNT
%% The flow stress is described by Preston-Tonks-Wallace
% (PTW) constitutive model
%% herein the maximum heat flux is used for calculation as an example
%%%%  reference title:
%%    <<an evaluation of plastic flow stress models for the
simulation of
%%%% high-temperature and high-strain-rate deformation of metals>>
%%%  author name is:Biswajit Banerjee

clear all;
%%%% inputs of true strain rate,initial temperature of sample and IHF
before running the program
epsilon_dot=0.094; %strain rate, unit: /s
T0=77; %%initial temperature of sample,unit:Kelvin
IHF=0.7;%%value of IHF

%%% parameters of the deformed sample
A0=(2.1*0.001)*(5.7*0.001)*4; %%%initial area of the sample surface
contacting the liquid nitrogen, unit: m^2
V=(2.1*0.001)*(2.1*0.001)*(5.7*0.001); %%% volume of the sample, unit:
m^3
Cp0=0.0000416*T0^3-0.027*T0^2+6.21*T0-142.6; %specific heat of copper
sample while T<=270 Kelvin
```

```
%%% heat flux at the interface
B=0.19; %% contant in the equation for the maximum heat flux
Pg=4.66; %% the vapor density of LN2 at 77K; unit -kg/m^3
Pf=806; %% the liqud density of LN2 at 77K; unit -kg/m^3
sigma=0.00893; %% surface tension of the liquid at 77K; unit - N/m
g=10; %% gravitational constant; unit-m^3-kg^(-1)-s^(-2)
Hfg=199*1000; %% latent heat of vaporization at 77K; unit-j/kg


q_max = B*Hfg*Pg*((g*sigma*(Pf-Pg)/(Pg^2))^(1/4)); %%maximum heat
flux (J/(m^2-s))

%%% step of strain for calculation
step=0.0005; %% step of strain


%%% values of contant parameters in the PTW constitutive model
s0=0.0085;
s00=0.00055;
y0=0.0001;
y00=0.0001;
d=2;
kapa=0.11;
gama=0.00001;
theta=0.025;
M=63.546;
s1=0.25;
y1=0.094;
y2=0.575;
Tm0=1356.5; % unit: Kelvin
a=1.5; %parameter in the SCG model for the melting temperature of
copper


 %% calculation of yita=density/density0 (valid when T<700K);

Cw=8930*3933*3933*0.005; %%% constant to calculate yita


 %%%initial conditions
 yita=1;


 T_bar0=T0/Tm0;
 J0=1+exp((-1)*(1+(1/0.04))/(1+0.04/(1-T_bar0)));
 miu0=(1/J0)*((50.7+1.3356*1.99*8930*Cp0*(T0-300)*(1e-9))*(1-
T_bar0)+8930*yita*(1.3806E-23)*T0*(1E-9)/(0.057*63.55*(1.66E-27)));%%
unit:GPa
 xitadot0=0.5*((4*pi*8930/(3*M*(1.66E-
27)))^(1/3))*sqrt(miu0*(1E9)/8930);%% unit: /s
 tau_s0 = max(s0-(s0-
s00)*erf(kapa*T_bar0*log(gama*xitadot0/epsilon_dot)),
s0*((epsilon_dot/(gama*xitadot0))^s1));
 tau_y0 = max(y0-(y0-
y00)*erf(kapa*T_bar0*log(gama*xitadot0/epsilon_dot)),
min(y1*((epsilon_dot/(gama*xitadot0))^y2),s0*((epsilon_dot/(gama*xita
dot0))^s1)));
 alpha0=(s0-tau_y0)/d;
```

```
 bita0=(tau_s0-tau_y0)/alpha0;
 fi0 = exp(bita0)-1;
 sigmay0 = 2*(tau_s0+alpha0*log(1-fi0*exp((-1)*bita0-
(theta*0/(alpha0*fi0)))))*miu0*1000;%unit: MPa

 %%%% output data file
 stres=fopen('temp_max.txt', 'w');


 %% calculation of stress
 for i=1:10000

     epsilon(i)=i*step;
     sigmay(i)=2*(tau_s0+alpha0*log(1-fi0*exp((-1)*bita0-
(theta*epsilon(i)/(alpha0*fi0)))))*miu0*1000; %unit:MPa

deltaT_rise(i)=IHF*(0.5*(sigmay(i)+sigmay0)*step)*(1e6)/(Cp0*yita*893
0); %temperature rise due to plastic work
     deltaT_cool=q_max*A0*(step/epsilon_dot)/(Cp0*8930*V);
     T(i)=T0+deltaT_rise(i)-deltaT_cool;
     Tc=T(i);
     if Tc<77
         T(i)=77;
     end

     if T(i)>270
     Cpc=0.1009*T(i)+358.4; %specific heat while T>270 Kelvin
     else
     Cpc=0.0000416*T(i)^3-0.027*T(i)^2+6.21*T(i)-142.6; %specific
heat while T<=270 Kelvin
     end
    A(i)=4*sqrt(V*(5.7*0.001)/(exp(epsilon(i)))); %%% area of
deformed sample contacting liquid nitrogen
    P(i)=sigmay(i)*(10^6)/3; %pressure

    if T(i)<700
    Cs(i) = P(i)-1.99*8930*Cpc*(T(i)-300);  %%% constant to calculate
yita
    else
        Cs(i) = P(i)-2.12*8930*Cpc*(T(i)-300); %%% constant to
calculate yita
    end

    Q=Cs(i);
    a0=Q-4*Cw;
    b0=(-1)*(6*Q+792*Cw);
    c0=9*Q+796*Cw;
    poly=[a0 b0 c0];
    solution=roots(poly);

 for j=1:2
     if solution(j)>0
         yita=solution(j);
     end
 end
    Tm=Tm0*exp(2*a*(1-(1/yita)))*yita^(2*(1.99-a-(1/3)));
    T_bar(i)=T(i)/Tm;
    J(i)=1+exp((-1)*(1+(1/0.04))/(1+0.04/(1-T_bar(i))));
```

```
    miu(i)=(1/J(i))*((50.7+1.3356*(P(i)*(1e-9))/(yita^(1/3)))*(1-
T_bar(i))+8930*yita*(1.3806E-23)*T(i)*(1E-9)/(0.057*63.55*(1.66E-
27)));%% unit:GPa
    xitadot(i)=0.5*((4*pi*yita*8930/(3*M*(1.66E-
27)))^(1/3))*sqrt(miu(i)*(1E9)/(yita*8930)); %%% unit:/s
    tau_s(i) = max(s0-(s0-
s00)*erf(kapa*T_bar(i)*log(gama*xitadot(i)/epsilon_dot)),
s0*((epsilon_dot/(gama*xitadot(i)))^s1));
    tau_y(i) = max(y0-(y0-
y00)*erf(kapa*T_bar(i)*log(gama*xitadot(i)/epsilon_dot)),
min(y1*((epsilon_dot/(gama*xitadot(i)))^y2),s0*((epsilon_dot/(gama*xi
tadot(i)))^s1)));
    alpha(i)=(s0-tau_y(i))/d;
    bita(i)=(tau_s(i)-tau_y(i))/alpha(i);
    fi(i) = exp(bita(i))-1;
    A0=A(i);

    fprintf(stres,'%12.8f %12.8f %12.8f %12.8f\n', epsilon(i),
sigmay(i),T(i),miu(i));
    sigmay0=sigmay(i);
    miu0=miu(i);
    tau_s0=tau_s(i);
    alpha0=alpha(i);
    bita0=bita(i);
    fi0=fi(i);
    T0=T(i);
    Cp0=Cpc;


 end
     fclose (stres);
```